Stephan Dunkl, Dipl.-Ing.

Control Aspects of Single and Three Phase PM Drives in Fractional Power Applications

DOCTORAL THESIS

to achieve the university degree of

Doktor der technischen Wissenschaften

submitted to

Graz University of Technology

Supervisor

Univ.-Prof. Dr.-Ing. Annette Mütze
Electric Drives and Machines Institute, Graz University of Technology

Co-Supervisor

Prof. Dr. Zi-Qiang Zhu
Department of Electronic and Electrical Engineering, University of Sheffield

Graz, January 2016

AFFIDAVIT

I declare that I have authored this thesis independently, that I have not used other than the declared sources/resources, and that I have explicitly indicated all material which has been quoted either literally or by content from the sources used. The text document uploaded to TUGRAZonline is identical to the present doctoral thesis.

.....	.....
Date	Signature

Contents

Abstract

In order to secure today's automotive freedom under the increasingly tight environmental constraints of the near future, the energy usage of all of a vehicle's components needs to be drastically reduced. This considerably increases the demands on the on-board thermal management and requires the energy efficiencies of the fan and pump systems to be significantly improved and their sizes and costs reduced.

In the near past a rapid development of the electronic industry can be denoted, leading to lighter, faster and more efficient electronic system. Thus, power electronics have become the focus of attention in all kind of technical fields, changing the way we operate electronic systems. This has led to hydraulic, mechanical and throttled controlled drive systems being replaced by variable speed drives.

This work presents the design of a three phase permanent magnet brushless drive used for an auxiliary pump application in a modern vehicle. Furthermore, the design of a single phase permanent magnet brushless drive used for a fan application cooling a car's LED headlights will be presented. As customary for automotive applications, the electric drives used, need to fulfill some fairly restrictive operating conditions and specifications:

In order to meet these specifications, in contrast to classical system design concepts, in which the overall application is split into its individual technical fields, and all the components involved are designed separately, a modeling approach combining all components and their interactions is chosen. This multi-domain design approach thereby enables the energy, volume and mass savings potential to be exploited through the design of integrated concepts.

Furthermore, with the developed multi-domain models, different control strategies and topologies for both drives have been investigated, showing individual advantages of the different controls. Thereby, sensored as well as sensorless controls have been considered, leading to a final control design which suits the particular application of most.

Finally, the construction of a test bench capable of measuring all characteristics

of the two designed drives is presented and measurement results of the two drives are then compared to simulations, showing good congruity between the predicted and the actual behavior, and that both drives are able to fulfill the requirements determined by the specifications.

Zusammenfassung

Aufgrund der derzeitigen Belastungssituation unserer Umwelt sowie den damit, in Zukunft, verbundenen, immer strenger werdenden Umweltbeschränkungen, kann eine Veränderung der Automobilindustrie verzeichnet werden. Diese Veränderung betrifft dabei den Energie- sowie Treibstoffverbrauch aller Komponenten eines modernen Fahrzeuges. Im Wesentlichen werden dabei erhöhte Anforderungen an das thermische On-Board Management und den Energieverbrauch von Lüfter- sowie Pumpenanwendungen gestellt. Das beinhaltet eine drastische Effizienzverbesserung solcher Anwendungen als auch Größen- und Kostenreduzierung.

In den letzten zwei Jahrzehnten konnte eine starke Entwicklung der Elektroindustrie vernommen werden. Das führte im Besonderen in der Leistungselektronik zu immer kleineren, leichteren sowie energieeffizienteren Komponenten und elektronischen Systemen. Durch diese Entwicklung ist die Leistungselektronik in nahezu allen fachspezifischen Bereichen auf dem Vormarsch. Dabei ersetzen Antriebe mit integrierter Leistungselektronik in vielen Bereichen mechanische und hydraulische Antriebe. Im Weiteren verändern sie auch die Art wie wir diese neu eingesetzten drehzahlvariablen Antriebe betreiben und tragen daher einen großen Beitrag zu Energieeinsparung bei.

Diese Arbeit beschreibt die Entwicklung solcher moderner Antriebe. Dabei handelt es sich um Hilfsantriebe welche in einem modernen Vehikel eingesetzt werden. Im Detail wurde eine permanenterregte dreiphasige bürstenlose Gleichstrommaschine für eine Pumpenanwendung und eine permanenterregte einphasige bürstenlose Gleichstrommaschine für eine Lüfteranwendung entworfen und entwickelt. Wie üblich in der Automobilindustrie mussten dabei beide Antriebe stark einschränkenden Anforderungen genügen und auch unter härtesten Umgebungseinflüssen ihren Dienst verrichten.

Um den Anforderungen an die Antriebe gerecht zu werden, wurden beide Motoren im Gegensatz zum klassischen Designansatz, in welchem alle involvierten Fachbereiche getrennt betrachtet und deren Komponenten gesondert voneinander

entwickelt werden, ein Mehrbereichs-Designansatz gewählt. Dieser kombiniert alle implizierten Fachbereiche und ermöglicht dadurch die Entwicklung von Antrieben mit einer hohen Integrationsrate aller Komponenten sowie eine damit verbundene Optimierung der Antriebe hinsichtlich Masse, Volumen, Energieeffizienz und Leistungsdichte.

Mithilfe der entwickelten Mehrbereichsmodelle, wurden für beide Antriebe unterschiedliche Strategien zur Regelung und Schaltungen zur Ansteuerung untersucht. Dabei wurden sowohl geberbehaftete als auch geberlose Regelungen betrachtet. In der Arbeit werden anschließend Vor- und Nachteile der einzelnen Regelungen und Ansteuerschaltungen vorgestellt.

Abschließend präsentiert die Arbeit die Konstruktion eines Motorenprüfstandes für Antriebe kleiner Leistungsbereiche. Mit dem erarbeiteten Prüfstand wurden die designten Motoren vermessen und alle Simulationsergebnisse validiert. Der Vergleich von Simulations- und Messergebnisse zeigt dabei eine gute Übereinstimmung.

Acknowledgements

This thesis arose in the context of a scientific cooperation between the Electric Drives and Machines Institute of Graz University of Technology, under the direction of Prof. Dr. Annette Mütze, and Mechatronic Systems GmbH, Wies, Austria.

Firstly, I would like to express my sincere gratitude to my adviser Prof. Dr. Annette Mütze for her support and her caring for making this thesis possible and offering me the opportunity to work at the Electric Drives and Machines Institute at Graz University of Technology.

Next I want to thank Prof. Dr. Zi-Qiang Zhu from the Department of Electronic and Electrical Engineering of the University of Sheffield for accepting to co-examine my Ph.D. exam and the evaluation of my theses.

Next I want to thank Dipl.Ing. Hans-Jörg Gasser from Mechatronic Systems GmbH who agreed on financing the project and therefore making it possible for being a part of this scientific cooperation.

Special thanks go to Dr. Gerhard Schöner for many fruitful discussions, critical reflections on my results and always putting a great effort into providing hardware fabricated by Mechatronic Systems GmbH. All these essentially contributed to my better understanding of the topic.

I also would like to express my sincere gratitude to Dr. Johann Bacher, Dr. Klaus Krischan and Dr. Roland Seebacher for supporting me with valuable discussions, useful advices, and sharing their knowledge with me.

For interesting discussions about work but also on other possible topics and for spending a nice time together, also outside work, my sincere thanks go to colleagues Alex Connaughton, Klaus Lang, Klaus Sobe, Christian Paar, Werner Konrad, Alfred Traby, Helga Liebmann and Ewald Seelmeister.

Finally I want to thank my family for their endless support during and before the time I worked on this thesis and my girlfriend Tanja for her love and her constant encouragement.

Chapter 1

Introduction

1.1 Electric drives for automotive applications

The increasingly tight environmental constraints of the near future have been well recognized today and global electric energy supply has become a major concern for politicians, legislators, and scientists: According to the International Energy Agency, "demand for electric energy is set to continue to grow faster than for any other final form of energy", expanding by over 70 % between 2010 and 2035 (New Policies Scenario) [1]. Figure 1.1(a) shows that the transportation sector plays a key role in the world's total energy consumption. Furthermore, as shown in Figure 1.1(b), no change in this evolution is expected in the near future.

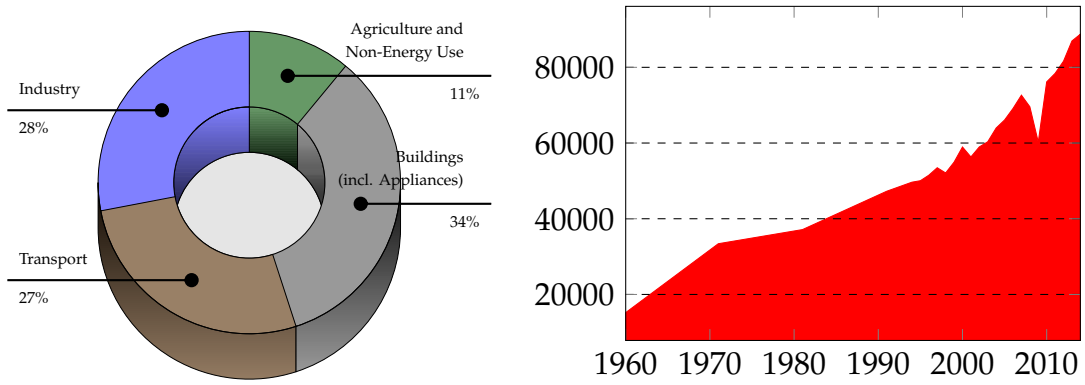

(a) Global energy demand by sector (2012) [1]

(b) Vehicle production volume in thousands of vehicles (data from [2])

Figure 1.1: World energy consumption per sector and trend of world vehicle production.

Recent agreements concerning CO_2 emission reduction demand for more "green" vehicles [3, 4]. This means that car producers (OEMs) need to reduce a vehicle's fuel consumption as well as pollution. To comply with these requirements new technologies like semi-hybrid, full hybrid and fuel cells vehicles have been developed [3, 5]. These technologies address the energy consumption of the vehicle's traction system itself.

In contrast to this, recently the energy consumption of a vehicle's auxiliaries has received increasing attention: Today, a modern vehicle may utilize up to one hundred auxiliary drives [6] (e.g. Figure 1.2). They are found in almost every vehicle application, e.g windshield wipers, window lifters, seat and mirror positioning, cooling fans, oil, fuel, and water pumps, electrical brakes and suspension systems [7]. Thus, as vehicle electrification is still constantly increasing, reducing energy

Figure 1.2: Modern vehicle showing a fraction of its auxiliary drive systems [8].

consumption of a vehicle's auxiliaries is becoming more and more important. This implies moving to electric drives with high energy conversion efficiencies, high power densities and less weight in order to reduce their energy consumption and thereby caused emissions.

1.2 Exploiting variable speed capabilities and mechanical integration

In the past two decades, the electronic industry has shown rapid developments towards cheaper, faster and lighter systems. These have transformed our society, as

for example illustrated by the changes in the way we communicate and exchange information. Of similar potential, yet currently still less obviously visible at the societal level, are such "rapid developments" within the field of "larger" electronic devices: The recent developments of these so-called "power electronics" devices with respect to power capability, reliability and price and their systems have significantly transformed the way we operate electric machines and the systems these machines are driving - such as pumps and fans - the main reason being the new variable speed capability, allowing motor speed and load to be optimized to the systems' requirements. For the variable speed applications of interest in this work, permanent magnet (PM) brushless machines with their flat torque/speed characteristics appear to be an excellent choice (Figure 1.3).

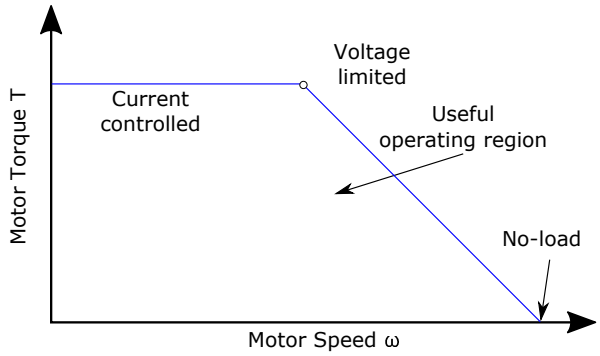

Figure 1.3: Torque/speed characteristic of a nonsalient-pole PM brushless motor [9].

The potential held by these systems is by far not fully exploited: The three fields involved, (i) electric machines, (ii) power electronics, and (iii) mechanical fan/pump, originate from historically separate, independent fields. They are therefore still frequently treated separately in the design processes, with the electric drive flanged onto the driven pump/fan. Systems design hence typically uses a "bottom-up" approach in which the different components are designed individually with predefined interfaces. Comprehensive "top-down" design techniques translating the demands on the overall system on the individual components and considering their interactions are lacking.

The work presented in the following, aims to contribute to closing this gap, presenting research on integrated concepts (Figures 1.4 and 1.6) and the required design and control techniques, so that eventually all available space may be exploited and the components be downsized.

(a) Cross-sectional drawing of a pump with integrated electric drive.

(b) External view of developed, integrated electric drive.

Figure 1.4: Pump for automotive applications with electric drive built by the company Mechatronic Systems GmbH and developed in the context of the work presented here.

1.3 Brushless permanent magnet drives

Ever since the first brushless machine type was presented, researchers have put enormous effort into designing and analyzing different topologies of these machines, resulting in many variations. This diversity is mainly driven by the fact that for individual applications particular machine designs are needed [9]. Nevertheless, in general all permanent magnet motors can be characterized as synchronous motors. Thereby, the majority of these motors consist of a rotor wearing permanent magnets and a stator having an armature stator winding mounted onto it. Since brushless motors have no mechanical commutation system, the rotating field has to be produced by the armature winding. For this reason, typically permanent magnet motors have an electronic commutation system supplying the armature windings with alternative currents [10]. Thus, due to the absence of a mechanical commutation system, brushless PM or electronically commutated (EC) motors provide advantageous properties as high efficiency, silent operation, compact form, reliability, and low maintenance [11, 12].

These advantages also make them the proper choice for small motors in automotive industry, as drives in this field tend to need the following characteristics [13]:

- Low cost,

- High reliability,
- Low acoustic noise and torque ripple,
- Long life cycle,
- Variable speed control,
- Integrated protection functions,
- High efficiency.

Three phase brushless permanent magnet machines

The main cost drivers for brushless permanent magnet motors can be defined by [14]:

- The number of motor strands and windings,
- Type of windings and how the windings are manufactured,
- The amount and quality of the built-in permanent magnets,
- The number and size of semiconductors in the inverter bridge,
- The complexity of control algorithm and the number and type of sensors needed.

For fractional power levels and high power density demands, the three phase brushless machines are the best choice. "Because they have extremely good utilization of copper, iron magnet, insulation materials, connection cables and power electronic devices, in terms of the quantity of these materials and the number of components required for a given output power" [9, 15].

All three phase permanent magnet machines are physically similar but can be classified into two categories: (1) The permanent magnet synchronous motor (PMSM or BLAC) which has a sinusoidal distributed back-EMF and (2) the brushless permanent magnet DC (BLDC) motor which comes with a trapezoidal back-EMF. Both machine types can be driven by the same three phase voltage inverter source, as shown in Figure 1.5(a), but their driving methods differ [16]. A PMSM motor's armature winding is typically exited by a three phase sinusoidal current (e.g. Figure 1.5(c)) while a BLDC motor is usually powered by a set of currents with a quasi-square waveform aligned with the flat top of the back-EMF voltage (e.g. Figure 1.5(b)) [17].

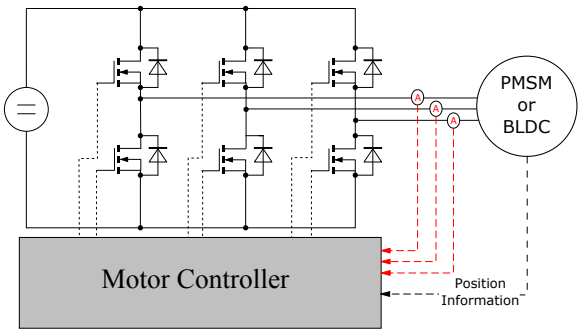

(a) Inverter for a three phase permanent magnet motor.

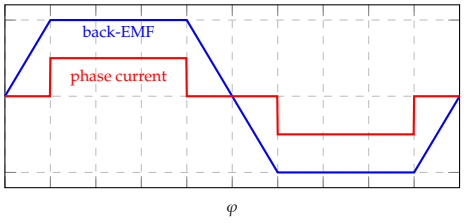

(b) Phase signals for trapezoidal control.

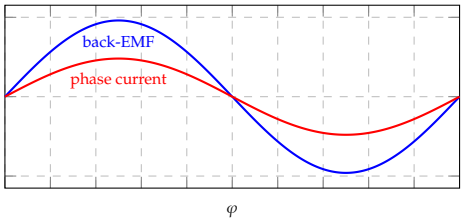

(c) Phase signals for sinusoidal control.

Figure 1.5: Principle circuit diagram of permanent magnet motor inverter with phase signals.

Thus, PMSM machines are preferred for applications where accuracy is desired, as in robotics, servo drives, solar tracking and numerically controlled machines [18]. Because of their higher demand for control complexity as well as position detection accuracy, these drives are often accompanied by increased costs.

For BLDC drives and their corresponding six step commutation scheme, only three hall sensors and a simple motor control are needed. Furthermore, if we compare a PMSM to a BLDC machine under the conditions that, both machines have same resistive losses and the same peak back-EMF voltages, the BLDC motor has approximately a 15% higher power density than the PMSM [19]. Thus, these drives seem to be the appropriate choice for fractional power drives in the automotive sector.

BLDC motors with trapezoidal back-EMF and rectangular current excitation are also well suited for concentrated winding arrangements. This will further decrease costs, comparing it to distributed windings as the coil and winding manufacturing processes are significantly easier.

Single phase BLDC machines

Though they typically have poorer operating characteristics as compared to their three phase counterparts, single phase PM BLDC motors are cost effective and easy

to mass manufacture. They are used in applications which require output power ranging from a fraction of a watt to a few tens of watts [20, 21].

Reviewing from [22], single phase BLDC machines in general suffer from slower starting characteristics, less efficient utilization of machine iron and copper, and higher losses. Therefore, single phase motors are limited to fractional power applications for which rapid response and high efficiency are not as important as costs. The primary advantage of single phase devices are simplified source requirements. For example, a single phase brushless dc motor requires only one-third the number of transistors and position sensors needed by a three phase motor.

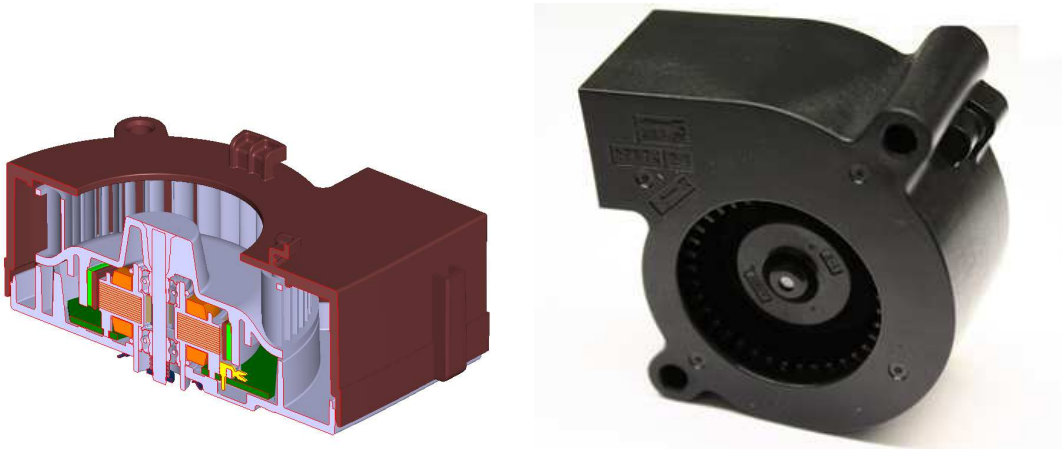

(a) Cross-sectional drawing of a fan with integrated electric drive.

(b) External view of developed, integrated electric drive.

Figure 1.6: Fan for automotive applications with electric drive built by the company Mechatronic Systems GmbH and developed in the context of the work presented here.

In principle, single phase BLDC machines have the same number of coils/slots as poles, provided that they have a unifilar winding pattern. Thereby, the coils are connected in series and wound on the stator in a vice-versa manner. In order to generate torque over one electrical period of the motor, the current has to alternate its polarity and, consequently, the motor windings must be fed by a full bridge inverter. If the motor is built with a bifilar winding pattern, only two switches are needed for the alternating phase current of the machine.

For single phase BLDC machines two types of torque may occur with non-salient PM motors [21]. 1) Cogging torque, generated by the interaction of the PMs on the

rotor and the stator teeth and 2) excitation torque, generated by the interaction of the stator winding field and the field from the magnets. However, as single phase motors always have same number of poles and slots they have the drawback that excitation and cogging torque have coincident zero torque positions which make these motors unable to start from these dead point positions. To overcome this starting problem, such motors are designed with an asymmetric air gap, which shifts the zero points of the excitation torque away from that of the cogging torque (e.g. [23–25]).

Often, external rotor designs are used for single phase BLDC machines. These designs have a high moment of inertia and therefore are able to compensate the relatively high torque ripple of single phase BLDC motors [26].

1.4 State of the art of fractional horsepower drives

Systems and applications used in every modern ship, car, train, plane and home are rapidly changing as a result of the second electronic revolution. The first revolution gave us microprocessors, PCs, cell phones and similar devices, and changed our ways of communication and concepts of information. The second electronic revolution, has given us power electronics, motor controllers, switching power supplies and hybrid cars and will enable more intelligence to be integrated into every system and therefore will redefine the way we control and operate systems [27].

Still, most of today's power electronic based drives and applications are designed by different companies and assembled from separately manufactured electric machines and power-electronics systems. This often entails an overall system design in which the separately developed subsystems are badly or not at all harmonized with one another. For example, as shown in Figure 1.7(a), many drives have their power electronics simply flanged onto the motor itself in the final assembly, causing a poorly integrated overall system which is bigger than necessary. Furthermore, a lag in design matching can cause subsystems to be oversized and therefore lead to additional costs. Therefore, combining the design and assembly processes of all system components often entails a highly integrated design, considering its individual components (e.g. Figure 1.7(b)), leaving no potential held by these systems unexploited.

The two drives developed in this work do not show a higher integration of power electronics and the electric machine than other products already on the market, due

(a) Power-electronics mounted directly onto the electric machine; Danfoss VLT®Drive Motor FCM 300 [28].

(b) Electric drive and power electronics integrated in a pump system [29].

Figure 1.7: Comparison of external and internal drive electronic placement.

to thermal limits of the power electronic devices. Nevertheless, as all components with all characteristics are well-known, the drives could be designed to be perfectly adjusted to the overall systems. This enables the energy conversion efficiencies of the individual design applications to be as high as possible.

1.5 Thesis overview

Chapter 2 starts with presenting the specifications for two drives for automotive applications which were designed. Furthermore, it introduces developed finite element motor models which have been used to investigate the behavior of the individual drives. The chapter ends by providing detailed information about the developed hybrid models. These models allow simulating the drives, operating within their actual applications and therefore behavior predictions of their final performances.

Chapter 3 investigates different constraints that arise during design process of machines the power and size of those investigated.

Chapters 4 and 5 review different topologies of controls for the two drives to be designed. Advantages and disadvantages of the particular drive topologies

are discussed. Furthermore, the techniques suiting the needs of the individual application at most are presented in more detail.

Chapter 6 gives a short review of the sensorless strategies which are available for three phase permanent magnet brushless machines and why these are not appropriate for the designed drives. Furthermore, the section will investigate the winding time sharing sensorless control the single phase BLDC drive. In contrast to the winding time sharing technique presented in [30], the sensorless control was analyzed for a single phase BLDC machine with a bifilar winding pattern.

The construction of a test bench which is applicable to measure the behavior of fractional power drives is presented in Chapter 7. The section also shows the practical implementation of the controls for the two drives, this includes description of hardware and explanation of key software features.

The chapter ends with a discussion of performance tests carried out on the prototype systems and their comparison with simulation results.

Chapter 2

Brushless DC motor & drive modeling

For the purpose of the investigations presented in this thesis, several simulation models have been implemented. This section describes these models in detail and discuss the advantages of the different approaches.

The section starts with presenting specifications for two automotive applications and continues with the description of the developed models on the basis of these systems.

2.1 Specifications

This section presents the specifications of the two drives designed. Furthermore, key choices of the particular designs that were made are detailed. These assumed that the target applications required customized high-efficiency and low-cost designs for small to medium volume production.

2.1.1 Pump application

The first target application was a diaphragm pump motor drive. The motor should meet the following specifications:

- The drive's dimensions, including its electronic parts, should not exceed a maximum diameter of $\varnothing = 42\,\text{mm}$ and a length of $l = 59\,\text{mm}$,
- Guaranteed performance for DC supply voltage of $U_{\text{dc}} \in \{10\,\text{V} \ldots 32\,\text{V}\}$,
- Operating temperature range of $\vartheta \in \{-40°\text{C} \ldots 110°\text{C}\}$,
- Maximum input current of $I_{\text{max}} = 2.5\,\text{A}$ for a supply voltage of $U_{\text{DC}} = 12\,\text{V}$.

The diaphragm pump should move air at a flow rate of $Q = 10\,\mathrm{Nl/min}$ and against a counter pressure of $p = 0.5\,\mathrm{bar}$. From these specifications of the pump system, the load profile shown in Figure 2.1 and an average load torque of $T_{\mathrm{AVG}} \approx 50\,\mathrm{mNm}$ can be extracted. As the motor, driving the diaphragm pump, should run at a rotational speed of $n_{\mathrm{r}} = 3900\,\mathrm{rpm}$ the motor should be able to supply an output power of $P_{\mathrm{out}} \approx 20\,\mathrm{W}$ at the motor shaft.

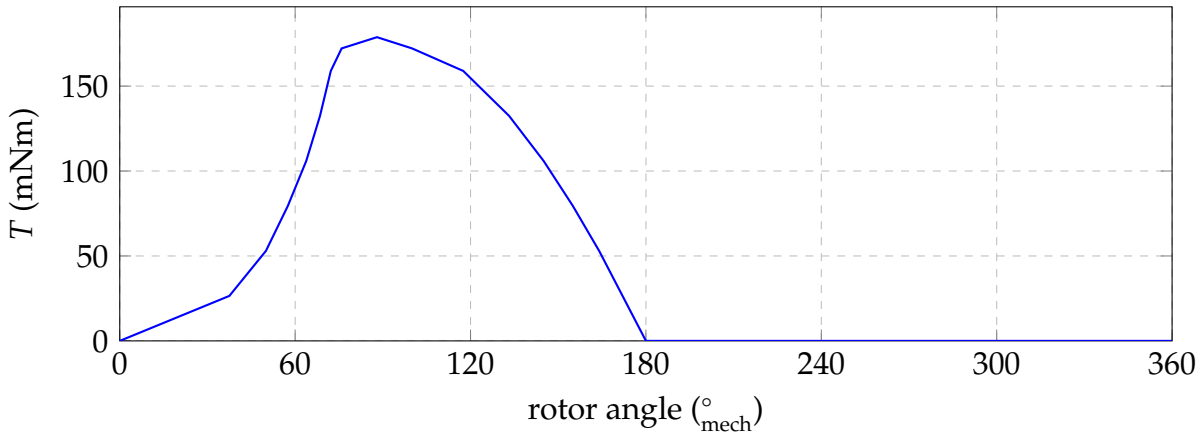

Figure 2.1: Load torque profile of diaphragm pump.

The specifications for the pump drive call for a motor with a high power density. As interior permanent magnet motors are known for high torque capabilities, a three phase spoke type BLDC motor appeared to be a good solution. Spoke type BLDC motors further concentrate the flux generated by the permanent magnets, resulting in an increase of higher torque per volume [31, 32].

In [33, 34] basic characteristics of fractional slot machine types exploiting a concentrated winding pattern are discussed. Feasible slot/pole combinations are further analyzed in [35, 36]. These machines are often called "modular permanent magnet machines" and combine advantages which are of prime interest to the underlying application, such as greater fault tolerance, easy and low cost manufacturability particular for the winding process and short end windings and therefore lower copper loss due to use of concentrated windings [37].

A modular machine design with 8 poles and 12 slots with a single layer concentrated winding was chosen for the pump drive (Figure 2.2). Furthermore, to enhance the air gap flux density, the spoke type BLDC machine was designed with a magnet overhang.

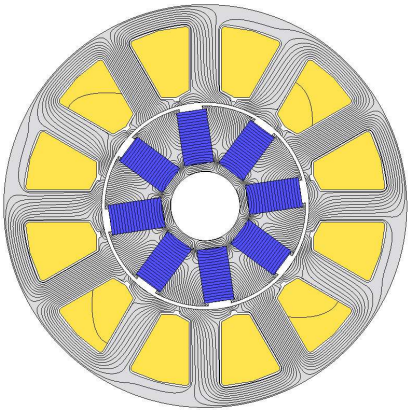

Figure 2.2: Chosen motor design driving the pump application.

2.1.2 Fan application

The second target application was a small fan drive motor. To meet the specifications and because fan applications do not need high starting torques, an outer rotor single phase BLDC appeared to be a good, cost effective solution. Furthermore, this choice ensures simple motor construction and minimal electronic part count [22, 38, 39].

The small fan drive to be designed should provide an output power of $P_{\text{out}} = 0.7\,\text{W}$ at a rotational speed of $n_{\text{r}} = 5000\,\text{rpm}$ at the motor shaft. Furthermore, the specifications of the small fan drive include some fairly restrictive operating conditions:

- Outer diameter of $\varnothing = 30\,\text{mm}$,
- Guaranteed performance for DC supply voltage of $U_{\text{dc}} \in \{8\,\text{V} \ldots 16\,\text{V}\}$,
- Maximum current of $I_{\text{max}} = 1\,\text{A}$.
- Operating temperature range of $\vartheta \in \{-40°\text{C} \ldots 110°\text{C}\}$,

2.2 Electric machine finite element modeling

2.2.1 Three phase (inner rotor)

Figure 2.3 shows the three phase BLDC machine to be modeled as well as its dimensions (in millimeters). Thereby, the motor has a stack length of $l_{\text{stator}} = 10.5\,\text{mm}$ and is designed with a symmetric permanent magnet overhang ($l_{\text{rotor}} = 12.25\,\text{mm}$). For

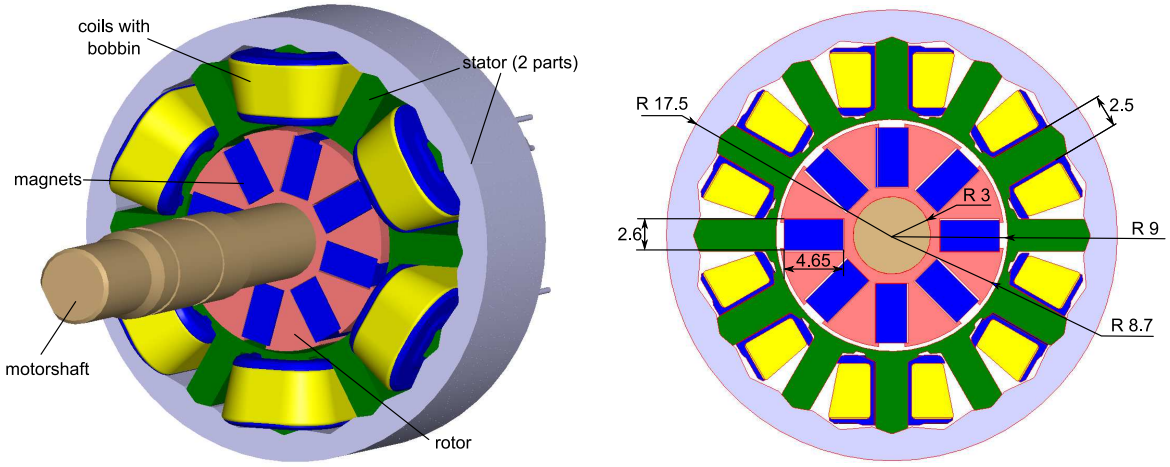

Figure 2.3: Motor model of three phase BLDC pump drive.

all simulation models, symmetry has been exploited and only half of the machine in circumferential direction was modeled. Figure 2.4 shows 3D and 2D FE models for the drive to be simulated. Despite the fact that the machine is relatively "short" in matters of ratio between its outer diameter and stack length, a 2D finite element model was eventually chosen to simulate the motor's behavior as the FE simulation results for both the 3D and the 2D model correspond well with each other, as illustrated in the following:

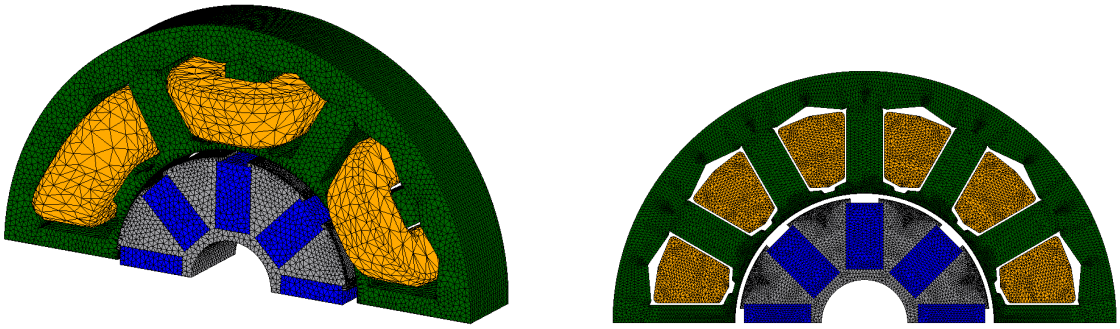

(a) 3D FE motor model.

(b) 2D FE motor model.

Figure 2.4: Finite element models of the pump motor implemented in JMAG® [40].

To take the different stack lengths of rotor and stator, as well as the magnet overhang for the 2D motor model into account, the magnetic remanence flux density B_r and the coercivity H_c was increased for the 2D model. The factor by which

the 2D model's magnetic properties are increased is called incremental value and determined by

$$\text{incremental value} = \frac{l_{\text{rotor}}}{l_{\text{stator}}} \tag{2.1}$$

as proposed in [41].

Figures 2.5 and 2.6 show results for the computed induced voltage, cogging torque and magnetic saturation of the motor for both the 2D and the 3D model. Hardly any differences can be seen in the models' magnetic saturation and the induced voltages. In detail, the back-EMF's first harmonics show a relative error of $\delta_{u\text{EMF}} \approx 1.25\,\%$. The cogging torques of both models show higher discrepancies. Here, a relative error of $\delta_{T_{\text{cogging}}} \approx 12\,\%$ can be denoted, which, however, is still considered to be acceptable.

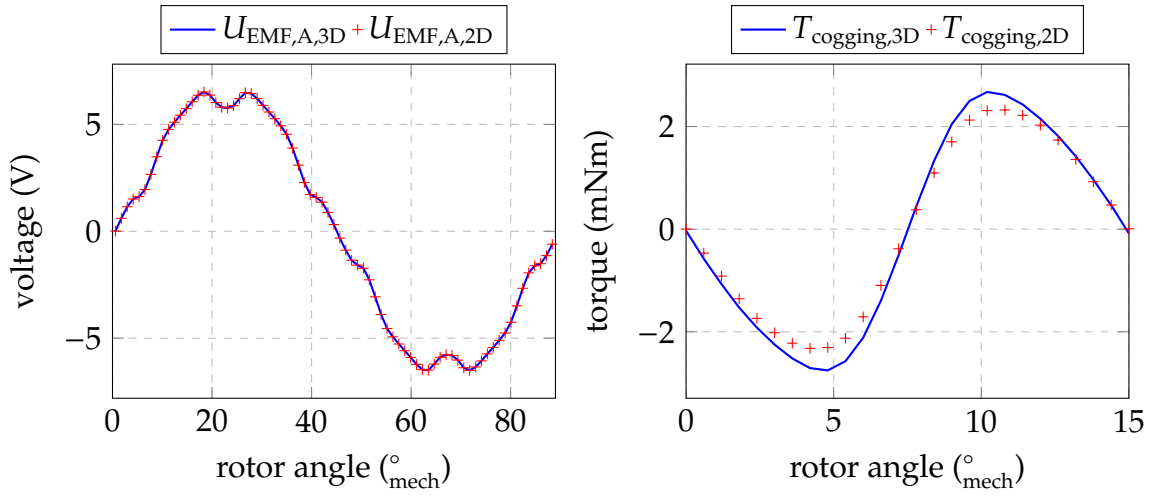

(a) Back-EMF waveforms.

(b) Cogging torque waveforms.

Figure 2.5: Back-EMF voltage comparison of 2D and 3D motor simulation models.

The eight permanent magnets used in the motor are sintered neodymium iron boron magnet ("N40Uh") from UMAG United Magnetics [42] with a remanence flux density of $B_{\text{r}} = 1.25\,\text{T}$ and a coercivity of $H_{\text{c}} = 899\,\text{kA/m}$.

The rotor as well as the stator steel sheets are made of the cold rolled non-oriented electrical steel sheets "M250-35A" from ThyssenKrupp [43]. The material's magnetization curve and loss data are provided in Appendix A.

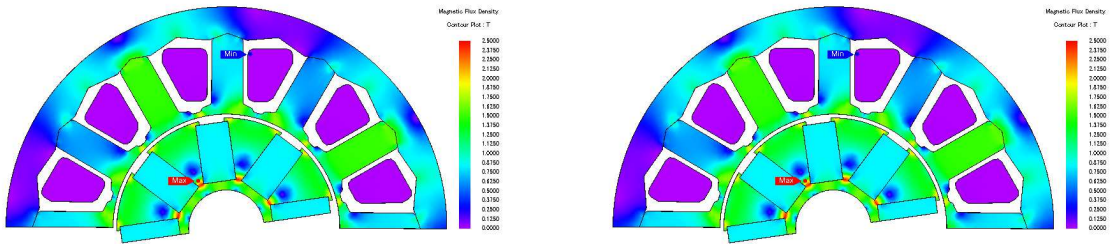

(a) Magnetic saturation of 3D model.

(b) Magnetic saturation of 2D model.

Figure 2.6: Comparison of magnetic saturation of 3D and 2D motor models.

The motor has concentrated windings with two coils per phase and 50 turns per coil. For the several coils a copper wire with a diameter of $d_{\mathrm{Cu}} = 0.45\,\mathrm{mm}$ has been used. The phase resistances were estimated to be $R_{\mathrm{ph}} = 2\,R_{\mathrm{coil}} = 2\,0.215\,\Omega = 0.43\,\Omega$.

In [44–47] influences on the electromagnetic properties of the steel sheets due to different production and manufacturing steps are shown. Since all investigated motors are manufactured the same way, also with respect to the laser cutting as well as the stacking technique, the degrading effect of the manufacturing process should not differ significantly from batch to batch. Preliminary analysis investigated the consequences of a degradation of the magnetic properties in different elements of the steel sheets. Thereby, it was observed that the stator stray path thickness has a high influence on the motor's coils linked flux and the cogging torque. As no data for the degradation effect on the magnetic properties of the motors steel sheets were available, simulation results of the motor's back-EMF voltages were compared to measurement results. The degrading effect of the manufacturing process on the motor's stator steel sheets was simulated by shortening the thickness of the magnetic stray paths ($l_{\mathrm{st}} \in \{0.4, 0.36, .., 0.24, 0.28\}$ mm in Figure 2.7). Figure 2.8 shows

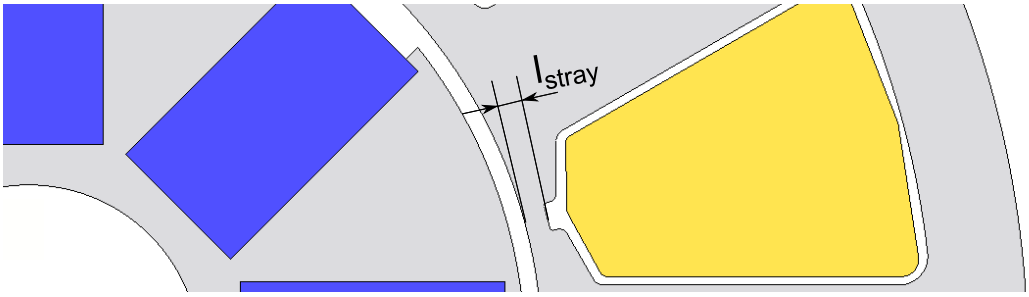

Figure 2.7: Variation of motors stray path thickness in the stator.

a comparison of measured and simulated results of the motor's back-EMF voltage and cogging torque for different stray path thicknesses. For cogging torque only the amplitude of the first harmonic was compared. An increase of the cogging

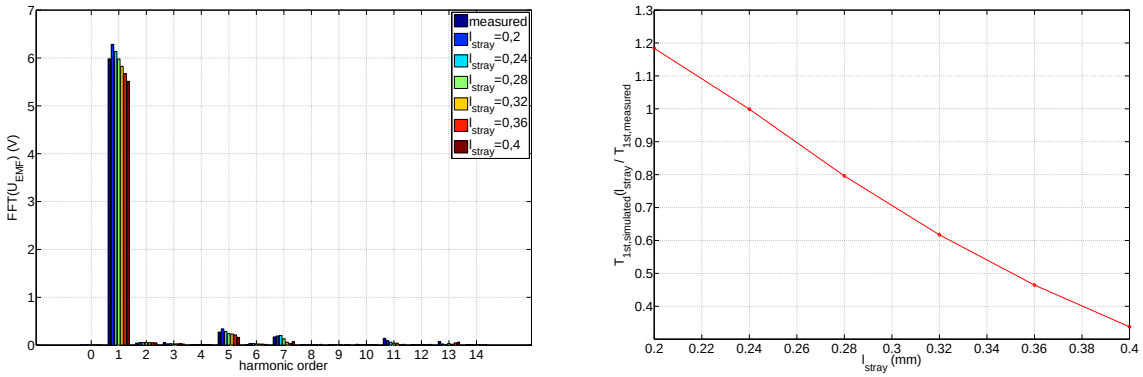

(a) Motors back-EMF voltages.

(b) Motors cogging torques.

Figure 2.8: Comparison of simulation and measurements for different stray paths.

torque towards smaller stray path thicknesses i.e. slot closures can be observed: the degradation of the slot closures' magnetic properties causes more magnetic saturation at these locations and therefore represents less attractive return paths for the flux of the permanent magnets. A similar trend can be observed for the back-EMF voltages from Figure 2.8(a). Due to the higher magnetic saturation of the stray paths, more flux will be linked by the motor coils. Thus, wider slot closures will result in lower induced voltages.

The best match between measurements and simulations were found with a stray path thickness of $l_{\text{stray}} = 0.28\,\text{mm}$ for the simulation models. Therefore all further simulations were carried out using this slot closure thickness.

2.2.2 Single phase (outer rotor)

Figure 2.9 shows the fan drive as modeled as well as the motor's dimensions in millimeters. The motor's stator stack length is $l_{\text{stator}} = 4.2\,\text{mm}$ and the magnet ring as well as the rotor yoke have a length of $l_{\text{rotor}} = 6\,\text{mm}$.

Preliminary investigations have shown, that 2D FE simulations of the drive show different results than those obtained from 3D motor model. Therefore, all simulation were carried out with the 3D FE motor model.

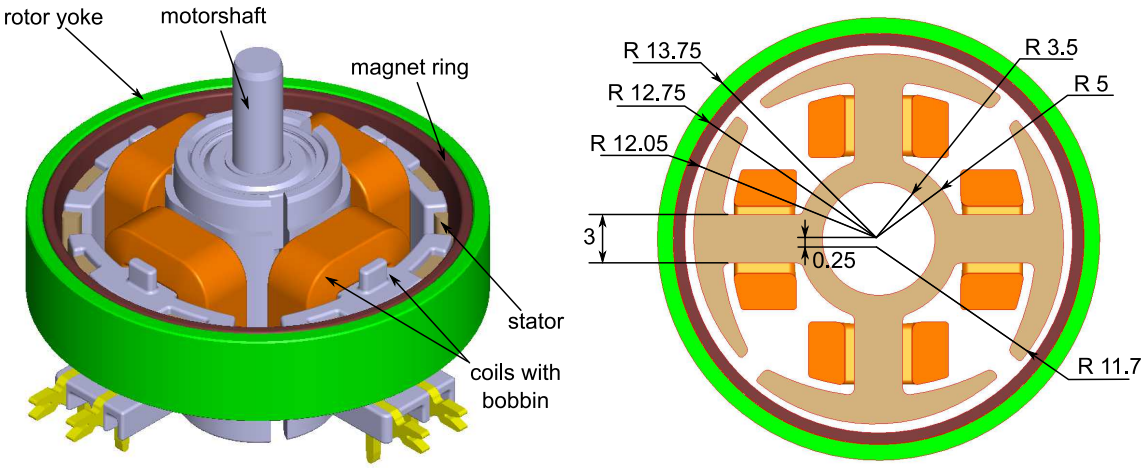

Figure 2.9: Motor model of single BLDC fan drive.

Figure 2.10 shows the developed FE motor model, which is used for computation of the motor for the fan application specified from Section 2.1.2. To reduce simulation time, symmetry was exploited and only one eighth of the total BLDC motor was implemented in the FE software.

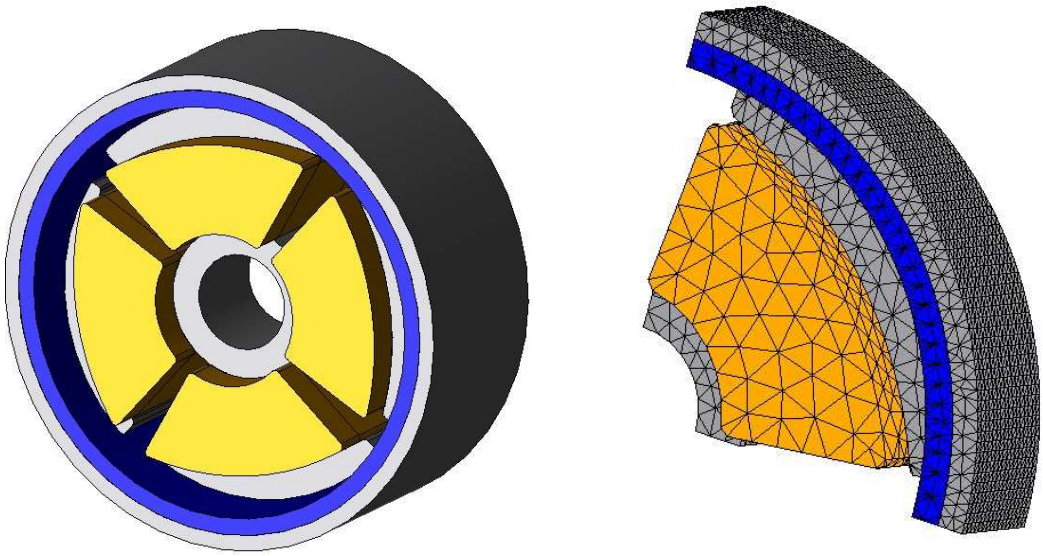

(a) Full model. (b) One eighths model.

Figure 2.10: Finite element model of the fan motor implemented in JMAG®.

The single phase drive uses a permanent magnet ring on the rotor which consists of plastic bound neodymium iron boron material with a remanence flux density of

B_r = 420 mT and a coercivity of H_c = 277 kA/m. Thereby, the magnet ring has 4 poles and is radially magnetized. As described in [48], two magnetic poles which are magnetized in one surface side by side cannot switch their field abruptly from one direction to another. Thus, a transition region between two poles of the magnet will appear where the opposing fields will cancel each other. In the FE model decaying regions for the magnet properties towards its pole edges were built in to consider the pole transition effect. Figure 2.11 shows measurement results for the radial flux distribution on the inner surface of the magnet ring. Furthermore, simulated results of the magnet's flux distribution have been included for a magnet ring having no pole transition regions and a magnet ring with a pole transition region of $\varphi_{\text{transition}} = 20°_{\text{mech}}$, which provides the best congruity of measured and simulated results. Depending on the motor control strategy and its corresponding phase current waveforms (Section 5.4.1), the output torque of these simulated models with different pole transition regions differs up to approximately 10 %. Therefore, all further simulations were carried out using the model which utilizes a pole transition region of $\varphi_{\text{transition}} = 20°_{\text{mech}}$.

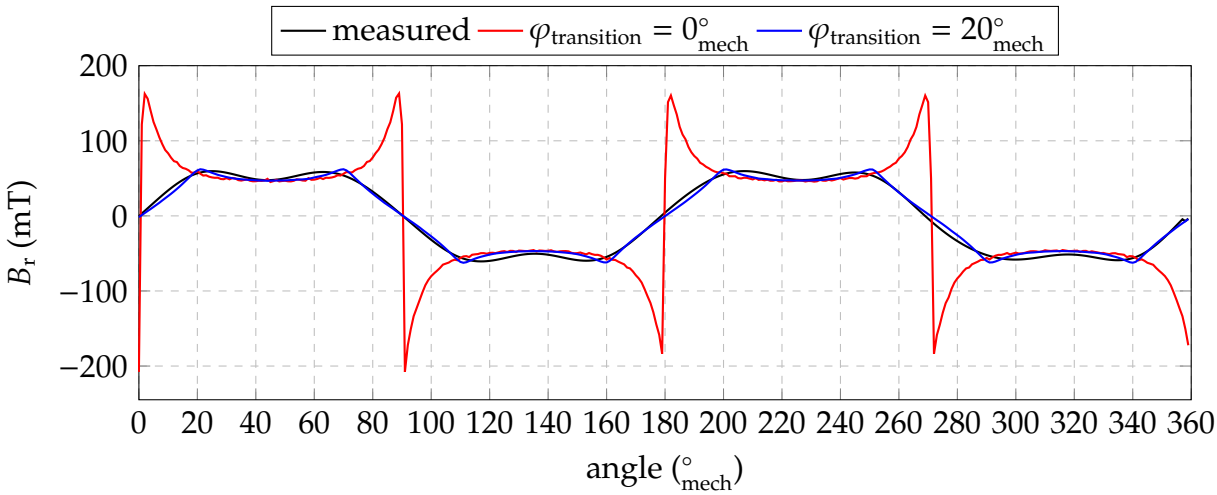

Figure 2.11: Flux distribution on the inner surface of the permanent magnet ring.

Cold rolled non-oriented electrical steel sheets "M250-35A" from ThyssenKrupp are used for the stator's laminations and the rotor yoke consists of free cutting steel ("11SMnPb30"). Detailed material data are provided in Appendix A. The single phase machine has been designed with bifilar windings. Thereby one phase has 4 coils. For the coils, copper wire with a diameter of d_{Cu} = 0.15 mm is used, every coil

has 92 turns. Thus, one coil's resistance was calculated to $R_{\text{coil}} = 2.35\,\Omega$.

2.3 BLDC drives hybrid models

This section presents the hybrid models developed for the investigations. These models allow simulating the drives' operation within their actual applications and therefore behavior predictions of their final performances. The models consist of several submodels which are responsible for simulating the different physical parts of the application. In general, these submodels will simulate the drive and its electrical to mechanical energy conversion, the inverter circuit feeding the drive with appropriate signals, the mechanical behavior of the overall system and additional control logic.

In the following, the different submodels will be described in detail. Furthermore, the interaction of the submodels will be presented as the submodels are modeled and simulated with different software packages.

2.3.1 BLDC motor model

Best motor behavior prediction of the BLDC motors could be achieved by directly coupling the FE model to the circuit and mechanical simulation of the whole application. In [49] a multi-domain model exploiting the direct coupling of FE simulations in an overall application system simulation is described in more detail. Unfortunately, this simulation structure cannot be used for the application context of the work presented here: Such multi-domain models exploit the fact that all motor windings/phases have a defined voltage potential at all times. In other words, the FE simulation represents a voltage controlled current source in the system simulation. Figure 2.12 shows the basic relationship between the interaction of the inverter circuit and the FE motor model. Assuming same simulation time steps for both models, in each time step the controlled current source of the inverter circuit receives an updated value of the FE simulated phase current for the BLDC motor. On the basis of this phase current, the inverter circuit simulates the full bridge's output voltage (motor phase voltage) and hands it over to the FE motor simulation model. Subsequently, with the updated motor's phase voltage, the FE software starts its electromagnetic field simulations, closing up the loop.

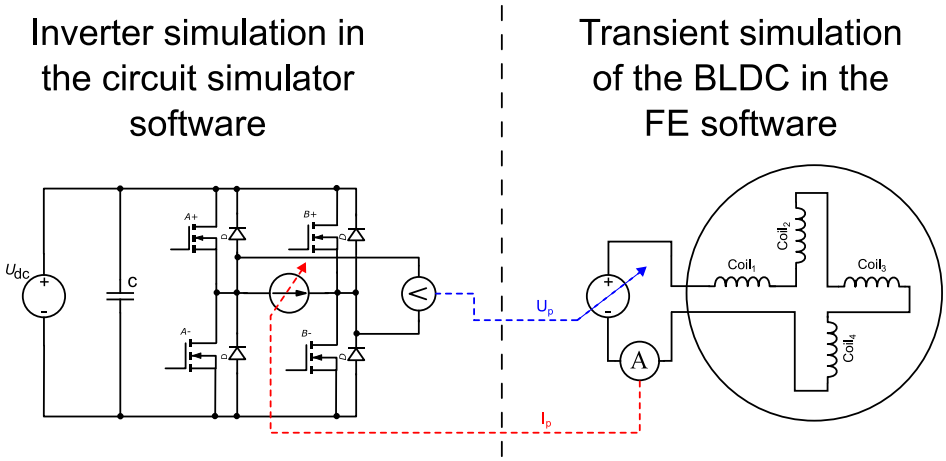

Figure 2.12: Interaction of multi-domain's inverter and BLDC models

Considering three phase BLDC machines with trapezoidal control scheme and single phase BLDCs with a bifilar winding pattern (Chapter 5) there are times when the motor phases have a floating voltage potential. During these times when the phase voltage is floating, a voltage potential will still be handed from the circuit simulation to the FE simulation software which will cause wrong simulation results. Therefore, the multi-domain model suits only BLDC motors with a control scheme with no floating motor phases, in the sense of motor clamp voltage, at all times.

Both motors simulated and designed in this work, as well as their control, use a strategy with temporarily floating motor clamps. Hence, FE coupled motor models could not be used for their behavior prediction within the application. To still ensure an accurate motor prediction, the different BLDC motor models are simulated in the circuit simulation software Gecko® Circuits [50] with FEM based equivalent circuits models as described in [21, 51, 52]. A description of the three phase and the single phase bifilar wound BLDC machines will be detailed in the following:

Three phase BLDC motor model

Figure 2.13 shows the equivalent circuit model used to simulate the three phase BLDC motor.

The equations for the phase variable motor model are given by

$$\begin{bmatrix} u_{\mathrm{AB}} \\ u_{\mathrm{BC}} \\ u_{\mathrm{CA}} \end{bmatrix} = \begin{bmatrix} R_{\mathrm{Cu,A}} & 0 & 0 \\ 0 & R_{\mathrm{Cu,B}} & 0 \\ 0 & 0 & R_{\mathrm{Cu,C}} \end{bmatrix} \begin{bmatrix} i_{\mathrm{p,A}} \\ i_{\mathrm{p,B}} \\ i_{\mathrm{p,C}} \end{bmatrix} + \begin{bmatrix} \frac{\mathrm{d}\psi_{\mathrm{A}}}{\mathrm{d}t} \\ \frac{\mathrm{d}\psi_{\mathrm{B}}}{\mathrm{d}t} \\ \frac{\mathrm{d}\psi_{\mathrm{C}}}{\mathrm{d}t} \end{bmatrix} \tag{2.2}$$

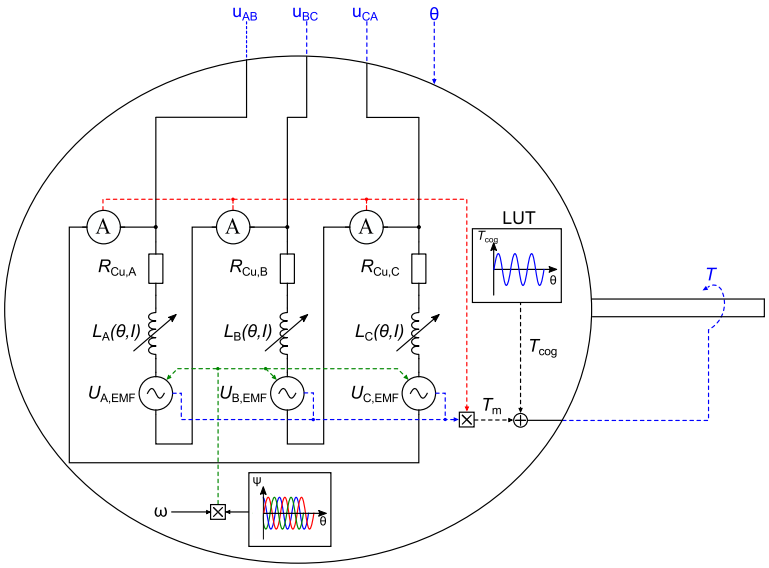

Figure 2.13: Equivalent circuit model of three phase BLDC motor.

$$\psi_{\mathrm{A,B,C}}(\theta, i) = L_{\mathrm{A,B,C}}(\theta, i)\, i \tag{2.3}$$

where $R_{\mathrm{Cu,i}}$ are the copper resistances of the motor coils, $i_{\mathrm{p,i}}$ the phase currents and $\frac{\mathrm{d}\psi,i}{\mathrm{d}t}$ the voltage drops due to flux variations in the individual coils (with i = A, B, C). As supposed in [51] expanding the derivative term of equation (2.2) results in

$$\begin{bmatrix} \frac{\mathrm{d}\psi_\mathrm{A}}{\mathrm{d}t} \\ \frac{\mathrm{d}\psi_\mathrm{B}}{\mathrm{d}t} \\ \frac{\mathrm{d}\psi_\mathrm{C}}{\mathrm{d}t} \end{bmatrix} = \begin{bmatrix} \frac{\partial\psi_\mathrm{A}}{\partial i_\mathrm{p,A}} & \frac{\partial\psi_\mathrm{A}}{\partial i_\mathrm{p,B}} & \frac{\partial\psi_\mathrm{A}}{\partial i_\mathrm{p,C}} \\ \frac{\partial\psi_\mathrm{B}}{\partial i_\mathrm{p,A}} & \frac{\partial\psi_\mathrm{B}}{\partial i_\mathrm{p,B}} & \frac{\partial\psi_\mathrm{B}}{\partial i_\mathrm{p,C}} \\ \frac{\partial\psi_\mathrm{C}}{\partial i_\mathrm{p,A}} & \frac{\partial\psi_\mathrm{C}}{\partial i_\mathrm{p,B}} & \frac{\partial\psi_\mathrm{C}}{\partial i_\mathrm{p,C}} \end{bmatrix} \begin{bmatrix} \frac{\mathrm{d}i_\mathrm{p,A}}{\mathrm{d}t} \\ \frac{\mathrm{d}i_\mathrm{p,B}}{\mathrm{d}t} \\ \frac{\mathrm{d}i_\mathrm{p,C}}{\mathrm{d}t} \end{bmatrix} + \begin{bmatrix} \frac{\partial\psi_\mathrm{A}}{\partial\theta} \\ \frac{\partial\psi_\mathrm{B}}{\partial\theta} \\ \frac{\partial\psi_\mathrm{C}}{\partial\theta} \end{bmatrix} \frac{\mathrm{d}\theta}{\mathrm{d}t}. \tag{2.4}$$

By substituting equation (2.3) in equation (2.4) we obtain

$$\begin{bmatrix} u_{\mathrm{AB'}} \\ u_{\mathrm{BC}} \\ u_{\mathrm{CA}} \end{bmatrix} = \begin{bmatrix} R_{\mathrm{Cu,A}} & 0 & 0 \\ 0 & R_{\mathrm{Cu,B}} & 0 \\ 0 & 0 & R_{\mathrm{Cu,C}} \end{bmatrix} \begin{bmatrix} i_{\mathrm{p,A}} \\ i_{\mathrm{p,B}} \\ i_{\mathrm{p,C}} \end{bmatrix} + \underbrace{\begin{bmatrix} L_{\mathrm{d,AA}} & L_{\mathrm{d,AB}} & L_{\mathrm{d,AC}} \\ L_{\mathrm{d,BA}} & L_{\mathrm{d,BB}} & L_{\mathrm{d,BC}} \\ L_{\mathrm{d,CA}} & L_{\mathrm{d,CB}} & L_{\mathrm{d,CC}} \end{bmatrix} \begin{bmatrix} \frac{\mathrm{d}i_\mathrm{p,A}}{\mathrm{d}t} \\ \frac{\mathrm{d}i_\mathrm{p,B}}{\mathrm{d}t} \\ \frac{\mathrm{d}i_\mathrm{p,C}}{\mathrm{d}t} \end{bmatrix}}_{\text{incremental inductance}} + \underbrace{\begin{bmatrix} \frac{\partial\psi_\mathrm{A}}{\partial\theta} \\ \frac{\partial\psi_\mathrm{B}}{\partial\theta} \\ \frac{\partial\psi_\mathrm{C}}{\partial\theta} \end{bmatrix} \omega}_{\text{induced voltage}} \tag{2.5}$$

In equation (2.5) $L_{\mathrm{d,ij}}$(i, j = A, B, C) represent the differential or incremental self and

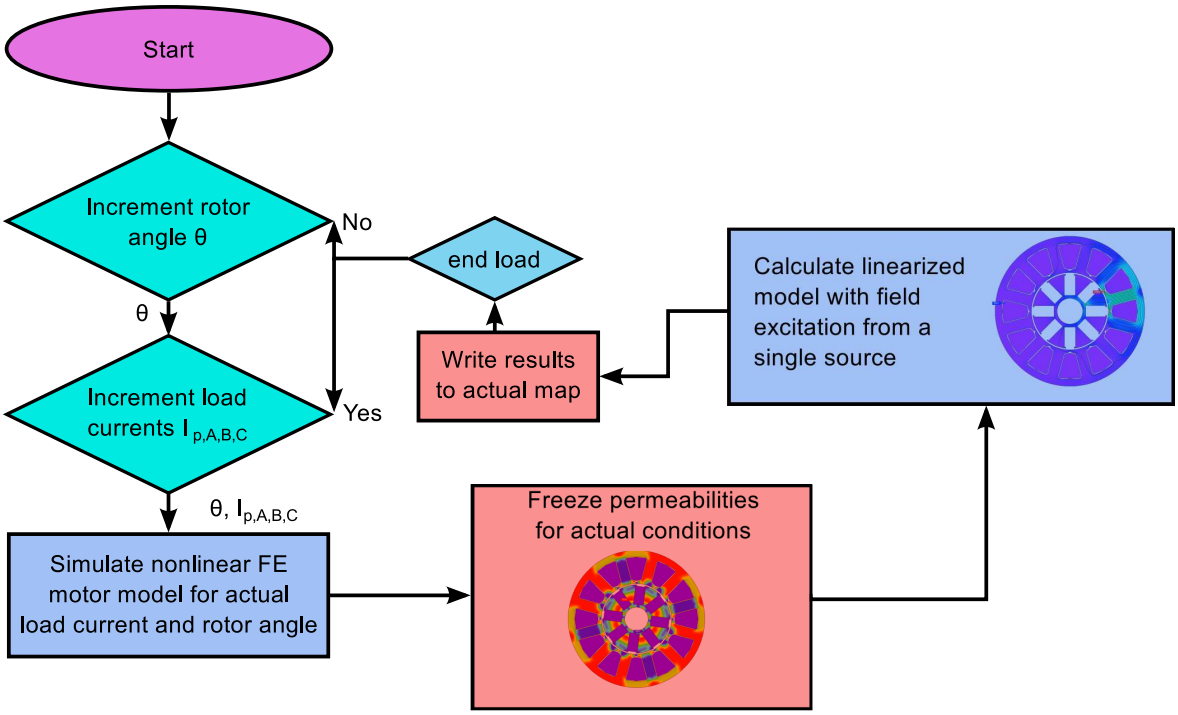

Figure 2.14: Flow chart of frozen permeability method.

mutual inductances and $\frac{d\psi_{A,B,C}}{dt}$ the induced voltage due to flux variations in the individual coils caused by rotation of the rotor.

Thereby, the incremental inductances have been determined by the frozen permeability method, which basically is a method to separate the total flux-linkage of a coil into contributions from currents and permanent magnets in FE-simulations [53]. Figure 2.14 shows the flow chart of the frozen permeability method subroutine created for the used FE-simulation package. As shown by the subroutine's flow chart, for a certain current and rotor angle a nonlinear FE simulation has been carried out. The simulation result regarding the permeability distribution is stored. With this frozen permeability distribution (linearized FE model for the actual load current and rotor angle), the coil's flux linkage changes caused by current perturbation can be simulated [54, 55]. By applying this procedure to the FE motor model for a given set of phase currents and rotor angles, an incremental inductance map for self and mutual inductances of the motor can be created.

Figure 2.15 shows the determined incremental self and mutual inductances for one phase of the three phase BLDC motor. Figure 2.15(c) shows low mutual inductance values, which can be explained by the stator teeth carrying no coils and sitting

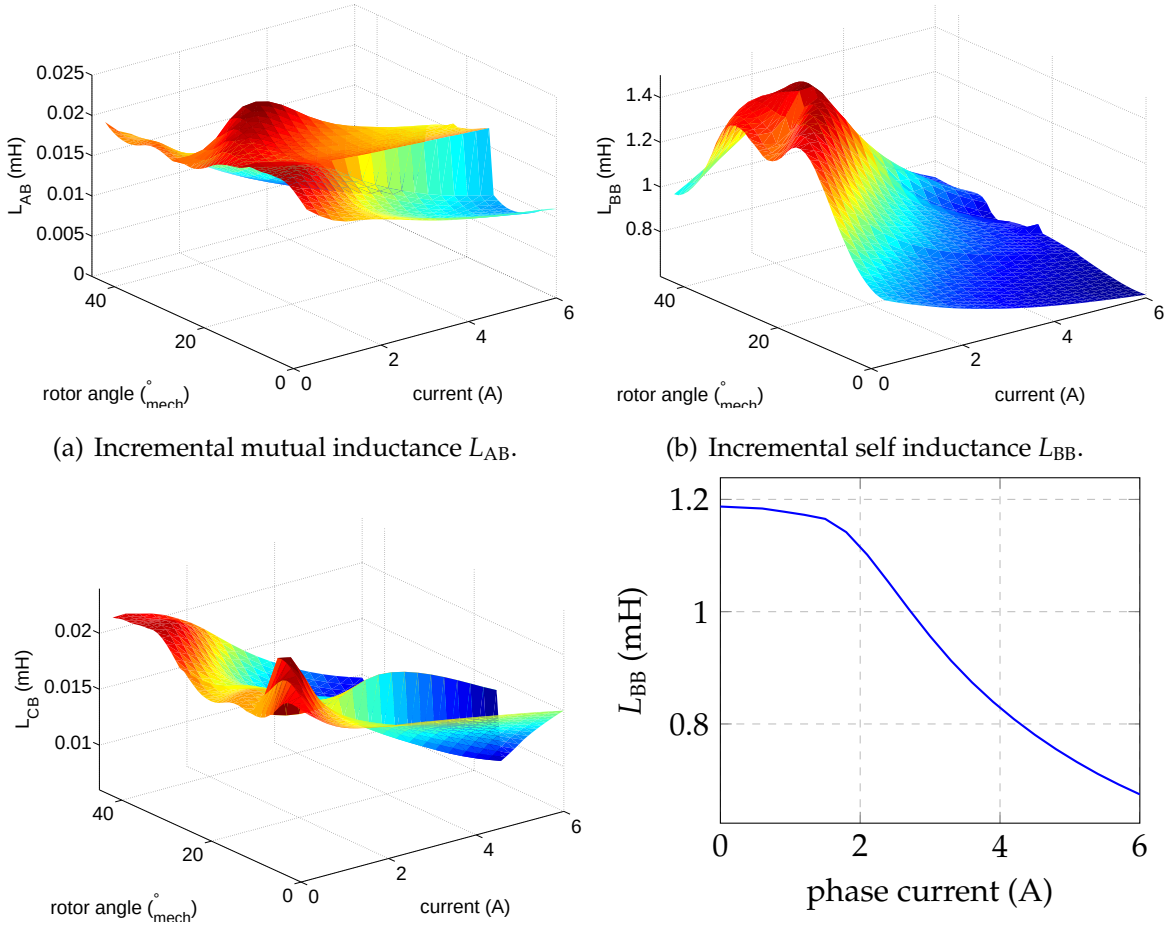

(a) Incremental mutual inductance L_{AB}.

(b) Incremental self inductance L_{BB}.

(c) Incremental mutual inductance L_{CB}.

(d) Self inductance L_{BB} averaged over rotor angle.

Figure 2.15: Incremental self and mutual inductances of the three phase BLDC motor

next to the wound stator teeth (Figure 2.3). Therefore, the mutual inductances were not modeled in the equivalent circuit model. Furthermore, the used circuit simulation software allows the inductances to only depend on one parameter. Therefore, only the saturation effect of the self inductances was considered by averaging the incremental self inductance over the rotor angle as the variation of the self inductance becomes smaller with increasing phase currents. Figure 2.15(d) shows the incremental inductances as implemented in the equivalent circuit model of the three phase BLDC motor.

As per equation (2.5) a voltage due to variations of the coil's flux linkage will be induced in every phase. Thereby, the linked flux has mainly two field sources, as the individual phases are weakly coupled. Separating the flux into contributions from

the permanent magnet and the armature field can be challenging due to the influence the two fields have on each other and the fact that this influence is itself effected by the magnetic saturation of the motor [56]. Figure 2.16 shows the current and rotor angle dependent flux and induced voltage map simulated with the FE motor model for the two coils of one motor phase. For low load currents, almost no influence of the permanent magnet linked coil flux can be observed. As the load currents become higher, the additionally generated magnetic flux will change the magnetic saturation of the corresponding stator teeth. Due to this change in magnetic saturation and the nonlinear magnetic behavior, depending on the rotor angle, different changes of the coils' flux linkages will cause distortions of the no load back-EMF voltages.

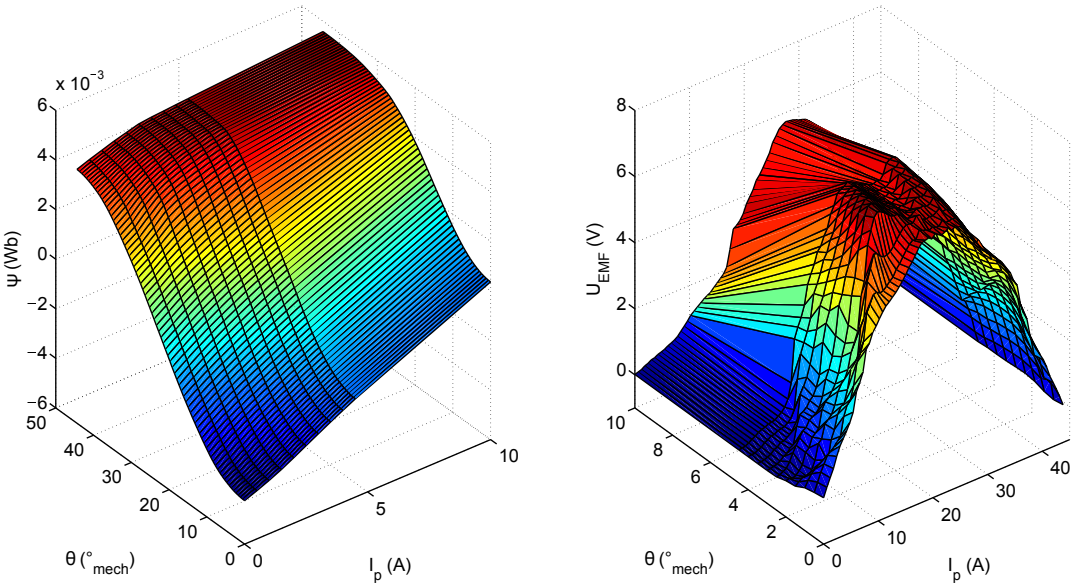

Figure 2.16: Flux and induced voltage of one motor's phase coils.

Figure 2.17 compares the torques computed with motor models using the no load flux linkages u_{EMF} as well as load dependent flux linkages $u_{\mathrm{EMF}}(i_{\mathrm{p}})$ to those from direct transient FE motor simulations, all being supplied by phase currents. The torques computed with the hybrid motor models were calculated by [51]:

$$T = T_{\mathrm{m}} + T_{\mathrm{cog}} = \frac{u_{\mathrm{EMF,A}}\, i_{\mathrm{p,A}} + u_{\mathrm{EMF,B}}\, i_{\mathrm{p,B}} + u_{\mathrm{EMF,C}}\, i_{\mathrm{p,C}}}{\omega_{\mathrm{mech}}} + T_{\mathrm{cog}} \tag{2.6}$$

The simulated average torques show differences in the range of $\approx$ 1%, thus, for further investigations, the no load permanent magnet coil flux linkages were used for the equivalent circuit motor model. In particular, the induced voltages were

modeled as variable voltage sources controlled by look up tables containing the permanent magnet rotor dependent flux linkages multiplied by the angular velocity.

$$u_{\mathrm{EMF,A,B,C}} = \frac{\partial \psi_{\mathrm{A,B,C}}(\theta)}{\partial \theta}\,\omega \tag{2.7}$$

As indicated in Figure 2.13 the cogging torque T_{cog} is also modeled by a look up table containing results drawn from prior FE no load motor simulations.

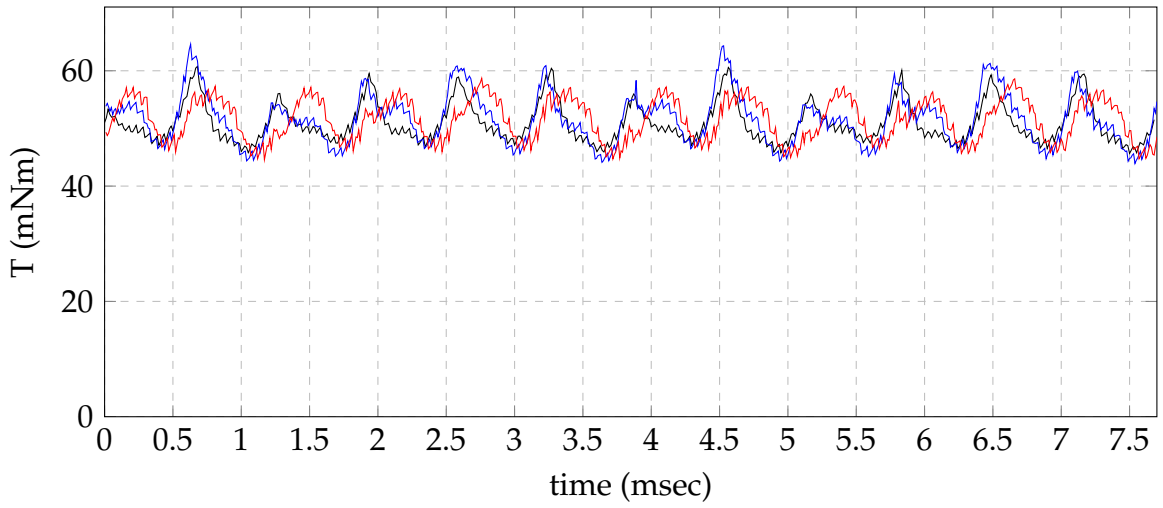

Figure 2.17: Comparison of computed motor torques for different motor models. — FE motor model, — equivalent circuit motor model using load dependent induced voltages, — equivalent circuit motor model using load independent induced voltages.

Single phase BLDC motor model

Figure 2.18 shows the equivalent circuit model used to simulate the single phase BLDC motor.

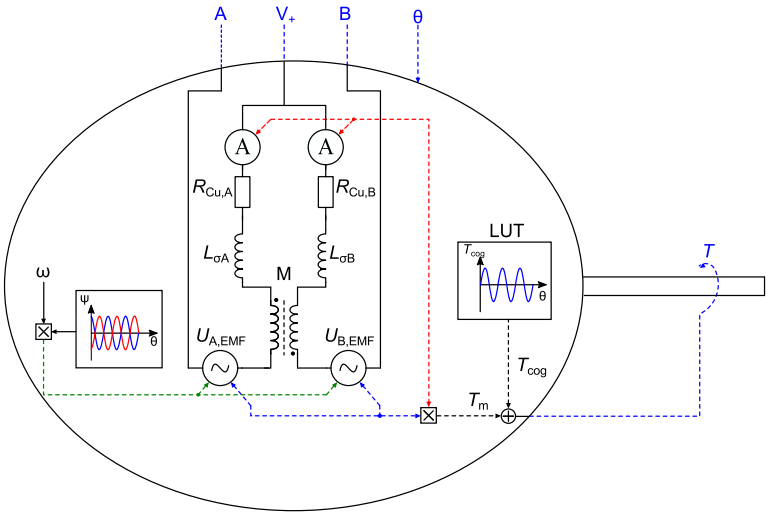

Figure 2.18: Equivalent circuit model of single phase BLDC motor.

The bifilar wound single phase motor can be described by the following equations [57]:

$$u_{+,\mathrm{A}} = R_{\mathrm{Cu,A}}\, i_{\mathrm{p,A}} + L_{\mathrm{A}} \frac{\mathrm{d}i_{\mathrm{p,A}}}{\mathrm{d}t} + M_{\mathrm{A,B}} \frac{\mathrm{d}i_{\mathrm{p,B}}}{\mathrm{d}t} + u_{\mathrm{EMF,A}} \tag{2.8}$$

$$u_{+,\mathrm{B}} = R_{\mathrm{Cu,B}}\, i_{\mathrm{p,B}} + L_{\mathrm{B}} \frac{\mathrm{d}i_{\mathrm{p,B}}}{\mathrm{d}t} + M_{\mathrm{B,A}} \frac{\mathrm{d}i_{\mathrm{p,A}}}{\mathrm{d}t} + u_{\mathrm{EMF,B}} \tag{2.9}$$

Assuming the two bifilar windings are symmetrical, each has the same total self inductance and resistance. Thereby, each self inductance is given by:

$$L_{\mathrm{A}} = L_{\sigma,\mathrm{A}} + M_{\mathrm{A,B}} = L_{\sigma,\mathrm{B}} + M_{\mathrm{B,A}} = L_{\mathrm{B}} \tag{2.10}$$

Since the magnetic axes are in opposite directions for positive current in each winding, the mutual inductance is negative. Furthermore, the symmetry as well as the configurations of the windings indicate that both have the same permanent magnet component of flux linkage ψ_{PM} but with opposite signs [22]. Making the appropriate changes equations (2.8) and (2.9) can be expressed by:

$$u_{+,\mathrm{A}} = R\, i_{\mathrm{p,A}} + L_{\sigma,\mathrm{A}} \frac{\mathrm{d}i_{\mathrm{p,A}}}{\mathrm{d}t} + M\left(\frac{\mathrm{d}i_{\mathrm{p,A}}}{\mathrm{d}t} - \frac{\mathrm{d}i_{\mathrm{p,B}}}{\mathrm{d}t}\right) + \frac{\partial \psi_{\mathrm{PM}}(\theta)}{\partial \theta}\,\omega \tag{2.11}$$

$$u_{+,\mathrm{B}} = R\, i_{\mathrm{p,B}} + L_{\sigma,\mathrm{B}} \frac{\mathrm{d}i_{\mathrm{p,A}}}{\mathrm{d}t} + M\left(\frac{\mathrm{d}i_{\mathrm{p,B}}}{\mathrm{d}t} - \frac{\mathrm{d}i_{\mathrm{p,A}}}{\mathrm{d}t}\right) - \frac{\partial \psi_{\mathrm{PM}}(\theta)}{\partial \theta}\,\omega \tag{2.12}$$

In equations (2.11) and (2.12), $L_{\sigma,\mathrm{A}}$ and $L_{\sigma,\mathrm{B}}$ are the leakage inductances and M represents the mutual inductance of the two bifilar windings. The values for each

inductance used for the equivalent circuit motor model have been drawn from FE simulations.

As the rotor of the single phase BLDC machine has surface mounted magnets, it will not show any saliency. Furthermore, due the lack of magnetic saturation, the inductances show a weak dependency of the phase current and rotor angle, thus the inductances have been modeled as constant. For the sake of completeness, Figure 2.19 shows the windings self inductances determined by the frozen permeability method, described in Section 2.3.1.

The leakage inductances have been estimated by exciting both windings of the FE motor model with the same current. Due to the opposite directions of the magnetic axis for the same winding current, the simulated voltage drop at the particular bifilar windings will be caused by the leakage inductances. Table 2.1 shows the determined inductances for the equivalent circuit model of the single phase BLDC machine.

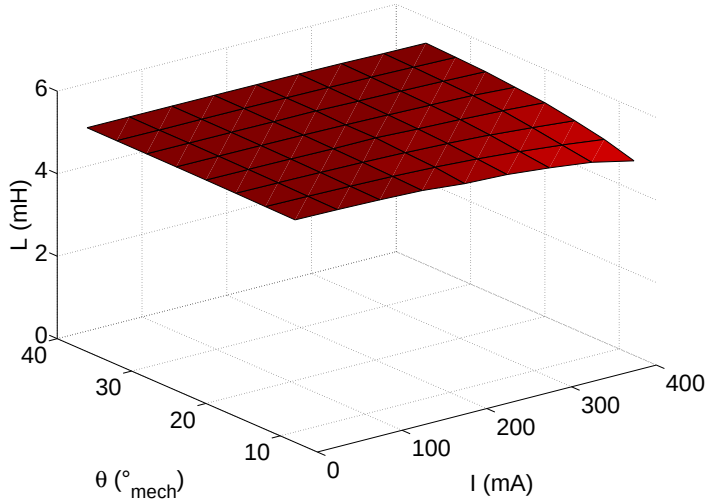

Figure 2.19: Incremental self inductances of the single phase BLDC motor.

Inductances (mH)	
$L_{\sigma,\mathrm{A}} = L_{\sigma,\mathrm{B}}$	0.1
$L_{\mathrm{s,A}} = L_{\mathrm{s,B}}$	5.2
M	5.1

Table 2.1: Inductance values for the equivalent circuit motor model.

The winding's permanent magnet flux linkages ψ_{PM} from equations (2.11) and (2.12)

were drawn from no load FE simulations and included in the motor model as lookup tables.

As indicated in Figure 2.18 the motor torque was simulated by exploiting the following torque equation [57].

$$T = T_{\mathrm{m}} + T_{\mathrm{cog}} = \frac{u_{\mathrm{EMF,A}}\, i_{\mathrm{p,A}} + u_{\mathrm{EMF,B}}\, i_{\mathrm{p,B}}}{\omega_{\mathrm{mech}}} + T_{\mathrm{cog}} \tag{2.13}$$

Therefore, the cogging torque is modeled as a rotor position dependent lookup table and its values were extracted from no load FE motor simulations.

Inverter models

To supply the BLDC motor models from Sections 2.3.1 and 2.3.1, inverter models were built. These models were also implemented in the circuit simulation software Gecko® Circuits and directly coupled to the previously elaborated motor models.

Figure 2.20 shows the used inverter models, as well as its input and output parameters. The inverter models comprise switches (MOSFETs) that are responsible

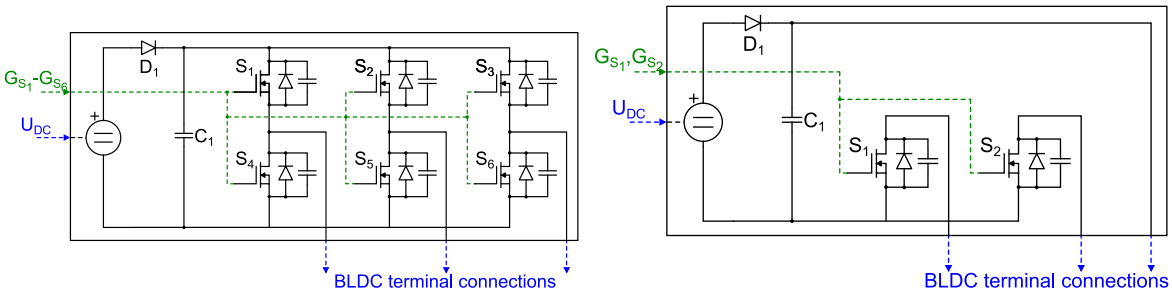

(a) Inverter model for three phase BLDC motor. (b) Half bridge inverter for single phase BLDC motor with bifilar windings.

Figure 2.20: Inverter models for hybrid BLDC motor simulations.

for the commutation states of the particular motor. The switches have been modeled with their parasitic components, thus the hybrid models are capable of capturing transient switching effects as shown in Chapter 5. Their on and off states are controlled in relation to the actual rotor position by a lookup tables which simulate the hall sensor signals. Furthermore, some switches are also used for the PWM speed control of the BLDC machine. Therefore, the drive signals ($G_{S_1} - G_{S_6}$) of the switches had to be linked to Matlab® Simulink [58].

Mechanical models

To simulate the mechanical behavior of the fan and the pump drive as well as the corresponding load torques, mechanical submodels were created. Acceleration and deceleration of the motor shafts are given by

$$\begin{aligned} \frac{\mathrm{d}\omega}{\mathrm{d}t} &= \frac{1}{J}\left(T - k_\mathrm{b}\,\omega - T_\mathrm{L}\right) \quad \text{with,} \\ \omega &= \frac{\mathrm{d}\theta}{\mathrm{d}t}, \end{aligned} \tag{2.14}$$

where ω is the rotational velocity. J is the moment of inertia of the particular drive and was estimated for both drives by their shape, materials and their specific weights as:

$$J_\mathrm{pump} = 3.37 \cdot 10^{-6}\,\mathrm{kgm}^2; \qquad J_\mathrm{fan} = 2.56 \cdot 10^{-6}\,\mathrm{kgm}^2 \tag{2.15}$$

k_b is a factor accounting for ball bearing's friction and was set up from empirical data. T_L are the load torques of the fan wheel as well as the diaphragm pump. The load torque of the diaphragm pump has been modeled as a lookup table containing the load profile from Section 2.1.1. The fan wheel's instantaneous load torque was calculated by using the fan affinity laws from [59].

$$T_\mathrm{L,fan} = \frac{P_\mathrm{out,fan}}{\omega} = \frac{P_\mathrm{out,ref}}{\omega}\left(\frac{\omega}{\omega_\mathrm{ref}}\right)^3 \tag{2.16}$$

The reference power and speed of the fan are taken from the fan's specifications (Section 2.1.2). Figure 2.21 shows the mechanical submodel as well as its coupling links used for the hybrid models.

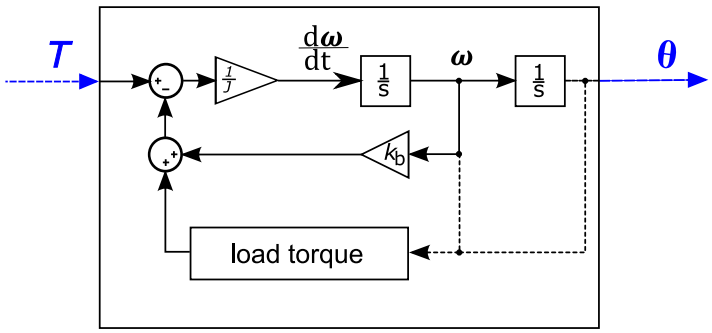

Figure 2.21: Mechanical models for hybrid BLDC motor models.

Commutation and speed estimation

The commutation of the BLDC drives is managed through the inverter models shown in Figure 2.20. The switches have to be controlled in relation to the drive's rotor position. Thus, the hybrid models had to be extended with logic controlling the switches. As the drives use hall sensors for detecting the rotor position, the commutation instances were generated by lookup tables simulating the appropriate hall signals.

Since the speed of the two drives is controlled, the rotational velocity has to be measured. Similarly to the real application, the hall signals are used to extract the speed of the drives. For the single phase four pole BLDC motor, the hall signal changes four times during one rotation, for the three phase eight pole BLDC machine 24 changes in the hall state will occur during one rotation. By measuring the time intervals (t_{hall}) of two successive hall signal changes, the speed can be determined as

$$\hat{n} = \frac{1}{t_{\text{hall}}\, 2\,p\, m}\, 60 \quad \text{(rpm)} \tag{2.17}$$

where $2\,p$ is the number of poles and m the number of phases of the motor. To ensure a stable speed estimation and filter out high frequency variations the speed signals are averaged over several samples with a finite impulse response (FIR) filter. Figure 2.22 shows the speed estimator.

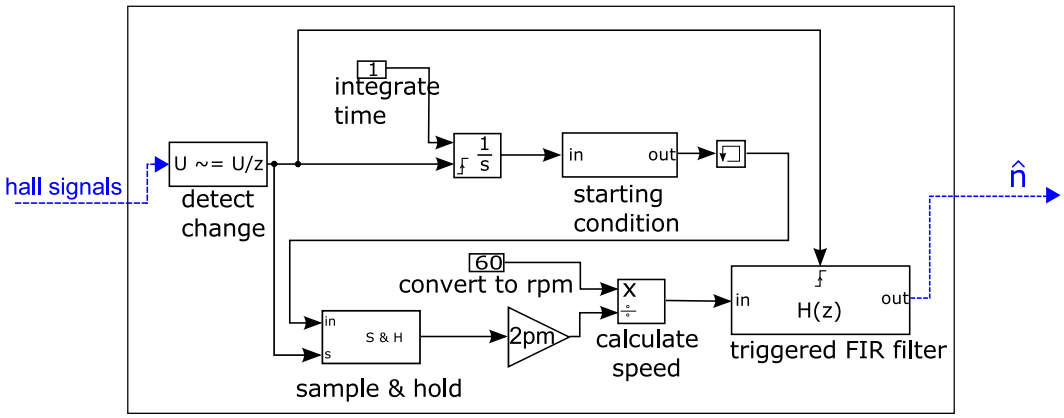

Figure 2.22: Speed estimator of the fan drive.

Speed controller

The speed of the drives is controlled with PI-controllers. For better comparison

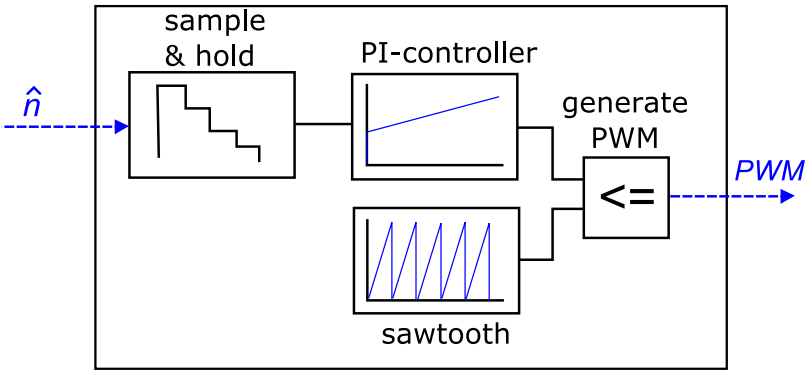

Figure 2.23: Speed control block for hybrid models.

with the experimental results, the PI controllers were set up with the same values used for the PI controllers that have been implemented on the microcontroller units (MCU) (Section 7.2). The PWM signals for the inverter switches are generated from the output value of the PI-controller. Figure 2.23 shows the flow chart of the speed control block.

Overall hybrid simulation models

For the sake of completeness, Figure 2.24 shows a principle flow chart of the two hybrid models. Figures 2.25 to 2.27 show the actual hybrid models, developed in Matlab® Simulink, with all their submodels and couplings described in previous sections.

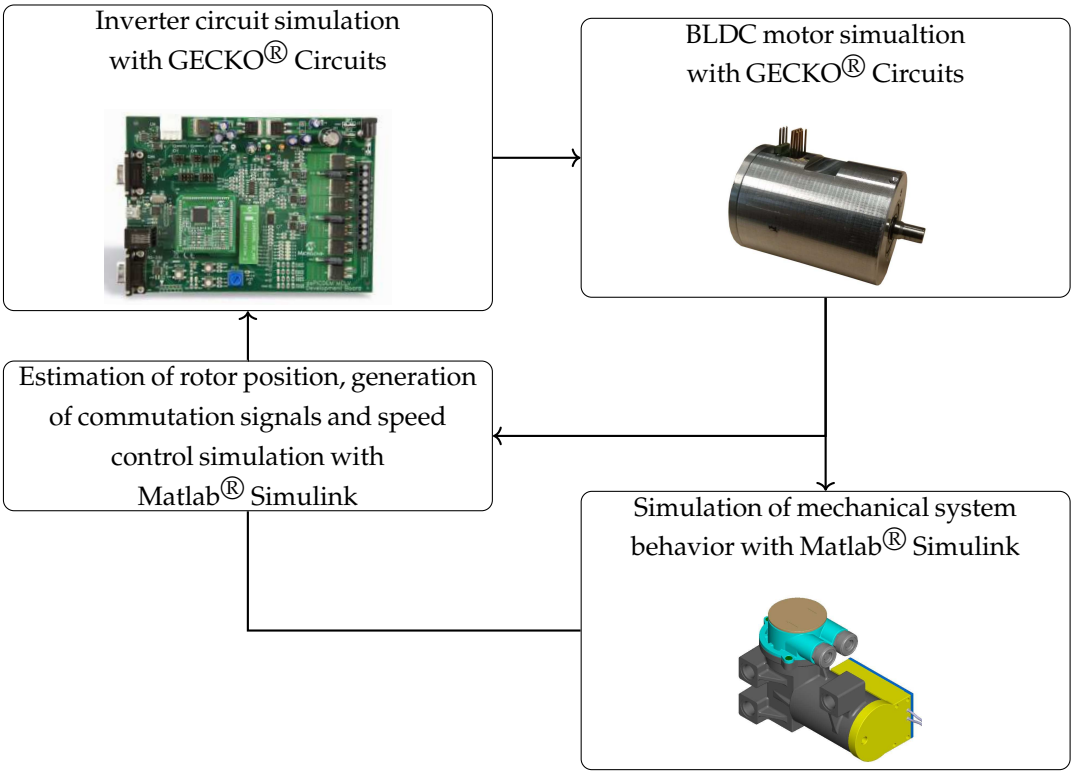

Figure 2.24: Flow-chart of the hybrid model simulation.

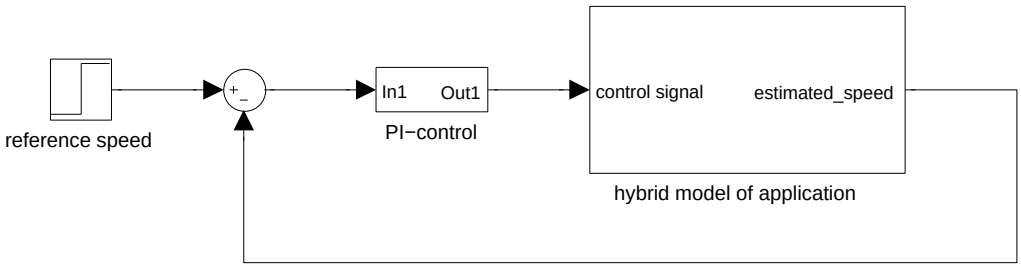

Figure 2.25: Speed control loop for hybrid models.

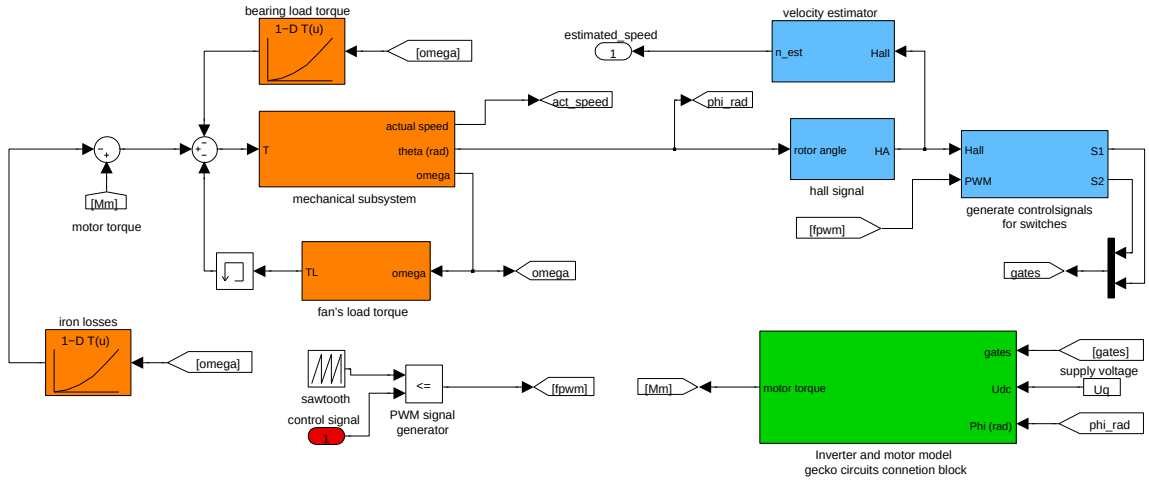

Figure 2.26: Hybrid model of fan application.

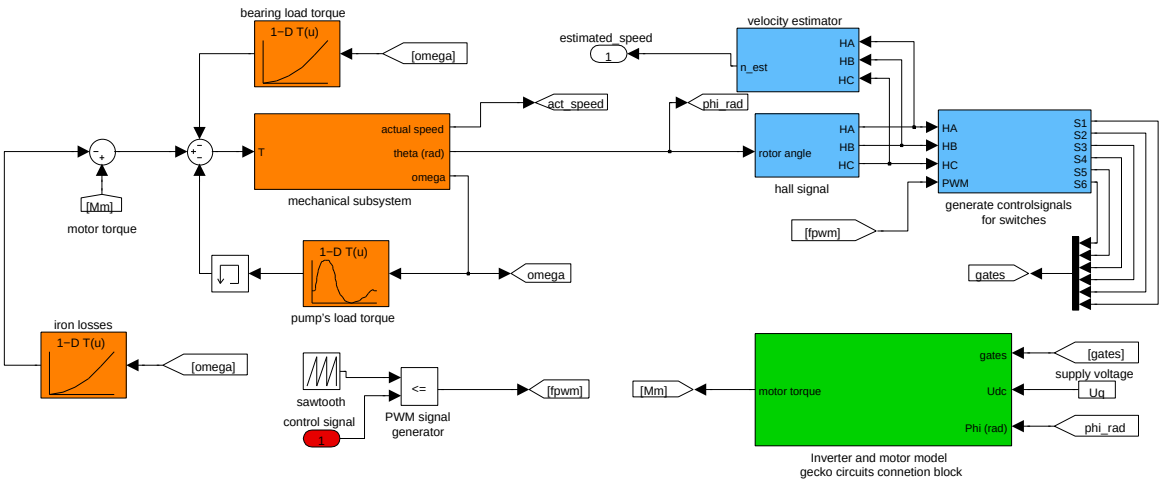

Figure 2.27: Hybrid model of pump application.

Chapter 3

Selected design investigations

This section investigates different constraints that may arise during the design process of machines of the power and size of those investigated in this work. While much of the analysis may appear to follow classical machine theory, aspects such as manufacturability and particular motor dimensions may require special treatment due to these machines' small sizes (Figure 3.1).

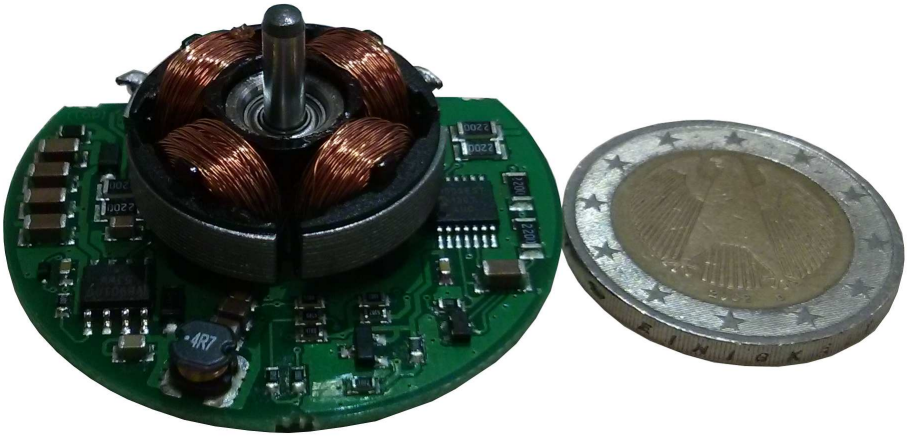

Figure 3.1: Stator and drive circuit of a single phase outer-rotor BLDC fan motor.

A single phase unifilar wound machine is used for illustration, and while the absolute numbers would differ, the same trends and limitations also apply for the three phase and single phase bifilar wound BLDC machines.

Different design constraints that arose during the design process are presented and the relationships between different design parameters and the final motor performance are discussed. With this aim in mind, three different parameter studies will be presented. These parameter studies will vary the height and material of the

magnets used, the number of turns of the winding and the dimensions of the motor.

Due to the small size of the fan as well as the operating constraints and specifications, selection of the motor parameters such as outer motor diameter, material and thickness of the permanent magnets, air gap length, number of turns and wire diameter are subject to numerous tight constraints. Note that many of these are common for electrical machine design. However, because of the operating conditions, such as low supply voltage, high winding resistance and high electrical time constant, some cannot be covered by analytic equations and show special sensitivity due to the small dimensions of the drive. Therefore, the coupled finite element model, described in [49], were built to illustrate new limits which arise for some motor parameters [60–63].[1]

Figure 3.2 gives an overview of the main parameter changes which will be made during the design process of a motor and design constraints which will arise. This variation-mindmap is separated into two parts. The upper part shows the machine and design parameters that were to be determined in the application discussed, such as air gap diameter, number of turns, magnet thickness, and magnet material. The lower part lists constraints which result from the parameters of the upper part of the mindmap.

[1] These findings have been presented in the journal publication [64].

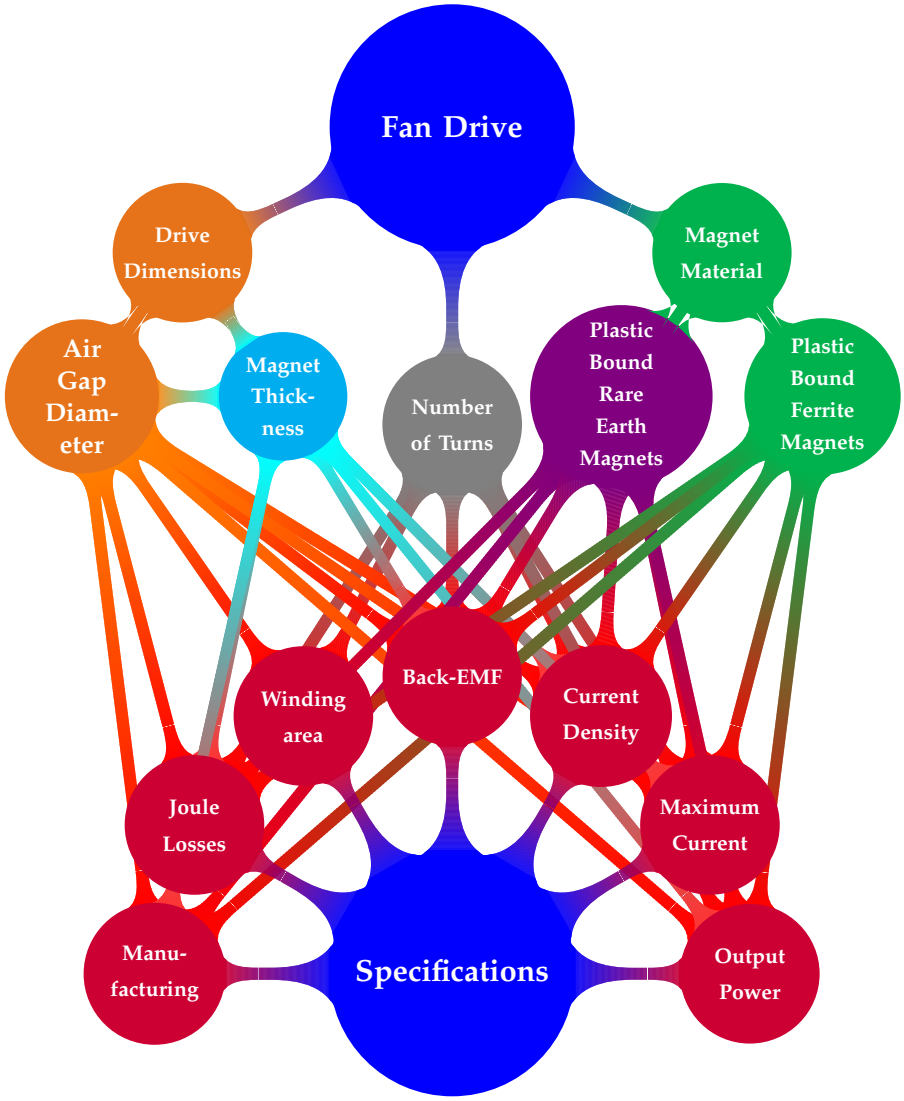

Figure 3.2: Design constraints of the small fan drive.

3.1 Magnet height

This first study focuses on the magnet height. In general, the magnet height defines the point of operation and therefore the magnetic flux that is driven through the motor. The lower boundary of the magnet height is limited by the manufacturing capability. The upper limit is either set by cost or, for a chosen winding arrangement, by the resistance. The resistance shows special sensitivity in small power applications with regards to the inductance and induced EMF voltage of the motor coils (shown below). The parameter variation study uses plastic bound ferrite magnets with different magnet thicknesses (Motors M_A and M_B) for the motor models

(Figure 3.3).

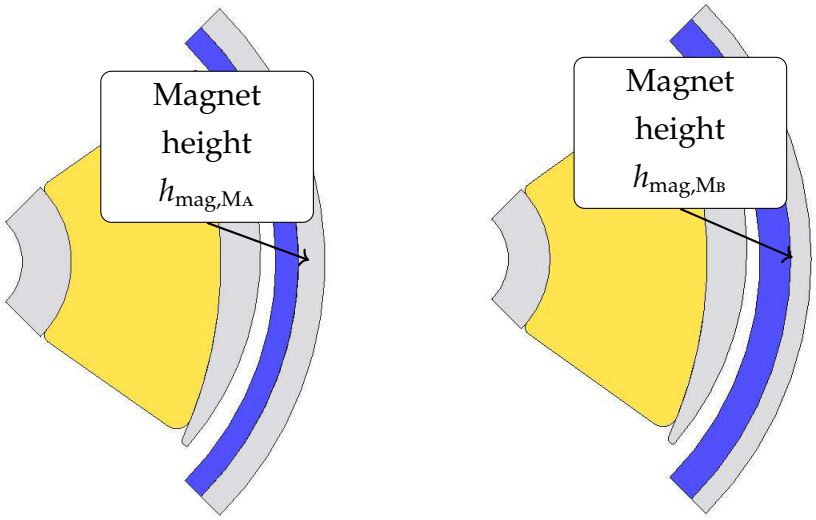

(a) Motor MA with magnet height $h_{\mathrm{mag,MA}}$.

(b) Motor MB with magnet height $h_{\mathrm{mag,MB}}$.

Figure 3.3: Two identical designs, except for the different magnet thicknesses.

The ratio of the magnet thicknesses of the two models is $h_{\mathrm{mag,MA}}/h_{\mathrm{mag,MB}} = 53\%$; the outer diameter of MB increases approximately by 9%. The stator dimensions, as well as the rotor yoke thickness, are kept constant. The two motors are studied for two different numbers of turns but with identical copper cross sectional areas. Figure 3.5 shows the transient simulation results for the maximum average produced torque, RMS current, as well as the RMS back-EMF voltage for the four cases.

Due to the higher air gap flux density of MB, the back-EMF voltage increases by 32 %, for an increase of magnet thickness of more than 50 %. Further, the current drawn by the motor decreases by $\approx$ 10 % and the maximum torque increases by $\approx$ 20 %, for 84 turns.

For the higher number of turns, this trend changes due to the coils' inductances and resistances, and since less of the source voltage remains to drive current through the coils (reduction by $\approx$ 27 %), less torque will be produced (maximum torque decrease by $\approx$ 27 %).

Figure 3.4 shows the maximum current, as well as the maximum torque waveforms for the given minimum supply voltage of $U_{\mathrm{dc,min}} = 8\,\mathrm{V}$ at a duty cycle of 100 %

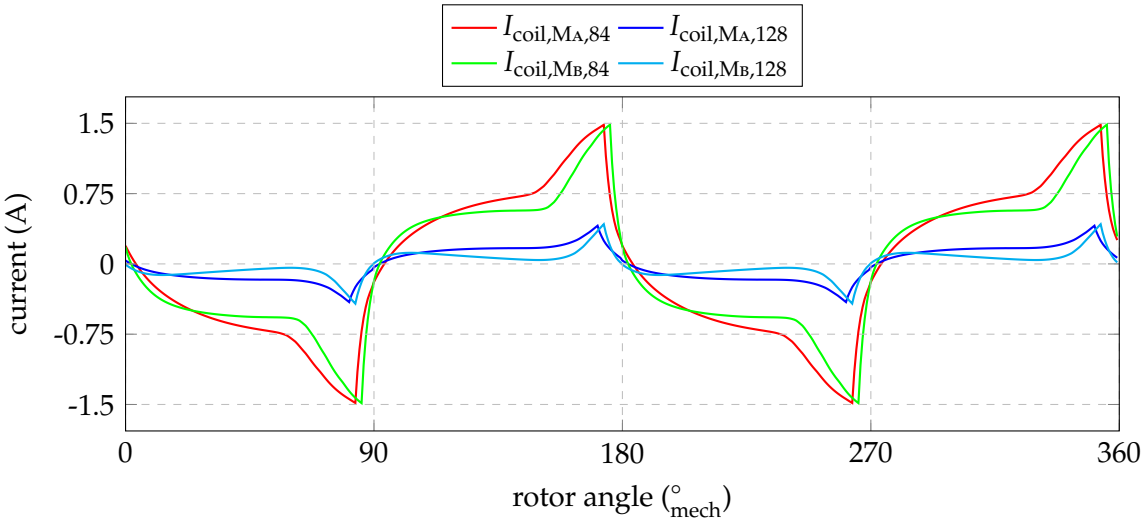

(a) Maximum winding current of MA & MB.

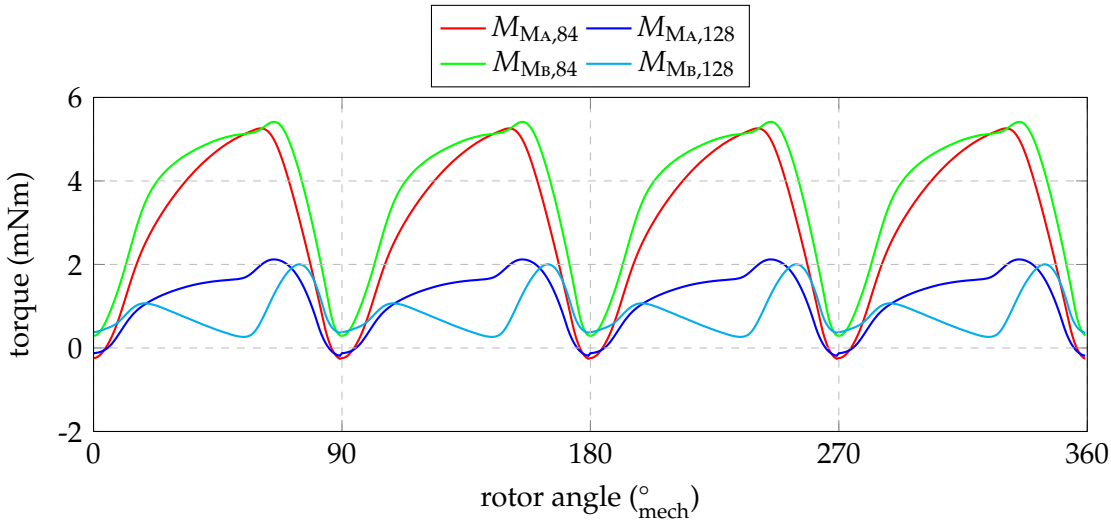

(b) Maximum torque of MA & MB.

Figure 3.4: Results of maximum torque simulation of MA & MB.

(max. control output). Note that short current peaks are eliminated by the control without appreciable changes on the developed torque. It can be noticed that the given value of $U_{\text{dc,min}}$ presents a tough design challenge. Furthermore, the current drawn by the entire fan system will always remain below the simulated maximum current limit from Figure 3.4(a).

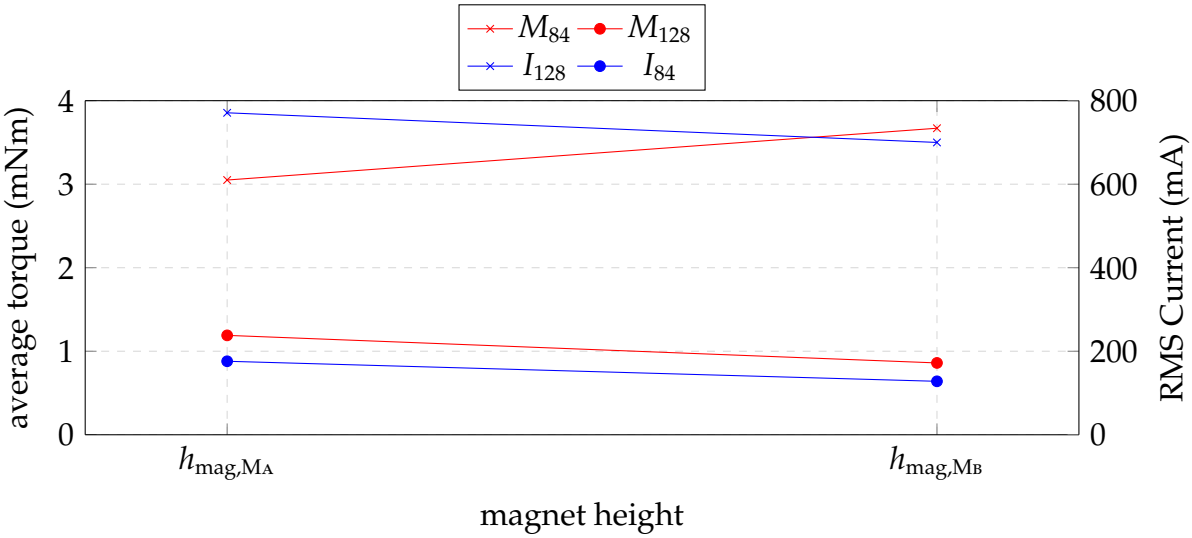

Figure 3.5: Results for maximum torque simulation at $U_{dc} = 8\,\text{V}$ and $n = 5000\,\text{rpm}$.

3.2 Air gap radius

For the sake of comparison, the study analyzed five motors (Motors MC - MG), with the same magnet material and height, but with five different air gap radii (ratio $r_{\text{MC}} : r_{\text{MD}} : r_{\text{ME}} : r_{\text{MF}} : r_{\text{MG}} = 0.8 : 0.9 : 1 : 1.1 : 1.2$). For these five different motor designs the magnet, rotor and stator yoke thickness are kept constant. Therefore, the air gap radius r_{MG} of Motor MG sets an upper limit, because further increasing the air gap radius would cause a wider magnet and higher flux. This would saturate the stator as well as the rotor yoke and result in a motor design with poor efficiency.

The various motors are analyzed with different number of turns in the windings[1] ($N_1 < N_2 < N_3 < N_4 < N_5$).

Considering the torque equation

$$T \approx V\,B\,A \approx D\,B\,N\,I, \tag{3.1}$$

where T describes the torque, N the number of turns, D the air gap diameter, I the current drawn by the motor and B the flux density of the permanent magnets, we would expect the torque to rise with the increase of air gap diameters and number of turns.

For this comparison, the motors (with different air gap radii and number of turns) were analyzed with the maximum torque simulation [64]. The latter was amended

[1] $N_1 : N_2 : N_3 : N_4 : N_5 = 104 : 114 : 128 : 145 : 161$

so that the current drawn by the machine was controlled to not exceed $I = 0.5\,\mathrm{A}$. In general, this simulation should keep the motor current from equation (3.1) constant and a linear behavior between the air gap diameter or number of turns and the torque could be expected.

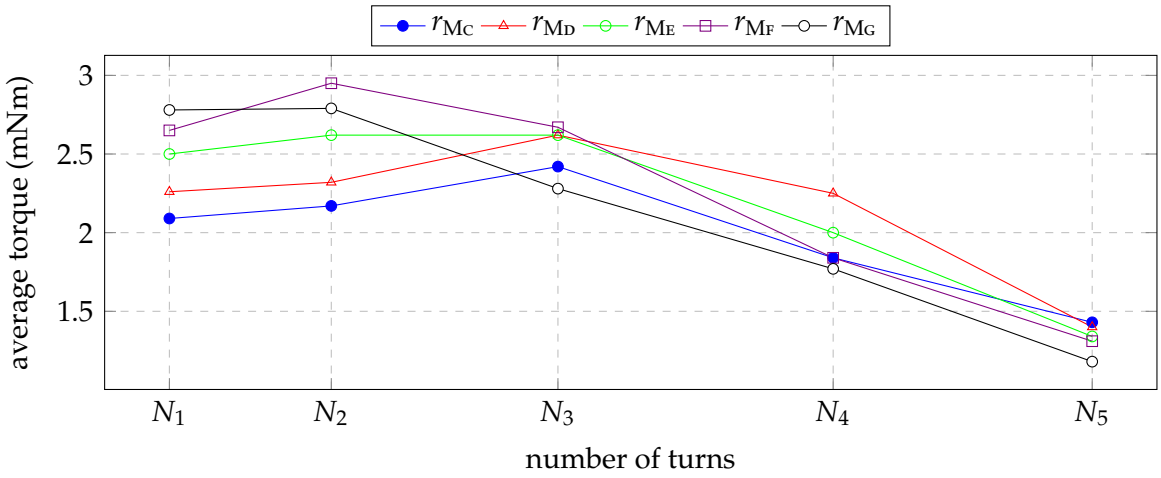

(a) Motor torque for different number of turns.

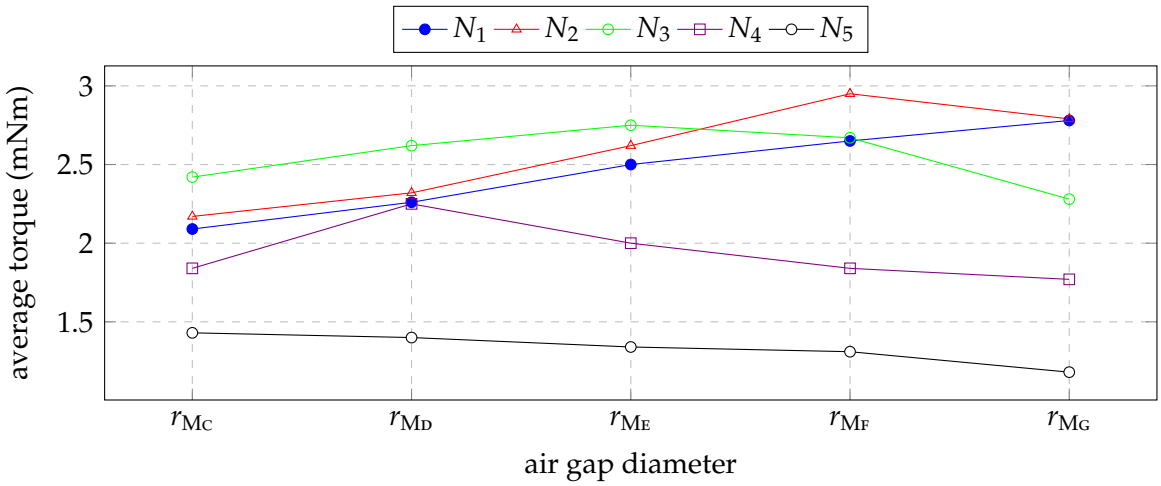

(b) Motor torque for different air gap diameters.

Figure 3.6: Controlled torque simulation results for motors MC, MD, ME and MF.

Figure 3.6(a) shows the torques of the motors with different numbers of turns. Differently than expected, the analyzed motors show a maximum in torque for a certain number of turns: For an increasing number of turns the winding resistances increase, too. At some point, the current drawn by the motors cannot reach the demanded value anymore and the torque decreases. The higher number of turns also

causes a higher flux linkage in the winding, which leads to less voltage remaining for driving the current through the winding. Figure 3.7 shows the loss of motor current due to the increasing number of turns.

The same torque trend can also be seen in Figure 3.6(b) for increasing air gap diameters. Again increasing diameters cause higher flux linkages in the motor coils and higher motor inductances. Furthermore, for a motor with a fixed number of turns, the winding resistances remain constant. These two effects result in higher winding time constants and therefore in slower current rises which also has a negative effect on the evolved motor torque. Again Figure 3.7 shows the differences between the ideal rectangular current drawn by a resistive motor (without coil inductances) and the actual drawn current by the motor with different air gap radii.

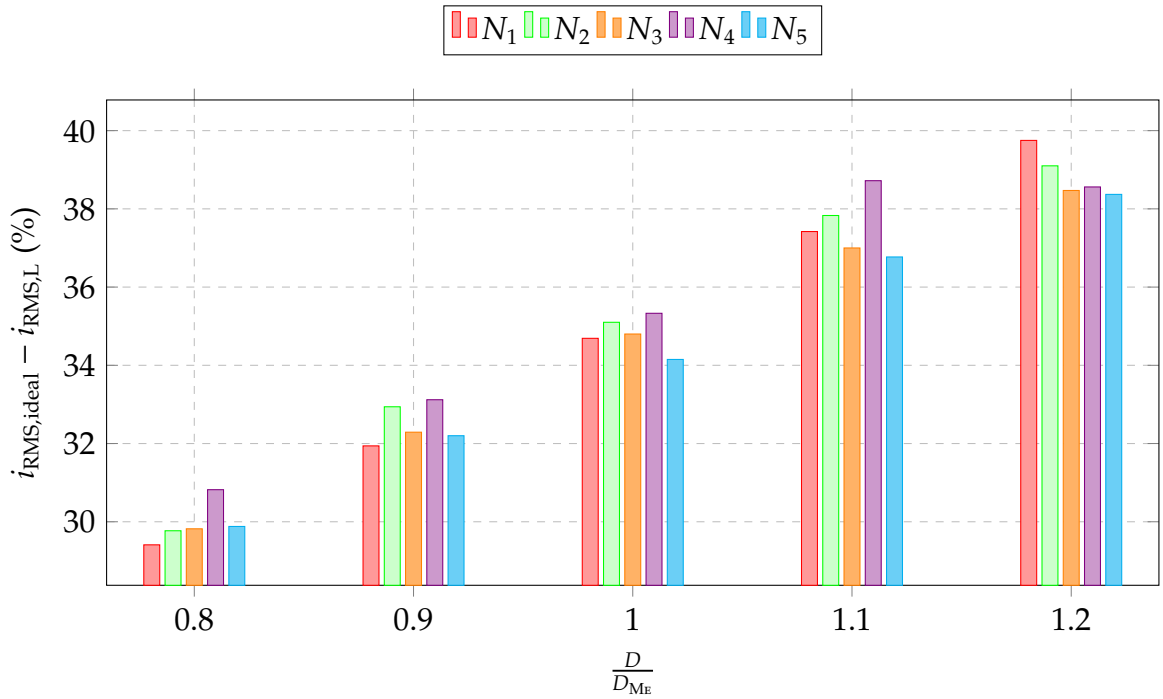

Figure 3.7: Difference in drawn motor current due to the coil inductances.

3.3 Magnet type

Again the multi-domain model from [49] is used to study two drives with the same dimensions. However, one motor (Motor MH) uses rare earth magnets, whereas the other one (Motor MI) uses ferrite magnets. Both models were simulated with the

multi-domain model of the entire fan system. A start up procedure was simulated and the results are shown in Figure 3.8.

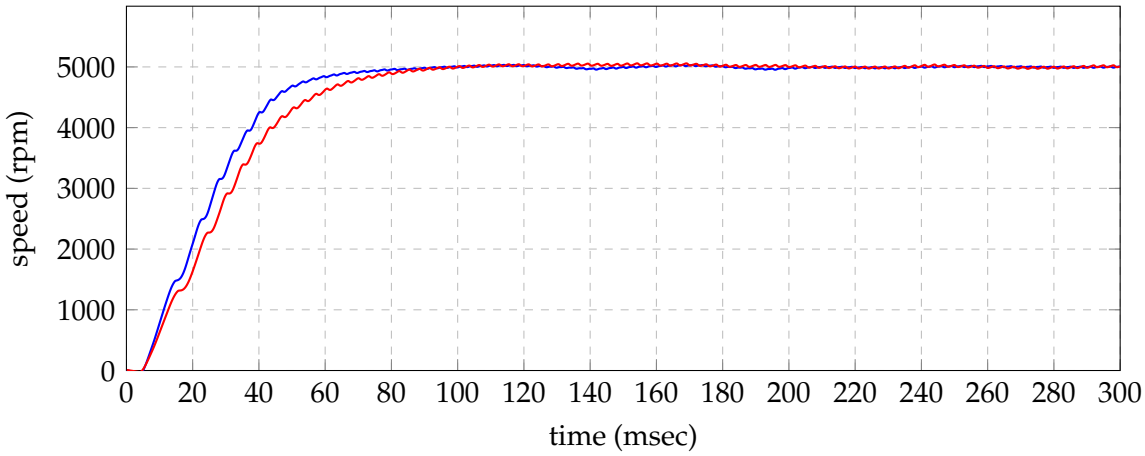

(a) Simulated speed.

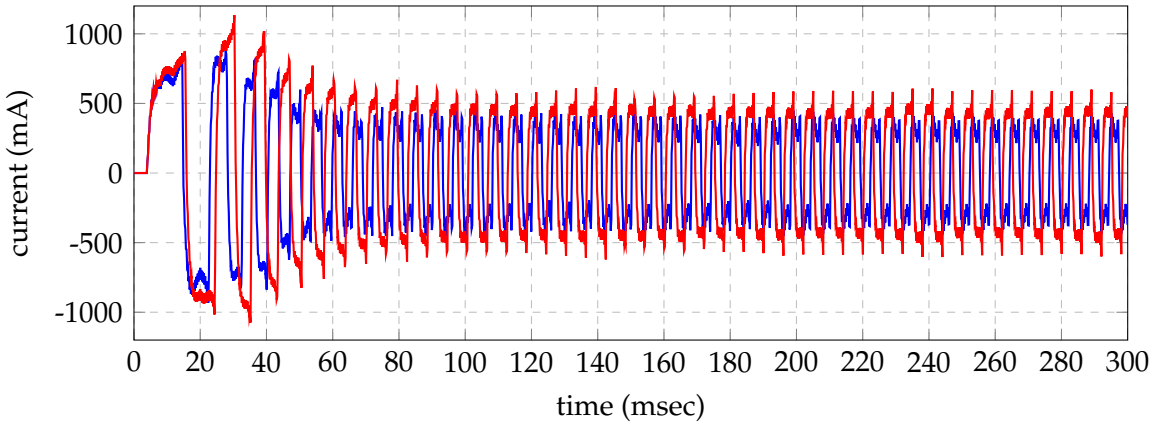

(b) Simulated winding current.

Figure 3.8: Multi domain simulation results of drives —MH & —MI.

The ratio of the remanence between both magnets is $B_{r,h}/B_{r,i} \approx 132\,\%$. Table 3.1 shows the results of the multi-domain model of the fan and drive system for steady-state. Using ferrite magnets instead of rare earth magnets leads to a reduction of the remanence, but since the same torque is needed to drive the motor at rated speed, the electromotive force ($\theta = IN$) has to be increased. As more current passes through the motor coils, more joule losses will be produced for the same winding and the efficiency of the fan will decrease significantly (losses increase by $(I_{\text{coil,MI}}/I_{\text{coil,MH}})^2 \approx 1.3^2 = 1.69$). Also, due to the higher current drawn, the current density will increase by approximately 30 %.

Motor	Speed (avg) [rpm]	Current (rms) [mA]	Joule Losses [W]	Efficiency [%]
MH	5001	312	0.6	71
MI	4998	407	1.02	59

Table 3.1: Multi-domain simulation results at $U_{dc} = 8\,\mathrm{V}$.

3.4 Discussion of number of turns

This discussion reviews the findings from the previous sections with respect to the motor's number of turns, which has been presented throughout the individual subsections.

In general, in the fractional horse power range, the selection and optimization of the motor's number of turns as well as other motor characteristics demand for transient simulation models. Nevertheless, from the previous investigation some general rules can be extracted:

First, increasing the number of turns from N_1 to N_2 entails that the motor inductance increases by approximately $L \propto (N_1/N_2)^2$. Furthermore, if the cross sectional area of the windings is kept constant, the copper wire's diameter has to be changed due to the additionally needed space for the added turns. Therefore, the winding resistance will also be increased by approximately $R \propto (N_1/N_2)^2$. This results in an almost constant electric time constant $\tau = L/R$. These trends are shown in Figure 3.9 for motor MD from Section 3.2. Thus, for a demanded current or torque to be reached, only the remaining supply voltage as well as the winding resistance are responsible.

In contrast, if only the motor inductance is changed, due to geometric changes or differences of the motor's saturation, the motor's electric time constant will also change. Thus, as shown in Figure 3.7, less current can be pushed through the motor windings, if compared to an ideal rectangular current drawn by a resistive motor, causing the torque to be decreased.

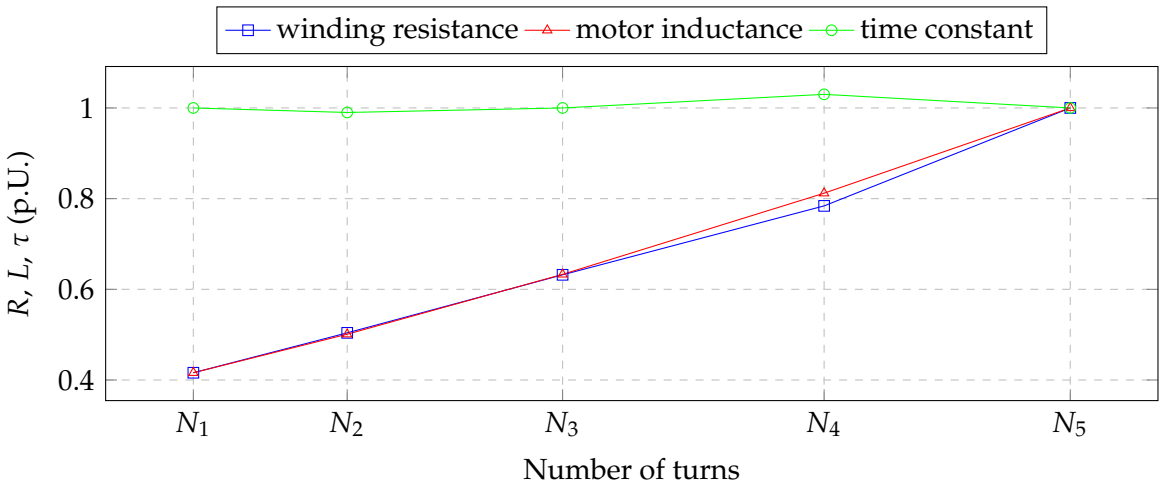

Figure 3.9: Trends for winding resistance R and inductance L as well as electric time constant τ as a function of the motor's number of turns (exemplary MD).

Chapter 4

Three phase BLDC motor control

This chapter will review different types of control for the three phase BLDC motor discussed earlier [9]. The control technique best suiting the needs of the pump application (Section 2.1.1) will be described more in detail.

Furthermore, as the discussed drive is controlled by hall sensors, the influence of the positioning of these sensors will be analyzed in detail. Figure 4.1 gives a classification of the numerous control techniques for three phase BLDC machines.

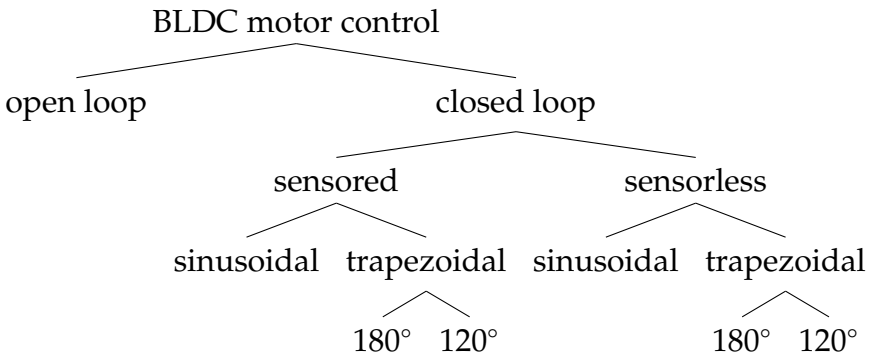

Figure 4.1: BLDC motor control techniques.

In this section a closer look on sensored BLDC motor control techniques will be taken. The sensorless controls will be discussed in Section 6. The power electronics for three phase trapezoidal as well as sinusoidal control techniques show hardly any noticeable differences [65]. Both controls use a pulse width modulated inverter for power supply, which either generates trapezoidal or sinusoidal phase currents. Nevertheless, sinusoidal commutation schemes need rotor position sensors with higher resolution, whereas for trapezoidal commutation three hall sensors are sufficient. Hence trapezoidal control schemes are less complex and therefore

comparatively inexpensive. Figure 4.2 shows an inverter for a three phase motor, working in trapezoidal and sinusoidal control mode.

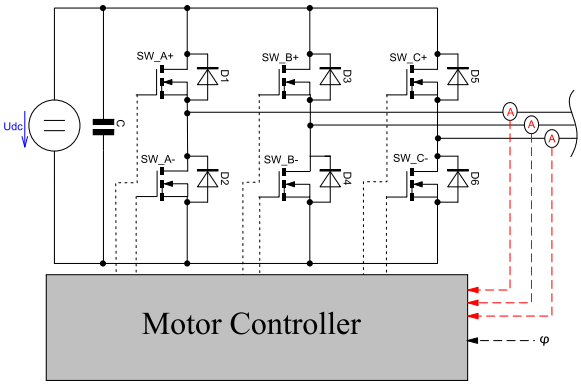

(a) Inverter for a three phase BLDC motor.

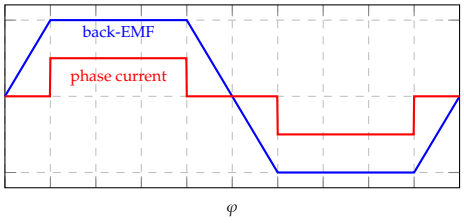

(b) Phase signals for trapezoidal control.

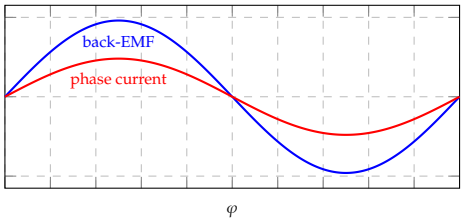

(c) Phase signals for sinusoidal control.

Figure 4.2: Principle circuit diagram of BLDC inverter with phase signals.

The waveforms of the induced voltages (back-EMF voltages) are defined by the motor geometry, the magnetization of the magnets and the winding arrangement. The waveforms of the phase currents are controlled by the inverter which controls the phase currents with respect to the actual rotor position.

4.1 Trapezoidal control: theoretical consideration

Trapezoidal control can be further distinguished into 120 degree and 180 degree control schemes (Figure 4.1). The difference between these two control schemes has already been discussed for star connected BLDC motors in [66, 67]. For the sake of completeness, the 120/180 degree trapezoidal control and their impacts on the motor phase parameters, for star as well as delta connected motors, will be reviewed in this section.

Figure 4.3 shows the inverter and motor models for the following comparison. To describe the control scheme and the motor winding arrangement, four terms will be introduced:

- **120/⅄→** 120 degree trapezoidal control driving a star connected BLDC motor,

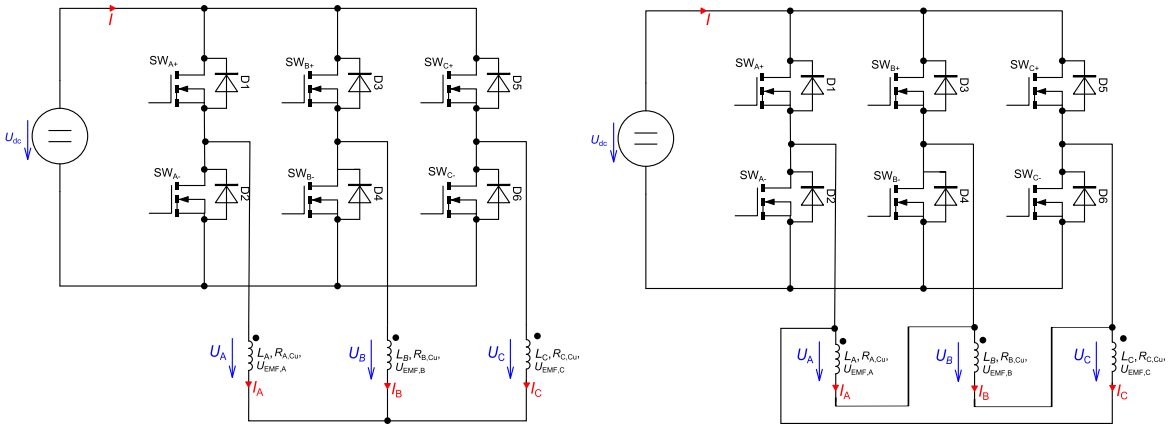

(a) Star connected BLDC inverter model.

(b) Delta connected BLDC inverter model.

Figure 4.3: Star/Delta connected BLDC inverter models.

- **180/⅄**→ 180 degree trapezoidal control driving a star connected BLDC motor,
- **120/Δ**→ 120 degree trapezoidal control driving a delta connected BLDC motor,
- **180/Δ**→ 180 degree trapezoidal control driving a delta connected BLDC motor.

For most machines with trapezoidal control, the rotor position information is obtained from three hall sensors. Therefore, the first difference between the particular trapezoidal controls can be found in the positioning of the hall sensors. Figure 4.4 shows the hall signals ($H_{\#}$) for all four control schemes.

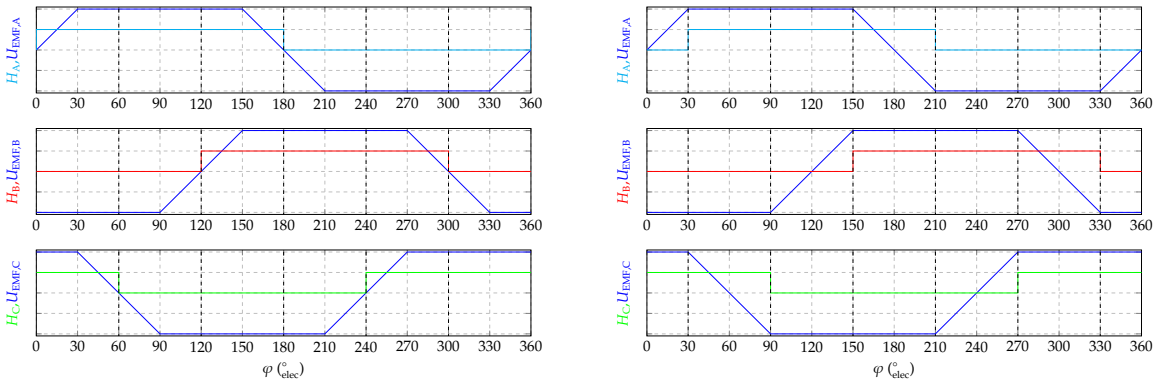

(a) Hall signals for 180/⅄ & 120/Δ.

(b) Hall signals for 120/⅄ & 180/Δ.

Figure 4.4: Hall signals for trapezoidal control.

The three hall signals divide an electrical period of the BLDC machine in six equal commutation intervals. For a 120 degree trapezoidal control, the DC current from the supply is fed to the motor via two motor connections. Therefore, at every commutation interval only one high side and one low side switch of the inverter is turned on. Further, the individual switches are always turned on for an interval of 120 degrees.

Contrarily, a 180 degree control turns on its individual inverter switches for 180 degrees. Therefore, at any commutation interval three switches will always feed the motor with current from the supply.

In the following, the four different control schemes will be analyzed and compared in more detail. First, the truth tables controlling the inverter switches as well as the corresponding hall signals are shown in Tables 4.1 to 4.4. Figures 4.5 to 4.8 show the ideal waveforms of the phase signals for the four control schemes assuming a back-EMF voltage with a 120 (solid lines) and 60 (dotted lines) degree flat top width. Then, characteristic parameters of the four controls as well as their influences on the motor behavior are analyzed.

Interval	H_A	H_B	H_C	SW_{A+}	SW_{A-}	SW_{B+}	SW_{B-}	SW_{C+}	SW_{C-}	φ_{start}	φ_{end}
-	0	0	0	-	-	-	-	-	-	-	-
1	0	0	1	0	0	0	1	1	0	330	30
2	1	0	1	1	0	0	1	0	0	30	90
3	1	0	0	1	0	0	0	0	1	90	150
4	1	1	0	0	0	1	0	0	1	150	210
5	0	1	0	0	1	1	0	0	0	210	270
6	0	1	1	0	1	0	0	1	0	270	330
-	1	1	1	-	-	-	-	-	-	-	-

Table 4.1: 120/⅄ commutation truth table.

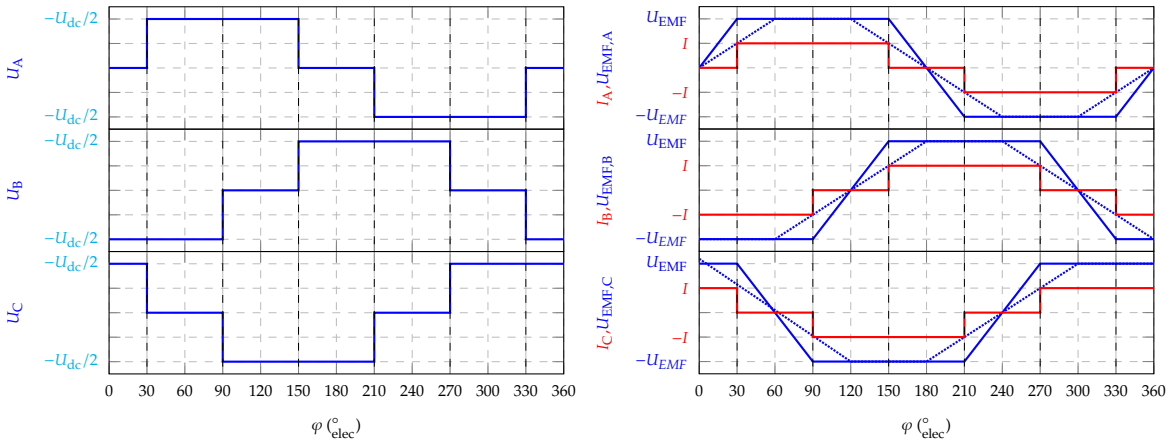

(a) 120/⅄ phase voltage.

(b) 120/⅄ phase current & EMF signals.

Figure 4.5: Phase signals for 120/⅄.

Interval	H_A	H_B	H_C	SW_{A+}	SW_{A-}	SW_{B+}	SW_{B-}	SW_{C+}	SW_{C-}	φ_{start}	φ_{end}
-	0	0	0	-	-	-	-	-	-	-	-
1	1	0	1	0	0	0	1	1	0	0	60
2	1	0	0	1	0	0	1	0	0	60	120
3	1	1	0	1	0	0	0	0	1	120	180
4	0	1	0	0	0	1	0	0	1	180	240
5	0	1	1	0	1	1	0	0	0	240	300
6	0	0	1	0	1	0	0	1	0	300	360
-	1	1	1	-	-	-	-	-	-	-	-

Table 4.2: 120/Δ commutation truth table.

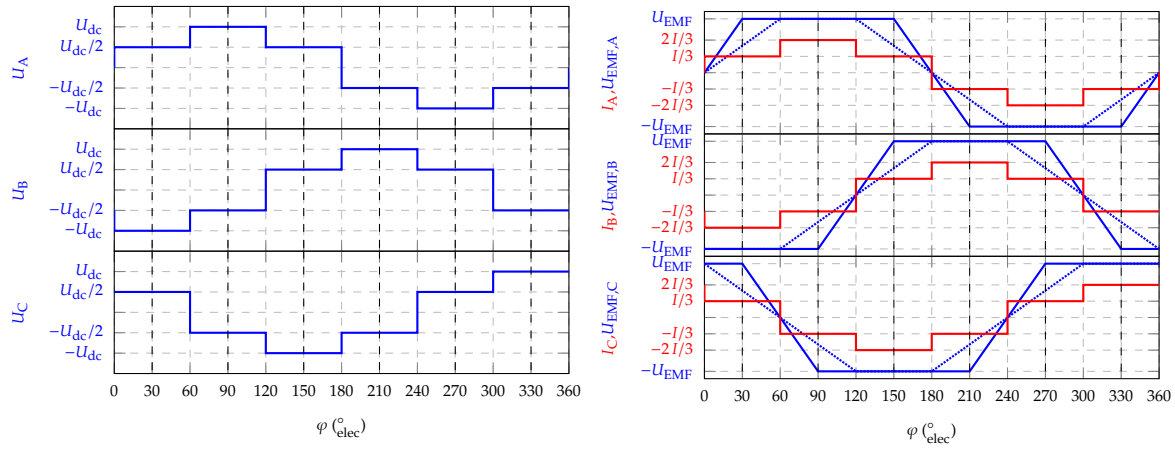

(a) 120/Δ phase voltage.

(b) 120/Δ phase current & EMF signals.

Figure 4.6: Phase signals for 120/Δ.

Interval	H_A	H_B	H_C	SW_{A+}	SW_{A-}	SW_{B+}	SW_{B-}	SW_{C+}	SW_{C-}	φ_{start}	φ_{end}
-	0	0	0	-	-	-	-	-	-	-	-
1	1	0	1	1	0	0	1	1	0	0	60
2	1	0	0	1	0	0	1	0	1	60	120
3	1	1	0	1	0	1	0	0	1	120	180
4	0	1	0	0	1	1	0	0	1	180	240
5	0	1	1	0	1	1	0	1	0	240	300
6	0	0	1	0	1	0	1	1	0	300	360
-	1	1	1	-	-	-	-	-	-	-	-

Table 4.3: 180/⅄ commutation truth table.

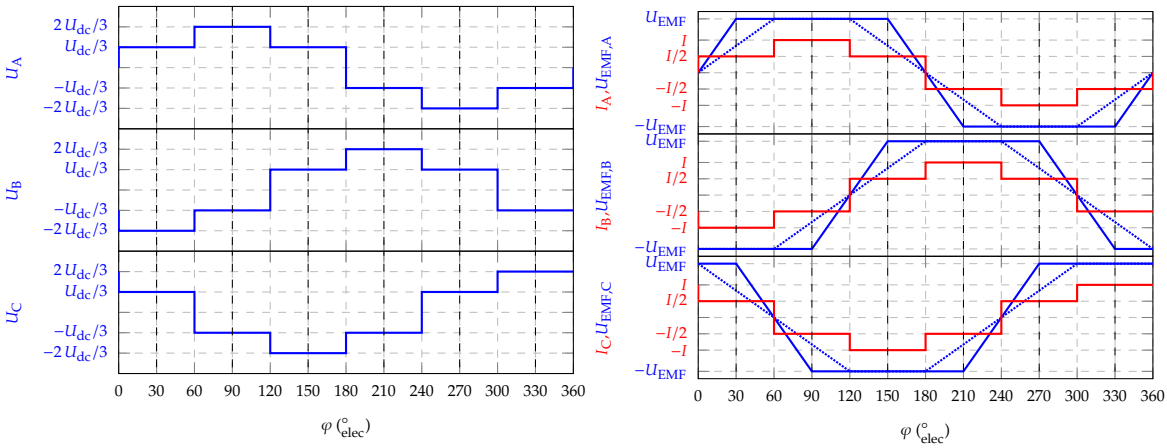

(a) 180/⅄ phase voltage.

(b) 180/⅄ phase current & EMF signals.

Figure 4.7: Phase signals for 180/⅄.

Interval	H_A	H_B	H_C	SW_{A+}	SW_{A-}	SW_{B+}	SW_{B-}	SW_{C+}	SW_{C-}	φ_{start}	φ_{end}
-	0	0	0	-	-	-	-	-	-	-	-
1	0	0	1	0	1	0	1	1	0	330	30
2	1	0	1	1	0	0	1	1	0	30	90
3	1	0	0	1	0	0	1	0	1	90	150
4	1	1	0	1	0	1	0	0	1	150	210
5	0	1	0	0	1	1	0	0	1	210	270
6	0	1	1	0	1	0	1	1	0	270	330
-	1	1	1	-	-	-	-	-	-	-	-

Table 4.4: 180/Δ commutation truth table.

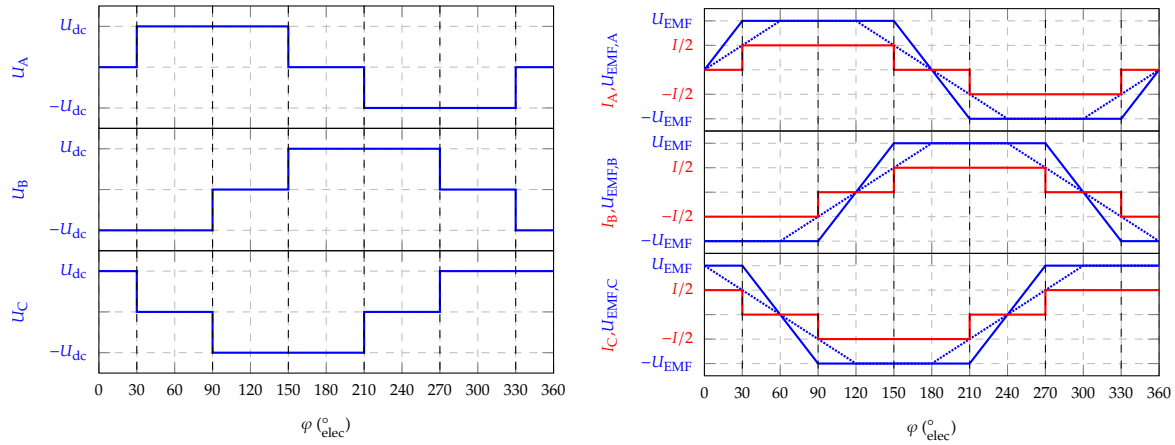

(a) 180/Δ phase voltage.

(b) 180/Δ phase current & EMF signals.

Figure 4.8: Phase signals for 180/Δ.

4.2 Trapezoidal control: performance comparison

Characteristic parameters

The control schemes are analyzed with respect to the following four criteria ("characteristic parameters"):

$$I_{\mathrm{p,rms}} = \sqrt{\frac{1}{T}\int_0^T i_{\mathrm{p}}^2 \,\mathrm{d}t} \qquad U_{\mathrm{p,rms}} = \sqrt{\frac{1}{T}\int_0^T u_{\mathrm{p}}^2 \,\mathrm{d}t} \tag{4.1}$$

$$P_{\mathrm{out}} = \tau\,\omega = \frac{3}{T}\int_0^T u_{\mathrm{EMF}}\, i_{\mathrm{p}} \,\mathrm{d}t \qquad \eta = \frac{P_{\mathrm{out}}}{3\,I_{\mathrm{rms}}^2\,R_{\mathrm{Cu}} + P_{\mathrm{out}}} \tag{4.2}$$

I_{p} and U_{p} describe the phase currents and voltages respectively, τ and ω_{m} the average torque and the mechanic angular velocity, η is an estimation of the motor efficiency neglecting the iron losses. Tables 4.5 and 4.6 give an overview of the characteristic parameters for the individual control schemes and corresponding EMFs flat top widths.

	120/⅄	120/Δ	180/⅄	180/Δ
$I_{\mathrm{p,rms}}$	$\frac{2}{\sqrt{6}}\,I$	$\frac{\sqrt{2}}{3}\,I$	$\frac{1}{\sqrt{2}}\,I$	$\frac{1}{\sqrt{6}}\,I$
$U_{\mathrm{p,rms}}$	$\frac{1}{\sqrt{6}}\,U_{\mathrm{dc}}$	$\frac{1}{\sqrt{2}}\,U_{\mathrm{dc}}$	$\frac{\sqrt{2}}{3}\,U_{\mathrm{dc}}$	$\sqrt{\frac{2}{3}}\,U_{\mathrm{dc}}$
P_{out}	$2\,U_{\mathrm{EMF}}\,I$	$\frac{7}{6}\,U_{\mathrm{EMF}}\,I$	$\frac{7}{4}\,U_{\mathrm{EMF}}\,I$	$U_{\mathrm{EMF}}\,I$
I	$\frac{\tau\,\omega}{2\,U_{\mathrm{EMF}}}$	$\frac{6\,\tau\,\omega}{7\,U_{\mathrm{EMF}}}$	$\frac{4\,\tau\,\omega}{7\,U_{\mathrm{EMF}}}$	$\frac{\tau\,\omega}{U_{\mathrm{EMF}}}$
η	$\frac{2\,U_{\mathrm{EMF}}^2}{P_{\mathrm{out}}\,R_{\mathrm{Cu}}+2\,U_{\mathrm{EMF}}^2}$	$\frac{49\,U_{\mathrm{EMF}}^2}{24\,P_{\mathrm{out}}\,R_{\mathrm{Cu}}+49\,U_{\mathrm{EMF}}^2}$	$\frac{49\,U_{\mathrm{EMF}}^2}{24\,P_{\mathrm{out}}\,R_{\mathrm{Cu}}+49\,U_{\mathrm{EMF}}^2}$	$\frac{2\,U_{\mathrm{EMF}}^2}{P_{\mathrm{out}}\,R_{\mathrm{Cu}}+2\,U_{\mathrm{EMF}}^2}$

Table 4.5: Characteristic parameters of the four trapezoidal control schemes and a back-EMFs flat top width of 120 degree.

In the following, individual characteristic parameters and related performances of the four control schemes will be compared. At the end of this section, the findings regarding the individual characteristic parameters of the four discussed control schemes will be summarized and the final choice regarding the drive topology for the developed three phase BLDC machine will be explained.

	120/⅄	120/Δ	180/⅄	180/Δ
$I_{\mathrm{p,rms}}$	$\frac{2}{\sqrt{6}}\,I$	$\frac{\sqrt{2}}{3}\,I$	$\frac{1}{\sqrt{2}}\,I$	$\frac{1}{\sqrt{6}}\,I$
$U_{\mathrm{p,rms}}$	$\frac{1}{\sqrt{6}}\,U_{\mathrm{dc}}$	$\frac{1}{\sqrt{2}}\,U_{\mathrm{dc}}$	$\frac{\sqrt{2}}{3}\,U_{\mathrm{dc}}$	$\sqrt{\frac{2}{3}}\,U_{\mathrm{dc}}$
P_{out}	$\frac{7}{4}\,U_{\mathrm{EMF}}\,I$	$U_{\mathrm{EMF}}\,I$	$\frac{3}{2}\,U_{\mathrm{EMF}}\,I$	$\frac{7}{8}\,U_{\mathrm{EMF}}\,I$
I	$\frac{4\,\tau\,\omega}{7\,U_{\mathrm{EMF}}}$	$\frac{\tau\,\omega}{U_{\mathrm{EMF}}}$	$\frac{2\,\tau\,\omega}{3\,U_{\mathrm{EMF}}}$	$\frac{8\,\tau\,\omega}{7\,U_{\mathrm{EMF}}}$
η	$\frac{49\,U_{\mathrm{EMF}}^2}{32\,P_{\mathrm{out}}\,R_{\mathrm{Cu}}+49\,U_{\mathrm{EMF}}^2}$	$\frac{3\,U_{\mathrm{EMF}}^2}{2\,P_{\mathrm{out}}\,R_{\mathrm{Cu}}+3\,U_{\mathrm{EMF}}^2}$	$\frac{3\,U_{\mathrm{EMF}}^2}{2\,P_{\mathrm{out}}\,R_{\mathrm{Cu}}+3\,U_{\mathrm{EMF}}^2}$	$\frac{49\,U_{\mathrm{EMF}}^2}{32\,P_{\mathrm{out}}\,R_{\mathrm{Cu}}+49\,U_{\mathrm{EMF}}^2}$

Table 4.6: Characteristic parameters of the four trapezoidal control schemes and a back-EMFs flat top width of 60 degree.

Efficiency

Considering the efficiency, the four trapezoidal control schemes are almost identical. Equation (4.3) and Figure 4.9(a) show the differences in efficiency for the four control schemes driving a three phase motor with a 120 degree flat top width back-EMF. Equation (4.4) and Figure 4.9(b) show the differences in efficiency for the same four control schemes driving a three phase motor with a 60 degree flat top width back-EMF.

$$\frac{\eta_{1,120}}{\eta_{2,120}} := \frac{\eta_{180/\Delta}}{\eta_{180/\curlywedge}} = \frac{\eta_{120/\curlywedge}}{\eta_{120/\Delta}} = \frac{48\,P_{\mathrm{out}} + \frac{U_{\mathrm{EMF}}^2}{R_{\mathrm{Cu}}}\,98}{49\,P_{\mathrm{out}} + \frac{U_{\mathrm{EMF}}^2}{R_{\mathrm{Cu}}}\,98} \tag{4.3}$$

$$\frac{\eta_{1,60}}{\eta_{2,60}} := \frac{\eta_{180/\curlywedge}}{\eta_{180/\Delta}} = \frac{\eta_{120/\Delta}}{\eta_{120/\curlywedge}} = \frac{96\,P_{\mathrm{out}} + \frac{U_{\mathrm{EMF}}^2}{R_{\mathrm{Cu}}}\,147}{98\,P_{\mathrm{out}} + \frac{U_{\mathrm{EMF}}^2}{R_{\mathrm{Cu}}}\,147} \tag{4.4}$$

Power

The four trapezoidal control schemes differ significantly with respect to the maximum power that a single motor is able to provide for a given supply voltage (equations (4.5) to (4.8)):

$$P_{\mathrm{out},120/\curlywedge} = \frac{\eta\,U_{\mathrm{dc}}}{2\,R}(U_{\mathrm{dc}} - 2\,U_{\mathrm{EMF}}) \tag{4.5}$$

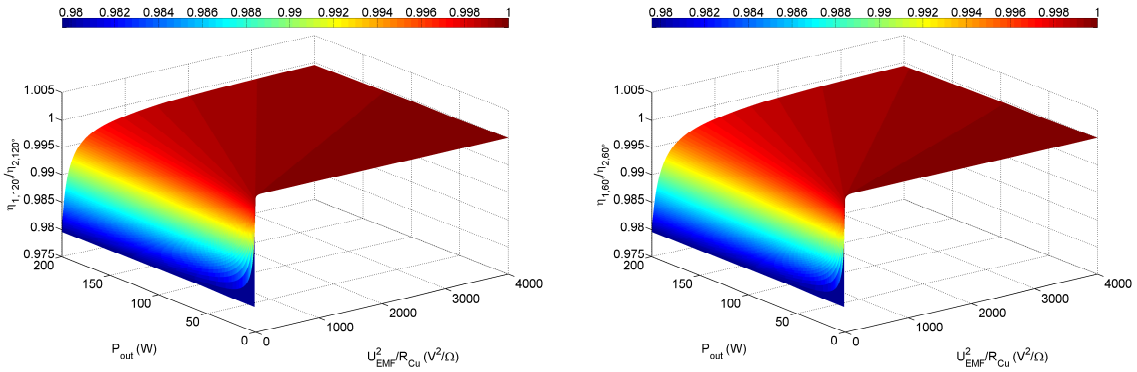

(a) BLDC motor having a back-EMF with a 120 degree flat top width.

(b) BLDC motor having a back-EMF with a 60 degree flat top width.

Figure 4.9: Efficiency comparison of trapezoidal controls

$$P_{\text{out},180/\curlywedge} = \frac{\eta\, U_{\text{dc}}}{3\,R}\left(\frac{6\,U_{\text{dc}}}{3} - \frac{7\,U_{\text{EMF}}}{2}\right) \tag{4.6}$$

$$P_{\text{out},120/\Delta} = \frac{\eta\, U_{\text{dc}}}{4\,R}\left(6\,U_{\text{dc}} - 7\,U_{\text{EMF}}\right) \tag{4.7}$$

$$P_{\text{out},180/\Delta} = \frac{2\,\eta\, U_{\text{dc}}}{R}\left(U_{\text{dc}} - U_{\text{EMF}}\right) \tag{4.8}$$

Assuming that the induced voltage $U_{\text{EMF,rms}}$ is negligibly small compared to the supply voltage U_{dc}, the following ratios of the maximum output power and the corresponding line currents are obtained:

$$\begin{aligned} P_{\text{max,out},120/\curlywedge} : P_{\text{max,out},120/\Delta} : P_{\text{max,out},180/\curlywedge} : P_{\text{max,out},180/\Delta} &= 1 : 3 : \frac{4}{3} : 4 \\ I_{120/\curlywedge,\text{P}_{\text{max}}} : I_{120/\Delta,\text{P}_{\text{max}}} : I_{180/\curlywedge,\text{P}_{\text{max}}} : I_{180/\Delta,\text{P}_{\text{max}}} &= 1 : 3 : \frac{4}{3} : 4 \end{aligned} \tag{4.9}$$

Furthermore, from equations (4.5) to (4.8) also the winding parameters for two motors can be derived, from which an approximate equality of the output power is desired. These motors will be driven by two different trapezoidal controls and should behave almost equally (e.g. equations (4.10) to (4.12)).

$$R_{120/\curlywedge} = \frac{R_{120/\Delta}}{3} \tag{4.10}$$

$$U_{\text{EMF},120/\curlywedge} = \frac{U_{\text{EMF},120/\Delta}}{\sqrt{3}} \tag{4.11}$$

$$
\begin{aligned}
P_{\text{out,120/}\curlywedge} &= \frac{\eta\, U_{\text{dc}}}{2\, R_{120/\curlywedge}} \left(U_{\text{dc}} - 2\, U_{\text{EMF,120/}\curlywedge}\right) = \\
&= \frac{\eta\, U_{\text{dc}}\, 3}{2\, R_{120/\Delta}} \left(U_{\text{dc}} - \frac{2\, U_{\text{EMF,120/}\Delta\text{,rms}}}{\sqrt{3}}\right) \\
&= \frac{\eta\, U_{\text{dc}}}{4\, R_{120/\Delta}} \left(6\, U_{\text{dc}} - 6.93\, U_{\text{EMF,120/}\Delta\text{,rms}}\right) \approx P_{\text{out,120/}\Delta}
\end{aligned}
\tag{4.12}
$$

In the following, more practical aspects of selecting the drive's control strategy will be examined.

If we assume constant inductances for a three phase BLDC motor, the instantaneous torque (T_{e}) developed is

$$
T_{\text{e}} = \frac{P_{\text{out}}}{\omega_{\text{m}}} = \frac{u_{\text{EMF,A}}\, i_{\text{p,A}} + u_{\text{EMF,C}}\, i_{\text{p,C}} + u_{\text{EMF,C}}\, i_{\text{p,C}}}{\omega_{\text{m}}}. \tag{4.13}
$$

As stated in [68], the major determining factor in whether to connect the motor windings in delta or star, is a requisite width of the phase back-EMF flat top.

Torque ripple

From Figures 4.5 to 4.8 and equation (4.13) it can be predicted that the torque ripple depends on the phase EMF's flat top and the control's phase current waveforms. Table 4.7 shows the torque ripple of the four trapezoidal control schemes for different flat top widths (α_{top}) of the phase back-EMFs and ideal current waveforms. The torque ripple was calculated with

$$
\Delta T_{\text{e}} = \frac{(T_{\text{e,max}} - T_{\text{e,min}})}{T_{\text{e,average}}}. \tag{4.14}
$$

Harmonics

Another selection aspect arises from the harmonic contents of the back-EMF phase voltages. Some combinations of windings and pole-arcs give rise to triplen harmonics of the phase back-EMFs. These triplen harmonics will drive circulating currents in delta connected motors and cause additional copper and iron losses and thus decrease the efficiency [9].

α_{top} ° elec	$\Delta T_{\text{e},120/\curlywedge}$ %	$\Delta T_{\text{e},120/\Delta}$ %	$\Delta T_{\text{e},180/\curlywedge}$ %	$\Delta T_{\text{e},180/\Delta}$ %
60	28.6	0	0	28.6
70	25.1	2.9	2.9	25.1
80	21.4	6.4	6.4	21.4
90	17.4	10.3	10.3	17.4
100	12.8	15.0	15.0	12.8
110	7.1	21.0	21.0	7.1
120	0	28.6	28.6	0

Table 4.7: Impact of EMF's flat top on torque ripple.

Short circuit intervals

Short circuit currents can cause problems for the 180/Δ control. In Figure 4.8 every phase current is zero two times over one electrical period. Figure 4.10 shows the electrical circuits for these two time intervals for phase *A*.

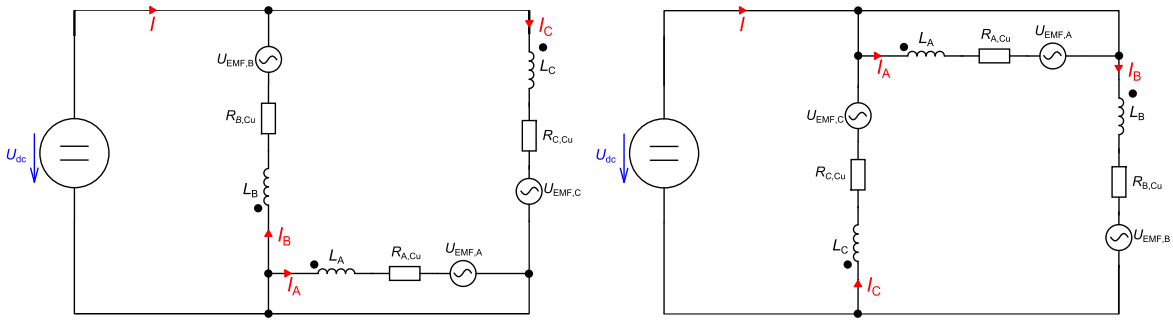

(a) 180/Δ → commutation interval 1 (*I*1). (b) 180/Δ → commutation interval 4 (*I*4).

Figure 4.10: Circuit diagram for zero current intervals of phase A.

Figure 4.11 shows the back-EMF and phase current for one electrical period of phase *A* of a BLDC machine driven with the 180/Δ control strategy and simulated with the hybrid model from Section 2.3. For commutation intervals 1 and 4 phase *A* is shortened, therefore the energy stored in the phase will be dissipated and generate a driving torque (areas in Figure 4.11). Once the energy is exhausted, the back-EMF drives the phase current and generates a breaking torque(areas in Figure 4.11).

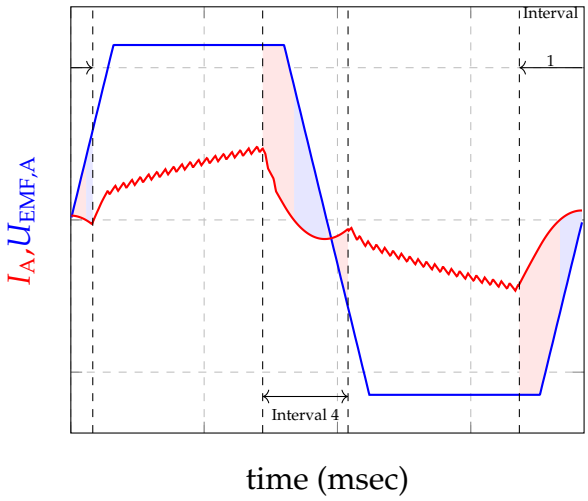

Figure 4.11: Phase signals for a 180/Δ controlled motor.

Sinusoidal control

The sinusoidal control was not analyzed in more detail for the motor from Section 2.1.1 as it would, as mentioned earlier in this section, raise the costs for the rotor position detection and control unit.

Selected control scheme

Considering the output power and the ratio U_{EMF}^2/R_{Cu} of the three phase drive, an efficiency difference less than 0.5 % can be expected for all analyzed control schemes. Furthermore, the maximum output power also provides no advantages of a particular control scheme, as the winding parameters for two motors can always be changed so that the motors behave electrically equal.

Practically speaking, inverter circuits designed for a 120/Δ control scheme and suiting the needs of the machine to be designed were already available. Furthermore, considering that no circulating currents will be produced as the induced voltages contain no triplen harmonics and that the rotor design for the three phase drive of the pump application and the regarding back-EMF has a rather flat top width of 60 degrees, the 120/Δ control scheme was chosen to drive the BLDC machine as less torque ripple can be expected.

4.3 Impact of hall sensor positioning on motor efficiency

In this section the placement of the hall sensors, which are responsible for commutation, and the influence on the motor behavior will be discussed.

The electromagnetic torque developed by a three phase brushless DC machine can be expressed as,

$$T = \frac{P_{\text{out}}}{\omega_{\text{m}}} = \frac{u_{\text{EMF,A}}\, i_{\text{p,A}} + u_{\text{EMF,B}}\, i_{\text{p,B}} + u_{\text{EMF,C}}\, i_{\text{p,C}}}{\omega_{\text{m}}}. \tag{4.15}$$

As per equation (4.15), the motor will generate most torque when the induced voltages and the respective phase currents are in phase.

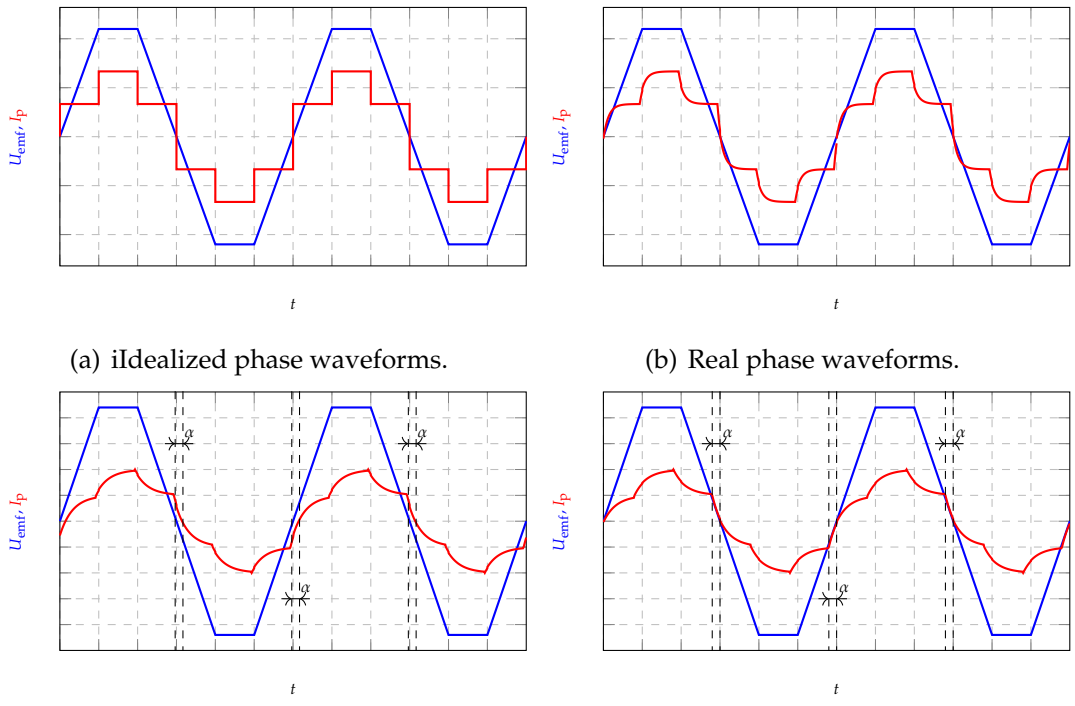

(a) iIdealized phase waveforms.

(b) Real phase waveforms.

(c) Waveforms for high speed.

(d) Waveforms for advanced angle control.

Figure 4.12: Back-EMF an phase currents for BLDC motors: (a) idealized waveforms; (b) real phase waveforms; (c) waveforms for high speed; (d) waveforms for advanced angle control.

Figure 4.12(a) shows the ideal back-EMF and phase current waveform of one phase and for a delta connected motor.

Due to the resistances and inductances of the motor windings, the waveforms of the actual phase currents will lag the ideal waveforms as can be seen in Figure 4.12(b) [69,70]. Further increasing the speed will worsen the situation, because firstly, lager back-EMF voltages reduce the voltage available for driving the currents through the motor windings and secondly, the time the back-EMF voltage changes sign gets faster which increases the ratio between the winding time constant to the back-EMF voltage slope. Figure 4.12(c) shows the result of the higher rotational speed: The phase currents lag the back-EMF voltages by α and cause negative torques during these times.

To avoid lagging phase currents and increase motor efficiency, the commutation angles have to be advanced (Figure 4.12(b)). Thereby, the phase advanced angle depends on the actual motor speed and load.

As the three phase motor driving the pump will be operated only at a specific speed and load, the advanced angle does not have to be controlled. A simple displacement of the hall sensors will be sufficient to ensure advanced commutation.

To find the most efficient commutation instances, the hybrid model from section (Section 2.3) was used for simulation. The average load of the pump as well as the actual pump load profile were simulated to identify changes in the commutation angle due to the high peak torque of the pump load and its regarding speed variations.

Table 4.8 and Figures 4.13(a) to 4.13(d) show the results of the hybrid simulations with different advanced commutation instances and advanced angles α.

Figure 4.13(a) shows a relatively weak dependency between the motor's efficiency and the advanced commutation angle. Furthermore, simulating the average pump load torque gives the same results as simulating the pump with its varying load profile over one revolution.

The best motor efficiency can be achieved with an advanced angle of $\alpha \approx 10{-}13^{\circ}_{\text{elec}}$. As the BLDC machine has four pole pairs, the hall sensors should be shifted with respect to their neutral positions by 3 mechanical degrees.

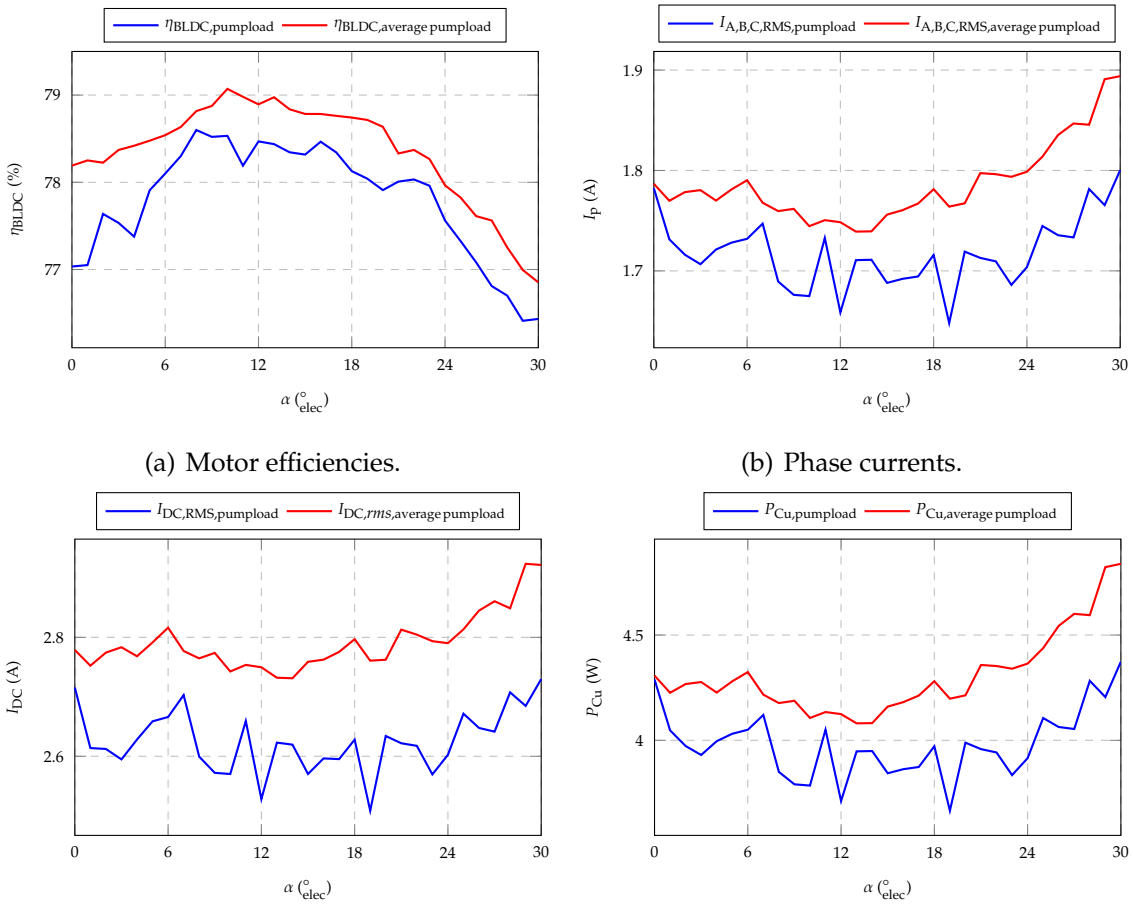

(a) Motor efficiencies.

(b) Phase currents.

(c) Total currents for $U_{DC} = 12\,V$.

(d) Copper losses.

Figure 4.13: Simulation results for different advanced commutation angles.

α	$I_{DC,RMS}$ (A)		$I_{A,B,C,RMS}$ (A)		$\hat{I}_{A,B,C,RMS}$ (A)		P_{In} (W)		P_{Cu} (W)		η_{BLDC} (%)	
$^{\circ}_{elec}$	a)	b)	a)	b)	a)	b)	a)	b)	a)	b)	a)	b)
0	2.78	2.72	1.79	1.78	3.10	3.56	25.85	25.06	4.31	4.29	78.2	77.0
1	2.75	2.61	1.77	1.73	3.05	3.55	25.64	24.11	4.23	4.05	78.3	77.1
2	2.77	2.61	1.78	1.72	3.06	3.45	25.90	24.28	4.27	3.97	78.2	77.6
3	2.78	2.59	1.78	1.71	3.05	3.48	26.02	24.16	4.28	3.93	78.4	77.5
4	2.77	2.63	1.77	1.72	3.06	3.44	25.92	24.45	4.23	4.00	78.4	77.4
5	2.79	2.66	1.78	1.73	3.07	3.37	26.15	24.84	4.28	4.03	78.5	77.9
6	2.82	2.67	1.79	1.73	3.06	3.32	26.44	24.93	4.32	4.05	78.5	78.1
7	2.78	2.70	1.77	1.75	3.05	3.34	26.10	25.38	4.22	4.12	78.6	78.3
8	2.76	2.60	1.76	1.69	2.99	3.29	26.01	24.37	4.18	3.85	78.8	78.6
9	2.77	2.57	1.76	1.68	2.99	3.28	26.13	24.11	4.19	3.79	78.9	78.5
10	2.74	2.57	1.74	1.67	2.99	3.30	25.85	24.10	4.11	3.78	79.1	78.5
11	2.75	2.66	1.75	1.73	3.00	3.26	25.95	24.78	4.13	4.05	79.0	78.2
12	2.75	2.53	1.75	1.66	2.95	3.05	25.91	23.57	4.12	3.71	78.9	78.5
13	2.73	2.62	1.74	1.71	2.96	3.44	25.75	24.53	4.08	3.95	79.0	78.4
14	2.73	2.62	1.74	1.71	2.99	3.46	25.74	24.47	4.08	3.95	78.8	78.3
15	2.76	2.57	1.76	1.69	3.01	3.38	25.97	23.95	4.16	3.84	78.8	78.3
16	2.76	2.60	1.76	1.69	2.97	3.33	25.95	24.33	4.18	3.86	78.8	78.5
17	2.78	2.60	1.77	1.69	2.98	3.36	26.07	24.27	4.21	3.87	78.8	78.3
18	2.80	2.63	1.78	1.72	3.01	3.40	26.23	24.50	4.28	3.97	78.7	78.1
19	2.76	2.51	1.76	1.65	3.01	3.27	25.87	23.51	4.20	3.67	78.7	78.0
20	2.76	2.63	1.77	1.72	2.99	3.41	25.85	24.61	4.21	3.99	78.6	77.9
21	2.81	2.62	1.80	1.71	3.06	3.28	26.27	24.48	4.36	3.96	78.3	78.0
22	2.80	2.62	1.80	1.71	3.02	3.27	26.13	24.45	4.35	3.94	78.4	78.0
23	2.79	2.57	1.79	1.69	3.04	3.22	25.99	23.96	4.34	3.83	78.3	78.0
24	2.79	2.60	1.80	1.70	3.01	3.24	25.86	24.32	4.36	3.92	78.0	77.6
25	2.81	2.67	1.81	1.74	3.03	3.35	26.03	24.96	4.44	4.11	77.8	77.3
26	2.84	2.65	1.84	1.74	3.06	3.30	26.24	24.65	4.54	4.06	77.6	77.1
27	2.86	2.64	1.85	1.73	3.08	3.25	26.34	24.50	4.60	4.05	77.6	76.8
28	2.85	2.71	1.85	1.78	3.12	3.32	26.16	24.96	4.59	4.28	77.3	76.7
29	2.92	2.68	1.89	1.77	3.16	3.30	26.76	24.78	4.82	4.21	77.0	76.4
30	2.92	2.73	1.89	1.80	3.17	3.37	26.68	25.08	4.84	4.37	76.9	76.4

Table 4.8: Results of the advanced angle switching simulations with a) constant load & b) the pump load profile.

Chapter 5

Single phase BLDC motor control

This chapter will review types of control for single phase BLDC motors. The control technique best suiting the needs of the fan application (Section 2.1.2) will be described more in detail.

Furthermore, as the discussed control types use hall sensors for position detection, the influence of these sensors on the motor behavior will be analyzed in detail. Single phase PM BLDC motors are cost effective and easy to manufacture machine types [20]. Therefore, costs are also a driving factor for the design and selection of the motor control. In this section, two different types of single phase motors and the corresponding controls will be analyzed (Figure 5.1).

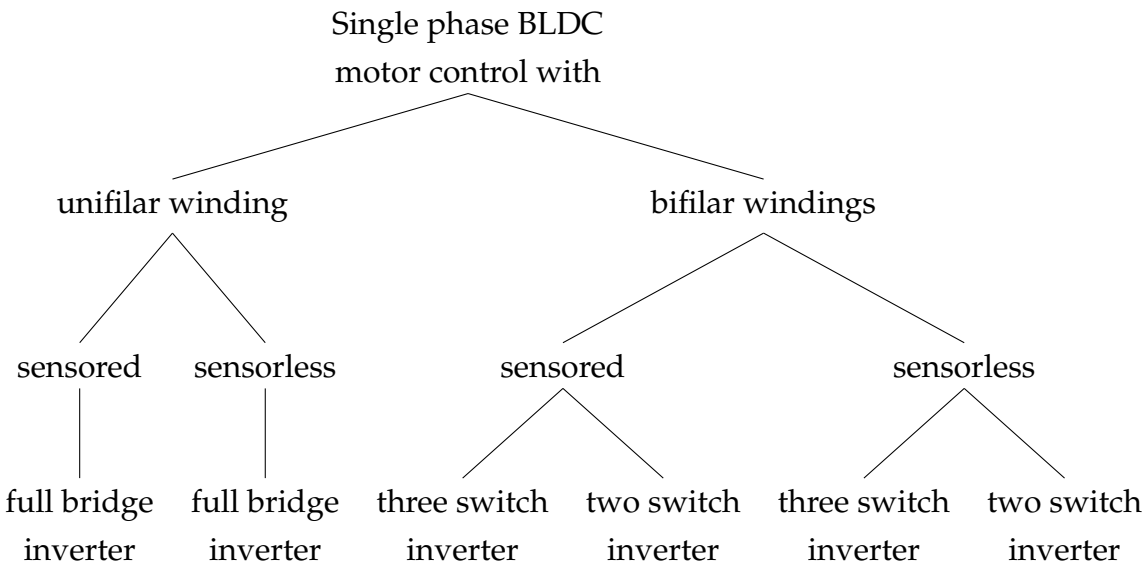

Figure 5.1: Single phase BLDC motor types and control techniques.

The following sections concentrate on sensored motor control techniques for the

individual single phase motor types. Sensorless techniques will be discussed in detail in Section 6.2.

The inverters for all topologies presented in Figure 5.1 have in common, that only one hall sensor is needed to detect the rotor position and commutate the phase current.

5.1 Motor control for a single phase motor with a unifilar winding pattern

First, we concentrate on a conventional single phase BLDC machine with a unifilar winding. This machine is controlled by one full bridge inverter as shown in Figure 5.2.

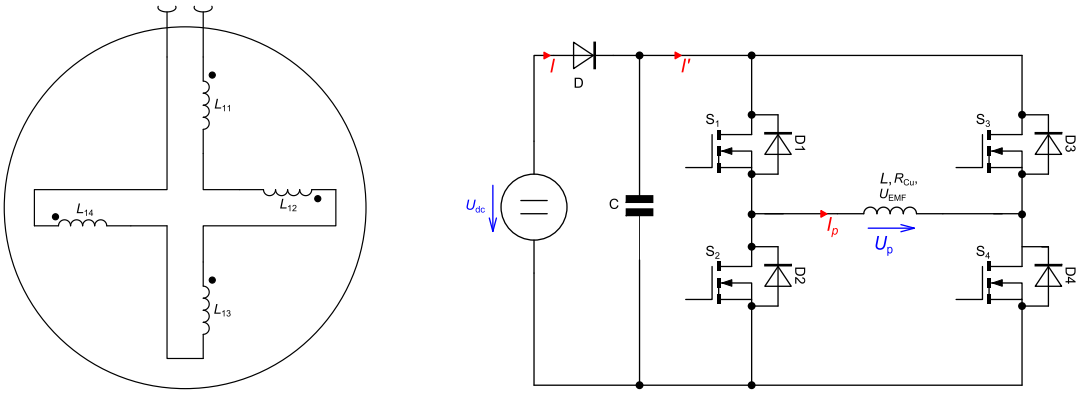

(a) Unifilar winding of a four pole four slot single phase BLDC motor.

(b) Full bridge inverter for a single phase BLDC machine with a unifilar winding.

Figure 5.2: Conventional single phase BLDC machine and inverter circuit.

Considering the electrical signals over one electrical period the waveforms shown in Figure 5.3 are obatained:

During the time interval t_0 - t_1 the back-EMF voltage is negative. Therefore, the current has to be fed to the machine through the switches S_2 and S_3 in order to generate a positive torque. S_2 is turned on during the whole time interval and S_3 assumes the role of the PWM switch. For the PWM-OFF times the body diode of switch S_4 provides the freewheeling path for the phase current.

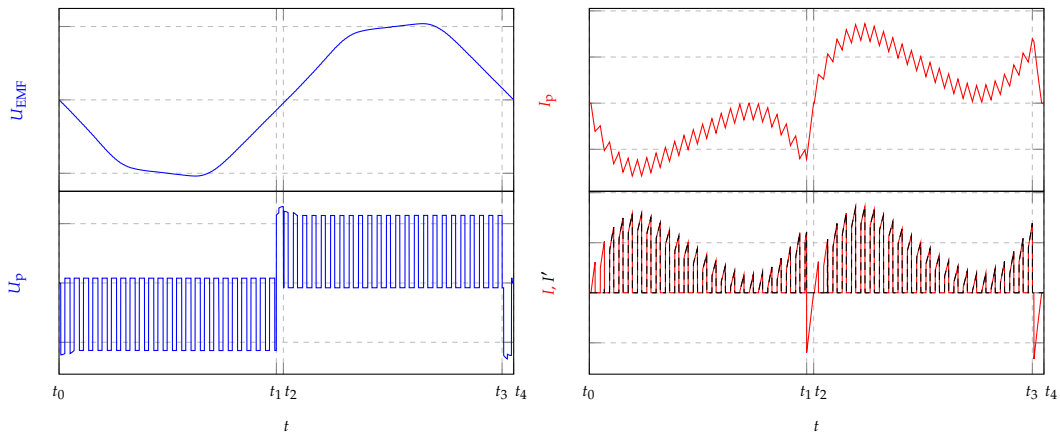

Figure 5.3: Electrical signals for a single phase BLDC machine with unifilar windings.

At t_1, the single phase motor has to commutate its phase current and therefore switches S_2 and S_3 are turned off and S_1 and S_4 are now responsible for the machine's supply. In the time interval (t_1 - t_2) the phase current has to change its polarity and as long as it has negative polarity, the current will charge the DC link capacitor C and produce a negative current I'. During the time interval (t_2 - t_3) the second commutation period takes place, in which switch S_4 stays ON and S_1 works as the PWM switch. Consistently, switch S_2 builds the freewheeling path for the PWM-OFF times in this commutation interval.

5.2 Motor control for a single phase motor with a bifilar winding pattern

In Section 5.3, the reason for the existence of this drive topology will be described in more detail, even though it suffers from worse efficiency as compared to the drive topology for a unifilar wound single phase BLDC machine.

In this section two different drive circuits for a single phase motor with a bifilar winding pattern will be presented.

Motor control using two switches

The principle winding arrangement of the single phase motor is shown in Figure 5.4(a). The inverter circuit as well as motor, modeled by its individual parts, can be seen in Figure 5.4(b).

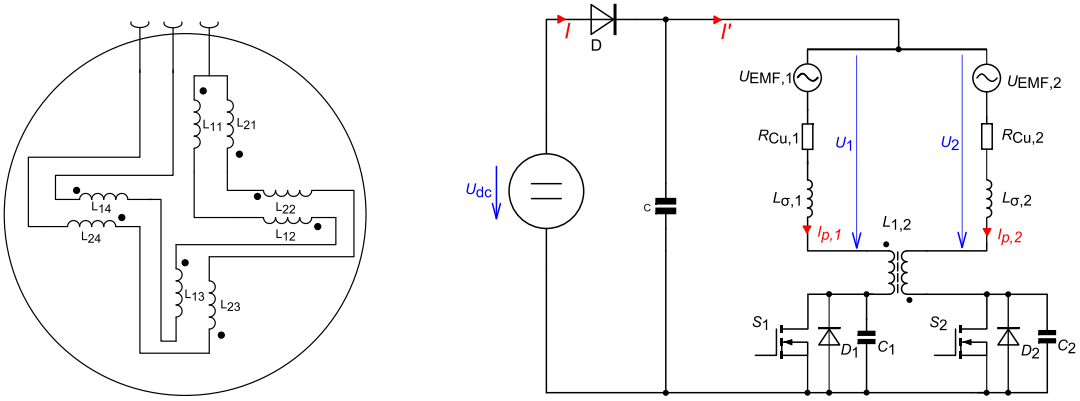

(a) Bifilar windings of a four pole four slot single phase BLDC motor.

(b) Inverter for a single phase BLDC machine with bifilar windings.

Figure 5.4: Single phase BLDC machine with bifilar windings and its inverter circuit I.

A bifilar winding can be modeled as a transformer, where $L_{\sigma,1}$ and $L_{\sigma,2}$ represent the stray inductances and $L_{1,2}$ the mutual inductance of the bifilar winding. $R_{\mathrm{Cu},1}$ and $R_{\mathrm{Cu},2}$ describe the resistances of the winding. $U_{\mathrm{EMF},1}$ & $U_{\mathrm{EMF},1}$ represent the induced voltages in the individual windings due to the changing field of the rotating magnets.

Figure 5.5 shows the simulated electrical signals over one period. During the first commutation interval (t_0 - t_1) winding 1 should draw current to generate a positive

torque.

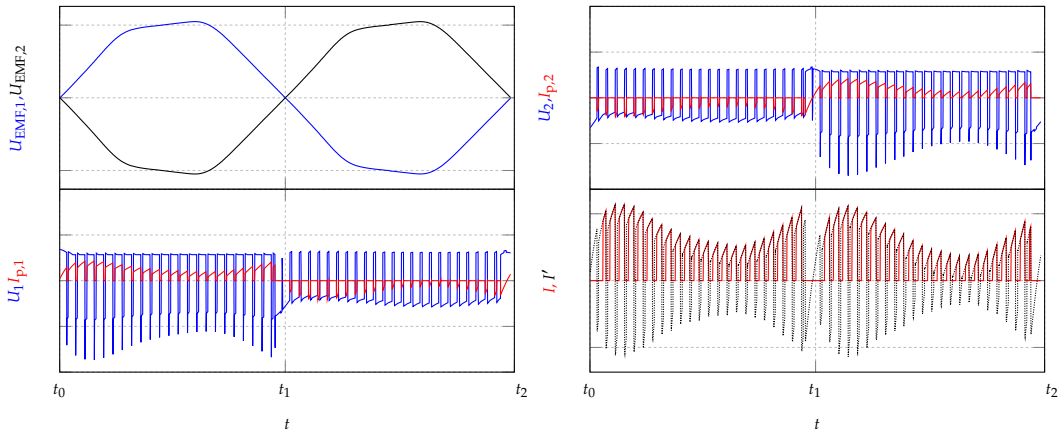

Figure 5.5: Electrical signals for a bifilar wound BLDC and a two-switch inverter.

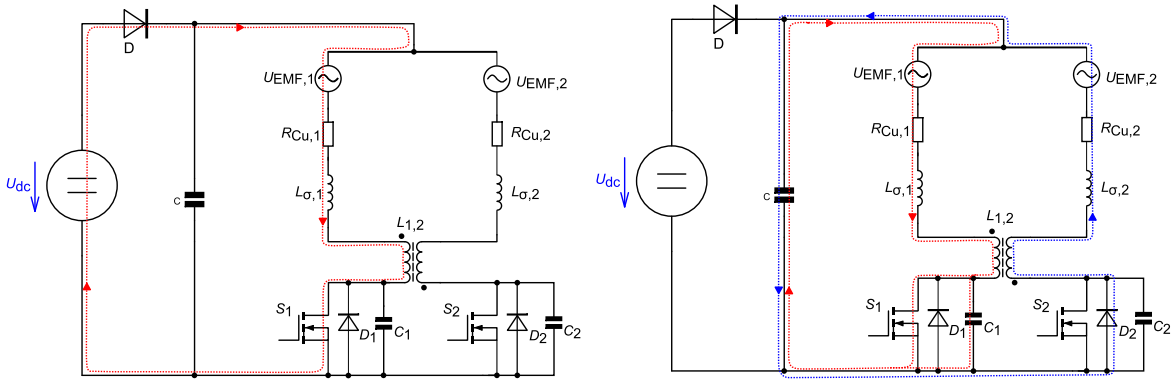

(a) Current flow during PWM-ON times.

(b) Current flow during PWM-OFF times.

Figure 5.6: Current paths of two switch inverter topology.

Figure 5.6(a) shows the current path during PWM-ON times of this commutation period. After the duty cycle of the PWM, switch S_1 will be turned off and the energy stored in the main inductance $L_{1,2}$ will be transfered to the secondary winding freewheeling through the body diode D_2 of the switch S_2 (blue path in Figure 5.6(b)). The energy stored in the stray inductance $L_{\sigma,1}$ cannot be transferred to the winding of the secondary side and therefore has to dissipate through switch S_1 (red path in Figure 5.6(b)). If the switch is turned off aggressively, the energy from the stray inductance will charge the switch's parasitic capacitance, causing voltage spikes

(e.g Figure 5.5) at the switch. These voltage spikes can exceed the switch's breakdown voltage and additionally cause electromagnetic interferences.

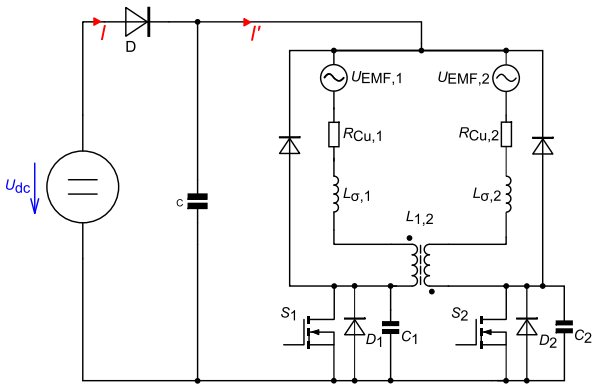

Figure 5.7: Two switch inverter topology with freewheeling diodes.

If the switch is turned off gently, more of the energy stored in stray inductance will be dissipated in the switch's conduction path and therefore cause higher losses, which can bring the switch to its thermal limits.

A modification of the circuit (shown in Figure 5.4(b)) overcoming the problems described above is to equip the motor windings with additional freewheeling diodes (Figure 5.7). The disadvantage of the inverter circuit using two additional freewheeling diodes would be that the drive suffers from reduced efficiency as the additional diodes will be shortened during the negative half periods of the induced voltages generating breaking torques.

Motor control using three switches

The winding arrangement for this inverter topology is the same as that shown in Figure 5.4(a). The inverter topology itself is shown in Figure 5.8.

For the three switches single phase motor control S_1 and S_2 are responsible for commutating the phase current depending on the rotor position and switch S_3 assumes the role of the PWM control. Figure 5.9 shows again the electrical signals over one period of the induced voltage.

During the positive half cycle of the induced voltage $U_{\mathrm{EMF},1}$, the switch S_1 remains closed. Thus, during PWM-ON times the current path, shown in Figure 5.10(a), will

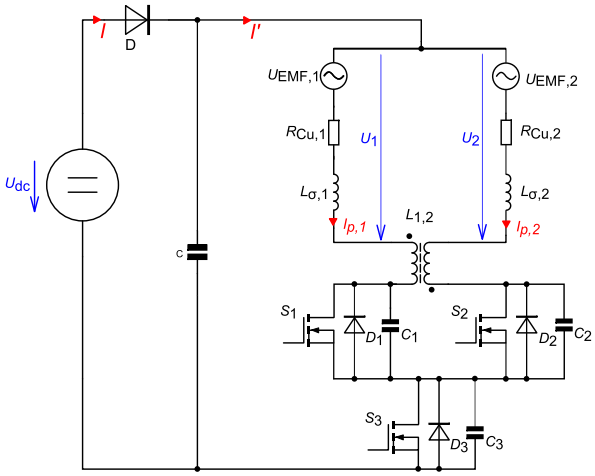

Figure 5.8: Single phase BLDC machine with bifilar windings and its inverter circuit II.

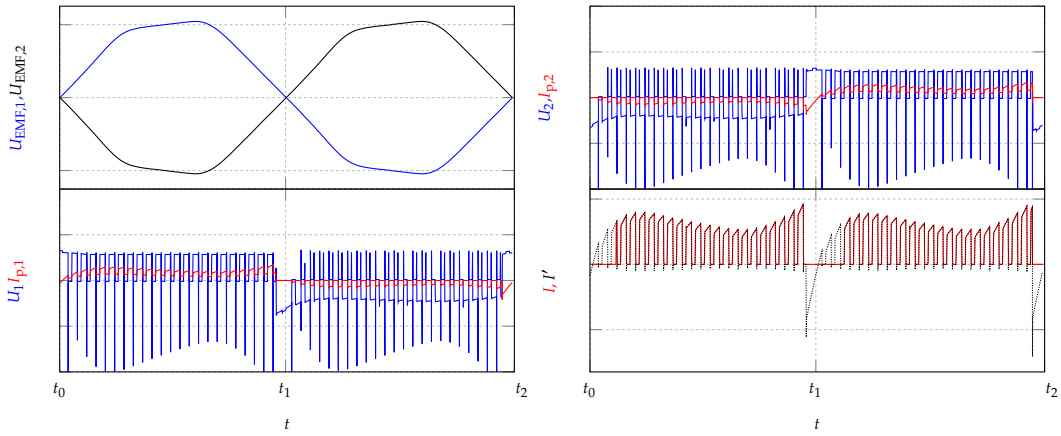

Figure 5.9: Electrical signals for a bifilar wound BLDC and a three-switch inverter.

build up.

By turning off the "PWM switch S_3" most of the energy stored in bifilar winding 1 will be transfered to the secondary side and freewheel through the body diodes D_2 and D_{D3} (blue path in Figure 5.10(b)). The energy stored in the stray inductance again has to dissipate through the switch's parasitic capacitance , in case of aggressive switching. This will produce voltage spikes over the switch S_3 as shown in Figure 5.9. If a gentle switching strategy is chosen, the energy will dissipate through the switch's conduction path, during transient switching time, and therefore cause higher switching losses (red path in Figure 5.10(b)).

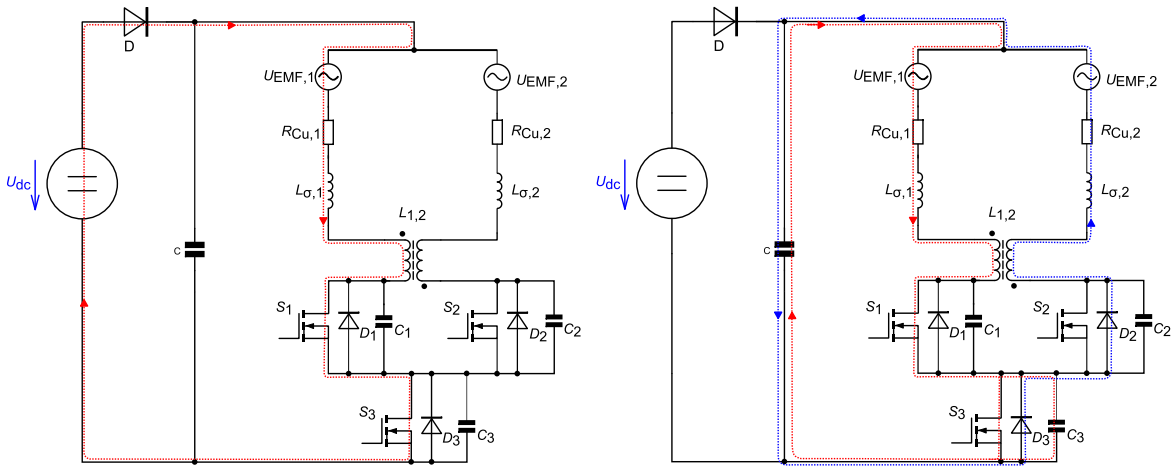

(a) Current flow during PWM-ON times. (b) Current flow during PWM-OFF times.

Figure 5.10: Current paths of three switch inverter topology.

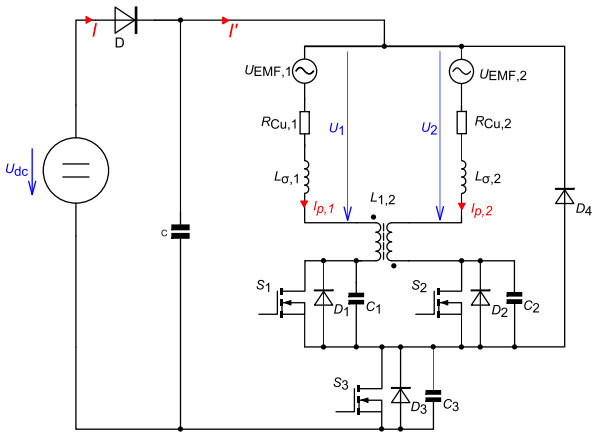

Figure 5.11: Three switch inverter topology with freewheeling diode

Providing the three switch inverter topology with an additional freewheeling diode, allows control of the voltage spikes caused by the PWM switching. Furthermore, for the negative half wave of the induced voltage, the corresponding commutation switch (S_1 or S_2) is turned off, no short circuit currents will be driven by the back-EMF voltage and no breaking torque developed by the motor.

Nevertheless, the control of the switches of the modified three switch inverter topology needs special care: To avoid energy dissipation in the PWM switch as described above, it has to be insured that the individual phase currents have already reached zero before commutation. This is done by switching off the PWM switch (t_1 at Figure 5.12) before commutating the phase current (t_2 at Figure 5.12).

Figure 5.12 shows again the electrical signals over one period of the induced voltage.

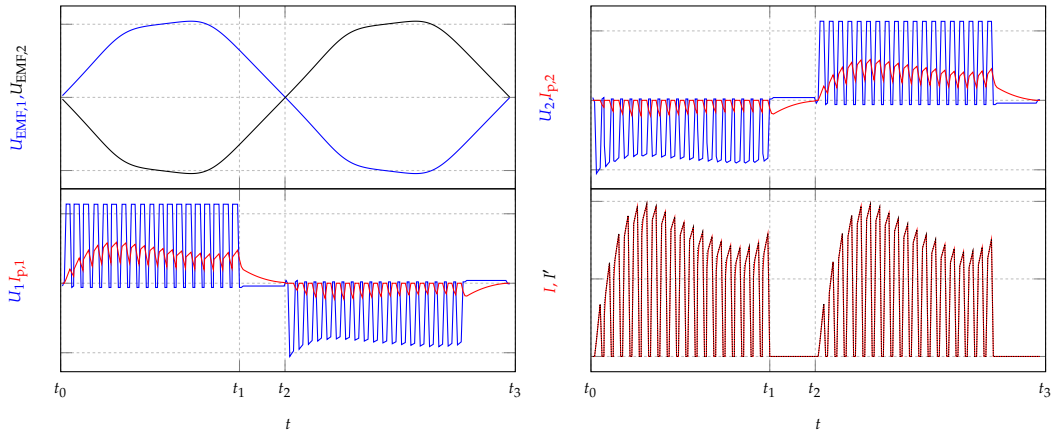

Figure 5.12: Electrical signals for a bifilar wound BLDC and a three-switch inverter with an additional freewheeling diode.

5.3 Single phase motor control: performance comparison

In this section the controls and corresponding motor winding concepts discussed in the previous sections are investigated with regard to their energy conversion efficiencies. Figure 5.13 shows the simplified electrical signals over one electrical period for both motor control methods.

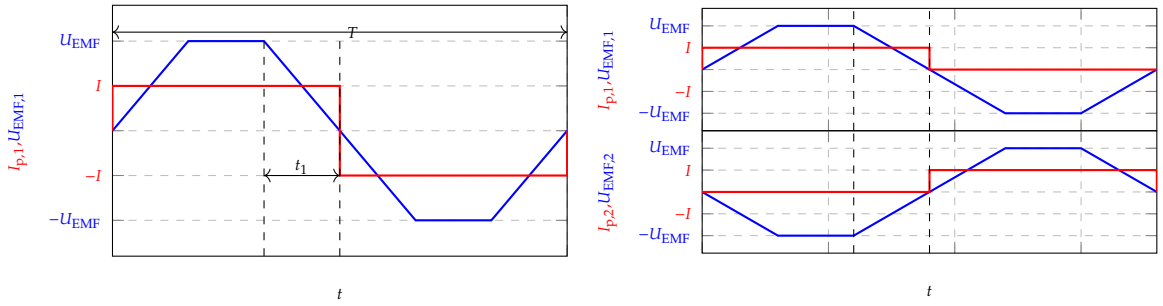

(a) Single phase BLDC motor with a unifilar winding pattern.

(b) Single phase BLDC motor with a bifilar winding pattern.

Figure 5.13: Principle electrical signals for a single phase BLDC motor.

The two motor controls were again analyzed with respect to the characteristic parameters from equation (4.2). Table 5.1 gives an overview of the characteristic parameters for the individual control schemes.

winding pattern	unifilar	bifilar
$I_{p,rms,1}$	I	$\frac{I}{2}$
$I_{p,rms,2}$	-	$\frac{I}{2}$
P_{out}	$U_{EMF}\, I\left(1-\frac{2t_1}{T}\right)$	$U_{EMF}\, I\left(1-\frac{2t_1}{T}\right)$
I	$\frac{P_{out}}{U_{EMF}}\left(1-\frac{2t_1}{T}\right)^{-1}$	$\frac{P_{out}}{U_{EMF}}\left(1-\frac{2t_1}{T}\right)^{-1}$
η	$\frac{P_{out}}{I^2_{p,rms,1} R_{Cu,U}+P_{out}} =$	$\frac{P_{out}}{(I^2_{p,rms,1}+I^2_{p,rms,2})\, 2\, R_{Cu,U}+P_{out}} =$
$\eta(t_1)$	$\frac{U^2_{EMF}\left(1-\frac{2t_1}{T}\right)}{P_{out}\, R_{Cu,U}+U^2_{EMF}\left(1-\frac{2t_1}{T}\right)}$	$\frac{U^2_{EMF}\left(1-\frac{2t_1}{T}\right)}{P_{out}\, 2\, R_{Cu,U}+U^2_{EMF}\left(1-\frac{2t_1}{T}\right)}$

Table 5.1: Characteristic parameters of the single phase motor controls.

In the comparison (Table 5.1) it was assumed, that the unifilar and bifilar windings have the same number of turns per coil. Furthermore, as the same space is available for the windings, the resistance of one coil of the bifilar winding is two times higher than its unifilar counterpart ($R_{\mathrm{Cu,B}} = 2\,R_{\mathrm{Cu,U}}$).

Equation 5.1 and Figure 5.14 show the differences in efficiency for the four control schemes.

$$\begin{aligned}
\frac{\eta_{\mathrm{U}}(t_1 = 2\,T/12)}{\eta_{\mathrm{B}}(t_1 = 2\,T/12)} &= \frac{\eta_{\mathrm{U},60^\circ}}{\eta_{\mathrm{B},60^\circ}} = 2\,\frac{9\,P_{\mathrm{out}} + \dfrac{U^2_{\mathrm{EMF}}}{R_{\mathrm{Cu,U}}}\,2}{9\,P_{\mathrm{out}} + \dfrac{U^2_{\mathrm{EMF}}}{R_{\mathrm{Cu,U}}}\,4} \\
\frac{\eta_{\mathrm{U}}(t_1 = T/12)}{\eta_{\mathrm{B}}(t_1 = T/12)} &= \frac{\eta_{\mathrm{U},120^\circ}}{\eta_{\mathrm{B},120^\circ}} = 2\,\frac{36\,P_{\mathrm{out}} + \dfrac{U^2_{\mathrm{EMF}}\,25}{R_{\mathrm{Cu,U}}\,2}}{36\,P_{\mathrm{out}} + \dfrac{U^2_{\mathrm{EMF}}}{R_{\mathrm{Cu,U}}}\,25}
\end{aligned} \tag{5.1}$$

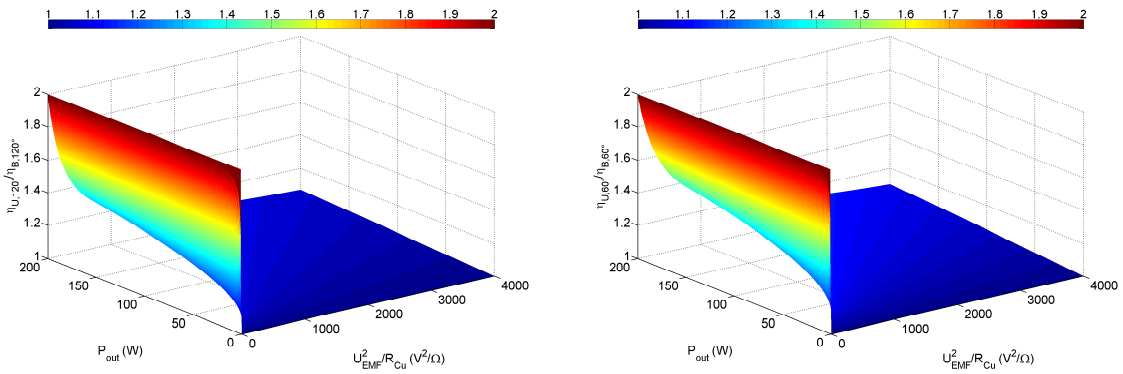

(a) BLDC motor having a back-EMF with a 120 degree flat top width.

(b) BLDC motor having a back-EMF with a 60 degree flat top width.

Figure 5.14: Efficiency comparison of single phase motor controls.

Selected control scheme

Considering the flat top of the single phase machine's back-EMF voltage and the corresponding efficiencies (Equation (5.1) and Figure 5.14(b)), low $U^2_{\mathrm{EMF}}/R_{\mathrm{Cu}}$ ratios

cause drastic efficiency reductions, if a machine with bifilar winding is compared to a unifilar one. However, Figure 5.14(b) also reveals that the $U_{\mathrm{EMF}}^2/R_{\mathrm{Cu}}$ ratio influences the efficiency reduction less with decreasing output power of a motor. For the machine designed in this work, an efficiency reduction of $\approx 21\,\%$ is expected, with the change of winding type.

Despite worse energy conversion efficiencies, a single phase BLDC motor with a bifilar winding and a two switch inverter topology was chosen. Because in addition to the reduction of the needed switches for this inverter, no high side drivers are needed. Thus, the inverter's switches can be driven directly from the motor controller and the electronics part count can be further reduced. This will drastically lower the costs and improve the manufacturability of the inverter circuit's PCB.

A gentle switching strategy was chosen to overcome the problems of a two switch inverter while switching off the PWM switches.

5.4 Impact of hall sensor positioning on motor efficiency

5.4.1 Advanced angle switching strategy

This section will describe the general idea of advanced angle switching for single phase BLDC machines as described in [38,71–73]. The torque developed by a single phase machine with a bifilar winding can be written as:

$$T = \frac{P_{\text{out}}}{\omega_{\text{m}}} = \frac{u_{\text{EMF,A}}\, i_{\text{p,A}} + u_{\text{EMF,B}}\, i_{\text{p,B}}}{\omega_{\text{m}}}. \tag{5.2}$$

again as in the case of the three phase machine, a high efficient drive needs its phase currents aligned with the corresponding back-EMF voltages. Figures 5.15(a) and 5.15(b) show ideal current and voltage waveforms for single phase drives with unifilar and bifilar windings. Figure 5.15(c) shows more realistic waveforms for the back-EMF voltages and the phase currents for a single phase motor with bifilar motor windings, while Figure 5.15(d) shows the waveforms for a unifilar wound motor: Due to the non ideal rectangular back-EMF voltages the phase currents will change during one half period, as the voltages driving the phase currents through the motor phases vary over time.

$$U_{\text{DC}} - U_{\text{EMF}}(t) = L\,\frac{\mathrm{d}i(t)}{\mathrm{d}t} + i(t)\,R \tag{5.3}$$

This change in driving phase voltages will cause high current peaks at the end of every commutation period, as for most single phase motor control strategies the PWM duty cycle is not updated during one commutation cycle. These current peaks at the end of every commutation cycle may cause problems for single phase drives. Firstly, the machines will suffer from reduced efficiencies as the back-EMF voltages are almost zero during these times and therefore not much torque is generated. Secondly, the high current peaks will generate relatively high copper losses. Thirdly, due to the motor winding inductances the slope of the phase currents will be decreased, increasing the times the phase currents:

- need for changing their polarities in case of the unifilar wound motor winding.
- need for building up the freewheeling current in the case of the bifilar wound motor winding.
- causing breaking torques (areas in Figures 5.15(c) and 5.15(d)).

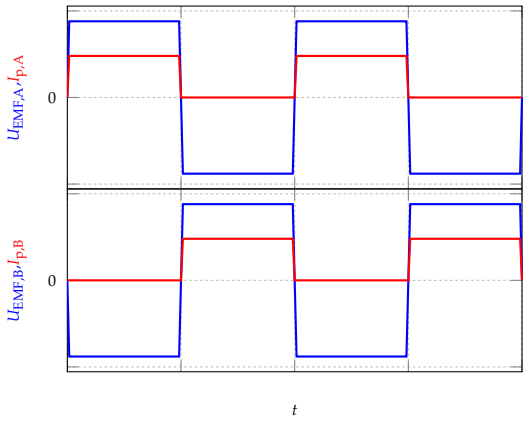

(a) Idealized phase waveforms (bifilar wound motor windings).

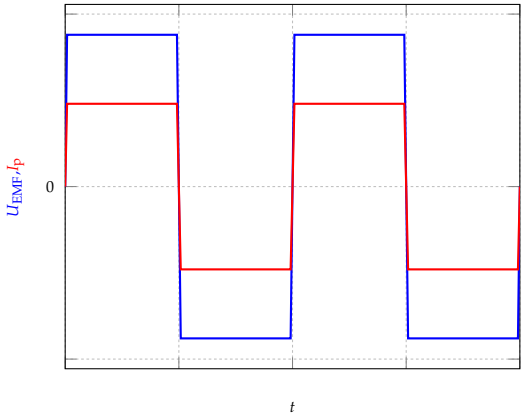

(b) Idealized phase waveforms (unifilar wound motor windings).

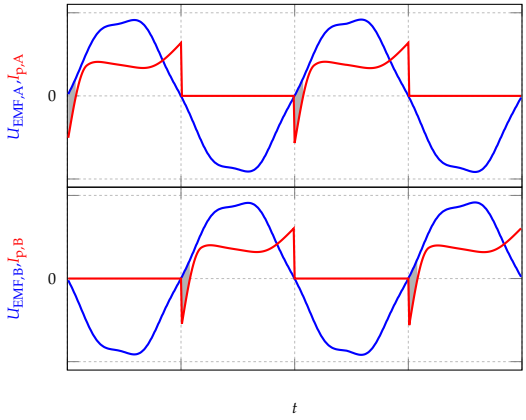

(c) Real phase waveforms (bifilar motor windings).

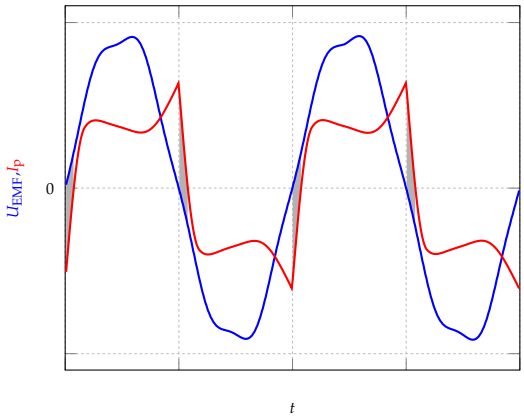

(d) Real phase waveforms (unifilar motor windings).

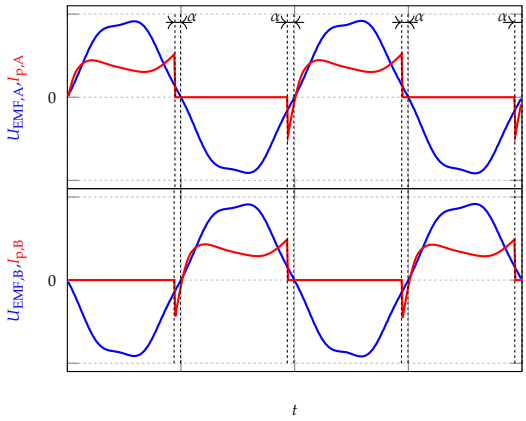

(e) Waveforms for advanced angle control (bifilar motor windings).

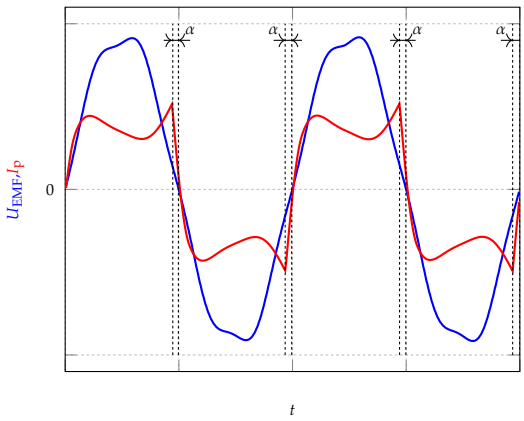

(f) Waveforms for advanced angle control (unifilar motor windings).

Figure 5.15: Back-EMF and phase currents for a single phase BLDC motors: (a,b) idealized waveforms; (c,d) real phase waveforms; (e,f) waveforms for advanced angle control.

To avoid lagging of the phase currents and increase the efficiency of the drive, the commutation instances have to be advanced. Figures 5.15(e) and 5.15(f) show the motor back-EMF voltages and the respective phase currents for unifilar and bifilar wound single phase motor with an advanced angle (α) commutation strategy.

As the fan application is designed to work in one point of operation (Section 2.1.2) the advanced angle for current commutation does not need to be controlled. To find the most efficient advanced angle for the drive, the hybrid model, described in Section 2.3 was used to simulate the fan application.

Table 5.2 and Figures 5.16(a) to 5.16(d) show the results of the fan simulation. A strong relationship between the advanced commutation angle and the motor energy conversion efficiency is observed. The best efficiency can be reached with an advanced angle of approximately ten electrical degrees, corresponding to a hall sensor displacement of 5 mechanical degrees ($\alpha = 10\,^{\circ}_{\text{elec}} = 5\,^{\circ}_{\text{elec}}$).

α	$I_{\text{DC,RMS}}$	$I_{\text{A,B,RMS}}$	$\hat{I}_{\text{A,B,RMS}}$	P_{In}	P_{Cu}	η_{BLDC}	α	$I_{\text{DC,RMS}}$	$I_{\text{A,B,RMS}}$	$\hat{I}_{\text{A,B,RMS}}$	P_{In}	P_{Cu}	η_{BLDC}
$^{\circ}_{\text{elec}}$	mA	mA	mA	W	W	%	$^{\circ}_{\text{elec}}$	mA	mA	mA	W	W	%
0	156	217	550	1.73	0.86	40.1	1	154	214	542	1.71	0.84	40.6
2	153	212	524	1.70	0.83	41.0	3	152	211	524	1.68	0.82	41.2
4	151	209	520	1.67	0.80	41.5	5	150	208	495	1.66	0.80	41.7
6	149	207	481	1.65	0.79	42.0	7	149	206	480	1.65	0.78	42.1
8	148	206	472	1.65	0.78	42.2	9	148	205	464	1.64	0.78	42.3
10	148	205	437	1.64	0.77	42.4	11	148	205	433	1.64	0.77	42.4
12	148	205	425	1.64	0.78	42.3	13	148	206	421	1.65	0.78	42.3
14	149	206	426	1.65	0.78	42.1	15	149	207	431	1.66	0.79	42.0
16	150	208	439	1.66	0.80	41.8	17	151	209	444	1.67	0.81	41.5
18	152	211	452	1.69	0.82	41.3	19	153	212	458	1.70	0.83	41.0
20	154	214	453	1.71	0.84	40.8	21	155	215	472	1.72	0.85	40.4
22	157	218	481	1.74	0.87	40.0	23	158	220	486	1.76	0.89	39.6
24	160	222	497	1.78	0.91	39.1	25	162	224	503	1.79	0.92	38.8
26	164	227	510	1.82	0.95	38.2	27	166	229	516	1.84	0.97	37.8
28	168	233	524	1.87	1.00	37.3	29	170	235	527	1.89	1.02	36.9
30	173	239	537	1.92	1.05	36.2							

Table 5.2: Results of the advanced angle switching simulations for the hybrid fan model.

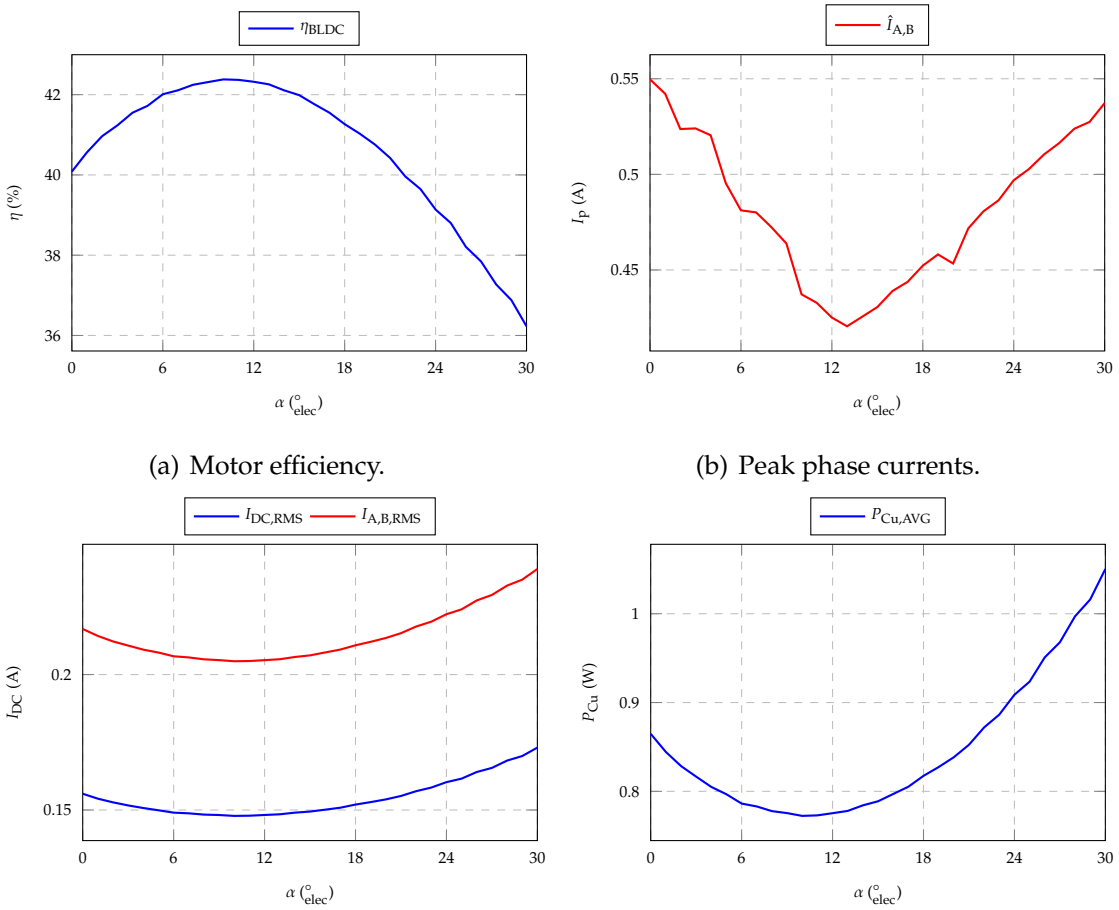

(a) Motor efficiency.

(b) Peak phase currents.

(c) RMS currents for $U_{DC} = 12\,V$.

(d) Copper losses.

Figure 5.16: Fan simulation results for different advanced commutation angles.

5.4.2 Time sharing switching strategy

This section will discuss problems which may occur during the practical implementation of the advanced angle switching strategy and propose a more stable and efficient control strategy for single phase BLDC machines.

As mentioned above, the advanced switching for motors, which will be driven only into one direction, can be achieved by a simple displacement of the hall sensor. Next, the optimal positioning of the hall latch will be discussed in further detail. Therefore, firstly the magnetic flux in axial direction B_z surrounding the motor (possible hall sensor positions) will be determined. Figure 5.17 shows the areas (green blocks) for which the magnetic field was calculated and furthermore gives a short description of the several motor and fan elements.

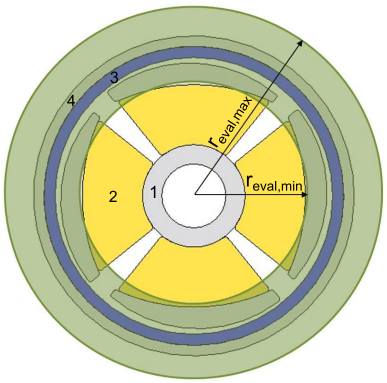

(a) Frontview.

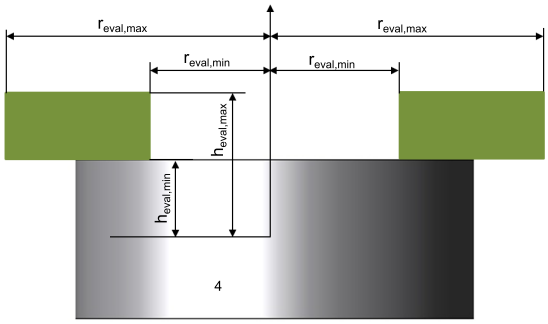

(b) Sideview.

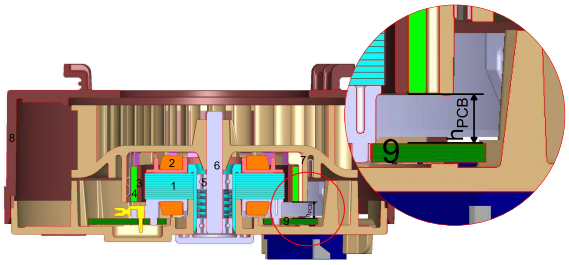

(c) Whole fan.

1 Stator steel sheets
2 Coils
3 Magnet ring
4 Rotor yoke
5 Bearings
6 Rotor shaft
7 Fan wheel
8 Fan housing
9 PCB

Figure 5.17: Areas for field calculation.

Figure 5.17(c) shows the position of the machine's PCB board where the hall latch could be placed and Figure 5.18 shows the magnetic flux field, calculated on a plane at the distance of the machine's PCB (h_{PCB}) and for no load conditions. The magnetic field was calculated by static FEM simulations where the rotor of the BLDC motor was turned to the rotational point of the most efficient commutation point according to Table 5.2. Figure 5.18(b) shows the field distribution from top view with a point marked where a hall sensor, having its threshold limit at $B_z = 2\,\mathrm{mT}$, should be placed.

Next, the field at the sensor position will be analyzed for no load as well as for load conditions. Therefore, two transient FEM simulation have been carried out. Figure 5.19 shows the results of these two simulations, determining the axial magnetic flux density at the location of the hall sensor:

The stray field of the windings distorts the magnetic field, as measured by the sensor. Instead of switching at the advanced angle of α_1, the switching instant gets delayed by $\Delta\alpha$ and results in a delayed switching angle of α_2. In this case, this would be equivalent to driving the motor without any advanced switching strategy and

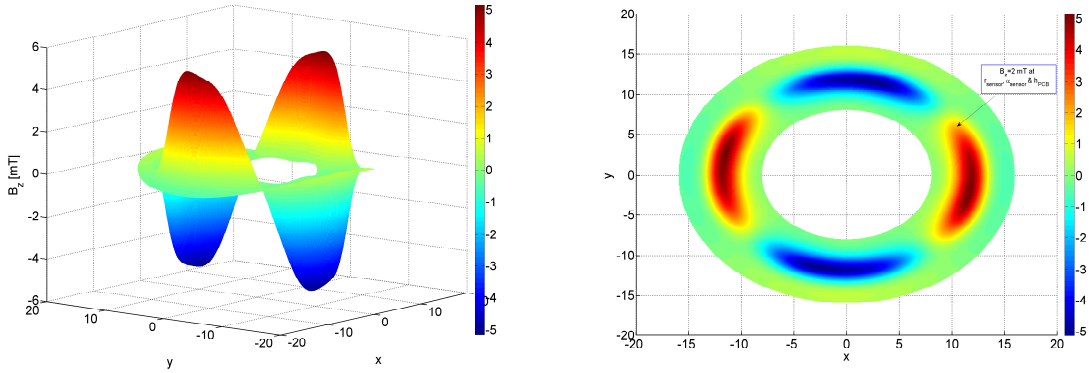

(a) Field distribution.

(b) Top view hall sensor position.

Figure 5.18: Field distribution at distance of PCB board.

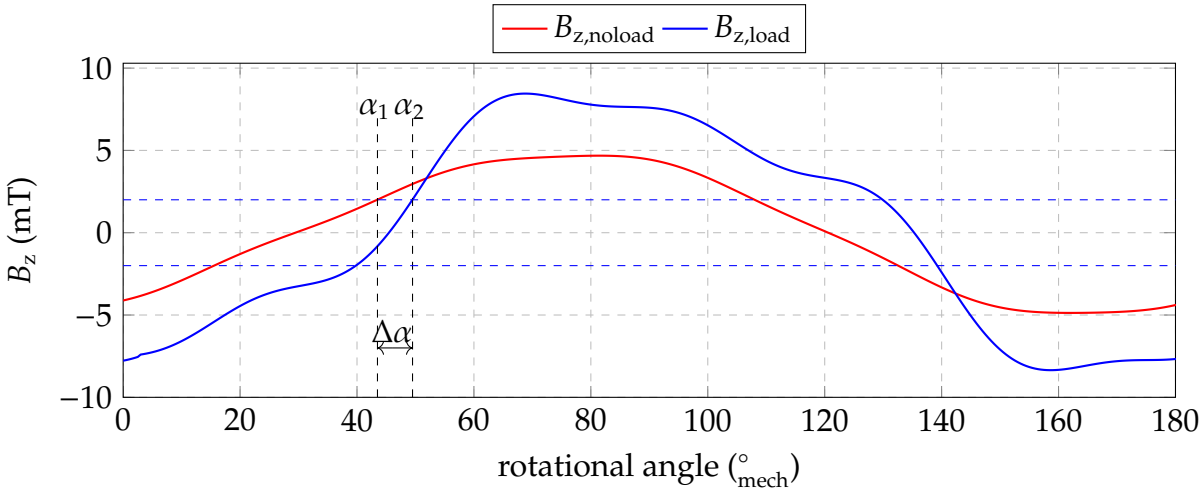

Figure 5.19: Axial magnetic flux density at sensor position over half a revolution.

therefore would not improve the motor's efficiency.

A way around can be found in not using the whole commutation period for current excitation, as described in the sensorless control technique introduced in [30] or in the pulse width control strategy proposed in [73]. Figure 5.20 shows the basic idea of turning off the current of the actual driven phase before the back-EMF's zero crossing (t_{OFF}), so that the hall latch can again detect the axial field under no load conditions (t_D). The back-EMF waveforms as well as the corresponding phase currents, which can be seen in Figure 5.20, are from a single phase BLDC machine with bifilar windings and use two MOSFETs for current commutation.

In the following, different advanced phase switch off times (as well as angles α_p)

will be analyzed regarding their impact on the machine's efficiency. Furthermore, a delayed turning on (α_d & t_{ON}) of the phases will be investigated as it might also have a positive effect on the machine's efficiency as single phase BLDC machine types do not develop much torque at the start and end of the individual commutation periods.

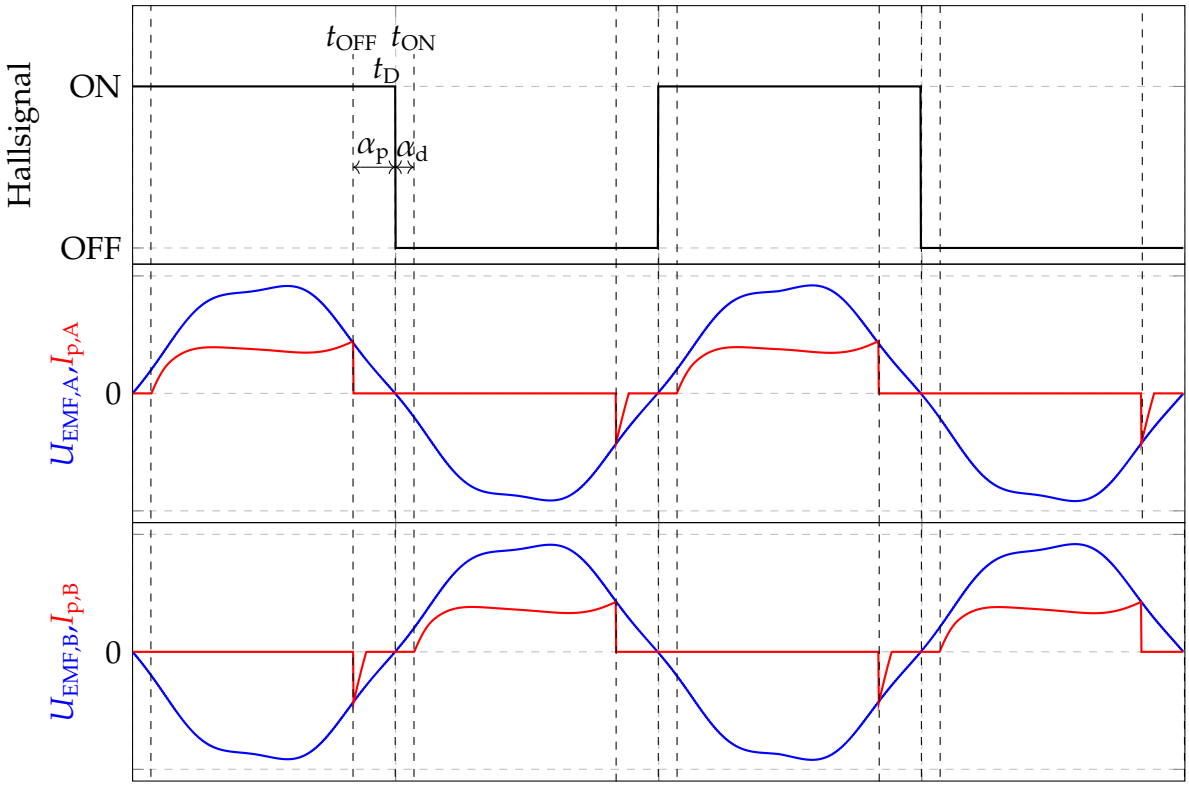

Figure 5.20: Phase signals of the time sharing switching strategy.

To find the best switching angles for the fan application, 900 simulations, using the hybrid simulation model from Section 2.3 have been carried out. Figure 5.21 shows the results of these fan hybrid simulations. Additionally, selected results from the hybrid simulations with different premature switch off and delayed switch on times are shown in Table 5.3.

According to Table 5.3, the best energy conversion efficiency will be reached for an advanced switch off angle of $\alpha_p = 29\,^\circ_{elec} \hat{=} 14.5\,^\circ_{mech}$ and a delayed switch on angle of $\alpha_d = 13\,^\circ_{elec} \hat{=} 7.5\,^\circ_{mech}$.

If we compare the hybrid fan simulation results using the advanced switching strategy from Table 5.2 with the ones exploiting the time sharing switching strategy

(Table 5.3), a relative efficiency increase of approximately 11.6 % can be observed. Furthermore, a detailed look at the current values shows a decrease of the total current by ≈ 16.5 %, the phase RMS current is lowered by ≈ 14.5 % and the phase current's peak value decreases by ≈ 18.8 %. The smaller current demand will cause about 30 % less copper losses.

α_p $^\circ_{elec}$	α_d $^\circ_{elec}$	$I_{DC,RMS}$ mA	$I_{A,B,RMS}$ mA	$\hat{I}_{A,B,RMS}$ mA	P_{In} W	P_{Cu} W	η_{BLDC} %	α_p $^\circ_{elec}$	α_d $^\circ_{elec}$	$I_{DC,RMS}$ mA	$I_{A,B,RMS}$ mA	$\hat{I}_{A,B,RMS}$ mA	P_{In} W	P_{Cu} W	η_{BLDC} %
10	26	137	189	385	1.53	0.66	46.5	11	26	137	189	392	1.53	0.66	46.6
12	26	137	189	412	1.53	0.66	46.5	13	26	137	189	409	1.53	0.66	46.6
14	26	138	189	409	1.54	0.66	46.6	10	27	133	185	384	1.48	0.63	46.8
11	27	139	191	404	1.55	0.67	46.5	12	27	133	185	385	1.48	0.63	46.9
13	27	138	190	409	1.54	0.66	46.6	14	27	130	182	404	1.45	0.61	47.0
10	28	131	183	381	1.47	0.62	47.0	11	28	133	185	375	1.48	0.63	46.9
12	28	140	191	401	1.56	0.67	46.6	13	28	133	185	399	1.48	0.63	47.0
14	28	133	185	400	1.49	0.63	46.9	10	29	135	186	376	1.50	0.64	46.8
11	29	142	194	395	1.59	0.69	46.4	12	29	135	187	399	1.51	0.64	46.9
13	29	127	179	368	1.42	0.59	47.3	14	29	132	183	397	1.47	0.62	47.1
10	30	133	185	370	1.49	0.63	46.9	11	30	134	186	388	1.49	0.63	46.9
12	30	136	188	393	1.52	0.65	46.8	13	30	135	187	386	1.51	0.64	46.9
14	30	134	186	389	1.50	0.63	47.0								

Table 5.3: Selected results of the time sharing switching strategy for the hybrid fan model.

For the sake of completeness, Figure 5.22 shows the control signals of the two MOSFETs (S_A & S_B) as well as the phase & DC link voltages ($U_{p,A}$, $U_{p,B}$ & U_{DC}) and currents ($I_{p,A}$, $I_{p,B}$ & I_{DC}) for the hybrid simulation using the two switching angles $\alpha_d = 13\,^\circ_{elec}$ and $\alpha_p = 29\,^\circ_{elec}$.

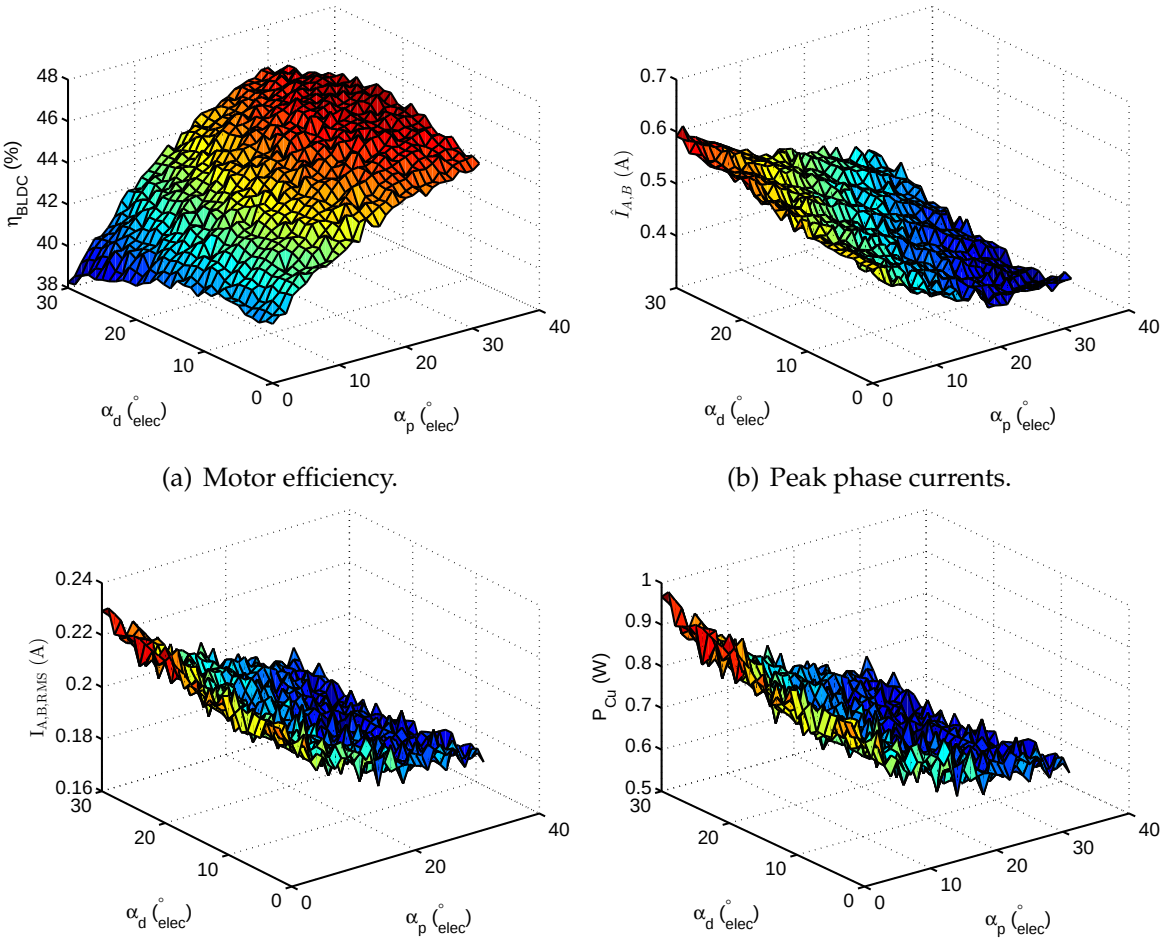

(a) Motor efficiency.

(b) Peak phase currents.

(c) RMS currents for $U_{DC} = 12\,V$.

(d) Copper losses.

Figure 5.21: Fan simulation results for the time sharing switching strategy.

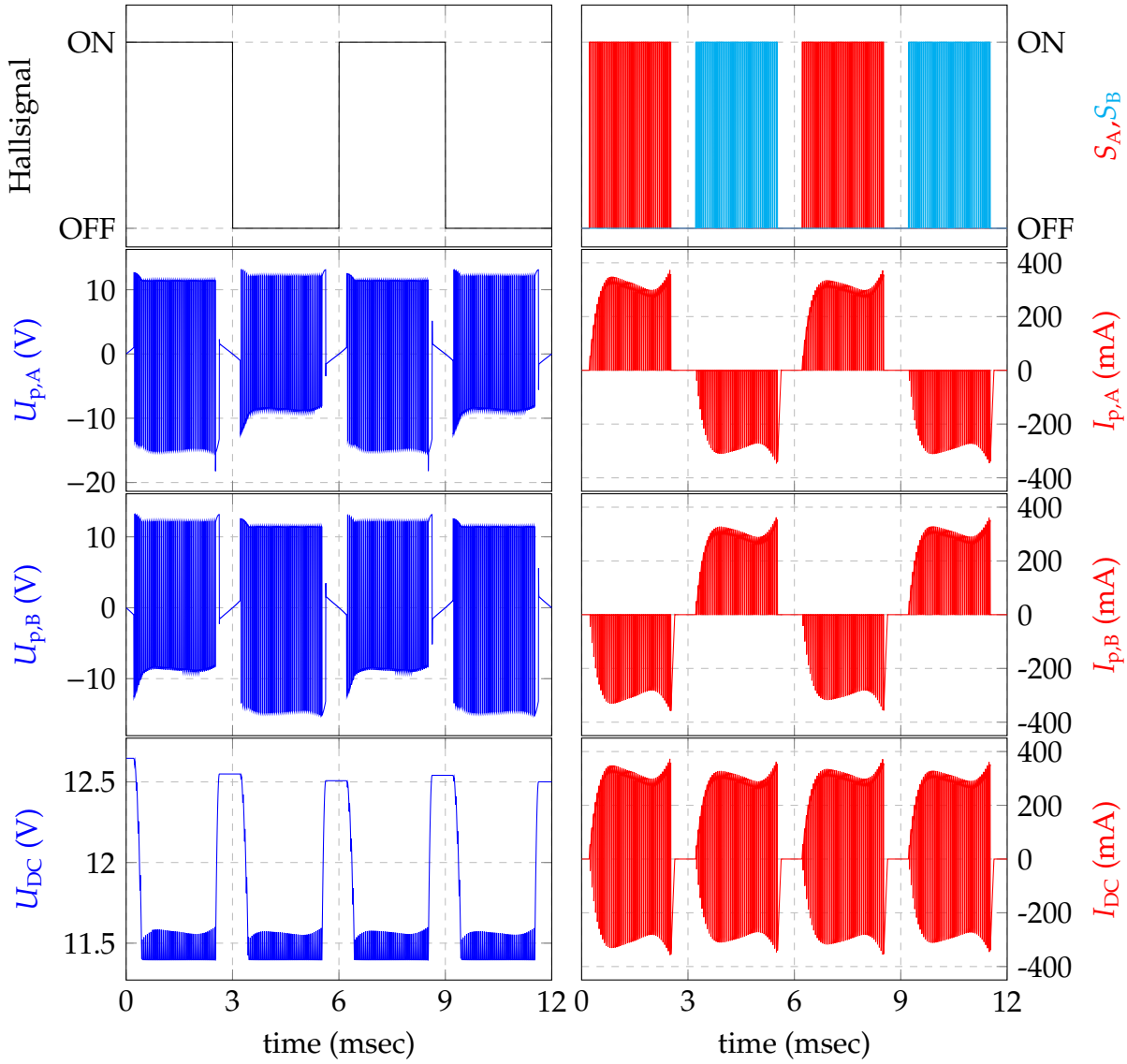

Figure 5.22: Phase signals of the hybrid fan model using the time sharing switching strategy.

Chapter 6

Sensorless control of three- and single phase BLDC motors

While PM brushless machines have been gaining increased attention, additional electronics for commutation and a position sensing system are still commonly needed. Such additional drive components must be cost-minimized since affordability is a vital requirement of fractional power motors.

BLDC drives usually use a shaft encoder, resolver or hall sensors to measure the rotor angle [74]. However, the presence of such position sensors increases the costs and reduces robustness of the overall system. Therefore, a sensorless control scheme is desired [75,76].

This section will analyze the feasibility and advantages of sensorless control techniques for the considered pump and fan applications. Figure 6.1 shows sensorless control techniques for three phase and single phase BLDC machines.

Considering the sensorless techniques for three phase BLDC motors, the flux observer technique tries to extract the rotor position via a flux observer model. As described in Section 2.1.1 the operating conditions for the three phase machine, driving the pump, vary significantly regarding operating temperature and the effects on the machine's parameters involved. Since, this method is quite sensitive to variations of the machine parameters, a high computational capability of the controllers is needed, which makes it not suitable for the present application, as costs are a sensitive term in the overall machine design [77].

The arbitrary signal injection technique tries to exploit saliency or actual saturation of the motor by inducting a high frequency signal. This method finds its range of application in the low speed area and has its drawback in additional noise and

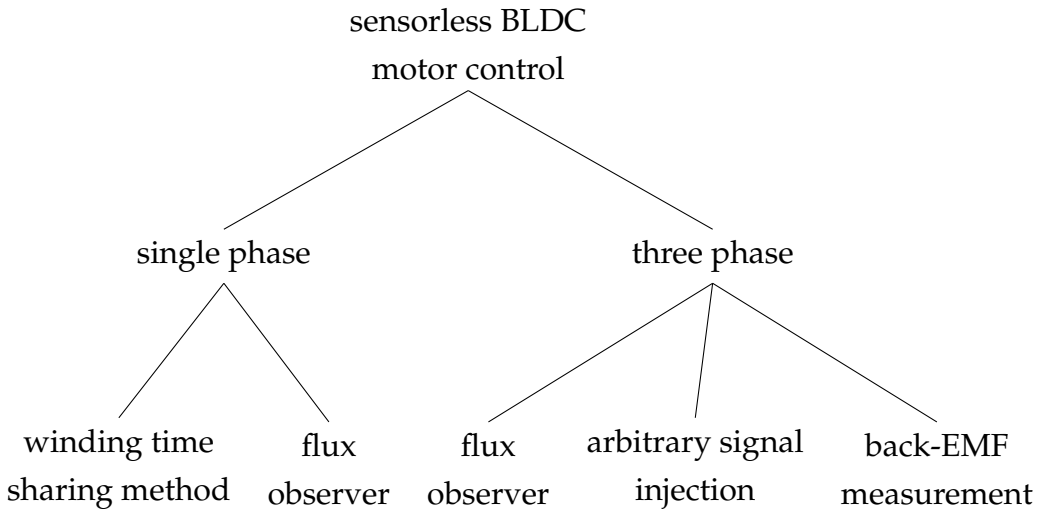

Figure 6.1: Sensorless BLDC motor control techniques.

torque ripple generation [76].

The last method is based on measuring the back-EMF voltage which is induced in the motor coils. These methods are often used for the mid to high speed range as the back-EMF is generated as a function of the actual rotor speed. However, a drawback to this scheme is that it will not work for low speed ranges [76, 78, 79]. The direct back-EMF sensorless control strategy suits low cost applications most and will be further investigated in Section 6.1.

Figure 6.1 also shows two common methods for sensorless control of a single phase BLDC machine. Thereby, the flux observer method described in [39] uses a mathematical motor model to observe the rotor angle and speed. The disadvantages of this method are the same as those mention earlier for the three phase sensorless control using a flux observer.

The second sensorless control technique proposed for a single phase machine is the winding time sharing method described in [30]. This method again extracts the rotor angle by measuring the back-EMF voltage induced in the motor windings. Due to its simplicity, this sensorless technique appears to be the most suitable one for the fan drive. Therefore, this control scheme is further investigated in Section 6.2.

6.1 Direct back-EMF sensorless control strategy of small delta-connected BLDC machines

This section will investigate the use of the direct back-EMF sensorless control strategy for the delta-connected three phase BLDC pump drive. In general, this sensorless control estimates the rotor position by detecting zero crossings of the phase induced voltages. Considering the motor circuit shown in Figure 6.2 and applying the corresponding control signals to the driver circuit, the ideal current and voltage waveforms, seen in Figure 6.3, can be expected. It can be seen, since the drive's phases are connected in delta, against a star connected machine, that all three motor phases are leading currents at all times. Therefore, the zero crossing events cannot be detected directly at the unexcited motor phase as is the case for star connected machines. Despite the fact that also delta connected machines have unexcited motor phases at all times, these phases do still carry currents at those times and therefore also contain information about the phases' resistive and inductive voltage drops.

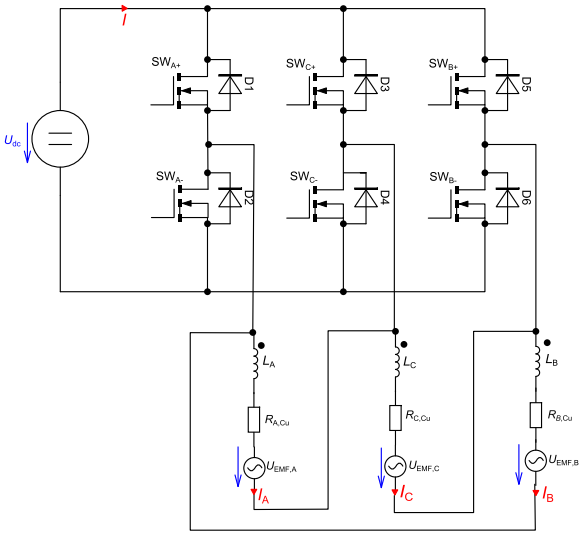

state (-)	φ_{Rotor} ($^\circ_{\text{elec}}$)	SW_{A+} (-)	SW_{A-} (-)	SW_{B+} (-)	SW_{B-} (-)	SW_{C+} (-)	SW_{C-} (-)
1	0-60	1	0	0	1	0	0
2	60-120	1	0	0	0	0	1
3	120-180	0	0	1	0	0	1
4	180-240	0	1	1	0	0	0
5	240-300	0	1	0	0	1	0
6	300-360	0	0	0	1	1	0

Figure 6.2: BLDC motor model with inverter circuit & control signals.

In Figure 6.3(a) the colored boxes define times during which the corresponding terminal is not connected to a defined voltage potential (U_{dc}, GND) and therefore can be used for back-EMF measurements.

For a given commutation step (e.g rotor angle $\in \{180^\circ - 240^\circ\}$) the circuit can be

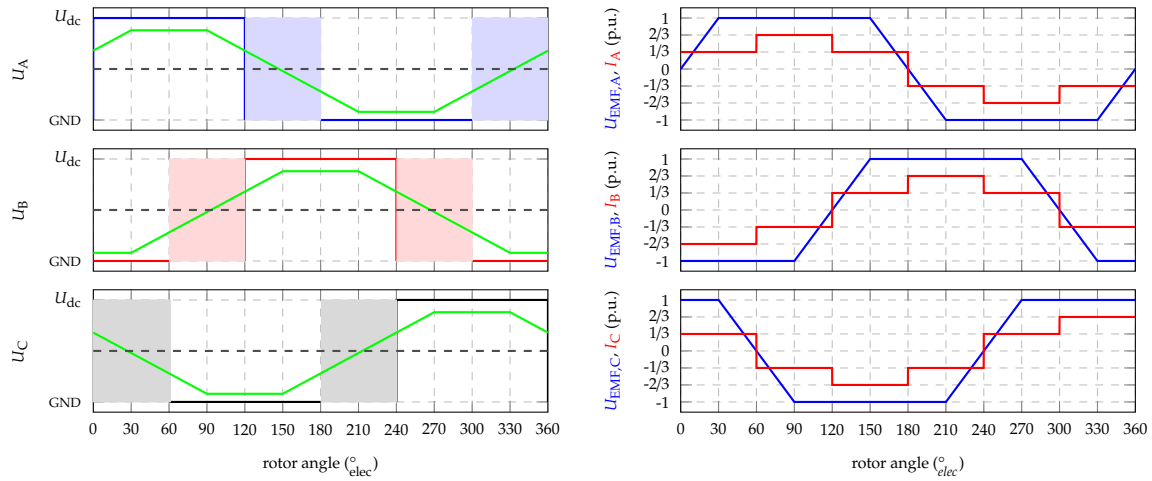

(a) Voltages at motor terminals and floating voltages from equation (6.7).

(b) Back EMF voltages and phase currents.

Figure 6.3: Ideal phase current and voltage waveforms.

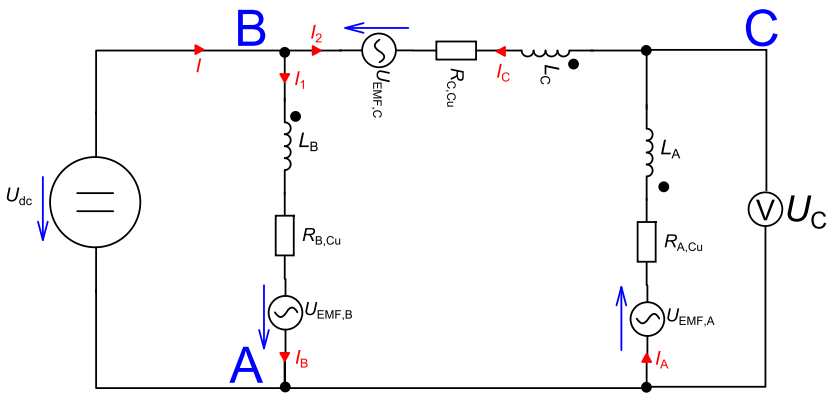

Figure 6.4: Simplified circuit for the given commutation state 4 & PWM ON.

simplified (Figure 6.4).

For this simplified circuit following equations can be extracted [80]:

$$U_{AC} + U_{CB} + U_{BA} = 0; \quad U_{EMF,A} + U_{EMF,B} + U_{EMF,C} = 0 \tag{6.1}$$

$$U_C = -U_{AC} = i_2 R_A + L_A \frac{di_2}{dt} - U_{EMF,A} \tag{6.2}$$

$$U_{DC} = i_2 R_C + L_C \frac{di_2}{dt} - U_{EMF,C} + i_2 R_A + L_A \frac{di_2}{dt} - U_{EMF,A} \tag{6.3}$$

If we assume same balanced resistors ($R = R_A = R_B = R_C$) as well as inductors

($L = L_A = L_B = L_C$), equations (6.2) and (6.3) can be rewritten as:

$$U_C + U_{EMF,A} = i_2 R + L \frac{di_2}{dt} \tag{6.4}$$

$$\frac{U_{DC}}{2} + \frac{U_{EMF,C} + U_{EMF,A}}{2} = i_2 R + L \frac{di_2}{dt} \tag{6.5}$$

Subtracting equation (6.4) from equation (6.5), the line voltage U_C can be determined by:

$$U_C = \frac{U_{DC}}{2} + \frac{U_{EMF,C} - U_{EMF,A}}{2} . \tag{6.6}$$

If we carry on calculating the line voltages for their corresponding commutation steps we obtain:

$$U_{(k)} = \frac{U_{DC}}{2} + \frac{U_{EMF,(k)} - U_{EMF,(k-1)}}{2} \tag{6.7}$$

These line voltages can also be seen in Figure 6.3(a) (green waveforms) and will be used for generating the commutation instances.

In the following, practical aspects of the direct back-EMF control scheme are investigated. To simulate behavior of the BLDC motor, the hybrid model from Section 2.3 is used.

Figure 6.5 gives an overview of the sensorless control scheme developed. It basically includes the superior control, realized with a simple statemachine, which starts the motor and decides when to switch to the sensorless control strategy.

As described in the introduction of Chapter 6, the back-EMF detection only works if the motor speed exceeds a certain value. So, to start from standstill, the motor has to be fed with a particular voltage sequence [81, 82].

When the motor is started, the state machine lingers in "wait state" until a zero crossing in commutation state "6 → 1 1 0" is detected. Afterwards, the statemachine changes its state to "State 1" where it waits to detect a zero-crossing event in commutation "State 1". This procedure repeats itself for every commutation state. In general, for any given state, the dashed arrows (blue font) in Figure 6.6 represent the command (zero-crossing) required to proceed to the following state, all other commands (red font, solid arrows) return the state machine to "wait".

In order to detect the zero-crossing events, a simple logic decides which motor clamp (channel) is selected for the back-EMF voltage measurement. Assume for

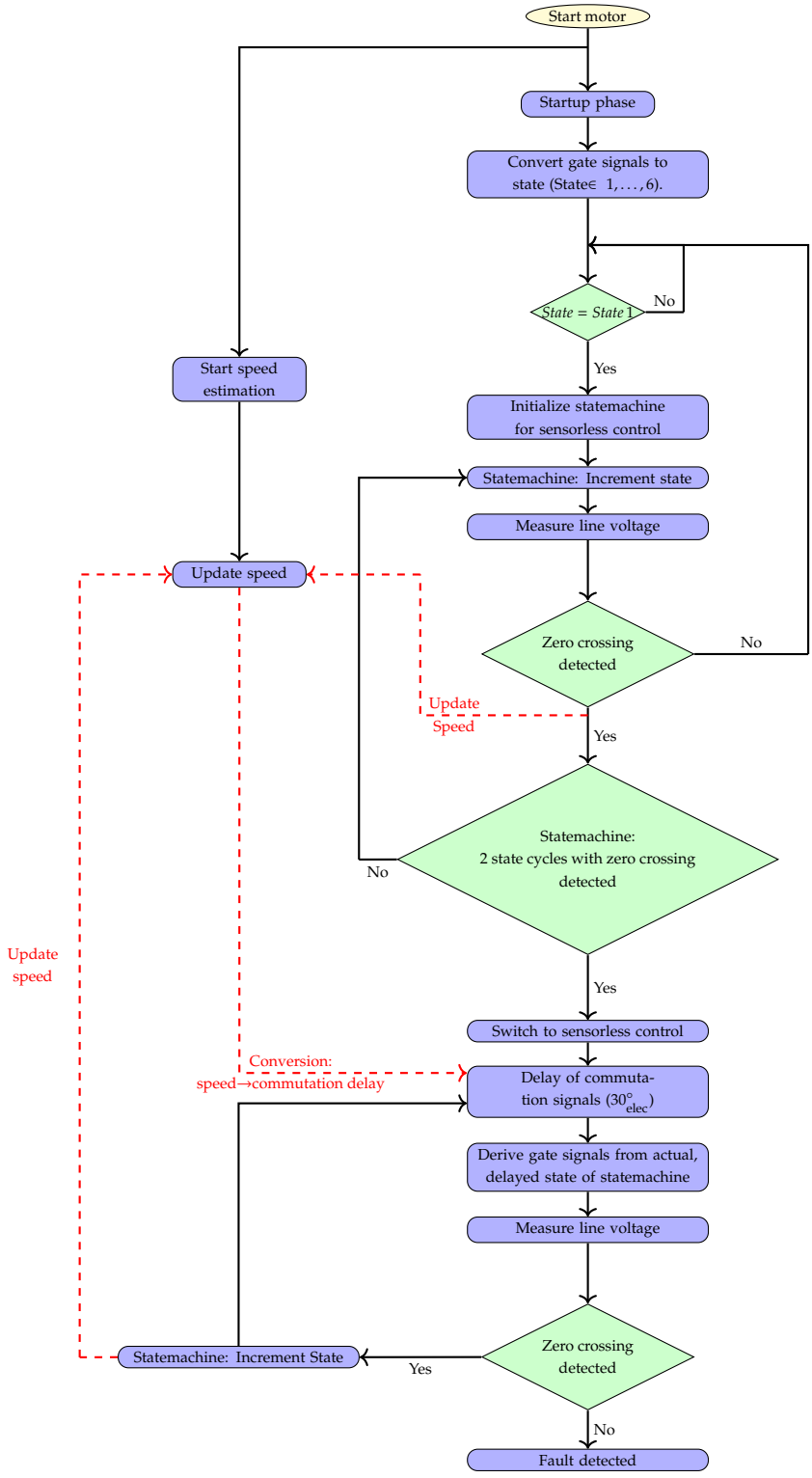

Figure 6.5: Flow chart of proposed sensorless control scheme.

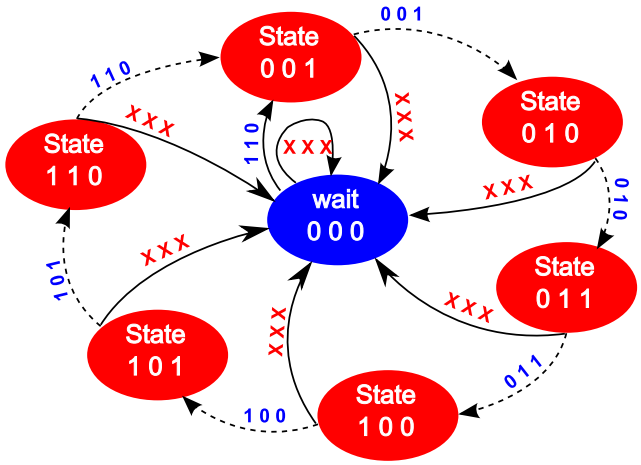

Figure 6.6: Statemachine of sensorless control.

a moment that the statemachine is in "State 4" (Table from Figure 6.2). As the BLDC motor is driven with PWM signals, two simplified circuits can be extracted during one commutation state (Figure 6.4 → PWM ON & Figure 6.7 → PWM OFF). These PWM ON and OFF states lead to the following voltage waveform shown in

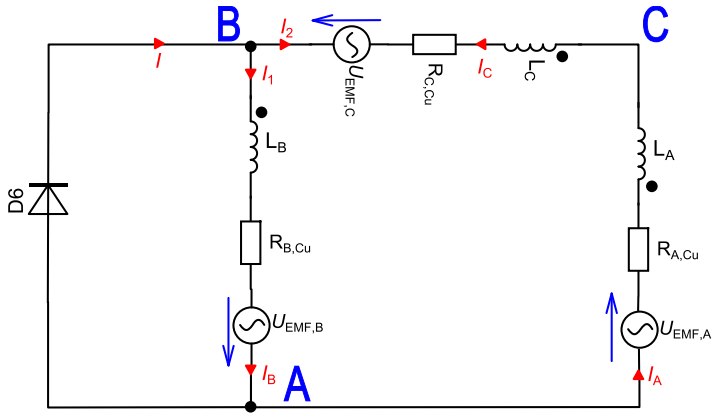

Figure 6.7: Simplified circuits for a given commutation state 4 & PWM OFF.

Figure 6.8.

As the back-EMF information from equation (6.7) was derived for voltage supplied conditions, the zero crossing information can be found on the actual selected measurement channel during PWM ON times. During PWM OFF times, the voltage potential gets pulled to an incorrect value due to the freewheeling currents.

Another effect, which can lead to missing zero crossing events of the back-EMF

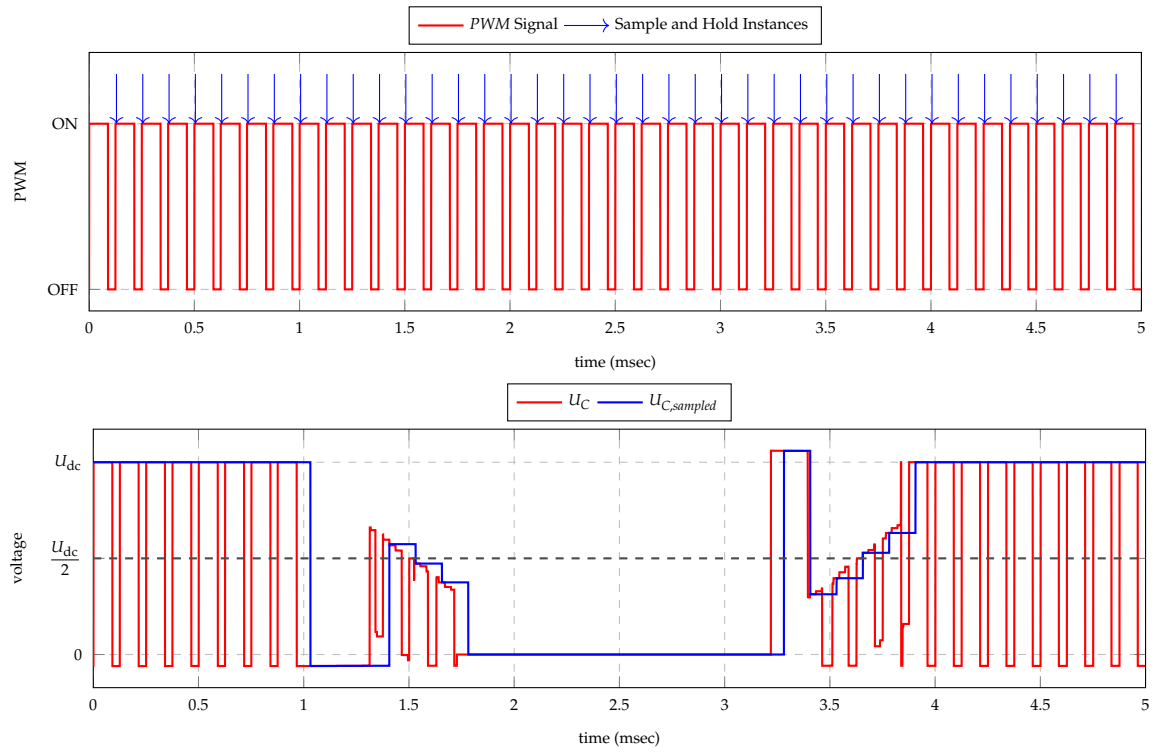

Figure 6.8: PWM signal, sampling instances and line voltages.

measurement, appears during commutation: Supposing we are in commutation "State 4" (Figure 6.4) the following commutation step will be reached by opening switch SW_{B+} and close SW_{C+}. During this commutation the current in phase C has to

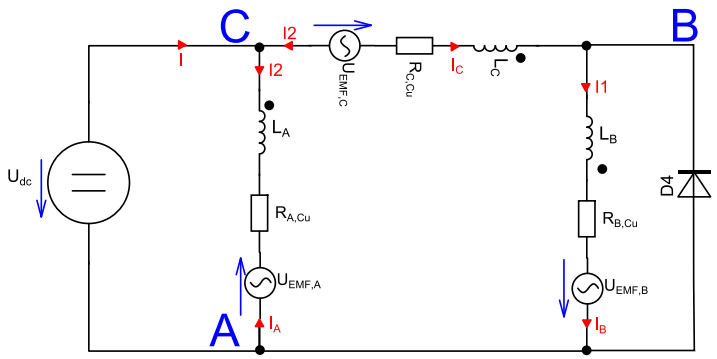

Figure 6.9: Simplified circuit after commutation from step 4 to 5.

invert its sign, which will cause a freewheeling current path as shown in Figure 6.9 and pull the regarding voltage measurement channel below zero voltage potential. The length of the transient commutation time will depend on the current that has to

be dissipated. This current dissipation time must elapse before the upcoming zero crossing event. To achieve this, the control has to ensure an adequate commutation time corresponding to the magnitude of the phase current. Figure 6.10 shows the voltage which is used for the zero detection. It can be seen, that a certain combination of current and switching instant due to wrong estimation of speed, will cause too long freewheeling periods and therefore result in missing the zero crossing event.

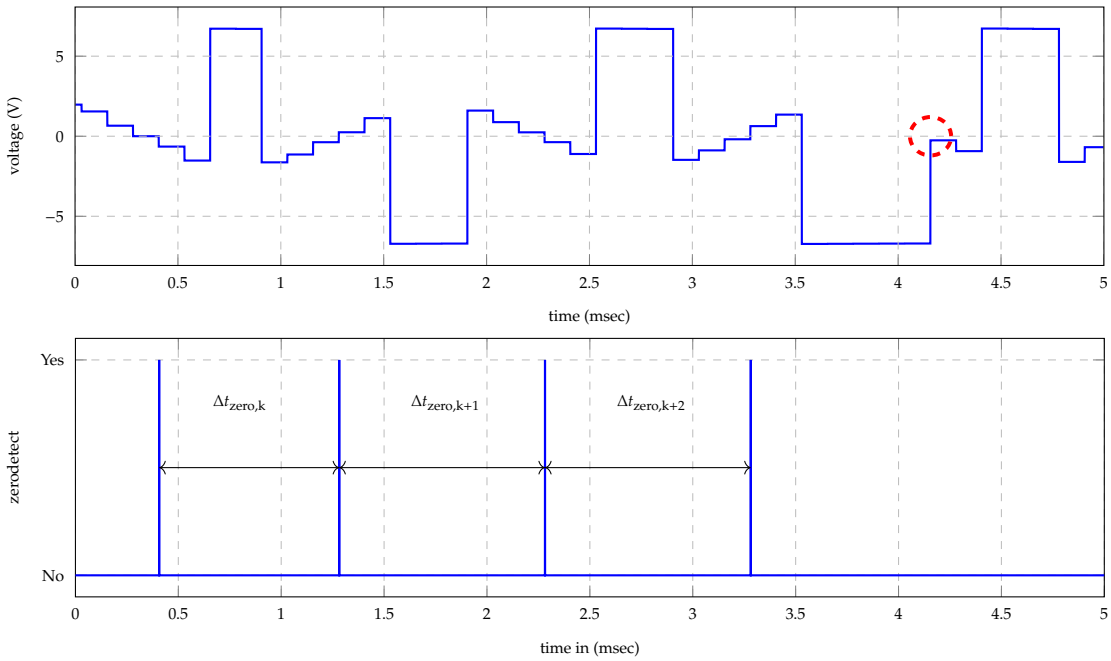

Figure 6.10: Voltage for zero detection and corresponding zero detection signal.

This effect will also be the crucial factor for failures in zero crossing detection of large varying load profiles as it is the case for pump systems. Because the strongly varying pump load and the relatively slow PWM controller update will cause a speed ripple and therefore wrong commutation instances.

Figure 6.11 shows a simple flow chart for the zero crossing detection. This flow chart also shows the capability of detecting missing zero crossing events by detecting the missing change in sign of the regarding measurement voltage (U_{det}) after the freewheeling period. This detection of failures can then be used for generating a zero detection impulse and further adjust the commutation instances. To determine the actual speed, the zero detection signal can be used. As the simulated machine has 8 poles, 24 zero crossing events should occur during one revolution. Adding a

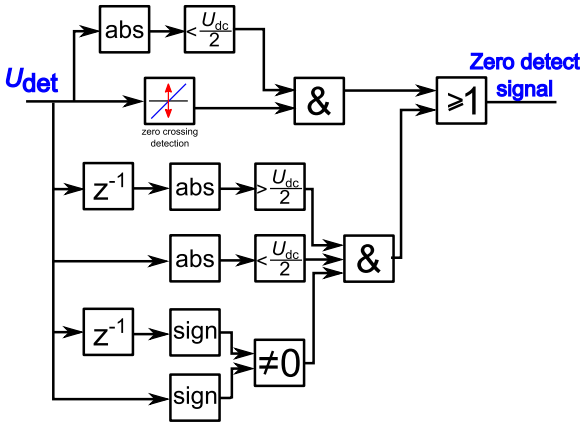

Figure 6.11: Flowchart of zero crossing detection.

digital FIR filter, the speed can be calculated by

$$\overline{\Delta t_{\text{zero}}} = \frac{1}{N}\sum_{k}^{N} \Delta t_{\text{zero,k}}\,, \qquad n_{\text{estimated}} = \frac{60}{24\,\overline{\Delta t_{\text{zero}}}}\,. \tag{6.8}$$

It can be shown that the line voltage from equation (6.7) has a constant phase shift of $\varphi = 30°$ to the corresponding back-EMF voltage (Figure 6.3). In order to generate the commutation instances, the zero detect signal has to be delayed as a function of the actual speed.

Conclusion

For the sake of completeness, Figure 6.12 shows the overall MatLab®Simulink simulation model. For a better overview the MatLab®Simulink model is split into functional parts. Everything within the red box is needed to simulate the motor behavior. All parts that are surrounded by blue are responsible for the sensorless commutation and the others have a help or displaying function.

Figure 6.13 shows said signal graphs for a sensorless control routine of a BLDC machine driving a varying load. With these approaches a stable sensorless control scheme can be reached.

However, as the operational conditions for the pump drive, and automotive drives in general vary in a wide range, additional changes have to be made to properly implement a working sensorless control running.

Firstly, the start up sequence has to be realized with a fixed current sequence instead of a voltage sequence, since the supply voltage can change during operation. This necessitates at least two current measurements.

Furthermore, due to the required high starting torque, temperature dependent load change on the bearings and changing magnetic characteristics, a stable start up routine cannot be guaranteed as long as the temperature is not additionally measured.

Because of these requirements as well as the need for a faster controller with special I/O ports and more programmability, the sensorless solution was not found to offer any cost benefits or decrease reliability compared to a traditional sensored control strategy.

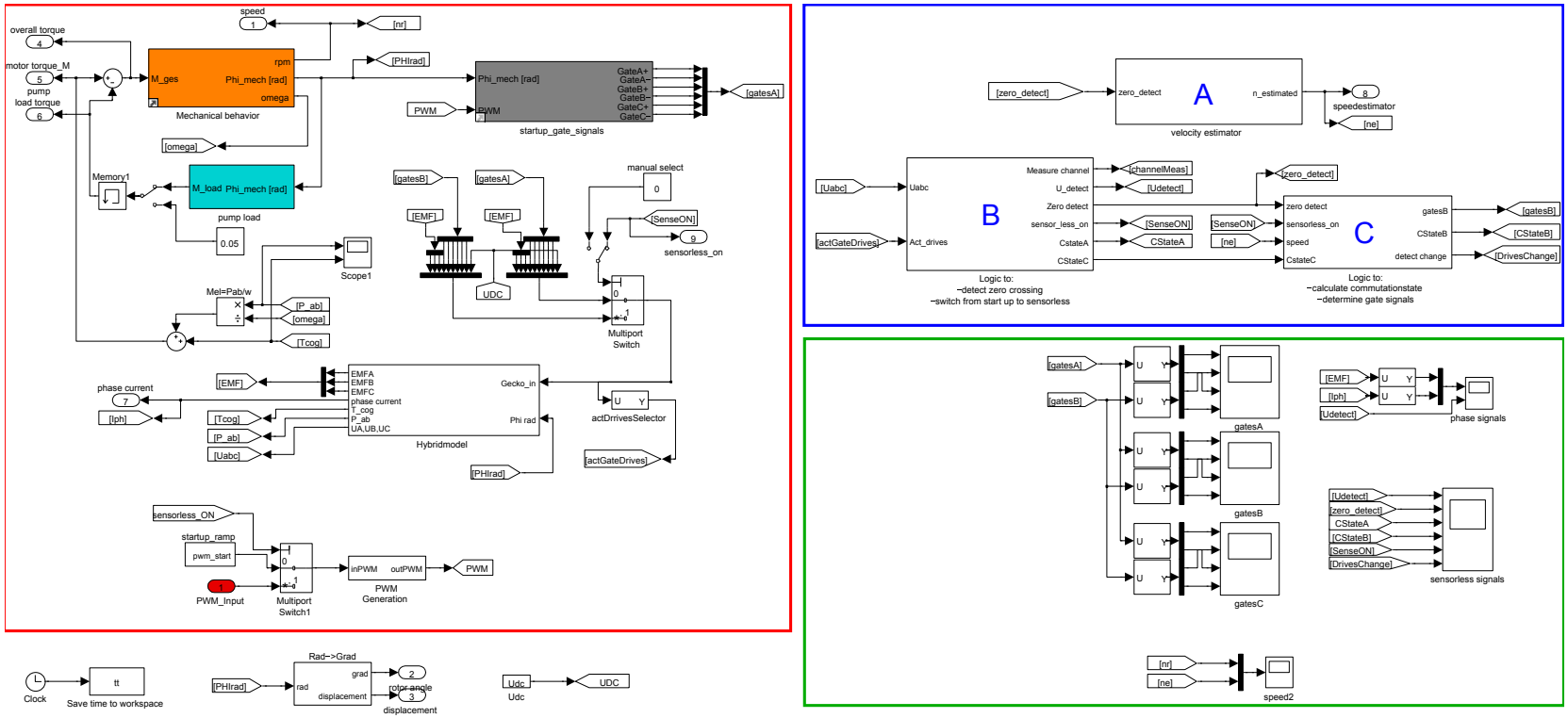

Figure 6.12: Simulink model of the sensorless control.

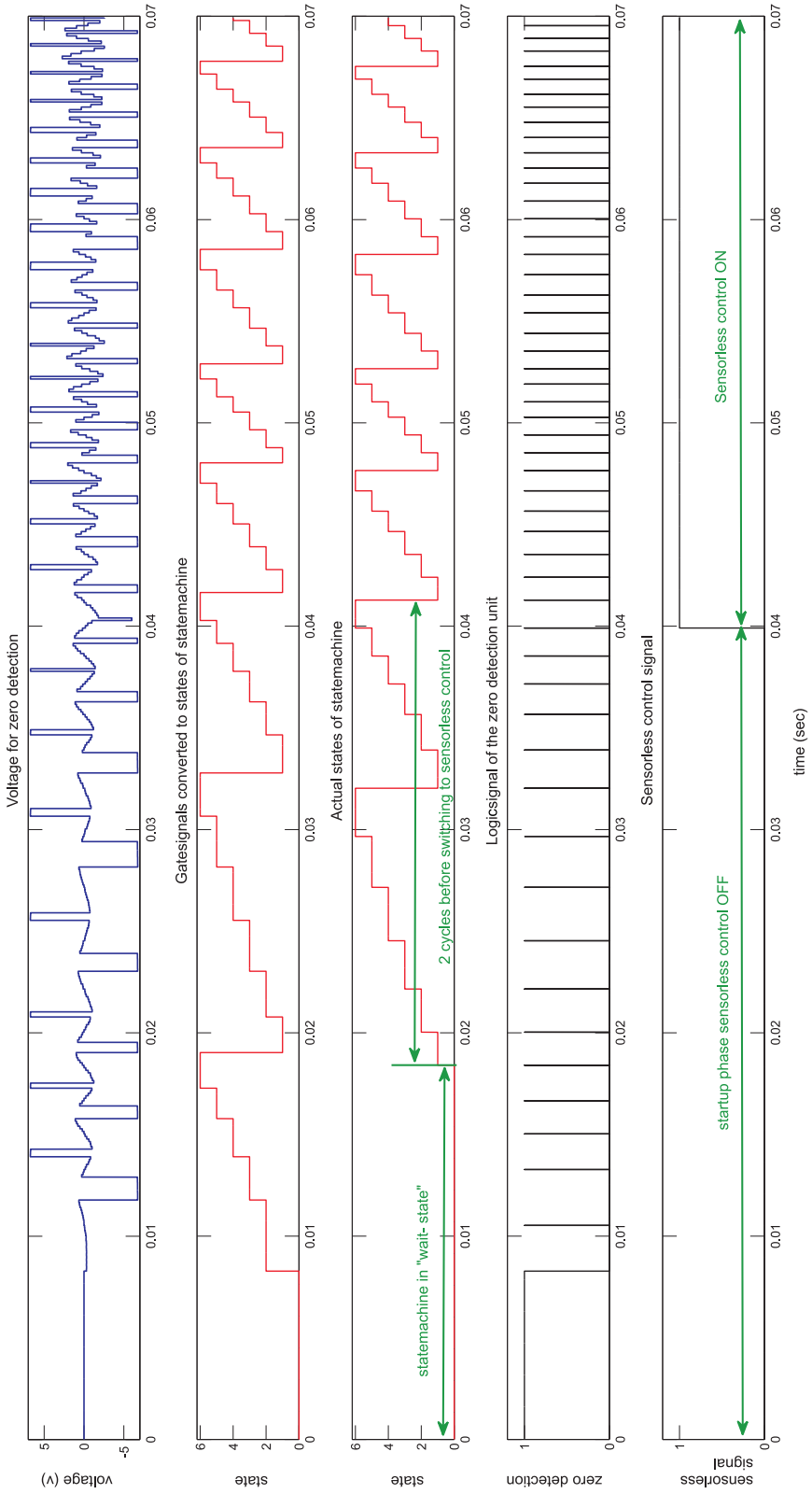

Figure 6.13: Signal graphs for the sensorless control of the BLDC machine.

6.2 Winding time sharing strategy for a single phase BLDC motor

This section will investigate the winding time sharing sensorless control method for the fan drive. In contrast to the winding time sharing technique presented in [30], the sensorless control was analyzed for a single phase BLDC with a bifilar winding pattern. Figure 6.14(a) shows the motor driver circuit as well as the equivalent BLDC circuit. In Figure 6.14(b), the phase signals for the conventional single phase control can be seen.

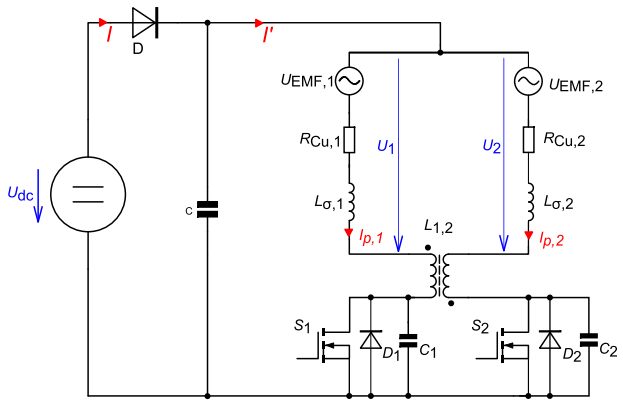

(a) Inverter for a single phase BLDC machine with bifilar windings.

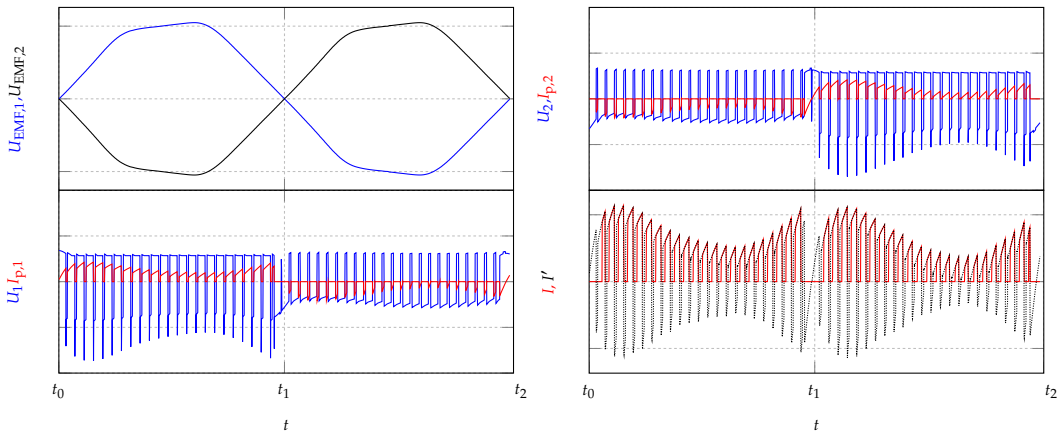

(b) Phase signals for conventional single phase BLDC control.

Figure 6.14: Single phase BLDC machine with bifilar windings and its inverter circuit.

The phase voltages from Figure 6.14(b) indicate that if the conventional single

BLDC control is used, the two back-EMF voltages of the motor windings cannot be detected. However, if we use the control strategy described in Section 5.4.2, in addition to the improved energy conversion efficiency, instances occur during which information about the winding back-EMF voltages can be extracted. Figure 6.15 shows the phase signals for the optimal winding time sharing method for the fan drive.

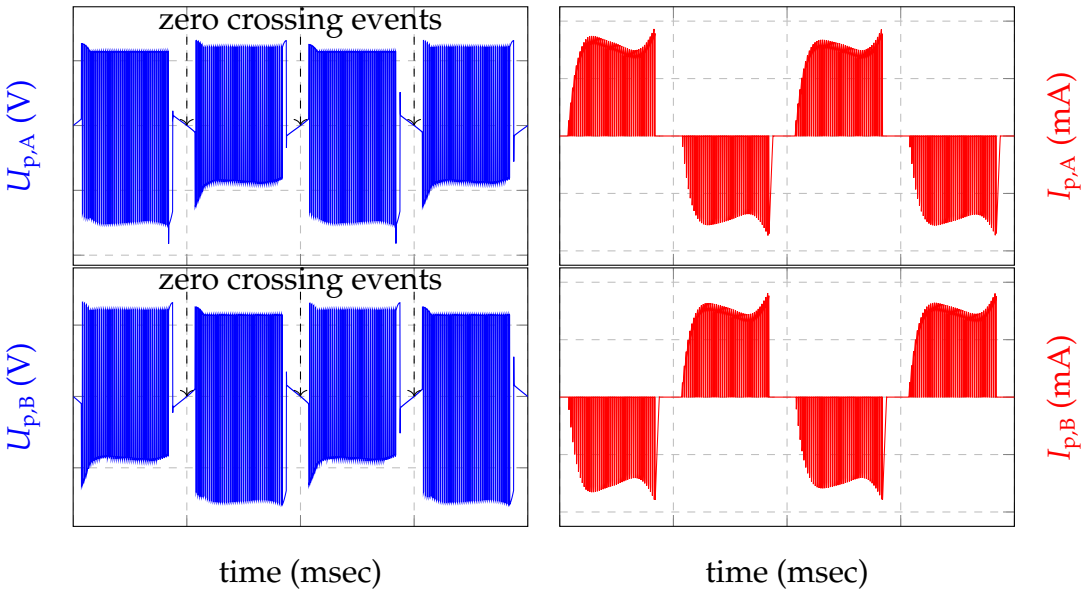

Figure 6.15: Phase signals for a single phase BLDC machine using the time sharing switching strategy.

As seen in the phase voltages, the zero crossing events can be found in between the supply pulses of the motor windings. These events can be used for commutating the BLDC motor.

A sensorless solution exploiting the time sharing sensorless control method for the fan drive will now be presented. Figure 6.16 shows the principle circuit for the sensorless control technique. As seen in the circuit diagram, our first prototype used two zero crossing detectors. Figure 6.17 shows the flow chart of the sensorless control scheme as programmed on the microcontroller unit.

The control sequence starts with a rotor alignment. Afterwards, the fan is ramped up from a known position with a fixed voltage pulse pattern. If the fan is running at a sufficient speed for measuring the back-EMF voltages, the sensorless control

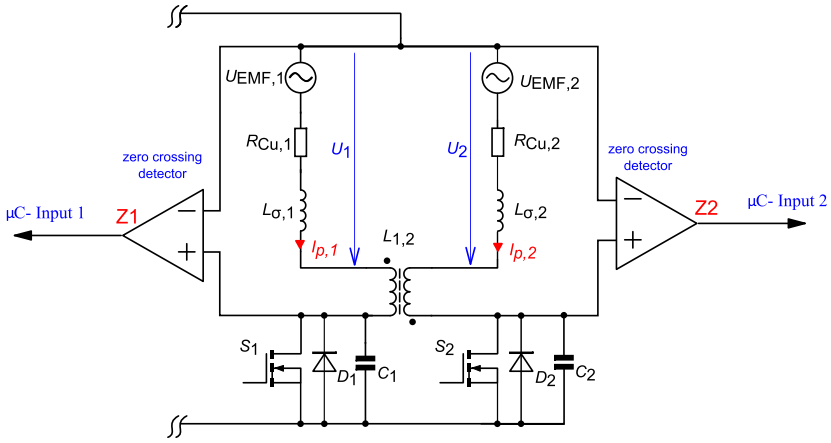

Figure 6.16: Circuit diagram of BLDCs sensorless control.

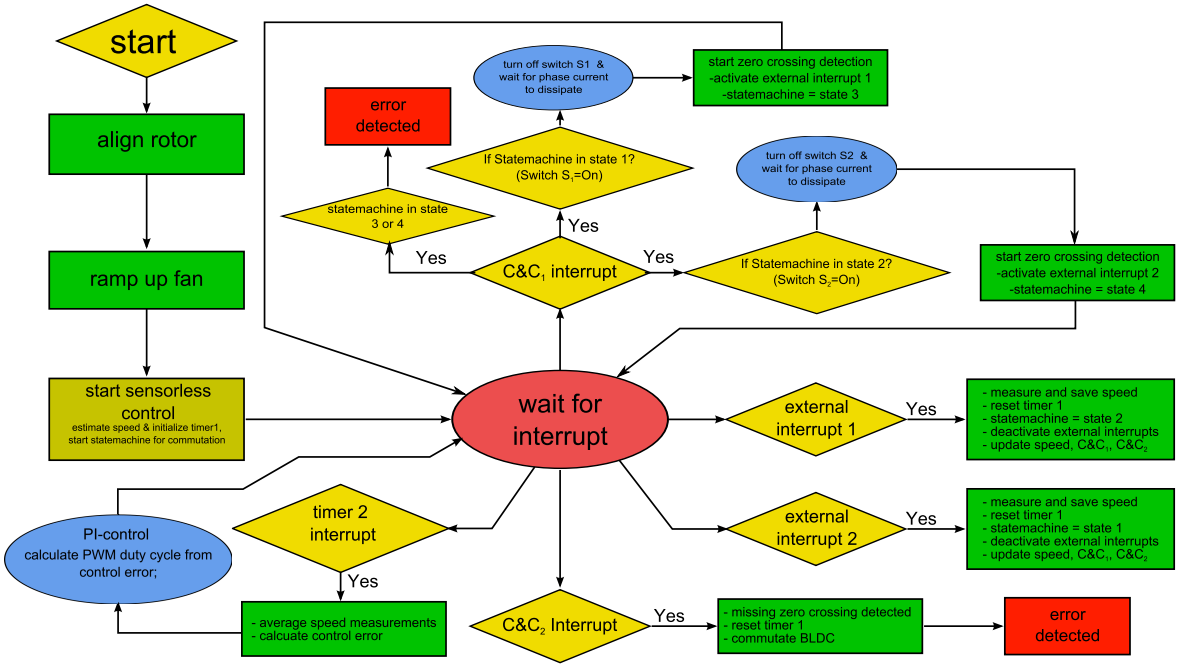

Figure 6.17: Flow chart of the sensorless control scheme.

scheme starts.

The sensorless control starts by lingering in the wait state, waiting for an interrupt to occur. If a zero crossing event occurs, it triggers an external interrupt which will reset and restart timer 1 (which is responsible for the speed measurement and the winding time sharing pulse pattern). Furthermore, the current will be commutated to the correct phase by applying the PWM signal from the PI controller to the appropriate switch (S_1 or S_2). Afterwards, the statemachine moves back to the

wait state and remains there until timer 1 counts up to the compare and capture value ($C\&C_1$), which is set up by the estimated speed. The value stored in the $C\&C_1$-register denotes the instant for breaking the phase supply and reinitiating the back-EMF measurement.

Figure 6.18 shows the principle phase and the controller signals for the sensorless control scheme described above. As can be seen in Figures 6.17 and 6.18, the second

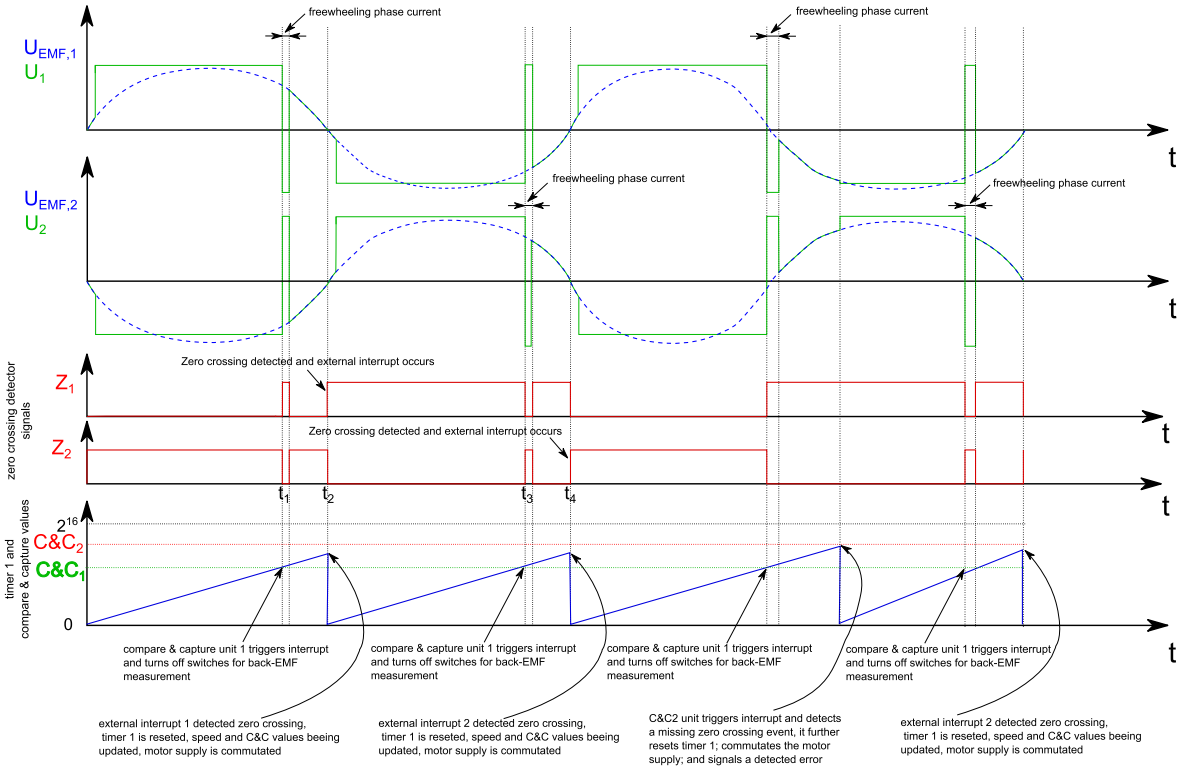

Figure 6.18: Phase and controller signals of the single phase sensorless control scheme.

compare and capture unit ($C\&C_2$) is used for increasing the stability of the control. If the statemachine lingers in wait state, waiting for a zero crossing event to occur, timer 1 still increases its value by increments. When the timer value equals the ($C\&C_2$)-register value, which is set in dependency of the actual fan speed, it is supposed that a zero crossing event was missed. The ($C\&C_2$) unit itself triggers an interrupt, resets the timers and continues with the next commutation step.

Caution is advised after turning off the actual phase which supplies the motor, because the freewheeling currents generate additional zero crossings. This problem can be solved by waiting a fixed time after turning off the motor phase before starting

with the back-EMF detection.

Conclusion

With the described technique a stable sensorless control for the fan drive can be achieved. In general, fan applications suit sensorless control methods better than pump applications do, because they have almost no starting torques, and the load torque of a fan is only speed dependent and does not vary over one revolution.

Nevertheless, the sensorless control scheme faces the same problems as discussed in the conclusion of Section 6.1: As the drive has to work for a wide range of voltage supply, a stable start up sequence cannot be reached with a preset voltage puls pattern. A solution can be found by starting the fan with a current pulse sequence, but this again implies a current measurement and increasing costs.

A more sensitive parameter for the control stability is the operating temperature and its impact on the ball bearing of the fan drive. At an operating temperature of $-40\,°C$ the bearing grease becomes viscous which increases the starting as well as the load torque of the fan by almost a factor of three. Therefore, the start up current pulse sequence has to be a function of the actual operating temperature, whereby a temperature measurement will be required.

For these reasons and because of the absence of a clear cost benefit, a conventional sensored control technique was chosen to drive the BLDC fan drive.

Chapter 7

Hardware implementation and experimental validation

In the following, the realized motor test bench for fractional horse power drives is introduced. Furthermore, this section will discuss the validation of the BLDC motors and drive simulation models.

7.1 Test-bench for fractional power machines

Figure 7.1 shows a picture of the overall testbench. In this section its components

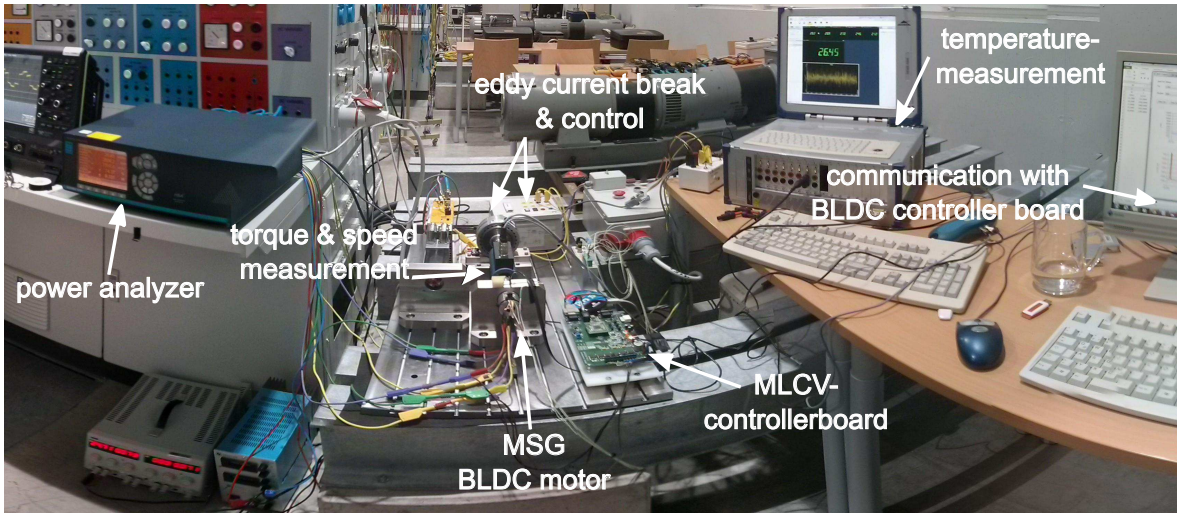

Figure 7.1: Realized test-bench for fractional horse power machines.

are described in more detail and challenges which notably occur for fractional horse power drive test benches will be pointed out.

Due to the small power rating of the machines, the mechanical set up needs to be very precise. That implies that all mechanical parts (ground plate, motor holds and torque sensor hold) need to be made of steel. Furthermore, any misalignment of measurement equipment will result in non negligible additional load. So, in order to ensure that all components of the measurement system fall perfectly in line, all holds and the ground plate were constructed with a tongue and slot system (red circles in Figure 7.2).

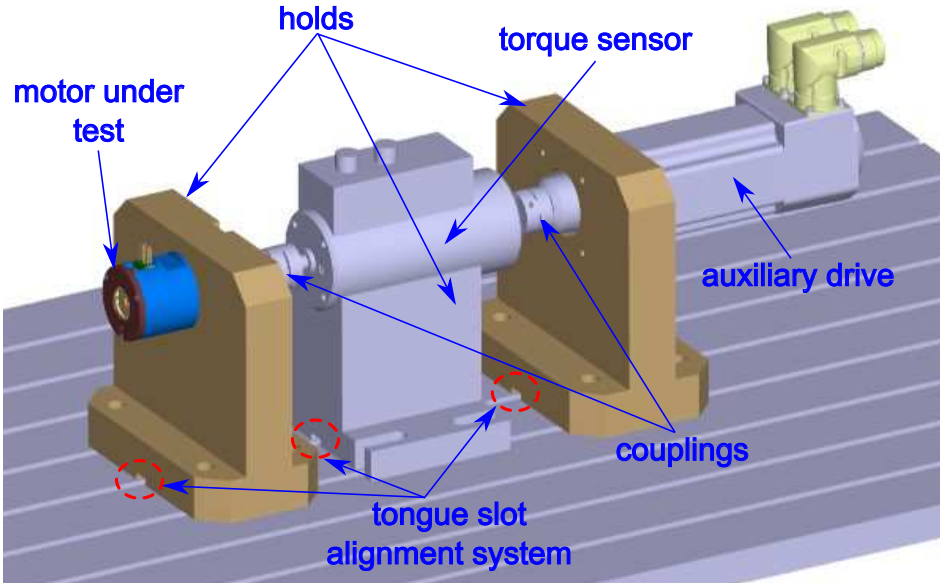

Figure 7.2: Tongue slot system for test setup alignment.

To load the device under test, a hysteresis break is used to guarantee a constant, ripple free load torque. The hysteresis break was chosen to have a relatively high moment of inertia compared to the BLDC motor. This ensures that torque ripple of the BLDC machine does not cause speed ripple at stationery operation points and therefore guarantees better comparability to simulation results.

For an accurate torque measurement, a two domain torque sensor is used. The sensor is capable of measuring torque waveforms up to a speed of $n = 20000\,\text{rpm}$ and has its two full scale values at $T_{\text{fullscale},1} = 1\,\text{Nm}$ and $T_{\text{fullscale},2} = 200\,\text{mNm}$ with an accuracy class of 0.1.

To compensate for any possibly remaining misalignments, the motor under test, the torque sensor and the hysteresis break are coupled together with flexible bellow couplings.

The electric as well as the mechanical signals were measured with a power analyzer ("Norma 5000"). Additional signal graphs for visualization are captured by a digital storage oscilloscope ("LeCroy HDO4000").

A schematic block diagram of the test bench with its described components can be seen in Figure 7.3.

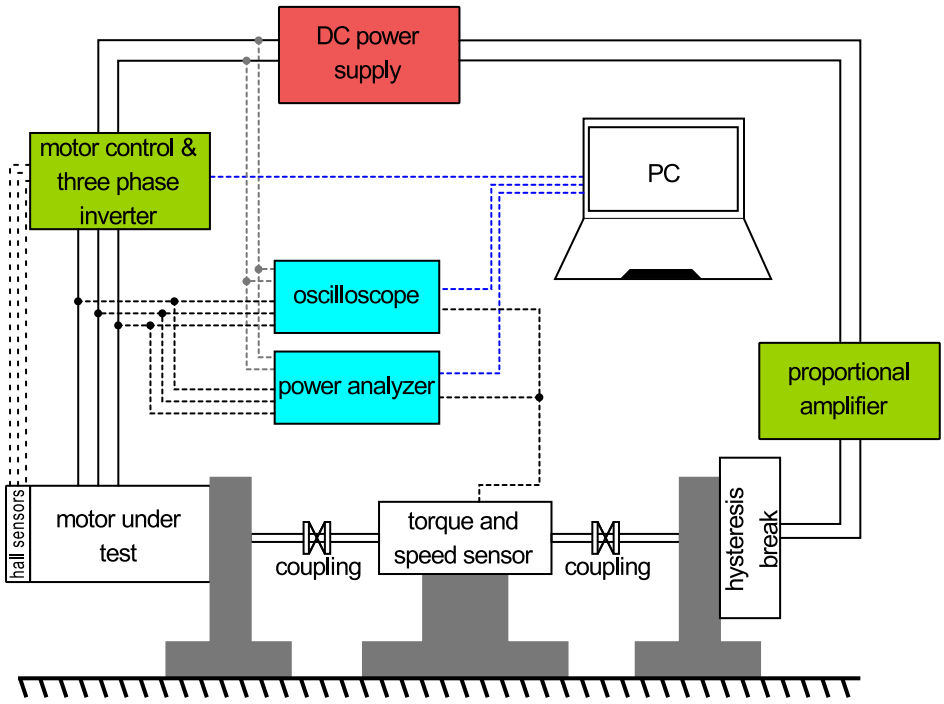

Figure 7.3: Bloc diagram of the test bench.

7.2 Hardware implementation of BLDC control

This section will describe, how the findings from Chapter 4 were implemented in the control hardware of the BLDC motor drives.

7.2.1 Three phase motor control hardware

A dsPICDEM MCLV-2 development board from microchip [83] is used to implement the BLDC control. Figure 7.4 shows the development board with all its features.

The board is composed of

(a) dsPICDEM MLCV-2 development board.

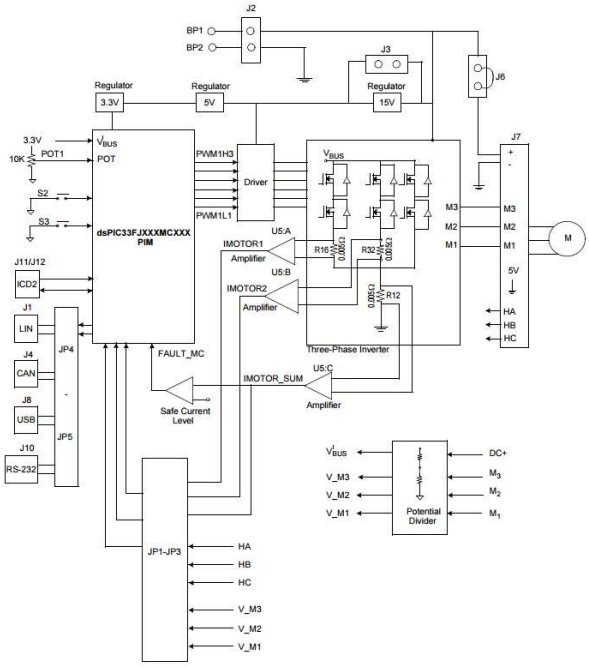

(b) Bloc diagram of the development board

Figure 7.4: Development board for BLDC motor control.

- Driver circuit for the inverter bridge,
- Three phase inverter bridge with a maximum power rating of 48V/15A,
- On board opportunities for phase and DC bus current sensing,
- dsPIC33F 16-bit digital motor controller,

- Communication interfaces for monitoring and motor control.

Figure 7.5 shows a flow chart of the motor control software implemented on the development board. The flow chart is split into two parts, the main loop and the interrupt service routines, which handle time critical events.

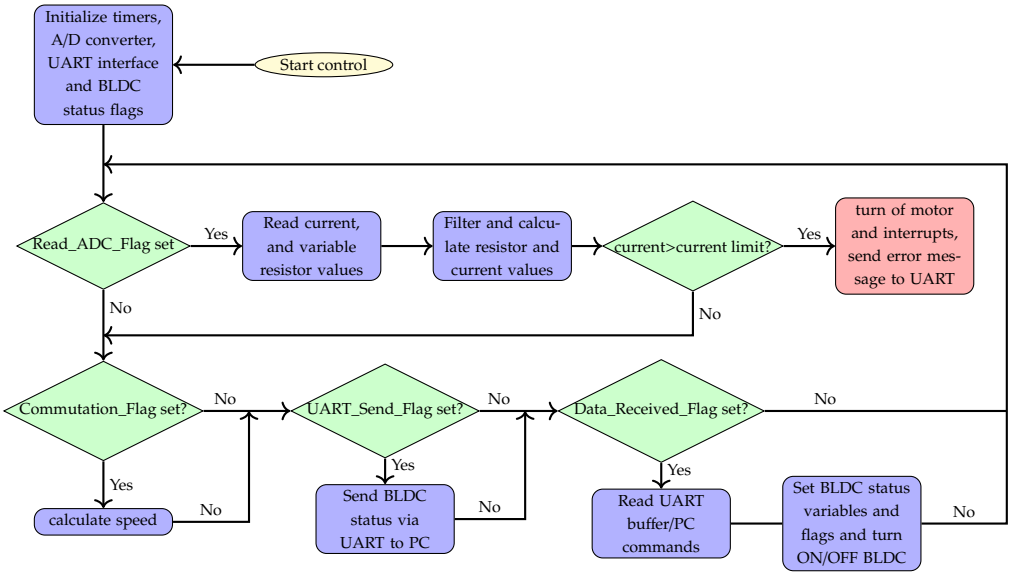

(a) Main loop of control program.

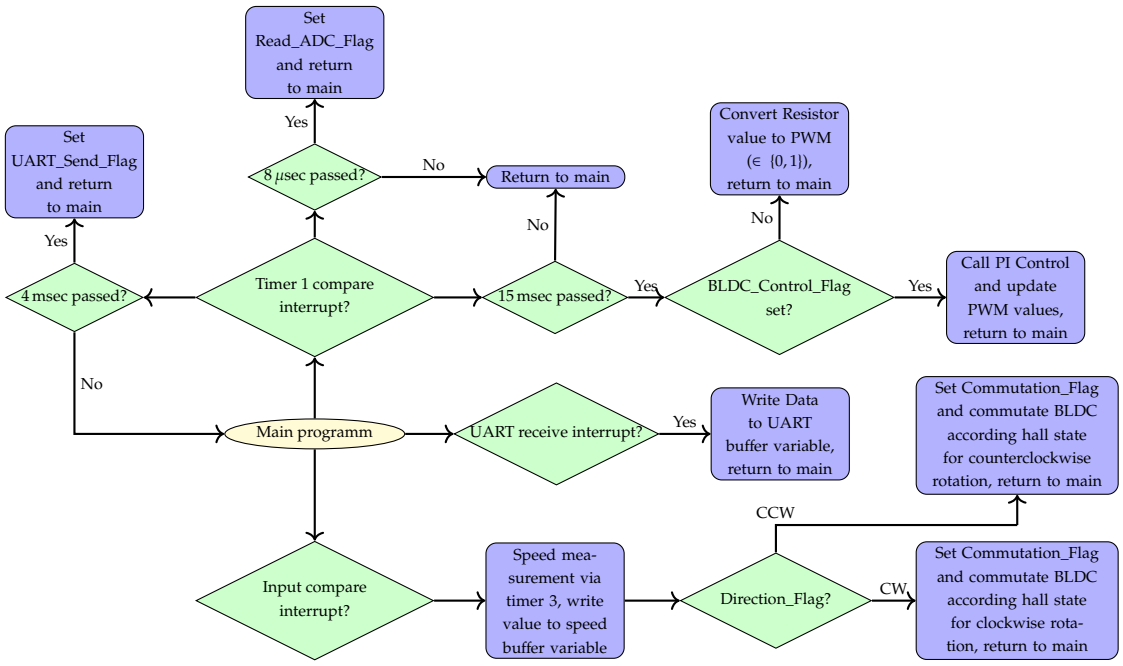

(b) Interrupt service routines.

Figure 7.5: Flow chart of implemented motor control.

In general, the BLDC control program is controlled via the UART interface of a PC. Figure 7.6 shows the user interface of the created PC program which is used to communicate with the controller board.

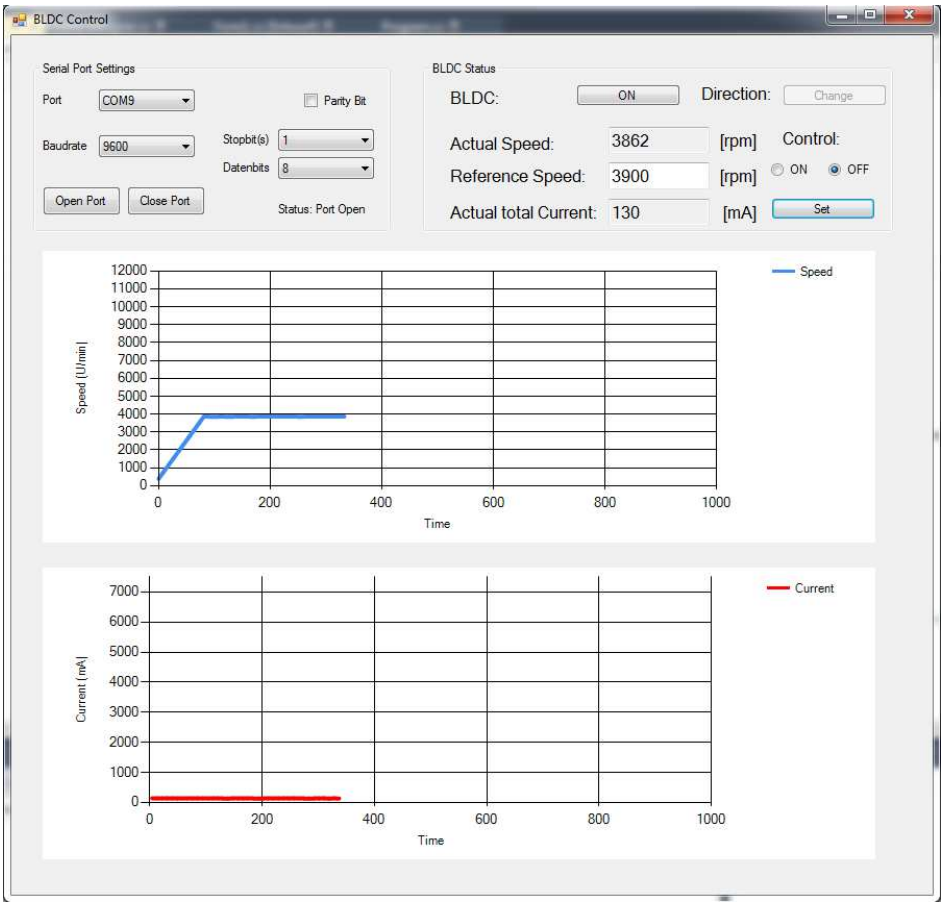

Figure 7.6: Program window of BLDC control user interface.

The control program was designed so that the user can operate the BLDC in closed loop speed control or with a fixed PWM duty cycle. For the closed loop control the user sets up a reference speed on the PC; for fixed PWM mode the PWM duty cycle is set up with a variable resistor. The closed loop control is done by a PI control with a sampling frequency of 15 msec.

The speed is measured at every commutation step and averaged over one electric period; therefore speed variations due to different commutation periods, which can be caused by hall displacements, are canceled out. The DC current is measured with a shunt resistor: high frequency variations again are eliminated by a FIR filter. Additionally, a current limiter which is built in the software prevents the board from

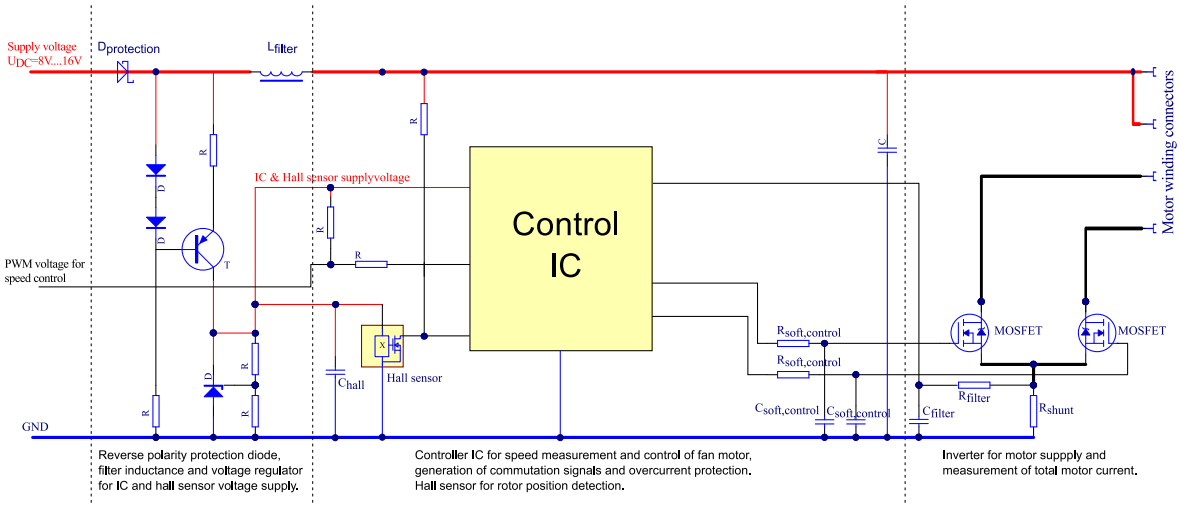

Figure 7.7: Bloc diagram of the single phase BLDC motor control.

damages.

7.2.2 Single phase motor control hardware

The motor control implementation as well as the board layout were realized by a third party company. Therefore, the control algorithm cannot be shown in full detail. Nevertheless, Figure 7.7 shows a simplified version of the controller board for the single phase BLDC machine. The board's inputs are the supply voltage ($U_{dc} \in \{8\,\text{V}...16\,\text{V}\}$ and a PWM input, which sets up the reference speed for the fans speed control ($n_{\text{fan}} \in \{1500\,\text{rpm}...5000\,\text{rpm}\}$). A hall sensor is used for detecting the rotor position. A microcontroller is used for speed control and measurement as well as commutating the single phase BLDC motor depending on the actual hall state. The soft switching of the motor (described in Section 5.2) is achieved by using low pass filtered gate signals for switching the MOSFETs. To indicate a motor stall as well as prevent overcurrents, the total current consumed by the motor is monitored.

7.3 Experimental results and model verifications

In this section experimental results of both drives will be presented. Furthermore, a comparison of the measured and the simulated results will be made to verify the

different motor and drive models used and discussed in Chapter 2.

7.3.1 Pump Drive

No load measurements

In order to verify the back-EMF voltages, the motor beeing tested was driven at rated speed by an auxiliary machine. Figure 7.8(a) shows the signal waveforms of measured and simulated (FE-model) back-EMF voltages, Figure 7.8(b) shows the FFT analysis.

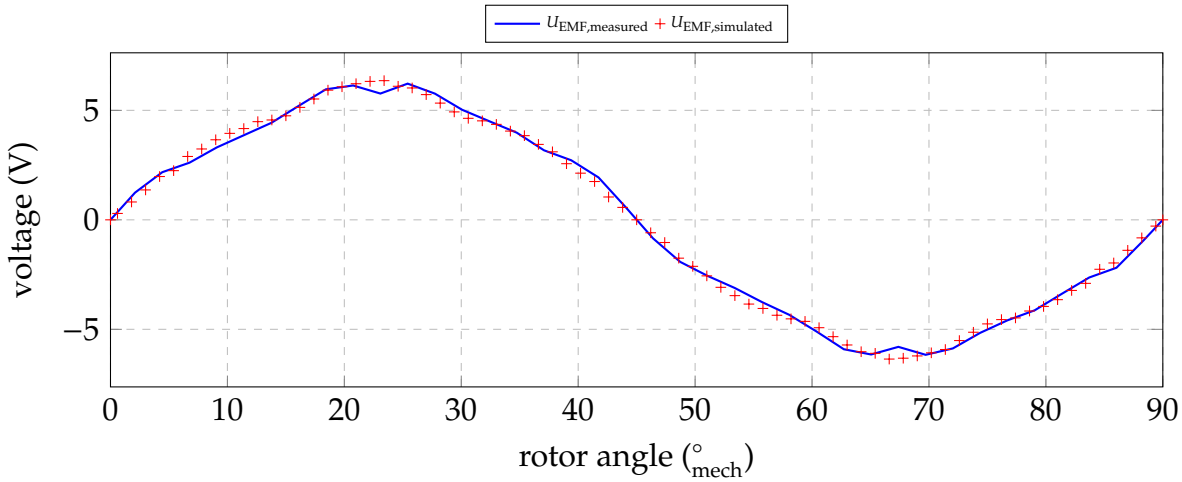

(a) Voltage waveforms.

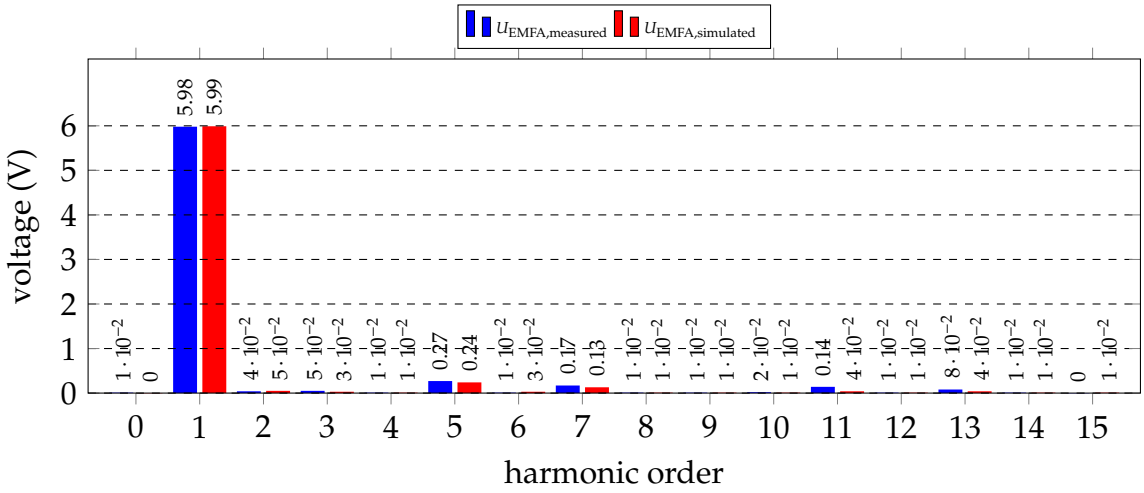

(b) FFT analysis.

Figure 7.8: Back-EMF voltage comparison

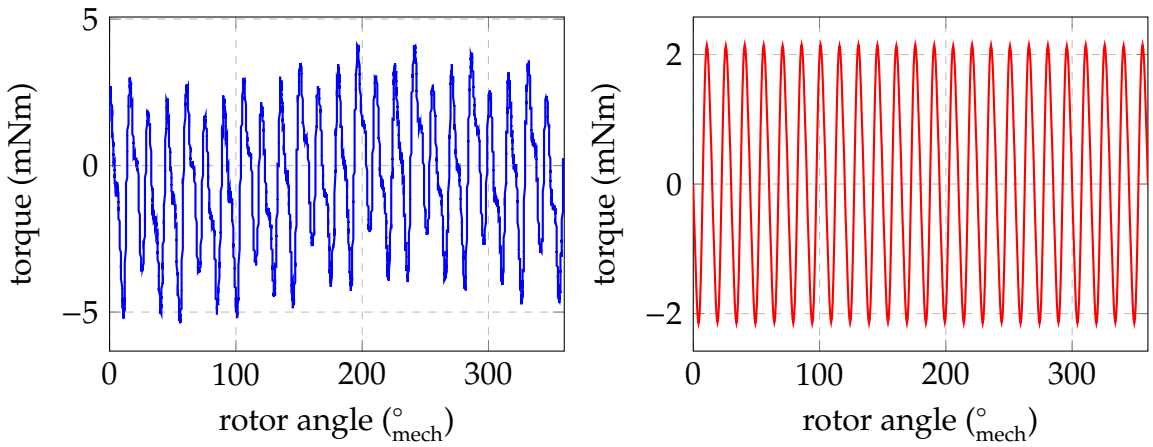

(a) Measured Cogging torque.

(b) Simulated Cogging torque.

Figure 7.9: Measured cogging torque.

The simulated and measured signals correspond well with each other for lower harmonics (relative error for first harmonic $\delta_{U_{EMF,1}}$ smaller one than percent). Discrepancies can be seen among the higher harmonics, e.g. $\delta_{U_{EMF,5}} \approx 11\%$, $\delta_{U_{EMF,7}} \approx 23\%$, $\delta_{U_{EMF,11}} \approx 71\%$. This is explained by the fact that the higher harmonics show a high sensitivity to different saturation of the flux stray paths, as shown in Chapter 2.

For the cogging torque measurement the same test setup is used. Measuring the cogging torque at high speeds can lead to wrong measurement results as, due to speed variations, an additional reaction torque from the test motor's moment of inertia is produced. Therefore, the cogging torque was measured at a speed of $n = 2\,\text{rpm}$. Figure 7.9 shows the measured cogging torque.

To cancel out the cogging torque effect by the auxiliary machine as well as error caused by displacements of the test setup, a FFT analysis of the cogging torque is shown in Figure 7.10. The cogging torque of the BLDC motor should be found at the harmonic order of least common multiplier between the slots and poles of the machine

$$LCM\{\text{slots} = 12, \text{poles} = 8\} = 24^{\text{th}}\,\text{harmonic}. \tag{7.1}$$

In Figure 7.10 the DC content of the measured torque represents the ball bearings' friction and iron losses, the first harmonic content stands for displacements in the measurement setup, and the higher harmonics can be explained by the cogging torque of the auxiliary machine and not uniformly magnetized permanent magnets.

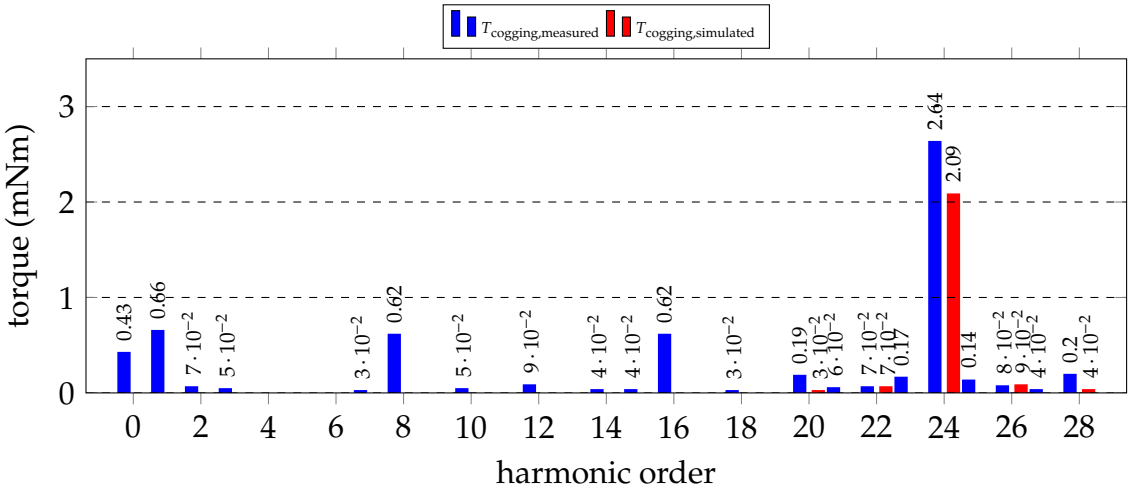

Figure 7.10: FFT analysis of cogging torque

The cogging torque can be found in the 24th harmonic; the relative error between measured and simulated values is approximately $\delta_{T_{cog,24}} \approx 20\%$. Again a potential explanation can be found in material variations due to punching of steel sheets as described in Chapter 2.

For later consideration the described torque measurement was repeated at different speed values. Figure 7.11 shows the measured average load torques.

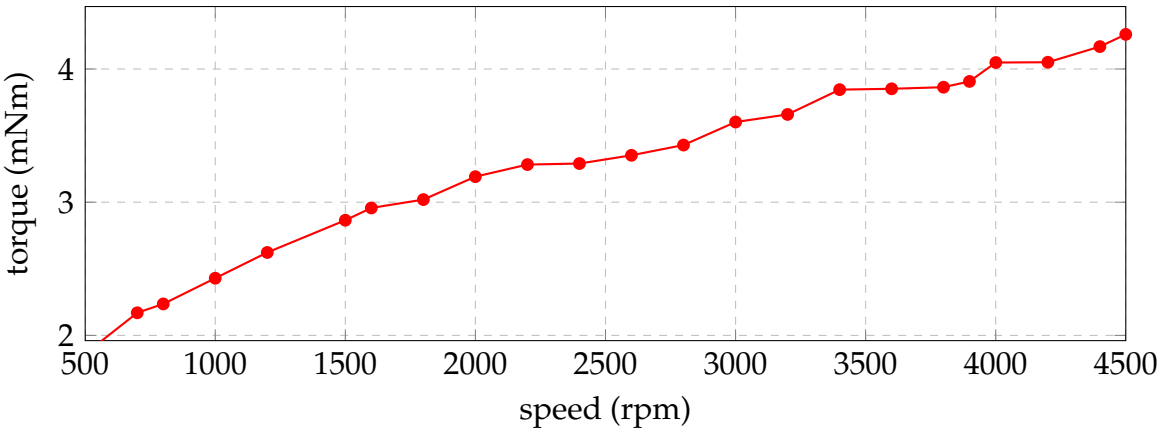

Figure 7.11: Torque of no load measurements.

Thereby, the measured torque represents two parameters of the motor beeing tested. First the friction losses of the motor's ball bearings and second the iron losses.

To separate these two losses, a measurement setup including a motor without magnets would be needed to measure only the ball bearings' friction losses. As no such motor assembly was available, the frictional torque of the ball bearings was estimated with the calculation method proposed in [84]. Figure 7.12 shows the calculated bearing frictional torques and the derived iron losses. For comparison, the FE simulation results of the iron losses have been included in the graph.

At rated speed a relative error of $\delta_{P_{Fe}} \approx 28\,\%$ can be denoted. This error can again be explained by different material properties as well as inaccuracies of the frictional bearing torque estimation, as the estimated bearing losses are highly sensitive to different operational parameters such as temperature, static bearing mounting forces, condition of bearings lubricant and actual load.

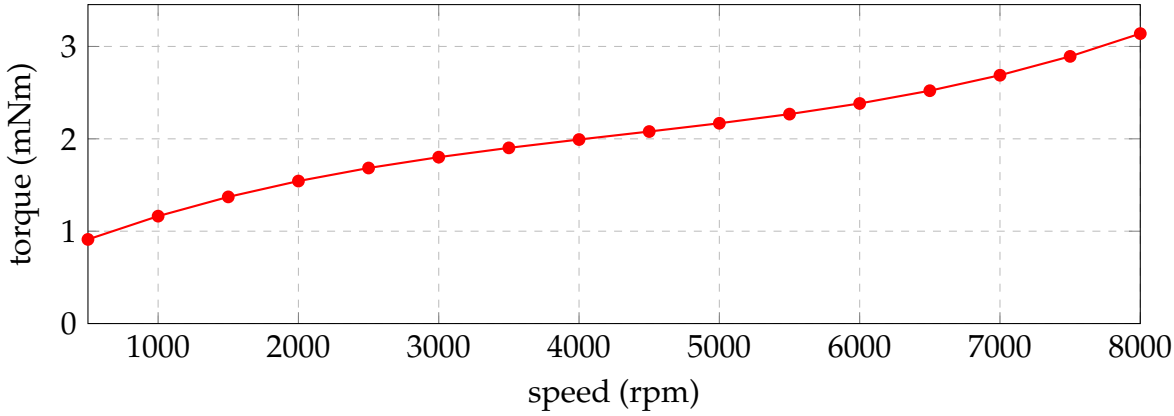

(a) Estimated bearing losses.

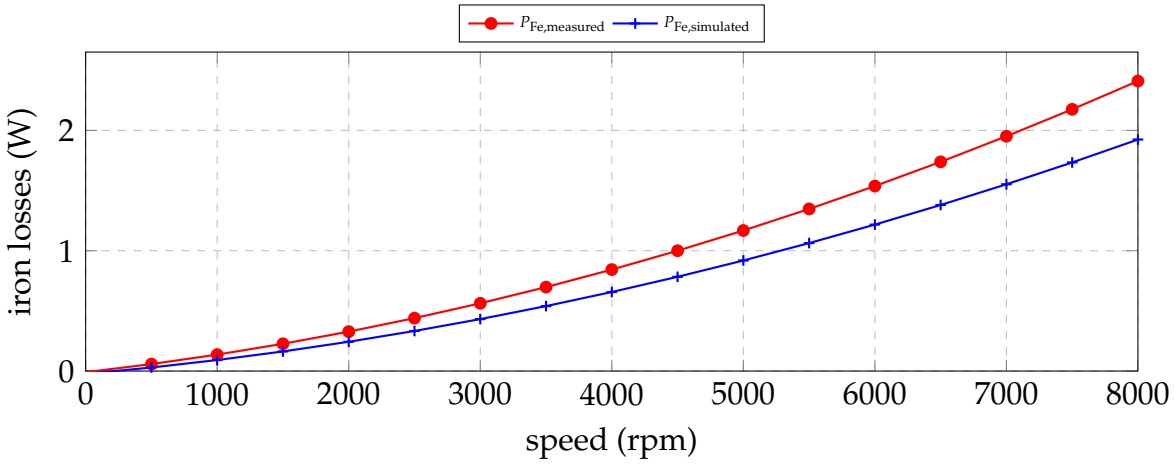

(b) Measured and simulated iron losses.

Figure 7.12: Frictional bearing and iron losses.

Efficiency measurements

To ensure an accurate measurement of the BLDC's energy conversion efficiency and take temperature influences on the winding resistances into account, the test setup from Figure 7.3 was amended by temperature measurements of the winding and housing temperatures ($T_{w,1}$, $T_{w,2}$ & T_S). Figure 7.13 shows a schematic diagram of the measurement set up. The measured results were compared to those of the

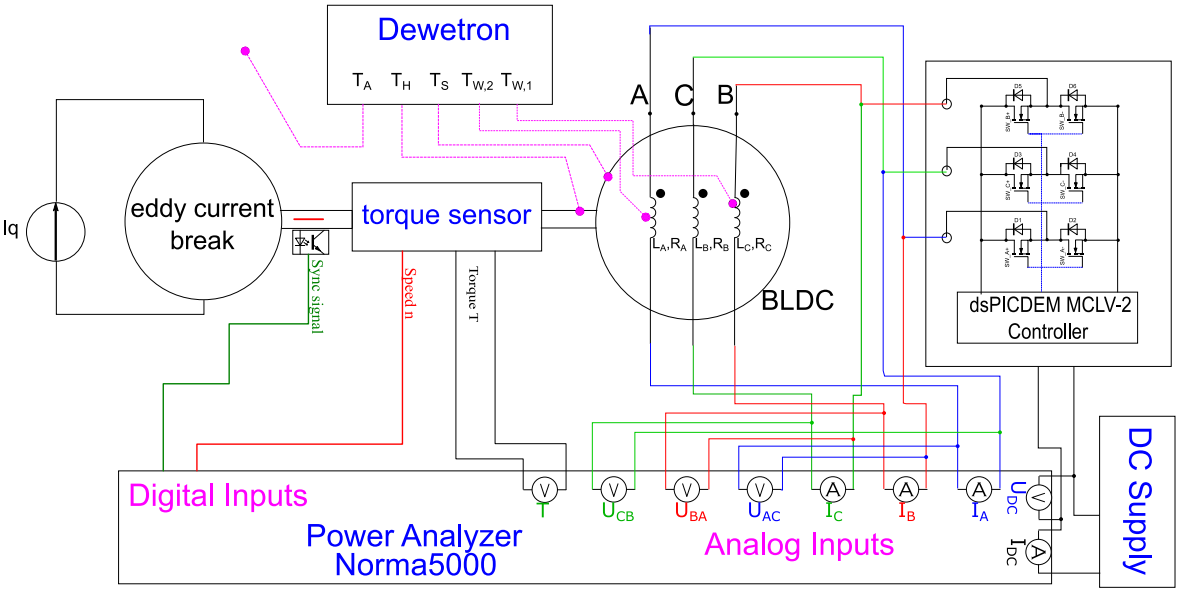

Figure 7.13: Measurement set up for efficiency measurement.

hybrid BLDC model from Section 2.3. Thereby, the hybrid model was simulated for the same points of operation and temperature as those that were measured.

Figures 7.14 to 7.18 show both measured and simulated results for motor energy conversion efficiency, phase currents, phase voltages, motor input and output power as well as iron and copper losses.

Detailed data is provided in Appendix B.1, showing the measured and simulated results of different points of operation.

The graphical comparisons show good congruence between simulation and measurement results. Figure 7.19 shows the relative errors between measured and com-

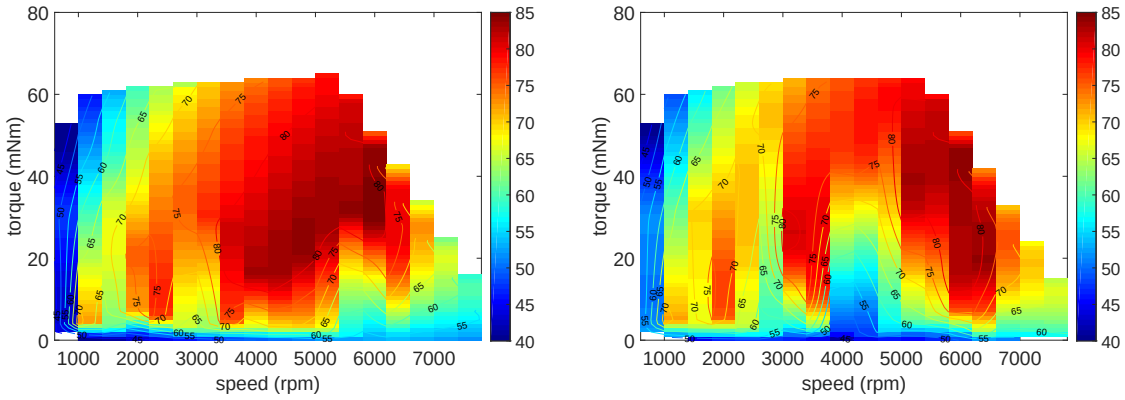

(a) Measured motor efficiency (%). (b) Simulated motor efficiency (%).

Figure 7.14: Measured versus computed efficiency map of BLDC drive.

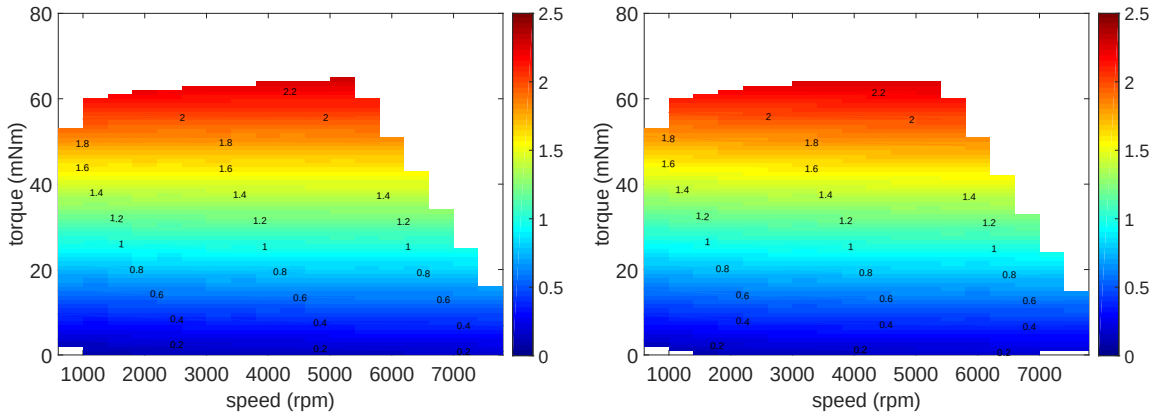

(a) Measured motor phase current (A). (b) Simulated motor phase current (A).

Figure 7.15: Measured versus computed average RMS phase currents of BLDC drive.

puted results for the motor's efficiency and iron losses. The discrepancy of the efficiency in low torque areas can be explained by wrongly estimated values for the motor's bearing loads. At these points of operation, the frictional bearing torque is a higher percentage of the motor's overall torque and therefore produces a higher relative error.

The iron losses for hybrid BLDC simulation were taken from no load simulations and therefore, for higher loads, the iron losses produced by the stator field are not taken into account. Therefore, the iron losses diverge stronger for higher load torques.

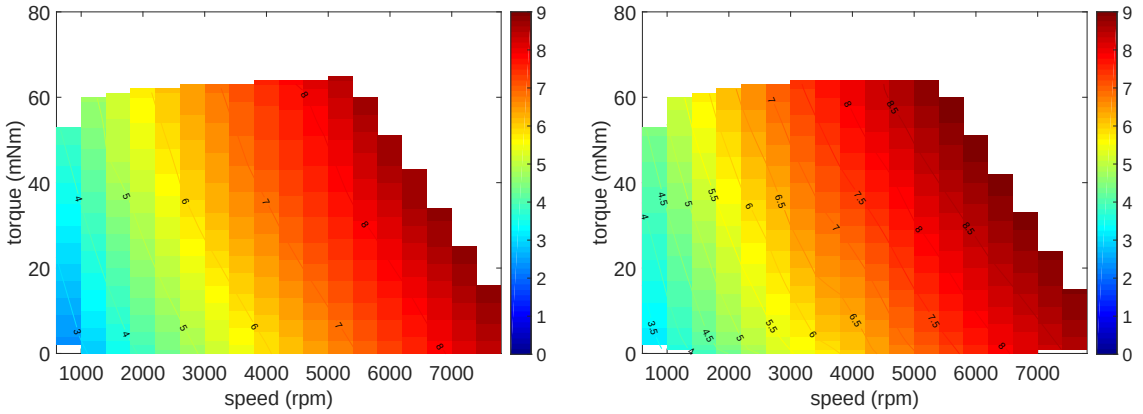

(a) Measured motor phase voltage (V). (b) Simulated motor phase voltage (V).

Figure 7.16: Measured versus computed average RMS phase voltages of BLDC drive.

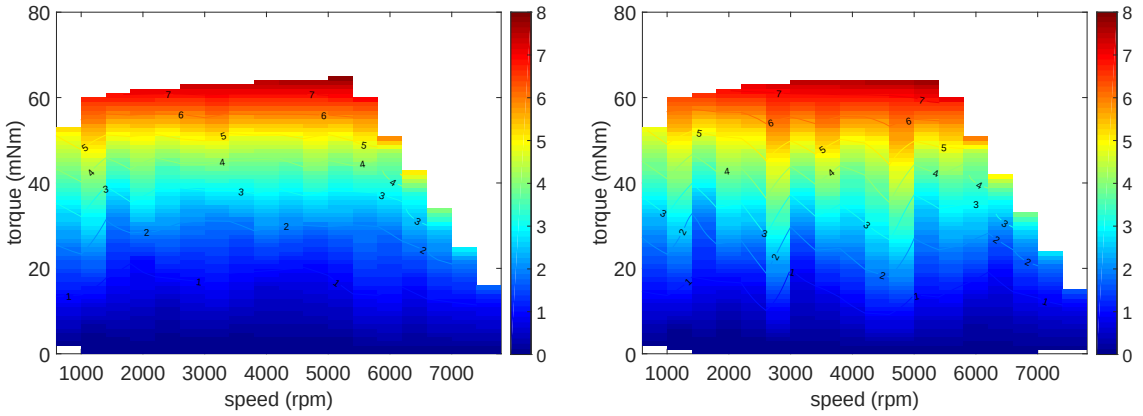

(a) Motors measured copper losses (W). (b) Motors simulated copper losses.

Figure 7.17: Measured versus computed copper losses of BLDC drive.

In Figure 7.16 differences of the motor's phase voltages, for a whole range of points of operation, can be observed. This is explained by the fact that the simulated inverter parameters differ from those of the prototyping board: Unfortunately, the simulation model used with higher ON resistances for the MOSFETs resulted in an higher energy demand drawn by the MOSFETs.

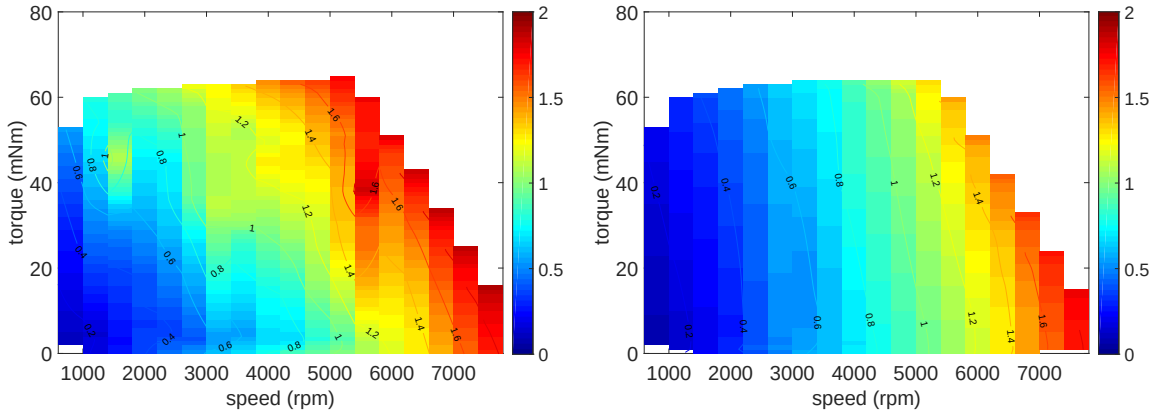

(a) Motors measured iron losses (W). (b) Motors simulated iron losses.

Figure 7.18: Measured versus computed iron losses of BLDC drive.

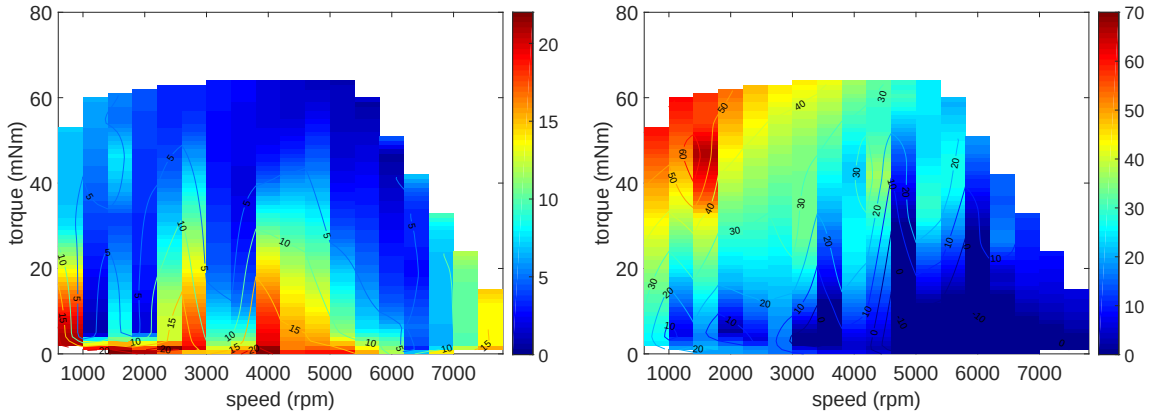

(a) Relative error of efficiency (%). (b) Relative error of iron losses (%).

Figure 7.19: Measured versus computed relative error of efficiency and iron losses.

Pump application measurements

This section shows measurements of the overall pump application. The same measurement setup as the one shown in Figure 7.13 was used, but the eddy current break was replaced by a diaphragm pump. Section 2.1.1 specifies that within its application the pump should work against a counter pressure of $p_{\text{pump}} = 0.5\,\text{bar}$. Table 7.1 shows results from measurement (gray) and simulation (white). The hybrid model from Section 2.3 was used to simulate the pump application.

p_{pump} bar	T_{AVG} mNm	n_{AVG} rpm	$U_{DC,AVG}$ V	$I_{DC,AVG}$ A	$U_{A,RMS}$ V	$I_{A,RMS}$ A	$U_{B,RMS}$ V	$I_{B,RMS}$ A	$U_{C,RMS}$ V	$I_{C,RMS}$ A	P_{in} W	P_{BLDC} W	P_{out} W	$\eta_{control}$ %	η_{BLDC} %	η_{total} %
0.5	45.2	3935	12.00	2.12	7.65	1.63	7.57	1.66	7.70	1.76	25.43	24.10	19.44	95	81	76
0.5	44.6	3967	12.00	2.09	7.61	1.89	7.46	1.52	7.19	1.51	25.11	23.18	18.49	92	80	74

Table 7.1: Results of pump measurement/simulation.

The comparison of measurement and simulation results are highly congruent. Just phase currents and voltages show discrepancies. These are caused by the different commutation periods as shown in Figure 7.20. In the simulation every commutation periods lasts for exactly 15 mechanical degrees, whereas the measurement shows that due to hall sensors and magnets tolerances, the commutation periods lengths vary.

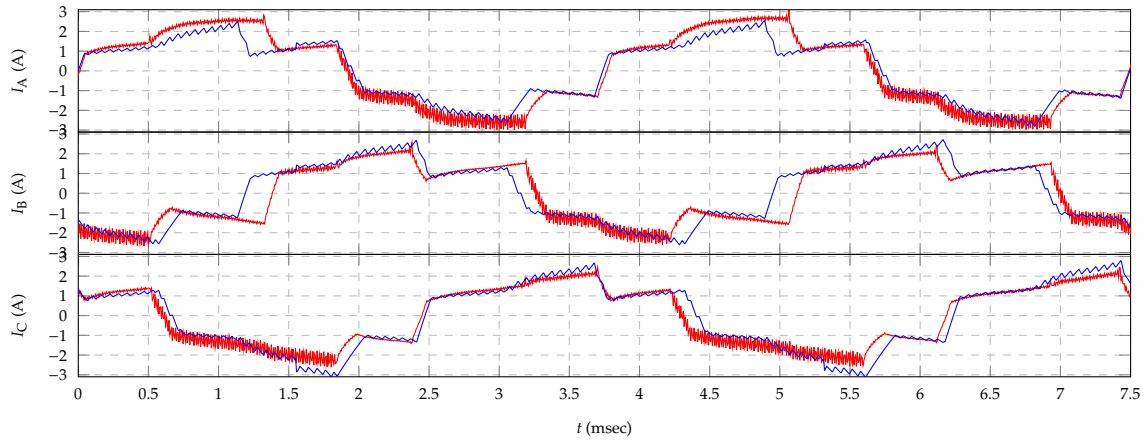

Figure 7.20: Phase currents over one electric period; — measured; — simulated.

7.3.2 Fan drive

In this section, measurements results of the fan drive will be presented and further fan simulation models will be validated. The test bench from Section 7.1 is not suitable for load measurements on the fan, as the load torques to be measured are too small and therefore even small displacements of the measurement equipment would result in huge additional loads as compared to the fan wheels load.

Fan wheel's load torque

For later comparisons, an estimation of the fan wheel's load is needed. As the fan drive could not be attached to the test bench, the load torque was determined by several coastdown tests. The fan drive's equation of motion can be described by:

$$J_F \frac{d\omega}{dt} = T_b + T_F(\omega) + T_{BLDC}. \tag{7.2}$$

Thereby, T_b presents the bearing load, $T_F(\omega)$ the speed depended load of the fan wheel and T_{BLDC} the torque of the drive. For a coastdown test equation (7.2) simplifies to:

$$J_F \frac{d\omega}{dt} = T_b + T_F(\omega) := T_L \tag{7.3}$$

If the coastdown test is made with the original fan drive (Figure 7.21(a)) and repeated with added moment of inertia J_H to fan's rotor (Figure 7.21(b)), the original moment of inertia can be determined by:

$$\begin{aligned} I.: & J_F \frac{d\omega}{dt} = T_L \\ II.: & (J_F + J_H) \frac{d\omega}{dt} = T_L \\ I. - II.: & J_F \frac{d\omega}{dt} - (J_F + J_H) \frac{d\omega}{dt} = 0 \\ & 0 = J_F \frac{\Delta\omega}{\Delta t_1} - (J_F + J_H) \frac{\Delta\omega}{\Delta t_2} \\ & J_F = J_H \frac{\Delta t_1}{(\Delta t_2 - \Delta t_1)} \end{aligned} \tag{7.4}$$

With the calculated moment of inertia, the speed dependent load torque can be determined by:

$$T_L = J_F \frac{2\pi}{60} \frac{dn}{dt}. \tag{7.5}$$

To ensure that there is no influence by the conservative cogging torque, the difference quotient from equation (7.4) has to be sampled at multiples of a cogging torque period such as back-EMF voltages zero crossings.

Figure 7.22 shows the determined average load torque of the fan wheel; the moment of inertia of the fan motor was calculated to be $J_F = 2.8327\,10^{-6}\,\mathrm{kg\,m^2}$. Furthermore, the graph shows the estimated instantaneous load torque calculated by the fan affinity laws from [59] on the basis of the the fan's rated power (Section 2.1.2).

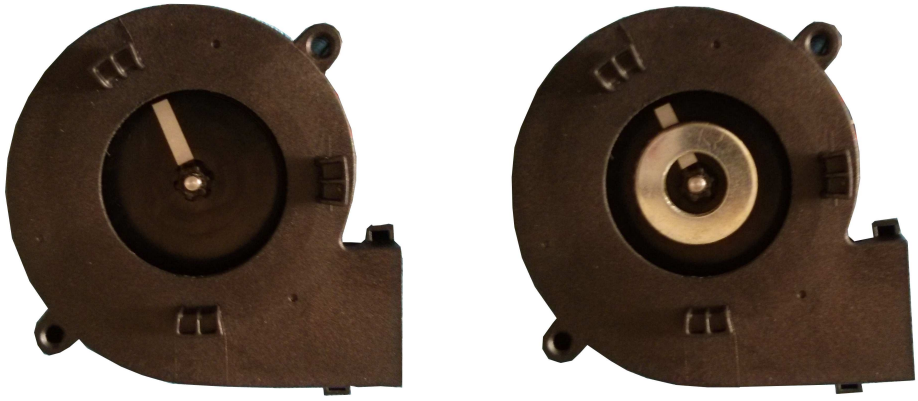

(a) Original fan drive.

(b) Fan drive with added moment of inertia.

Figure 7.21: Fans for coastdown tests.

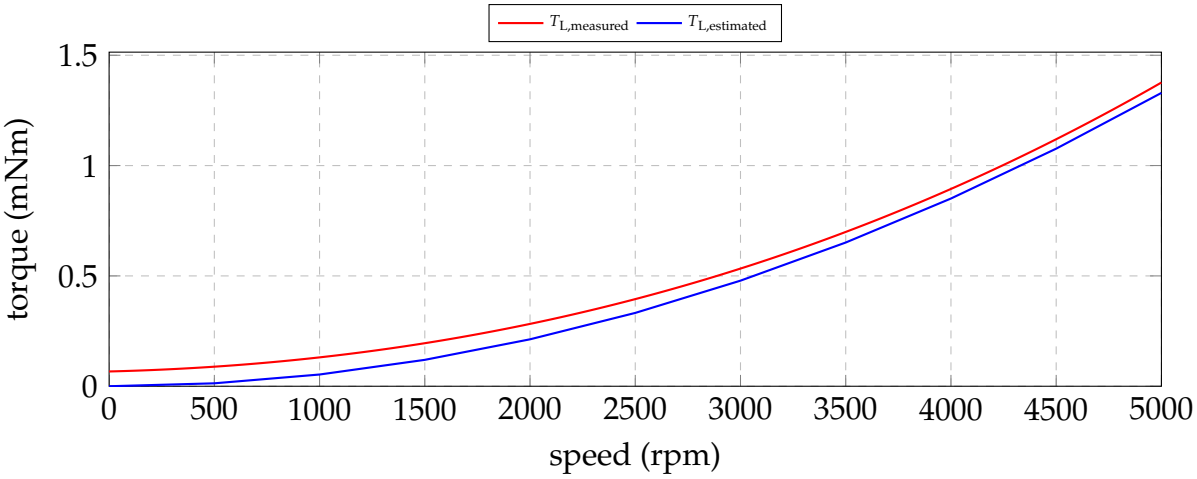

Figure 7.22: Determined load torque of fan's wheel.

No load measurements

First, the back-EMF voltages of the single phase motor were validated. Therefore, the drive was driven at rated speed and the back-EMF voltage waveforms were captured with an oscilloscope. Figure 7.23 shows the signal waveforms as well as the FFT analysis of measured and simulated (FE-model) back-EMF voltages for one phase of the bifilar windings.

The relative error of the back-EMF's first harmonic is $\delta_{U_{EMF,1}} \approx 7.5\,\%$. These discrepancies can be explained by the sensitivity of the FE model to magnet and

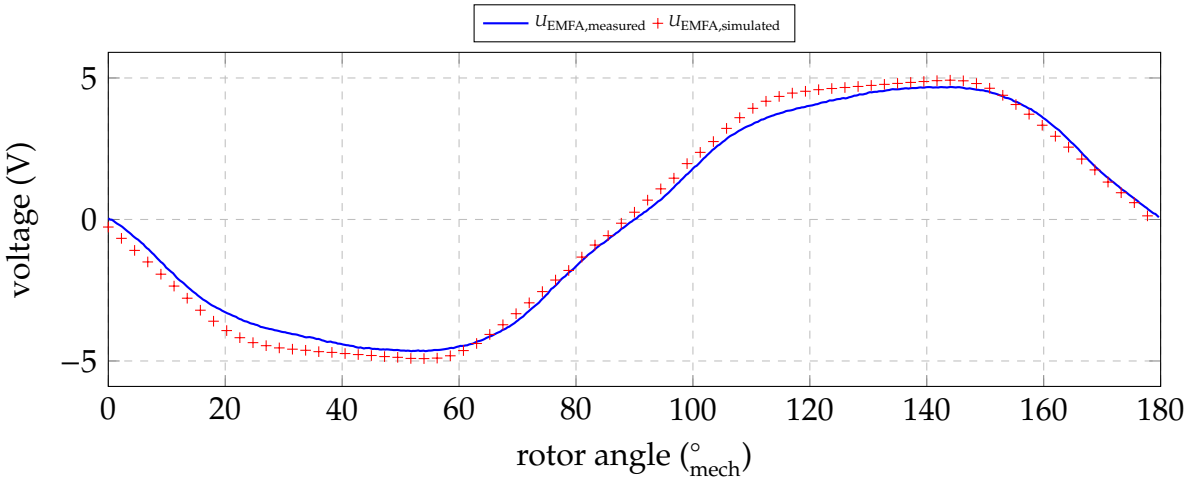

(a) Voltage waveforms.

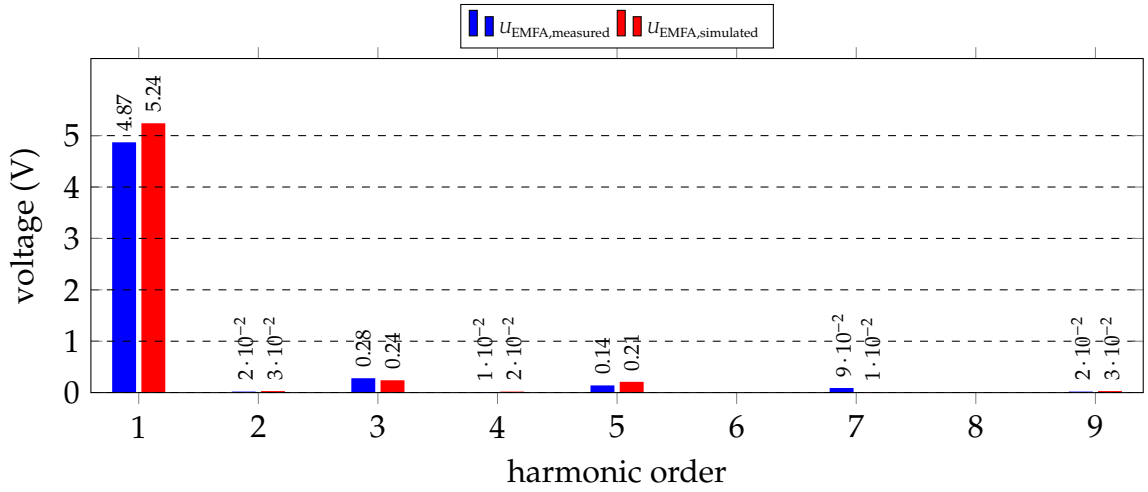

(b) FFT analysis.

Figure 7.23: Back-EMF voltage comparison

steel parameter variations as discussed in Section 2.2.2.

Measuring the iron losses was achieved by covering the fan's wheel. Thus, the fan wheel is not able to suck any air and therefore produces no load torque. Neglecting load torques from air turbulences, the iron losses were calculated by subtracting the copper losses and the frictional bearing losses from the input torque of the drive. Figure 7.24 shows a comparison of the measured and simulated iron losses.

The iron losses differ significantly due to imprecise data of the frictional bearing losses and wrong material data for the FE model Section 2.2.2.

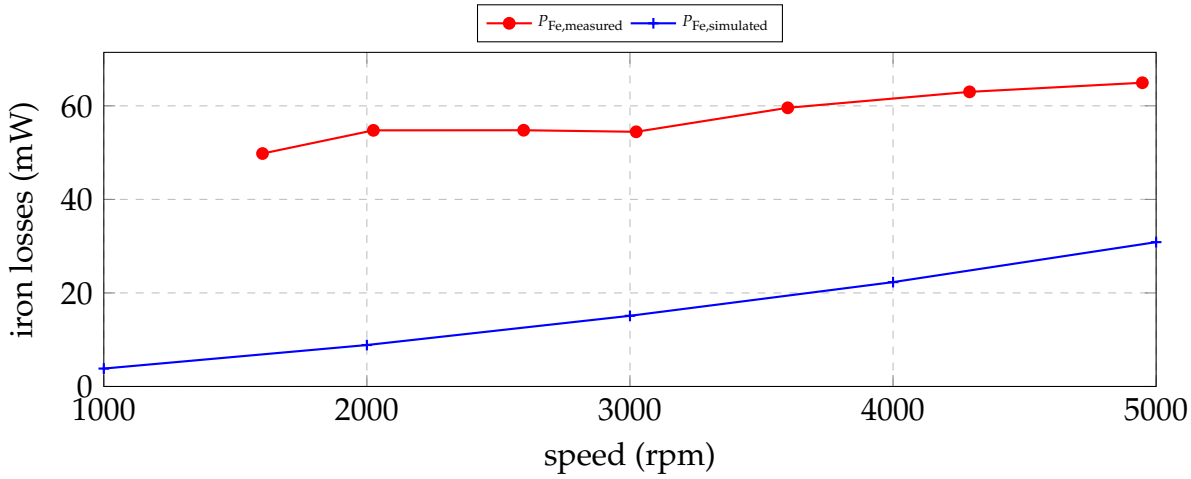

Figure 7.24: Measured and simulated iron losses.

Efficiency measurements

The efficiency measurements were carried out on the final fan application. Figure 7.25 shows the set up for measuring the fan's efficiency at different points of operation. The measured results were then compared with simulation results obtained from the hybrid fan model described in Section 2.3. To ensure a fair comparison the hybrid model was simulated with the same "advanced switch off" and "delayed switched on angle" as the real fan drive.

Figure 7.26 shows a comparison of measured and simulated energy conversion efficiencies of the drive. Detailed results of both simulation and measurement are shown in Appendix B.2.

Both efficiency curves, measured (—●—) and simulated (—+—), show the same trend, though the efficiency values show a significant difference. This difference mainly has its origin in the discrepancies between simulated and measured iron losses and estimated and measured load torques (Figure 7.22). Therefore, Figure 7.26 also comprises simulation results (—▫—) from a hybrid fan model which uses measured iron losses and load torques. Again, detailed results of the hybrid model simulation using measurement data are shown in Appendix B.2.

Figure 7.27 shows a comparison of measured and simulated results for motor input and output power as well as copper and iron losses. The overall input power is not included in the graph, as measured results comprise the power consumption

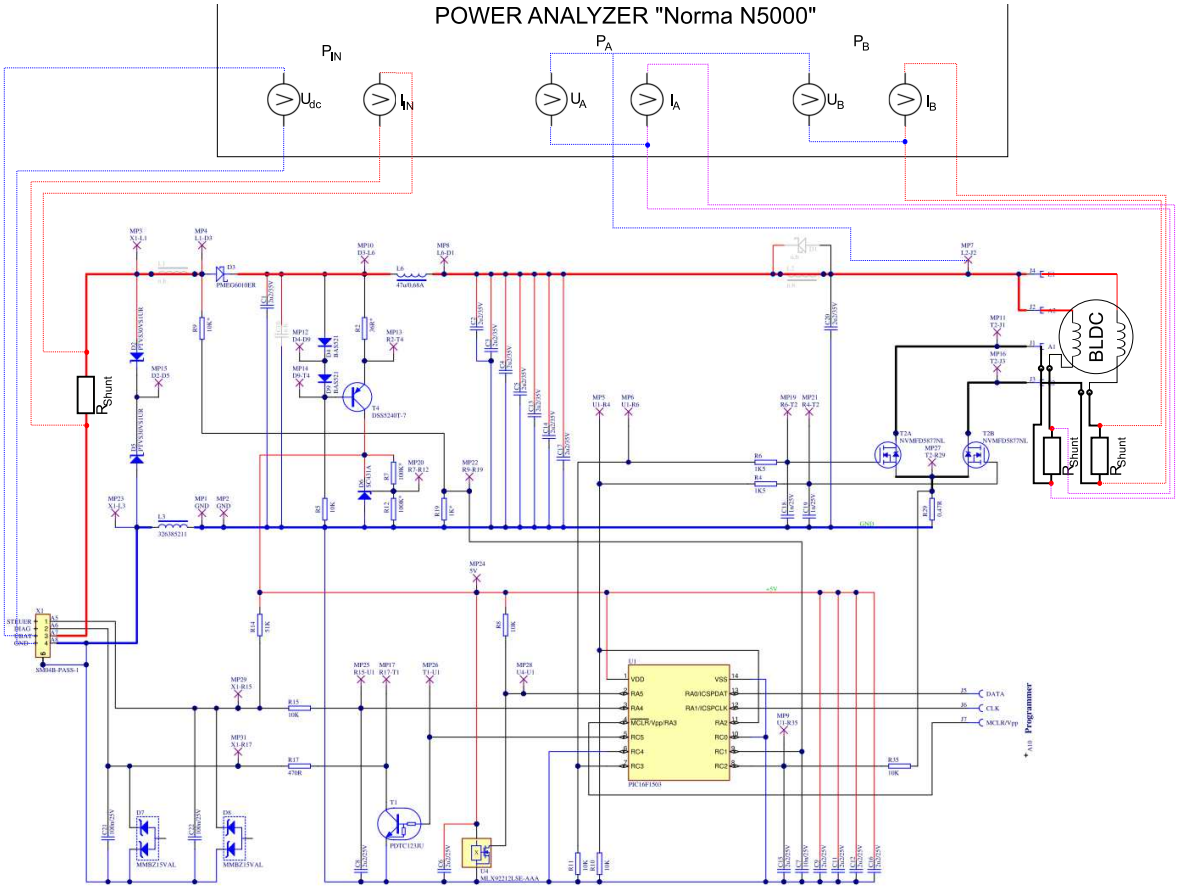

Figure 7.25: Set up for efficiency measurement.

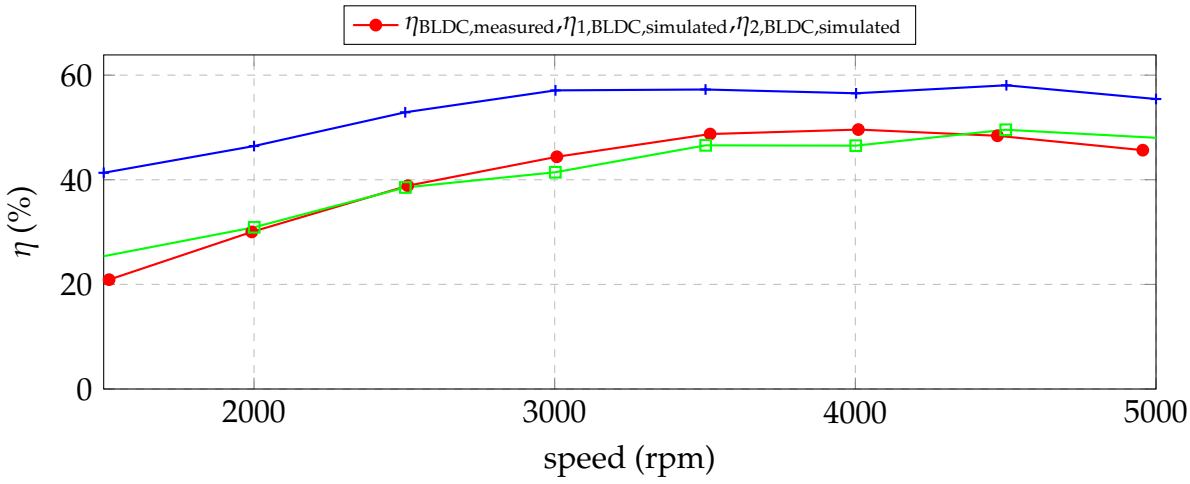

Figure 7.26: Measured and simulated motor efficiency.

of the controller and peripheral parts, whereas simulation results only cover losses caused by the inverter. The comparison proves, that the hybrid fan model provides good simulation results if the iron losses and the load are predicted accurately.

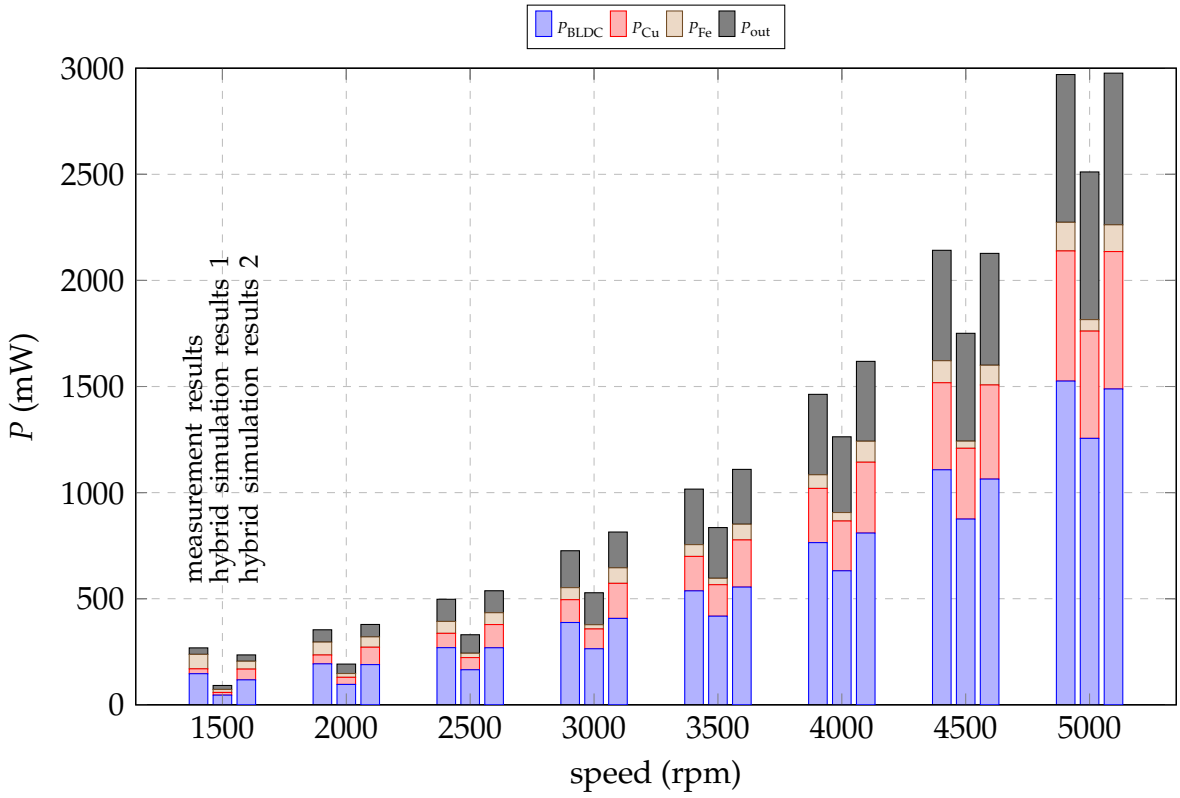

Figure 7.27: Comparison of measurements and simulation results of the fan drive.

Bibliography

[1] "World energy outlook 2012," *International Energy Agency (2012)*, vol. 978-92-64-18084-0, p. 179, 2012.

[2] United States Department of Transportation, "World Motor Vehicle Production, Selected Countries (Thousands of vehicles)," http://www.rita.dot.gov/bts/sites/rita.dot.gov.bts/files/publications/national_transportation_statistics/html/table_01_23.html_mfd, October 2014, accessed on 17-12-2015.

[3] G. Ombach and J. Junak, "Weight and efficiency optimization of auxiliary drives used in automobile," in *Electrical Machines (ICEM), 2010 XIX International Conference on*, Sept 2010, pp. 1–6.

[4] SMMT, "New car co2 report 2015," in *THE SOCIETY OF MOTOR MANUFACTURERS AND TRADERS, London*, 2015.

[5] Z. Zhu and D. Howe, "Electrical machines and drives for electric, hybrid, and fuel cell vehicles," *Proceedings of the IEEE*, vol. 95, no. 4, pp. 746–765, April 2007.

[6] T. Kenjō, *Electric motors and their controls: an introduction*, ser. Oxford Science Publications. Oxford University Press, Incorporated, 1991. [Online]. Available: https://books.google.at/books?id=zORSAAAAMAAJ

[7] J. Knezevic, "Low-cost low-resolution sensorless positioning of dc motor drives for vehicle auxiliary applications," *Vehicular Technology, IEEE Transactions on*, vol. 62, no. 9, pp. 4328–4335, Nov 2013.

[8] Bosch in Germany, "Invented for life," http://www.bosch.de/de/de/our_company_1/business_sectors_and_divisions_1/electrical_drives_1/electrical-drives.html, January 2016, accessed on 15-01-2016.

[9] J. Hendershot, J. Hendershot, and T. Miller, *Design of Brushless Permanent-magnet Machines*. Motor Design Books, 2010. [Online]. Available: https://books.google.at/books?id=n833QwAACAAJ

[10] J. Gieras and M. Wing, *Permanent Magnet Motor Technology: Design and Applications, Second Edition*,, ser. Electrical and Computer Engineering. Taylor & Francis, 2002. [Online]. Available: https://books.google.at/books?id=rJD-nQEACAAJ

[11] T.-H. Kim, H.-W. Lee, and M. Ehsani, "Advanced sensorless drive technique for multiphase bldc motors," in *Industrial Electronics Society, 2004. IECON 2004. 30th Annual Conference of IEEE*, vol. 1, 2004, pp. 926–931 Vol. 1.

[12] A. Darba, F. De Belie, and J. Melkebeek, "Sensorless commutation and speed control of brushless dc-machine drives based on the back-emf symmetric threshold-tracking," in *Electric Machines Drives Conference (IEMDC), 2013 IEEE International*, May 2013, pp. 492–497.

[13] L. Chang, "Switched reluctance motors: small motors of the next generation for automobiles?" in *Vehicular Technology Conference, 2003. VTC 2003-Fall. 2003 IEEE 58th*, vol. 5, Oct 2003, pp. 3316–3320 Vol.5.

[14] U. Jakobsen, "Hybrid switch reluctance drives for pump applications," Ph.D. dissertation, 2011.

[15] W. Yeadon and A. Yeadon, *Handbook of Small Electric Motors*. McGraw-Hill Education, 2001. [Online]. Available: https://books.google.at/books?id=TsXEHPofiAYC

[16] M. Miyamasu and K. Akatsu, "Efficiency comparison between brushless dc motor and brushless ac motor considering driving method and machine design," in *IECON 2011 - 37th Annual Conference on IEEE Industrial Electronics Society*, Nov 2011, pp. 1830–1835.

[17] G.-J. Su and J. McKeever, "Low-cost sensorless control of brushless dc motors with improved speed range," *Power Electronics, IEEE Transactions on*, vol. 19, no. 2, pp. 296–302, March 2004.

[18] B. Singh and S. Singh, "State of the art on permanent magnet brushless dc motor drives," *Journal of Power Electronics*, pp. 1–17, 2009.

[19] P. Pillay and R. Krishnan, "Application characteristics of permanent magnet synchronous and brushless dc motors for servo drives," *Industry Applications, IEEE Transactions on*, vol. 27, no. 5, pp. 986–996, Sep 1991.

[20] M. Fazil and K. Rajagopal, "Development of external rotor single-phase pm bldc motor based drive for ceiling fan," in *Power Electronics, Drives and Energy Systems (PEDES) 2010 Power India, 2010 Joint International Conference on*, Dec 2010, pp. 1–4.

[21] M. Fazil and K. R. Rajagopal, "Nonlinear dynamic modeling of a single-phase permanent-magnet brushless dc motor using 2-d static finite-element results," *Magnetics, IEEE Transactions on*, vol. 47, no. 4, pp. 781–786, April 2011.

[22] J. Mayer and O. Wasynczuk, "Analysis and modeling of a single-phase brushless dc motor drive system," *Power Engineering Review, IEEE*, vol. 9, no. 9, pp. 49–49, Sept 1989.

[23] C. L. Chiu, Y. T. Chen, and W. S. Jhang, "Properties of cogging torque, starting torque, and electrical circuits for the single-phase brushless dc motor," *Magnetics, IEEE Transactions on*, vol. 44, no. 10, pp. 2317–2323, Oct. 2008.

[24] S. Bentouati, Z. Zhu, and D. Howe, "Influence of design parameters on the starting torque of a single-phase PM brushless dc motor," *Magnetics, IEEE Transactions on*, vol. 36, no. 5, pp. 3533–3536, Sep. 2000.

[25] M. Fazil and K. R. Rajagopal, "A novel air-gap profile of single-phase permanent-magnet brushless dc motor for starting torque improvement and cogging torque reduction," *Magnetics, IEEE Transactions on*, vol. 46, no. 11, pp. 3928–3932, Nov 2010.

[26] S. Ahmed, "Investigations into the improvement of a single phase permanent magnet brushless dc motor," Ph.D. dissertation, Department of Engineering of the University of Leicester, 2011. [Online]. Available: https://lra.le.ac.uk/bitstream/2381/10114/1/Saeed_Final.pdf

[27] T. Ericsen, "The second electronic revolution (it's all about control)," *Industry Applications, IEEE Transactions on*, vol. 46, no. 5, pp. 1778–1786, Sept 2010.

[28] Danfoss, "VLT®DriveMotor FCM 300," http://vlt-drives.danfoss.de/produkte/frequenzumrichter-motoren/vlt-drivemotor-fcm-300/, January 2016, accessed on 15-01-2016.

[29] ECN, "The end of sensored BLDC control?" http://www.ecnmag.com/article/2012/04/end-sensored-bldc-control, January 2016, accessed on 15-01-2016.

[30] W. Wang, Z. Wu, W. Jin, and J. Ying, "Sensorless control technology for single phase bldcm based on the winding time-sharing method," in *Industrial Electronics Society, 2005. IECON 2005. 31st Annual Conference of IEEE*, Nov 2005, pp. 5 pp.–.

[31] H.-W. Kim, K.-T. Kim, Y.-S. Jo, and J. Hur, "Optimization methods of torque density for developing the neodymium free spoke-type bldc motor," *Magnetics, IEEE Transactions on*, vol. 49, no. 5, pp. 2173–2176, May 2013.

[32] B. kuk Lee, G.-H. Kang, J. Hur, and D.-W. You, "Design of spoke type bldc motors with high power density for traction applications," in *Industry Applications Conference, 2004. 39th IAS Annual Meeting. Conference Record of the 2004 IEEE*, vol. 2, Oct 2004, pp. 1068–1074 vol.2.

[33] F. Magnussen and H. Lendenmann, "Parasitic effects in pm machines with concentrated windings," *Industry Applications, IEEE Transactions on*, vol. 43, no. 5, pp. 1223–1232, Sept 2007.

[34] D. Ishak, Z. Zhu, and D. Howe, "Comparison of pm brushless motors, having either all teeth or alternate teeth wound," *Energy Conversion, IEEE Transactions on*, vol. 21, no. 1, pp. 95–103, March 2006.

[35] J. Wang, Z. Xia, and D. Howe, "Analysis of three-phase surface-mounted magnet modular permanent magnet machines," in *Power Electronics, Machines and Drives, 2004. (PEMD 2004). Second International Conference on (Conf. Publ. No. 498)*, vol. 3, March 2004, pp. 27–32.

[36] H. Dogan, F. Wurtz, A. Foggia, and L. Garbuio, "Analysis of slot-pole combination of fractional-slots pmsm for embedded applications," in *Electrical Machines and Power Electronics and 2011 Electromotion Joint Conference (ACEMP), 2011 International Aegean Conference on*, Sept 2011, pp. 611–615.

[37] W. Ouyang, *Modular Permanent Magnet Machine Drive System with Fault Tolerant Capability*. University of Wisconsin–Madison, 2007. [Online]. Available: https://books.google.at/books?id=QsNWZKubbRgC

[38] A. Lelkes and M. Bufe, "Bldc motor for fan application with automatically optimized commutation angle," in *Power Electronics Specialists Conference, 2004. PESC 04. 2004 IEEE 35th Annual*, vol. 3, June 2004, pp. 2277–2281 Vol.3.

[39] L. Iepure, I. Boldea, and F. Blaabjerg, "Hybrid i-f starting and observer-based sensorless control of single-phase bldc-pm motor drives," *Industrial Electronics, IEEE Transactions on*, vol. 59, no. 9, pp. 3436–3444, Sept 2012.

[40] JSOL Corporation, "Simulation Technology for Electromechanical Design," https://www.jmag-international.com/, accessed on 16-01-2016.

[41] P. Upadhayay and K. Rajagopal, "Permanent magnet overhang effect in pm bldc motor using 2d amp; 3d finite element analysis," in *Engineering (NUiCONE), 2012 Nirma University International Conference on*, Dec 2012, pp. 1–3.

[42] U. United Magnetics, "Neodymium magnets," http://umag.com.cn/product.asp?aaa=110419154341&bbb=20110419164628, accessed on 10-07-2015.

[43] Tyssen Krupp, "Developing the future," https://www.thyssenkrupp.com/en/index.html, accessed on 10-07-2015.

[44] A. Krings, "Iron losses in electrical machines- influence of material properties,manufacturing processes,and inverter operation," Ph.D. dissertation, Sweden KTH School of Electrical Engineering, Stockholm, Sweden, 2014.

[45] N. Takahashi, H. Morimoto, Y. Yunoki, and D. Miyagi, "Effect of shrink fitting and cutting on iron loss of permanent magnet motor," *Journal of Magnetism and Magnetic Materials*, vol. 320, no. 20, pp. e925 – e928, 2008, proceedings of the 18th International Symposium on Soft Magnetic Materials. [Online]. Available: http://www.sciencedirect.com/science/article/pii/S0304885308005283

[46] A. Schoppa, J. Schneider, and C.-D. Wuppermann, "Influence of the manufacturing process on the magnetic properties of non-oriented electrical steels," *Journal of Magnetism and Magnetic Materials*, vol. 216, pp. 74 – 78, 2000. [Online]. Available: http://www.sciencedirect.com/science/article/pii/S0304885300000706

[47] M. Bali and A. Muetze, "Influences of CO2 and FKL-laser cutting as well as mechanical cutting on the magnetic properties of electric steel sheets determined by epstein frame and stator lamination stack measurements," in *Energy Conversion Congress and Exposition (ECCE), 2014 IEEE*, Sept 2014, pp. 1443–1450.

[48] Joseph J. Stupak Jr. ,Oersted Technology Corp., "Methods of magnetizing permanent magnets," (pdf)-http://http://oersted.com/magnetizing.PDF, October 2000, accessed on 16-11-2015.

[49] S. Dunkl, A. Muetze, and G. Schoener, "Multi-domain modelling of a small single-phase brushless dc fan motor drive," in *Electric Machines Drives Conference (IEMDC), 2013 IEEE International*, May 2013, pp. 1310–1315.

[50] Gecko Research, "Power Electronics Simulation Software," http://www.gecko-research.com, accessed on 16-01-2016.

[51] O. Mohammed, S. Liu, and Z. Liu, "A phase variable model of brushless dc motors based on finite element analysis and its coupling with external circuits," *Magnetics, IEEE Transactions on*, vol. 41, no. 5, pp. 1576–1579, May 2005.

[52] Y. Guo, J. Zhu, and H. Lu, "Accurate determination of parameters of a claw-pole motor with smc stator core by finite-element magnetic-field analysis," *Electric Power Applications, IEE Proceedings* -, vol. 153, no. 4, pp. 568–574, July 2006.

[53] J. Walker, D. Dorrell, and C. Cossar, "Flux-linkage calculation in permanent-magnet motors using the frozen permeabilities method," *Magnetics, IEEE Transactions on*, vol. 41, no. 10, pp. 3946–3948, Oct 2005.

[54] N. Demerdash and T. Nehl, "Electric machinery parameters and torques by current and energy perturbations from field computations. i. theory and formulation," *Energy Conversion, IEEE Transactions on*, vol. 14, no. 4, pp. 1507–1513, Dec 1999.

[55] I. Gyimesi and D. Ostergaard, "Inductance computation by incremental finite element analysis," *Magnetics, IEEE Transactions on*, vol. 35, no. 3, pp. 1119–1122, May 1999.

[56] W. Chu and Z. Zhu, "Average torque separation in permanent magnet synchronous machines using frozen permeability," *Magnetics, IEEE Transactions on*, vol. 49, no. 3, pp. 1202–1210, March 2013.

[57] Z. Zhu, Y. Chen, Y. Li, D. Howe, and J. Gliemann, "Dynamic modelling of a high-speed single-phase pm brushless dc drive," in *Power Electronics, Machines and Drives, 2006. The 3rd IET International Conference on*, April 2006, pp. 484–488.

[58] MathWorks, "Accelerating the pace of engineering and science," http://www.mathworks.de/index.html, accessed on 16-01-2016.

[59] E. Stamper and R. Koral, *Handbook of Air Conditioning, Heating, and Ventilating*. Industr. Press, 1979. [Online]. Available: http://books.google.at/books?id=G47biva6gtwC

[60] G. Kumbhar, S. Kulkarni, R. Escarela-Perez, and E. Campero-Littlewood, "Applications of coupled field formulations to electrical machinery," *COMPEL: The International Journal for Computation and Mathematics in Electrical and Electronic Engineering,*, vol. 26, no. 2, pp. .489 – 523, 2007.

[61] B. Asghari, V. Dinavahi, M. Rioual, J. Martinez, and R. Iravani, "Interfacing techniques for electromagnetic field and circuit simulation programs ieee task force on interfacing techniques for simulation tools," *Power Delivery, IEEE Transactions on*, vol. 24, no. 2, pp. 939–950, 2009.

[62] G. Jang, J. Chang, D. P. Hong, and K. Kim, "Finite-element analysis of an electromechanical field of a bldc motor considering speed control and mechanical flexibility," *Magnetics, IEEE Transactions on*, vol. 38, no. 2, pp. 945–948, 2002.

[63] S. Kanerva, "Simulation of electrical machines, circuits and control systems using finite element method and system simulator," Ph.D. dissertation, Helsinki University of Technology, Espoo, Finland, 2005.

[64] S. Dunkl, A. Muetze, and G. Schoener, "Design constraints of small single-phase permanent magnet brushless dc drives for fan applications," *Industry Applications, IEEE Transactions on*, vol. 51, no. 4, pp. 3178–3186, July 2015.

[65] L. G. Cravero, "Entwurf, Auslegung und Betriebsverhalten von dauermagneterregten buerstenlosen Motoren kleiner Leistung," Ph.D. dissertation, Fakultaet fuer Elektrotechnik und Informationstechnik der Technische Universitaet Ilmenau, 2005.

[66] B. Hu, S. Sathiakumar, and Y. Shrivastava, "180-degree commutation system of permanent magnet brushless dc motor drive based on speed and current control," in *Intelligent Computation Technology and Automation, 2009. ICICTA '09. Second International Conference on*, vol. 1, Oct 2009, pp. 723–726.

[67] Q. Han, N. Samoylenko, and J. Jatskevich, "Comparison of brushless dc motor drives with 180/120-degree inverter systems," in *Electrical and Computer Engineering, 2007. CCECE 2007. Canadian Conference on*, April 2007, pp. 111–114.

[68] T.-Y. Lee, J.-Y. Song, J. Kim, Y.-J. Kim, S.-Y. Jung, and J.-M. Je, "Phase advance control to reduce torque ripple of brushless dc motor acceleratingording to winding connection, wye and delta," *Electrical Engineering & Technology, Journal of*, vol. 9, no. 6, pp. 2201–2208, 2014.

[69] S.-I. Park, T.-S. Kim, S.-C. Ahn, and D. seok Hyun, "An improved current control method for torque improvement of high-speed bldc motor," in *Applied Power Electronics Conference and Exposition, 2003. APEC '03. Eighteenth Annual IEEE*, vol. 1, Feb 2003, pp. 294–299 vol.1.

[70] S.-M. Sue, K.-L. Wu, J.-S. Syu, and K.-C. Lee, "A phase advanced commutation scheme for ipm-bldc motor drives," in *Industrial Electronics and Applications, 2009. ICIEA 2009. 4th IEEE Conference on*, May 2009, pp. 2010–2013.

[71] C.-L. Chiu, Y.-T. Chen, Y.-L. Liang, and R.-H. Liang, "Optimal driving efficiency design for the single-phase brushless dc fan motor," *Magnetics, IEEE Transactions on*, vol. 46, no. 4, pp. 1123–1130, April 2010.

[72] C.-L. Chiu, Y.-T. Chen, Y.-H. Shen, and R.-H. Liang, "An accurate automatic phase advance adjustment of brushless dc motor," *Magnetics, IEEE Transactions on*, vol. 45, no. 1, pp. 120–126, Jan 2009.

[73] Z. Zhu, S. Bentouati, and D. Howe, "Control of single-phase permanent magnet brushless dc drives for high-speed applications," in *Power Electronics and Variable Speed Drives, 2000. Eighth International Conference on (IEE Conf. Publ. No. 475)*, 2000, pp. 327–332.

[74] T. Skvarenina, *The Power Electronics Handbook*, ser. Industrial Electronics. Taylor & Francis, 2001. [Online]. Available: http://books.google.at/books?id=xxbvM40Wwa8C

[75] C. G. Kim, J. H. Lee, H. W. Kim, and M.-J. Youn, "Study on maximum torque generation for sensorless controlled brushless dc motor with trapezoidal back emf," *Electric Power Applications, IEE Proceedings -*, vol. 152, no. 2, pp. 277–291, March 2005.

[76] J. Hong, S. Jung, and K. Nam, "An incorporation method of sensorless algorithms: Signal injection and back emf based methods," in *Power Electronics Conference (IPEC), 2010 International*, June 2010, pp. 2743–2747.

[77] A. Stirban, I. Boldea, G. Andreescu, D. Iles, and F. Blaabjerg, "Motion sensorless control of bldc pm motor with offline fem info assisted state observer," in *Optimization of Electrical and Electronic Equipment (OPTIM), 2010 12th International Conference on*, May 2010, pp. 321–328.

[78] J. Shao, D. Nolan, and T. Hopkins, "Improved direct back emf detection for sensorless brushless dc (bldc) motor drives," in *Applied Power Electronics Conference and Exposition, 2003. APEC '03. Eighteenth Annual IEEE*, vol. 1, Feb 2003, pp. 300–305 vol.1.

[79] P. Damodharan and K. Vasudevan, "Sensorless brushless dc motor drive based on the zero-crossing detection of back electromotive force (emf) from the line voltage difference," *Energy Conversion, IEEE Transactions on*, vol. 25, no. 3, pp. 661–668, Sept 2010.

[80] S. Kim, "Modeling and fault analysis of bldc motor based servo actuators for manipulators," in *Robotics and Automation, 2008. ICRA 2008. IEEE International Conference on*, May 2008, pp. 767–772.

[81] Q.-V. Tran, T.-W. Chun, H.-H. Lee, H.-G. Kim, and E.-C. Nho, "Simple starting-up method of bldc sensorless control system for vehicle fuel pump," in *Power Electronics Conference (IPEC), 2010 International*, June 2010, pp. 2244–2248.

[82] W.-J. Lee and S.-K. Sul, "A new starting method of bldc motors without position sensor," *Industry Applications, IEEE Transactions on*, vol. 42, no. 6, pp. 1532–1538, Nov 2006.

[83] M. T. Inc., "The embedded control solutions company," http://www.microchip.com/DevelopmentTools/ProductDetails.aspx?PartNO=DM330021-2, accessed on 08-10-2015.

[84] SKF, "Estimating the frictional moment," http://www.skf.com/group/products/bearings-units-housings/\discretionary-ball-bearings/principles/friction/estimating-frictional-moment/index.html, accessed on 20-10-2015.

List of figures

List of tables

Appendix A

Material Data

A.1 M250-35A - electrical steel sheet

J T	H A/m	B T	$P_{f=50\,Hz}$ W/kg	$P_{f=100\,Hz}$ W/kg	$P_{f=200\,Hz}$ W/kg	$P_{f=400\,Hz}$ W/kg	$P_{f=500\,Hz}$ W/kg	$P_{f=1000\,Hz}$ W/kg	$P_{f=2000\,Hz}$ W/kg
0.2	-	-	-	-	-	0.91	1.27	3.60	10.41
0.3	-	-	-	-	-	1.93	2.65	7.52	21.54
0.4	-	-	-	-	-	3.21	4.44	12.59	37.00
0.5	52	0.52	0.3	0.71	1.80	4.76	6.60	18.79	55.61
0.6	60	0.60	0.4	0.97	2.46	6.57	9.15	26.21	79.02
0.7	69	0.69	0.52	1.25	3.21	8.64	12.06	35.56	107.24
0.8	80	0.80	0.65	1.56	4.04	10.99	15.39	46.03	-
0.9	94	0.90	0.79	1.91	4.96	13.65	19.43	58.25	-
1.0	113	1.00	0.95	2.29	5.99	16.91	23.87	72.36	-
1.1	141	1.10	1.12	2.72	7.13	20.35	28.86	88.91	-
1.2	187	1.20	1.32	3.21	8.45	24.28	34.57	108.16	-
1.3	290	1.30	1.57	3.81	10.02	28.91	41.28	130.45	-
1.4	621	1.40	1.88	4.57	12.19	-	-	-	-
1.5	1723	1.50	2.25	5.46	14.46	-	-	-	-
1.6	3852	1.60	2.53	6.21	-	-	-	-	-
1.7	7060	1.71	2.79	-	-	-	-	-	-
1.8	11809	1.81	3.03	-	-	-	-	-	-
1.9	20611	1.93	-	-	-	-	-	-	-

Table A.1: M250-35A electrical steel sheet's material data.

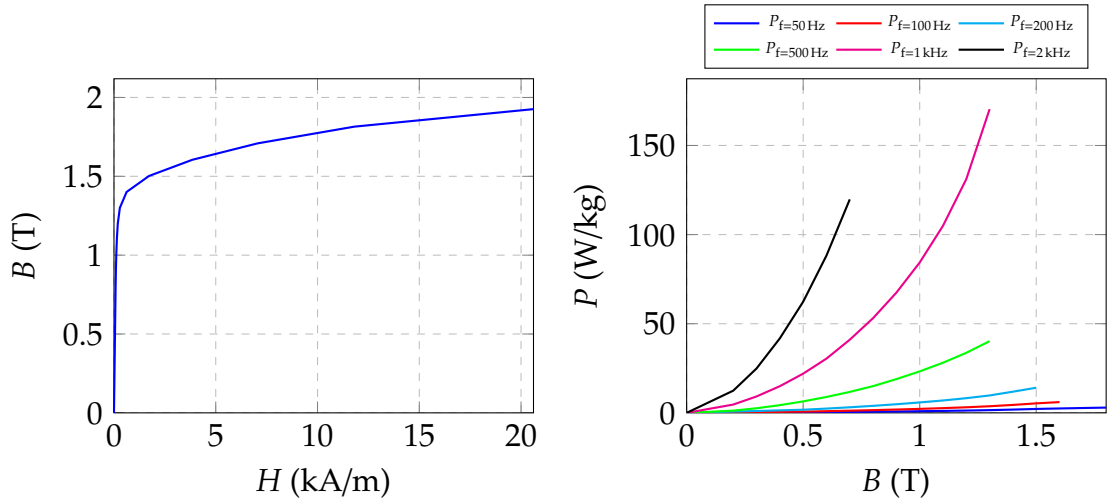

(a) M250-35A magnetization curve.

(b) M250-35A loss curves.

Figure A.1: M250-35A electrical steel sheets material data.

A.2 11SMnPb30 - free cutting steel

H A/m	B T	H A/m	B T	H A/m	B T
0	0	180	0.465	280	0.723
380	0.95	480	1.106	580	1.2
680	1.275	780	1.324	880	1.364
1080	1.422	1280	1.467	1480	1.496
1680	1.519	1880	1.54	2380	1.578
2880	1.608	3380	1.631	3880	1.65
4880	1.682	5880	1.71	7880	1.758
9880	1.8	14880	1.886	19880	1.95

Table A.2: 11SMnPb30 material data.

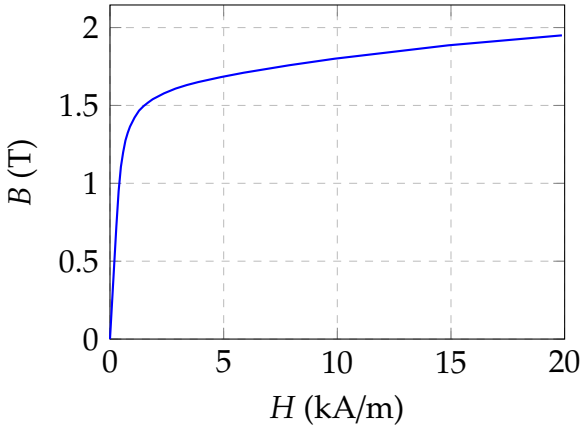

Figure A.2: 11SMnPb30 material data.

Appendix B

Measurement results

B.1 Efficiency comparison of pump drive

The following tables show measured as well as simulated results for the pump drive. For the simulation results the hybrid BLDC model from Section 2.3 was used.

measured																				calculated				
T_{AVG} (mNm)	$T_{b,AVG}$ (mNm)	n_{AVG} (rpm)	$U_{DC,AVG}$ (V)	$I_{DC,AVG}$ (A)	$U_{A,RMS}$ (V)	$I_{A,RMS}$ (A)	$U_{B,RMS}$ (V)	$I_{B,RMS}$ (A)	$U_{C,RMS}$ (V)	$I_{C,RMS}$ (A)	P_{in} (W)	P_A (W)	P_B (W)	P_C (W)	P_{out} (W)	T_W (°C)	T_S (°C)	T_H (°C)	T_A (°C)	P_{Cu} (W)	P_{Fe} (W)	$\eta_{control}$ (%)	η_{BLDC} (%)	η_{total} (%)
0	1.0	629	12.02	0.03	2.34	0.06	2.26	0.08	2.29	0.10	0.37	0.05	0.06	0.07	0.06	20.8	-	-	-	0.01	0.11	48	36	17
0	1.1	922	12.02	0.04	2.81	0.08	2.72	0.08	2.74	0.11	0.48	0.08	0.08	0.11	0.11	20.9	-	-	-	0.01	0.16	58	39	23
0	1.3	1330	12.02	0.06	3.38	0.11	3.28	0.08	3.29	0.13	0.66	0.14	0.12	0.19	0.18	20.9	-	-	-	0.02	0.25	68	41	28
0	1.5	1737	12.00	0.07	3.90	0.12	3.78	0.08	3.78	0.15	0.83	0.21	0.14	0.27	0.27	21.0	-	-	-	0.02	0.34	74	43	32
0	1.6	2145	12.01	0.09	4.36	0.14	4.23	0.08	4.23	0.16	1.03	0.29	0.16	0.36	0.35	21.2	-	-	-	0.02	0.43	79	44	35
0	1.7	2540	12.01	0.10	4.76	0.16	4.63	0.08	4.62	0.15	1.20	0.39	0.17	0.42	0.45	21.4	-	-	-	0.02	0.51	82	46	37
0	1.8	2944	12.02	0.12	5.15	0.17	5.02	0.08	5.00	0.16	1.40	0.49	0.19	0.50	0.55	21.8	-	-	-	0.03	0.60	84	47	39
0	1.9	3354	12.02	0.13	5.51	0.18	5.38	0.09	5.34	0.16	1.58	0.59	0.21	0.56	0.66	22.1	-	-	-	0.03	0.67	86	49	42
0	2.0	3753	12.02	0.15	5.85	0.18	5.72	0.09	5.67	0.16	1.76	0.69	0.23	0.63	0.77	22.3	-	-	-	0.03	0.75	88	50	44
0	2.0	4155	12.02	0.17	6.17	0.19	6.04	0.09	5.98	0.16	1.97	0.80	0.26	0.70	0.88	22.8	-	-	-	0.03	0.84	89	50	45
0	2.1	4560	12.02	0.18	6.47	0.19	6.35	0.09	6.27	0.16	2.16	0.90	0.28	0.76	0.99	23.1	-	-	-	0.03	0.92	90	51	46
0	2.1	4960	12.03	0.20	6.77	0.20	6.64	0.09	6.55	0.16	2.32	0.99	0.30	0.82	1.11	23.6	-	-	-	0.03	0.97	91	53	48
0	2.2	5380	12.03	0.22	7.06	0.20	6.94	0.10	6.83	0.16	2.56	1.11	0.34	0.90	1.23	24.0	-	-	-	0.03	1.08	92	53	48
0	2.2	5779	12.02	0.23	7.33	0.20	7.21	0.10	7.08	0.17	2.75	1.20	0.37	0.97	1.35	24.4	-	-	-	0.04	1.16	93	53	49
0	2.3	5978	12.02	0.24	7.46	0.20	7.35	0.10	7.21	0.16	2.82	1.25	0.38	0.98	1.41	24.8	-	-	-	0.04	1.17	93	54	50
0.0	2.4	8122	12.03	0.34	9.02	0.23	8.92	0.12	8.69	0.18	4.09	1.95	0.68	1.40	2.05	26.6	-	-	-	0.04	1.94	99	51	50
3.5	0.9	539	12.05	0.06	2.37	0.16	2.31	0.18	2.35	0.18	0.77	0.13	0.13	0.13	0.25	24.3	24.0	24.0	20.8	0.04	0.10	51	63	32
4.0	1.2	998	12.05	0.10	3.09	0.21	3.00	0.18	3.03	0.22	1.15	0.26	0.22	0.27	0.54	24.2	24.1	24.0	20.8	0.06	0.15	65	72	47
3.8	1.4	1434	12.05	0.13	3.68	0.22	3.57	0.18	3.60	0.25	1.50	0.38	0.30	0.41	0.78	24.2	24.1	24.0	20.8	0.06	0.24	72	72	52
4.1	1.5	1769	12.05	0.15	4.12	0.22	3.98	0.19	4.00	0.27	1.79	0.45	0.38	0.54	1.03	24.4	24.2	23.7	20.8	0.07	0.28	77	75	57
4.3	1.6	2186	12.05	0.18	4.55	0.26	4.43	0.19	4.43	0.27	2.17	0.65	0.44	0.65	1.34	24.6	24.3	23.7	20.8	0.08	0.33	80	77	62
4.6	1.7	2651	12.05	0.21	5.02	0.28	4.89	0.19	4.89	0.27	2.57	0.83	0.52	0.79	1.76	24.9	24.5	23.7	20.8	0.08	0.31	84	82	68
4.3	1.8	3052	12.05	0.24	5.39	0.29	5.25	0.19	5.24	0.27	2.92	0.99	0.60	0.91	1.95	25.1	24.6	23.6	20.9	0.09	0.47	86	78	67
4.5	1.9	3404	12.05	0.28	5.70	0.31	5.57	0.20	5.54	0.28	3.32	1.16	0.70	1.04	2.27	25.3	24.7	23.6	20.8	0.10	0.53	87	78	68
4.5	2.0	3837	12.05	0.31	6.05	0.32	5.92	0.21	5.87	0.28	3.72	1.35	0.79	1.16	2.61	25.6	25.1	23.6	20.8	0.10	0.59	89	79	70
4.5	2.0	4231	12.05	0.33	6.34	0.31	6.22	0.20	6.15	0.27	3.91	1.46	0.83	1.24	2.89	25.9	25.4	23.8	20.8	0.10	0.54	90	82	74
4.3	2.1	4616	12.05	0.36	6.64	0.33	6.50	0.21	6.43	0.28	4.36	1.65	0.94	1.38	3.11	26.3	25.5	23.8	20.9	0.10	0.75	91	78	71
4.3	2.1	5029	12.05	0.39	6.93	0.33	6.80	0.21	6.71	0.28	4.70	1.81	1.02	1.49	3.39	26.6	25.9	24.0	20.8	0.11	0.83	92	78	72
4.1	2.2	5507	12.04	0.42	7.24	0.33	7.13	0.21	7.01	0.28	5.08	1.98	1.11	1.62	3.64	27.1	26.2	24.0	20.8	0.11	0.97	93	77	72
4.3	2.3	6013	12.05	0.48	7.58	0.34	7.46	0.22	7.33	0.29	5.70	2.24	1.28	1.82	4.13	27.6	26.6	24.2	20.8	0.12	1.09	94	77	72

Table B.1: Results of efficiency measurements I.

measured																				calculated				
T_{AVG} (mNm)	$T_{b,AVG}$ (mNm)	n_{AVG} (rpm)	$U_{DC,AVG}$ (V)	$I_{DC,AVG}$ (A)	$U_{A,RMS}$ (V)	$I_{A,RMS}$ (A)	$U_{B,RMS}$ (V)	$I_{B,RMS}$ (A)	$U_{C,RMS}$ (V)	$I_{C,RMS}$ (A)	P_{in} (W)	P_A (W)	P_B (W)	P_C (W)	P_{out} (W)	T_W (°C)	T_S (°C)	T_H (°C)	T_A (°C)	P_{Cu} (W)	P_{Fe} (W)	$\eta_{control}$ (%)	η_{BLDC} (%)	η_{total} (%)
16.6	1.0	677	12.04	0.27	3.02	0.69	2.95	0.61	2.98	0.67	3.26	0.72	0.61	0.67	1.25	25.3	24.8	23.7	21.1	0.59	0.16	61	62	38
19.7	1.2	1051	12.04	0.41	3.70	0.82	3.61	0.72	3.66	0.79	4.85	1.23	1.03	1.13	2.30	25.7	24.9	23.7	21.1	0.83	0.26	70	68	48
17.5	1.4	1475	12.04	0.44	4.19	0.77	4.09	0.65	4.13	0.72	5.26	1.47	1.19	1.32	2.91	25.8	24.9	23.7	21.1	0.69	0.36	76	73	55
19.5	1.5	1794	12.04	0.56	4.65	0.85	4.53	0.72	4.57	0.79	6.62	1.95	1.57	1.73	3.95	26.1	25.1	23.7	21.1	0.85	0.44	79	75	60
17.1	1.6	2210	12.03	0.57	5.01	0.77	4.89	0.64	4.91	0.71	6.72	2.08	1.63	1.81	4.33	26.2	25.3	23.7	21.1	0.69	0.50	82	78	65
17.3	1.7	2426	12.04	0.61	5.23	0.78	5.12	0.65	5.13	0.71	7.21	2.27	1.78	1.97	4.82	26.4	25.4	23.8	21.1	0.69	0.52	84	80	67
16.8	1.8	2774	12.04	0.65	5.55	0.76	5.42	0.63	5.43	0.69	7.71	2.50	1.95	2.14	5.38	26.5	25.5	23.9	21.1	0.66	0.55	85	82	70
16.8	1.8	3177	12.04	0.73	5.90	0.77	5.78	0.64	5.77	0.69	8.62	2.86	2.23	2.44	6.20	26.8	25.8	23.9	21.1	0.67	0.66	87	82	72
17.3	1.9	3405	12.03	0.79	6.11	0.79	5.98	0.66	5.98	0.71	9.37	3.14	2.46	2.67	6.85	27.1	26.0	24.1	21.1	0.71	0.70	88	83	73
16.0	2.0	3797	12.03	0.81	6.39	0.75	6.26	0.62	6.24	0.67	9.58	3.28	2.54	2.76	7.16	27.5	26.3	24.2	21.1	0.64	0.79	90	83	75
16.0	2.0	4185	12.03	0.87	6.69	0.75	6.55	0.62	6.52	0.67	10.40	3.60	2.80	3.03	7.92	27.8	26.5	24.3	21.1	0.64	0.87	91	84	76
16.2	2.1	4605	12.03	0.97	7.00	0.77	6.87	0.64	6.82	0.68	11.49	4.03	3.14	3.38	8.83	28.3	27.0	24.5	21.1	0.67	1.04	92	84	77
17.4	2.1	5015	12.03	1.10	7.33	0.81	7.18	0.68	7.13	0.72	13.13	4.63	3.65	3.88	10.25	28.9	27.5	24.7	21.1	0.76	1.15	93	84	78
19.0	2.2	5364	12.03	1.27	7.61	0.87	7.46	0.73	7.41	0.78	15.08	5.32	4.25	4.48	11.93	29.4	28.0	24.9	21.1	0.88	1.24	93	85	79
19.5	2.2	5784	12.03	1.38	7.89	0.89	7.73	0.75	7.67	0.80	16.43	5.83	4.68	4.92	13.14	30.0	28.4	25.1	21.1	0.92	1.36	94	85	80
18.3	2.3	6023	12.03	1.36	8.01	0.85	7.85	0.72	7.78	0.76	16.19	5.78	4.62	4.86	12.95	30.4	28.6	25.2	21.1	0.84	1.46	94	85	80
25.7	0.9	532	12.04	0.41	3.09	1.00	3.00	0.92	3.07	0.98	4.85	1.04	0.92	0.98	1.48	26.4	25.2	24.2	21.1	1.27	0.19	61	50	31
26.2	1.2	1046	12.04	0.56	3.90	1.05	3.80	0.93	3.86	1.01	6.55	1.68	1.43	1.55	3.00	27.1	25.8	24.2	21.2	1.36	0.29	71	64	46
24.0	1.4	1462	12.03	0.61	4.40	0.99	4.29	0.86	4.34	0.94	7.20	2.01	1.67	1.82	3.88	27.4	26.1	24.4	21.2	1.19	0.43	76	71	54
25.3	1.5	1818	12.03	0.73	4.85	1.04	4.73	0.90	4.78	0.98	8.60	2.51	2.08	2.26	5.10	27.8	26.3	24.4	21.2	1.31	0.44	80	75	59
26.6	1.6	2164	12.03	0.87	5.27	1.09	5.14	0.95	5.19	1.03	10.20	3.09	2.55	2.75	6.39	28.4	26.7	24.6	21.2	1.45	0.55	82	76	63
26.1	1.7	2613	12.03	0.96	5.70	1.08	5.56	0.93	5.60	1.00	11.33	3.56	2.92	3.13	7.61	28.6	27.0	24.7	21.2	1.40	0.61	85	79	67
24.6	1.8	2949	12.03	1.02	5.99	1.05	5.85	0.91	5.89	0.97	12.01	3.86	3.16	3.38	8.15	28.9	27.2	24.8	21.2	1.32	0.92	87	78	68
25.5	1.9	3402	12.03	1.15	6.38	1.07	6.23	0.92	6.25	0.99	13.53	4.43	3.63	3.86	9.76	29.4	27.7	25.0	21.2	1.37	0.80	88	82	72
26.2	2.0	3775	12.03	1.28	6.70	1.10	6.54	0.95	6.57	1.01	15.08	5.01	4.12	4.36	11.14	29.9	28.0	25.1	21.2	1.45	0.89	89	83	74
26.2	2.0	4219	12.03	1.39	7.03	1.10	6.87	0.95	6.89	1.01	16.43	5.53	4.56	4.80	12.46	30.4	28.5	25.3	21.2	1.45	0.98	91	84	76
26.0	2.1	4594	12.03	1.48	7.30	1.10	7.13	0.95	7.13	1.01	17.53	5.97	4.91	5.16	13.51	30.8	28.8	25.5	21.2	1.45	1.07	91	84	77
26.2	2.1	5032	12.03	1.60	7.60	1.11	7.43	0.96	7.41	1.01	18.99	6.53	5.38	5.63	14.91	31.3	29.3	25.7	21.2	1.47	1.16	92	85	79
25.0	2.2	5381	12.03	1.62	7.79	1.07	7.62	0.92	7.60	0.97	19.24	6.67	5.50	5.73	15.31	31.5	29.5	25.8	21.2	1.37	1.22	93	86	80
26.5	2.2	5789	12.02	1.83	8.11	1.13	7.93	0.97	7.90	1.03	21.74	7.56	6.28	6.53	17.43	32.1	29.8	26.0	21.2	1.53	1.40	94	86	80
23.1	2.3	6038	12.03	1.66	8.17	1.01	8.00	0.87	7.95	0.91	19.77	6.96	5.71	5.94	16.02	32.2	30.0	26.1	21.2	1.22	1.38	94	86	81

Table B.2: Results of efficiency measurements II.

measured																					calculated				
T_{AVG} (mNm)	$T_{b,AVG}$ (mNm)	n_{AVG} (rpm)	$U_{DC,AVG}$ (V)	$I_{DC,AVG}$ (A)	$U_{A,RMS}$ (V)	$I_{A,RMS}$ (A)	$U_{B,RMS}$ (V)	$I_{B,RMS}$ (A)	$U_{C,RMS}$ (V)	$I_{C,RMS}$ (A)	P_{in} (W)	P_A (W)	P_B (W)	P_C (W)	P_{out} (W)	T_W (°C)	T_S (°C)	T_H (°C)	T_A (°C)	P_{Cu} (W)	P_{Fe} (W)	$\eta_{control}$ (%)	η_{BLDC} (%)	η_{total} (%)
29.6	0.9	523	12.00	0.48	3.19	1.13	3.10	1.04	3.17	1.11	5.65	1.24	1.11	1.18	1.67	23.4	21.9	20.3	20.0	1.61	0.24	62	47	30
31.0	1.1	915	12.01	0.64	3.87	1.20	3.75	1.09	3.82	1.16	7.45	1.87	1.62	1.74	3.08	24.6	23.0	20.8	20.1	1.80	0.35	70	59	41
31.3	1.3	1387	12.01	0.79	4.52	1.23	4.39	1.10	4.47	1.18	9.23	2.55	2.17	2.34	4.74	25.8	24.0	21.3	20.1	1.86	0.45	76	67	51
30.0	1.5	1833	12.01	0.90	5.03	1.21	4.89	1.06	4.96	1.15	10.48	3.08	2.58	2.78	6.05	26.2	24.4	21.7	20.1	1.78	0.61	80	72	58
29.9	1.6	2225	12.02	1.02	5.45	1.22	5.31	1.07	5.37	1.15	11.90	3.62	3.02	3.24	7.35	26.8	24.9	22.0	20.1	1.80	0.73	83	74	62
29.7	1.7	2640	12.02	1.13	5.85	1.21	5.70	1.06	5.75	1.13	13.21	4.15	3.44	3.68	8.70	27.4	25.5	22.4	20.2	1.78	0.80	85	77	66
30.7	1.8	3009	12.02	1.29	6.23	1.26	6.07	1.10	6.12	1.17	15.16	4.85	4.04	4.29	10.26	28.0	25.9	22.6	20.1	1.91	1.02	87	78	68
29.9	1.9	3404	12.02	1.37	6.53	1.24	6.38	1.08	6.42	1.15	16.14	5.26	4.38	4.63	11.35	28.6	26.4	22.9	20.2	1.84	1.08	88	80	70
30.3	2.0	3777	12.02	1.50	6.83	1.25	6.67	1.09	6.71	1.16	17.61	5.81	4.85	5.12	12.74	29.1	26.9	23.2	20.3	1.88	1.15	90	81	72
30.8	2.0	4179	12.02	1.65	7.15	1.27	6.98	1.11	7.00	1.18	19.39	6.47	5.41	5.68	14.38	29.9	27.5	23.6	20.3	1.95	1.24	91	82	74
30.3	2.1	4620	12.02	1.75	7.45	1.25	7.27	1.09	7.29	1.16	20.64	6.98	5.83	6.11	15.66	30.5	28.1	24.0	20.5	1.91	1.35	92	83	76
31.1	2.1	4989	12.02	1.91	7.72	1.28	7.54	1.12	7.54	1.19	22.57	7.67	6.44	6.72	17.37	31.2	28.6	24.3	20.5	2.00	1.46	92	83	77
31.1	2.2	5479	12.02	2.06	8.05	1.28	7.85	1.12	7.85	1.19	24.35	8.35	7.02	7.31	19.10	31.9	29.2	24.7	20.5	2.01	1.57	93	84	78
31.1	2.3	5970	12.01	2.22	8.44	1.29	8.23	1.13	8.22	1.19	26.27	9.08	7.66	7.95	20.86	32.4	29.7	24.9	20.4	2.03	1.80	94	84	79
37.7	0.9	495	12.04	0.66	3.41	1.41	3.30	1.32	3.39	1.39	7.81	1.74	1.56	1.67	2.00	27.8	25.5	22.9	20.5	2.60	0.37	64	40	26
36.7	1.2	1055	12.04	0.85	4.25	1.41	4.13	1.28	4.21	1.37	9.91	2.57	2.23	2.41	4.18	28.5	26.0	23.0	20.5	2.52	0.51	73	58	42
37.3	1.3	1324	12.04	1.00	4.76	1.43	4.62	1.29	4.71	1.38	11.64	3.22	2.76	2.98	5.36	29.3	26.7	23.4	20.5	2.59	1.01	77	60	46
37.0	1.5	1831	12.03	1.15	5.24	1.44	5.10	1.28	5.17	1.38	13.34	3.88	3.30	3.55	7.38	29.7	27.1	23.7	20.6	2.60	0.76	80	69	55
37.6	1.6	2210	12.03	1.32	5.67	1.47	5.53	1.30	5.59	1.40	15.29	4.60	3.90	4.18	9.07	30.6	27.8	24.0	20.6	2.69	0.92	83	72	59
36.1	1.7	2599	12.03	1.39	6.00	1.43	5.85	1.26	5.92	1.35	16.21	5.02	4.23	4.52	10.30	30.8	28.1	24.3	20.6	2.52	0.94	85	75	64
38.2	1.8	3064	12.03	1.67	6.50	1.50	6.34	1.33	6.40	1.41	19.42	6.15	5.22	5.53	12.82	31.9	28.9	24.7	20.6	2.79	1.28	87	76	66
37.0	1.9	3385	12.03	1.72	6.73	1.46	6.56	1.29	6.61	1.37	20.07	6.45	5.45	5.77	13.79	32.1	29.2	24.9	20.6	2.65	1.23	88	78	69
37.0	2.0	3756	12.03	1.86	7.04	1.46	6.87	1.29	6.91	1.37	21.75	7.09	6.00	6.33	15.30	32.5	29.5	25.2	20.7	2.66	1.45	89	79	70
38.9	2.0	4115	12.03	2.10	7.35	1.53	7.18	1.35	7.22	1.44	24.62	8.08	6.88	7.24	17.61	33.2	30.0	25.4	20.7	2.93	1.66	90	79	72
37.7	2.1	4533	12.02	2.18	7.61	1.49	7.43	1.32	7.46	1.40	25.55	8.49	7.22	7.57	18.88	33.6	30.4	25.7	20.7	2.77	1.63	91	81	74
37.5	2.1	4918	12.03	2.31	7.88	1.49	7.69	1.31	7.71	1.40	27.21	9.11	7.76	8.12	20.43	34.1	30.8	25.9	20.7	2.77	1.80	92	82	75
37.4	2.2	5422	12.03	2.49	8.23	1.49	8.03	1.31	8.04	1.39	29.28	9.89	8.45	8.81	22.48	34.7	31.3	26.1	20.7	2.77	1.91	93	83	77
36.4	2.3	5939	12.02	2.59	8.67	1.45	8.44	1.28	8.45	1.36	30.56	10.43	8.91	9.27	24.01	35.4	31.9	26.5	20.8	2.65	1.96	94	84	79

Table B.3: Results of efficiency measurements III.

measured																				calculated				
T_{AVG} (mNm)	$T_{b,AVG}$ (mNm)	n_{AVG} (rpm)	$U_{DC,AVG}$ (V)	$I_{DC,AVG}$ (A)	$U_{A,RMS}$ (V)	$I_{A,RMS}$ (A)	$U_{B,RMS}$ (V)	$I_{B,RMS}$ (A)	$U_{C,RMS}$ (V)	$I_{C,RMS}$ (A)	P_{in} (W)	P_A (W)	P_B (W)	P_C (W)	P_{out} (W)	T_W (°C)	T_S (°C)	T_H (°C)	T_A (°C)	P_{Cu} (W)	P_{Fe} (W)	$\eta_{control}$ (%)	η_{BLDC} (%)	η_{total} (%)
46.2	0.9	499	12.04	0.94	3.81	1.71	3.70	1.60	3.79	1.68	10.93	2.57	2.32	2.46	2.46	32.3	28.7	24.4	20.9	3.88	1.01	67	33	23
43.5	1.2	976	12.04	1.05	4.41	1.63	4.29	1.50	4.37	1.59	12.20	3.17	2.78	2.98	4.57	32.4	29.0	24.9	21.0	3.47	0.90	73	51	37
44.4	1.4	1457	12.04	1.32	5.13	1.68	5.00	1.52	5.08	1.63	15.29	4.29	3.71	4.00	6.98	33.5	30.0	25.4	21.0	3.66	1.37	79	58	46
44.6	1.5	1884	12.04	1.52	5.63	1.69	5.49	1.52	5.57	1.63	17.59	5.16	4.44	4.77	9.10	34.0	30.4	25.7	21.0	3.69	1.58	82	63	52
43.7	1.6	2199	12.04	1.54	5.75	1.67	5.61	1.49	5.68	1.60	17.82	5.29	4.54	4.87	10.43	35.5	31.7	26.9	21.0	3.58	0.70	83	71	58
44.5	1.7	2666	12.03	1.78	6.23	1.71	6.07	1.52	6.14	1.63	20.64	6.32	5.40	5.79	12.89	35.8	31.8	27.0	20.9	3.74	0.88	85	74	62
44.6	1.8	3142	12.03	1.98	6.64	1.70	6.48	1.52	6.54	1.63	22.96	7.18	6.17	6.57	15.28	36.2	32.1	27.2	21.0	3.73	0.91	87	77	67
45.6	1.9	3440	12.03	2.16	6.91	1.74	6.74	1.56	6.80	1.66	25.10	7.94	6.82	7.26	17.10	36.3	32.2	27.1	20.9	3.90	1.02	88	78	68
44.4	2.0	3833	12.03	2.26	7.19	1.70	7.01	1.52	7.07	1.62	26.31	8.45	7.25	7.69	18.62	36.6	32.5	27.3	20.9	3.72	1.05	89	80	71
45.2	2.0	4217	12.02	2.47	7.49	1.73	7.31	1.55	7.35	1.65	28.83	9.35	8.04	8.51	20.85	37.0	33.0	27.5	21.0	3.86	1.19	90	80	72
45.1	2.1	4629	12.02	2.64	7.78	1.73	7.58	1.54	7.62	1.65	30.91	10.13	8.72	9.20	22.90	37.5	33.4	27.7	21.0	3.87	1.29	91	82	74
45.0	2.1	5005	12.02	2.79	8.03	1.73	7.83	1.54	7.86	1.64	32.65	10.79	9.30	9.80	24.70	38.0	33.8	27.9	21.0	3.85	1.35	92	83	76
45.1	2.2	5532	12.02	3.02	8.48	1.73	8.25	1.54	8.28	1.65	35.43	11.83	10.21	10.72	27.39	38.9	34.4	28.1	21.0	3.88	1.49	92	84	77
44.7	2.3	5883	12.02	3.11	8.86	1.72	8.62	1.54	8.65	1.64	36.50	12.40	10.73	11.25	28.90	39.3	34.8	28.4	21.1	3.85	1.64	94	84	79
51.1	0.9	517	12.04	1.05	3.80	1.89	3.68	1.78	3.78	1.87	12.27	2.85	2.59	2.76	2.82	38.2	33.5	28.4	21.1	4.89	0.49	67	34	23
51.4	1.2	1047	12.04	1.32	4.58	1.91	4.46	1.76	4.55	1.87	15.22	3.95	3.51	3.77	5.77	38.5	33.8	28.4	21.2	4.90	0.56	74	51	38
52.6	1.3	1285	12.04	1.49	4.94	1.96	4.80	1.80	4.89	1.92	17.20	4.63	4.08	4.39	7.26	38.8	33.9	28.5	21.1	5.17	0.67	76	55	42
50.1	1.5	1835	12.04	1.66	5.52	1.88	5.38	1.71	5.47	1.83	19.14	5.48	4.76	5.14	9.91	38.6	34.0	28.6	20.9	4.71	0.75	80	64	52
50.8	1.6	2225	12.03	1.88	5.94	1.91	5.79	1.73	5.88	1.85	21.65	6.38	5.53	5.97	12.21	39.0	34.3	28.6	20.8	4.83	0.84	83	68	56
50.3	1.7	2663	12.03	2.05	6.35	1.89	6.19	1.70	6.27	1.83	23.70	7.19	6.21	6.68	14.51	39.3	34.5	28.7	20.8	4.71	0.85	85	72	61
50.7	1.8	3161	12.03	2.32	6.79	1.91	6.62	1.72	6.69	1.84	26.85	8.32	7.21	7.72	17.39	39.8	34.9	28.8	20.8	4.82	1.04	87	75	65
51.2	1.9	3404	12.03	2.46	7.00	1.93	6.83	1.74	6.89	1.86	28.52	8.92	7.73	8.27	18.93	40.0	35.2	29.0	20.8	4.91	1.07	87	76	66
50.4	2.0	3832	12.03	2.62	7.31	1.91	7.13	1.71	7.19	1.83	30.41	9.67	8.37	8.92	21.03	40.3	35.3	29.0	20.8	4.78	1.15	89	78	69
49.8	2.0	4244	12.03	2.77	7.60	1.88	7.41	1.69	7.46	1.81	32.22	10.36	8.99	9.55	23.06	40.5	35.5	29.1	20.8	4.66	1.18	90	80	72
49.3	2.1	4633	12.02	2.93	7.87	1.87	7.67	1.68	7.71	1.80	34.13	11.10	9.61	10.20	24.96	40.8	35.8	29.3	20.8	4.61	1.34	91	81	73
51.7	2.1	5014	12.02	3.27	8.20	1.95	7.98	1.75	8.03	1.87	38.10	12.45	10.82	11.48	28.26	41.6	36.4	29.5	20.8	5.03	1.44	91	81	74
51.0	2.2	5652	12.02	3.48	8.84	1.93	8.59	1.73	8.63	1.85	40.72	13.62	11.86	12.55	31.48	42.0	36.7	29.6	20.8	4.92	1.63	93	83	77
59.1	1.2	999	12.04	1.61	4.71	2.19	4.59	2.04	4.70	2.16	18.62	4.81	4.30	4.64	6.30	42.5	36.3	29.2	20.7	6.65	0.79	74	46	34
61.2	1.4	1642	12.03	2.08	5.55	2.27	5.41	2.09	5.51	2.23	23.82	6.63	5.86	6.35	10.76	43.8	37.1	29.5	20.6	7.10	0.97	79	57	45
61.3	1.6	2039	12.03	2.31	5.98	2.27	5.83	2.08	5.92	2.23	26.42	7.59	6.68	7.25	13.41	44.3	37.6	29.7	20.6	7.08	1.02	81	62	51
61.8	1.7	2550	12.03	2.63	6.48	2.29	6.32	2.09	6.41	2.25	30.17	8.94	7.84	8.51	16.95	45.0	38.1	30.0	20.6	7.20	1.14	84	67	56
62.4	1.9	3239	12.02	3.07	7.08	2.31	6.91	2.11	6.99	2.26	35.30	10.78	9.46	10.23	21.81	46.0	38.8	30.3	20.6	7.35	1.31	86	72	62
59.3	2.0	3959	12.02	3.27	7.57	2.21	7.39	2.00	7.45	2.15	37.78	11.87	10.39	11.17	25.41	46.2	39.3	30.7	20.6	6.66	1.36	88	76	67
60.9	2.1	4542	12.02	3.70	8.03	2.26	7.82	2.04	7.88	2.20	42.86	13.65	11.94	12.84	29.93	46.9	39.8	30.9	20.6	6.99	1.51	90	78	70
64.5	2.2	5179	12.01	4.30	8.77	2.38	8.53	2.16	8.59	2.33	49.91	16.19	14.26	15.35	36.14	49.2	41.2	31.5	20.7	7.87	1.79	92	79	72

Table B.4: Results of efficiency measurements IV.

simulated																from measurements				calculated				
T_{AVG} (mNm)	$T_{b,AVG}$ (mNm)	n_{AVG} (rpm)	$U_{DC,AVG}$ (V)	$I_{DC,AVG}$ (A)	$U_{A,RMS}$ (V)	$I_{A,RMS}$ (A)	$U_{B,RMS}$ (V)	$I_{B,RMS}$ (A)	$U_{C,RMS}$ (V)	$I_{C,RMS}$ (A)	P_{in} (W)	P_A (W)	P_B (W)	P_C (W)	P_{out} (W)	T_W (°C)	T_S (°C)	T_H (°C)	T_A (°C)	P_{Cu} (W)	P_{Fe} (W)	$\eta_{control}$ (%)	η_{BLDC} (%)	η_{total} (%)
0.3	1.0	629	12.02	0.03	3.37	0.10	3.36	0.11	3.34	0.06	0.33	0.06	0.08	0.04	0.08	20.8	-	-	-	0.01	0.09	57	45	25
0.2	1.1	919	12.02	0.04	3.73	0.11	3.70	0.12	3.71	0.07	0.43	0.10	0.12	0.06	0.13	20.9	-	-	-	0.01	0.14	65	46	29
0.2	1.3	1294	12.02	0.05	4.17	0.14	4.15	0.14	4.16	0.08	0.60	0.17	0.19	0.08	0.21	20.9	-	-	-	0.02	0.20	72	48	34
0.6	1.4	1633	12.00	0.07	4.58	0.17	4.53	0.17	4.55	0.09	0.86	0.26	0.27	0.12	0.35	21.0	-	-	-	0.03	0.28	76	53	40
0.2	1.5	1928	12.01	0.09	4.87	0.18	4.83	0.18	4.86	0.10	1.07	0.34	0.34	0.15	0.45	21.2	-	-	-	0.03	0.36	79	53	42
0.9	1.6	2231	12.01	0.11	5.18	0.20	5.15	0.19	5.16	0.11	1.32	0.45	0.43	0.20	0.59	21.4	-	-	-	0.04	0.44	81	55	45
0.3	1.7	2606	12.02	0.12	5.47	0.21	5.47	0.19	5.47	0.11	1.49	0.53	0.50	0.22	0.68	21.8	-	-	-	0.04	0.53	84	54	46
-0.4	1.8	3160	12.02	0.11	5.78	0.18	5.68	0.15	5.72	0.09	1.27	0.53	0.44	0.14	0.47	22.1	-	-	-	0.03	0.62	88	42	37
0	2.0	3726	12.02	0.11	6.06	0.17	6.02	0.14	6.08	0.09	1.29	0.59	0.46	0.12	0.43	22.3	-	-	-	0.03	0.71	91	37	33
-0.8	2.0	4235	12.02	0.12	6.47	0.18	6.39	0.15	6.46	0.09	1.47	0.70	0.52	0.15	0.52	22.8	-	-	-	0.03	0.81	92	38	35
0.2	2.1	4705	12.02	0.15	6.83	0.19	6.77	0.15	6.83	0.10	1.78	0.84	0.62	0.21	0.72	23.1	-	-	-	0.03	0.92	94	43	41
-0.4	2.2	5143	12.03	0.18	7.21	0.20	7.14	0.17	7.20	0.10	2.14	1.00	0.76	0.28	0.97	23.6	-	-	-	0.04	1.03	95	48	45
0.3	2.2	5588	12.03	0.20	7.50	0.20	7.43	0.17	7.51	0.10	2.41	1.12	0.88	0.31	1.13	24.0	-	-	-	0.04	1.14	96	49	47
-0.1	2.3	5984	12.02	0.23	7.73	0.21	7.65	0.17	7.80	0.11	2.72	1.28	0.95	0.41	1.34	24.4	-	-	-	0.04	1.26	97	51	49
0	2.3	6179	12.02	0.23	7.87	0.21	7.77	0.17	7.87	0.10	2.72	1.29	0.99	0.36	1.29	24.8	-	-	-	0.04	1.31	97	49	47
1.2	2.4	7953	12.03	0.42	8.89	0.26	8.75	0.23	8.87	0.15	5.02	2.18	1.80	1.04	2.98	26.6	-	-	-	0.06	1.96	100	60	59
3.8	0.9	538	12.05	0.07	3.62	0.20	3.60	0.22	3.60	0.18	0.84	0.14	0.15	0.12	0.26	24.3	24.0	24.0	20.8	0.05	0.08	48	66	32
4.3	1.2	997	12.05	0.11	4.23	0.24	4.21	0.26	4.21	0.19	1.31	0.28	0.30	0.22	0.57	24.2	24.1	24.0	20.8	0.07	0.16	61	71	43
4.0	1.4	1446	12.05	0.13	4.66	0.26	4.65	0.26	4.64	0.19	1.61	0.41	0.42	0.29	0.81	24.2	24.1	24.0	20.8	0.08	0.23	70	73	51
4.1	1.5	1785	12.05	0.16	5.01	0.27	4.98	0.27	5.00	0.19	1.89	0.53	0.53	0.35	1.03	24.4	24.2	23.7	20.8	0.08	0.29	75	73	55
4.2	1.6	2235	12.05	0.19	5.42	0.29	5.38	0.28	5.40	0.19	2.30	0.70	0.68	0.44	1.35	24.6	24.3	23.7	20.8	0.09	0.38	79	74	59
4.7	1.7	2735	12.05	0.24	5.87	0.32	5.80	0.31	5.85	0.22	2.94	0.95	0.89	0.60	1.85	24.9	24.5	23.7	20.8	0.11	0.47	83	76	63
4.3	1.8	3166	12.05	0.26	6.14	0.32	6.12	0.30	6.13	0.21	3.16	1.07	0.99	0.65	2.05	25.1	24.6	23.6	20.9	0.11	0.56	86	76	65
4.9	1.9	3552	12.05	0.31	6.47	0.34	6.42	0.32	6.45	0.23	3.75	1.30	1.19	0.80	2.52	25.3	24.7	23.6	20.8	0.12	0.64	88	77	67
4.8	2.0	4017	12.05	0.34	6.78	0.35	6.71	0.32	6.77	0.23	4.13	1.48	1.33	0.91	2.85	25.6	25.1	23.6	20.8	0.13	0.74	90	77	69
4.2	2.1	4432	12.05	0.35	7.01	0.33	6.95	0.31	6.98	0.21	4.22	1.56	1.39	0.92	2.92	25.9	25.4	23.8	20.8	0.11	0.84	92	75	69
4.5	2.1	4827	12.05	0.39	7.30	0.35	7.21	0.31	7.27	0.23	4.73	1.77	1.56	1.08	3.34	26.3	25.5	23.8	20.9	0.12	0.95	93	76	71
4.1	2.2	5243	12.05	0.41	7.52	0.34	7.44	0.31	7.52	0.22	4.91	1.87	1.64	1.12	3.46	26.6	25.9	24.0	20.8	0.12	1.05	94	75	71
4.9	2.2	5701	12.04	0.49	7.79	0.36	7.70	0.34	7.81	0.25	5.85	2.21	1.97	1.40	4.26	27.1	26.2	24.0	20.8	0.14	1.19	95	76	73
5.0	2.3	6185	12.05	0.53	8.11	0.37	8.01	0.34	8.09	0.25	6.41	2.45	2.18	1.56	4.72	27.6	26.6	24.2	20.8	0.15	1.32	97	76	74

Table B.5: Results of hybrid pump drive simulation I.

simulated																from measurements				calculated				
T_{AVG} (mNm)	$T_{b,AVG}$ (mNm)	n_{AVG} (rpm)	$U_{DC,AVG}$ (V)	$I_{DC,AVG}$ (A)	$U_{A,RMS}$ (V)	$I_{A,RMS}$ (A)	$U_{B,RMS}$ (V)	$I_{B,RMS}$ (A)	$U_{C,RMS}$ (V)	$I_{C,RMS}$ (A)	P_{in} (W)	P_A (W)	P_B (W)	P_C (W)	P_{out} (W)	T_W (°C)	T_S (°C)	T_H (°C)	T_A (°C)	P_{Cu} (W)	P_{Fe} (W)	$\eta_{control}$ (%)	η_{BLDC} (%)	η_{total} (%)
16.7	1.0	677	12.04	0.36	4.96	0.64	4.93	0.66	4.95	0.60	4.38	0.65	0.67	0.62	1.26	25.3	24.8	23.7	21.1	0.55	0.13	44	65	29
19.9	1.2	1053	12.04	0.52	5.51	0.76	5.51	0.79	5.51	0.71	6.30	1.12	1.14	1.03	2.33	25.7	24.9	23.7	21.1	0.77	0.19	52	71	37
17.7	1.4	1483	12.04	0.53	5.69	0.71	5.68	0.72	5.72	0.64	6.33	1.35	1.34	1.19	2.97	25.8	24.9	23.7	21.1	0.65	0.26	61	76	47
19.9	1.5	1806	12.04	0.66	6.08	0.80	6.03	0.80	6.05	0.70	7.90	1.81	1.77	1.57	4.03	26.1	25.1	23.7	21.1	0.80	0.32	65	78	51
17.1	1.6	2254	12.03	0.63	6.24	0.72	6.22	0.71	6.22	0.61	7.56	1.94	1.88	1.63	4.41	26.2	25.3	23.7	21.1	0.64	0.40	72	81	58
17.4	1.7	2483	12.04	0.68	6.43	0.73	6.39	0.72	6.42	0.63	8.15	2.15	2.09	1.82	4.96	26.4	25.4	23.8	21.1	0.66	0.43	74	82	61
17.0	1.8	2865	12.04	0.72	6.67	0.73	6.61	0.71	6.64	0.61	8.67	2.43	2.33	2.02	5.62	26.5	25.5	23.9	21.1	0.64	0.51	78	83	65
17.0	1.9	3294	12.04	0.79	6.94	0.74	6.86	0.72	6.92	0.61	9.57	2.82	2.67	2.31	6.52	26.8	25.8	23.9	21.1	0.66	0.62	82	84	68
17.5	1.9	3531	12.03	0.85	7.17	0.76	7.02	0.73	7.03	0.63	10.27	3.10	2.89	2.54	7.18	27.1	26.0	24.1	21.1	0.69	0.66	83	84	70
16.0	2.0	3951	12.03	0.85	7.30	0.71	7.24	0.69	7.29	0.59	10.20	3.18	3.00	2.60	7.43	27.5	26.3	24.2	21.1	0.61	0.75	86	85	73
15.9	2.0	4345	12.03	0.91	7.53	0.71	7.47	0.69	7.51	0.59	10.90	3.49	3.28	2.84	8.16	27.8	26.5	24.3	21.1	0.61	0.84	88	85	75
16.2	2.1	4762	12.03	0.99	7.78	0.73	7.69	0.70	7.75	0.60	11.90	3.92	3.65	3.18	9.14	28.3	27.0	24.5	21.1	0.64	0.97	90	85	77
16.7	2.2	5173	12.03	1.08	8.01	0.75	7.91	0.72	7.99	0.62	13.02	4.33	4.05	3.57	10.23	28.9	27.5	24.7	21.1	0.68	1.05	92	86	79
18.7	2.2	5499	12.03	1.25	8.27	0.82	8.17	0.79	8.21	0.69	15.07	5.07	4.71	4.21	12.04	29.4	28.0	24.9	21.1	0.81	1.15	93	86	80
20.1	2.3	5890	12.03	1.41	8.50	0.87	8.40	0.84	8.47	0.74	16.99	5.76	5.39	4.86	13.81	30.0	28.4	25.1	21.1	0.93	1.27	94	86	81
18.1	2.3	6115	12.03	1.33	8.54	0.80	8.43	0.77	8.51	0.67	15.97	5.50	5.13	4.58	13.07	30.4	28.6	25.2	21.1	0.79	1.35	95	86	82
25.9	0.9	533	12.04	0.61	5.51	0.94	5.50	0.96	5.50	0.91	7.39	0.95	0.96	0.92	1.50	26.4	25.2	24.2	21.1	1.20	0.12	38	53	20
26.3	1.2	1045	12.04	0.74	5.93	0.98	5.92	1.00	5.92	0.92	8.91	1.52	1.53	1.43	3.01	27.1	25.8	24.2	21.2	1.28	0.20	50	67	34
24.3	1.4	1473	12.03	0.76	6.12	0.93	6.08	0.94	6.09	0.85	9.11	1.85	1.83	1.67	3.95	27.4	26.1	24.4	21.2	1.13	0.27	59	74	43
25.6	1.5	1846	12.03	0.89	6.44	0.98	6.44	0.99	6.42	0.89	10.66	2.37	2.33	2.12	5.23	27.8	26.3	24.4	21.2	1.26	0.33	64	77	49
26.6	1.6	2208	12.03	1.01	6.76	1.03	6.74	1.03	6.74	0.93	12.13	2.89	2.82	2.59	6.52	28.4	26.7	24.6	21.2	1.37	0.41	68	79	54
26.3	1.7	2680	12.03	1.10	7.05	1.03	7.00	1.02	7.03	0.92	13.18	3.41	3.28	3.00	7.85	28.6	27.0	24.7	21.2	1.36	0.48	74	81	60
24.8	1.8	3040	12.03	1.10	7.18	0.98	7.16	0.98	7.19	0.87	13.27	3.59	3.50	3.17	8.46	28.9	27.2	24.8	21.2	1.24	0.56	77	82	64
25.5	1.9	3515	12.03	1.24	7.49	1.02	7.44	1.00	7.47	0.89	14.90	4.27	4.08	3.71	10.09	29.4	27.7	25.0	21.2	1.32	0.66	81	84	68
26.3	2.0	3909	12.03	1.37	7.75	1.05	7.70	1.03	7.74	0.93	16.45	4.86	4.63	4.28	11.58	29.9	28.0	25.1	21.2	1.40	0.79	84	84	70
26.2	2.0	4352	12.03	1.46	7.97	1.06	7.89	1.03	7.95	0.92	17.54	5.39	5.11	4.66	12.89	30.4	28.5	25.3	21.2	1.41	0.85	86	85	73
25.9	2.1	4719	12.03	1.52	8.18	1.05	8.09	1.03	8.14	0.91	18.31	5.76	5.48	4.98	13.84	30.8	28.8	25.5	21.2	1.39	1.00	89	85	76
26.3	2.2	5152	12.03	1.64	8.38	1.06	8.29	1.04	8.35	0.93	19.69	6.34	5.99	5.52	15.34	31.3	29.3	25.7	21.2	1.43	1.09	91	86	78
25.5	2.2	5484	12.03	1.67	8.50	1.04	8.41	1.01	8.47	0.91	20.04	6.58	6.19	5.71	15.92	31.5	29.5	25.8	21.2	1.37	1.19	92	86	79
26.0	2.2	5858	12.02	1.78	8.69	1.06	8.57	1.03	8.67	0.93	21.36	7.14	6.70	6.20	17.32	32.1	29.8	26.0	21.2	1.43	1.29	94	86	81
22.7	2.3	6107	12.03	1.62	8.68	0.95	8.58	0.92	8.66	0.82	19.45	6.60	6.19	5.67	15.96	32.2	30.0	26.1	21.2	1.14	1.36	95	86	82

Table B.6: Results of hybrid pump drive simulation II.

simulated																from measurements				calculated				
T_{AVG} (mNm)	$T_{b,AVG}$ (mNm)	n_{AVG} (rpm)	$U_{DC,AVG}$ (V)	$I_{DC,AVG}$ (A)	$U_{A,RMS}$ (V)	$I_{A,RMS}$ (A)	$U_{B,RMS}$ (V)	$I_{B,RMS}$ (A)	$U_{C,RMS}$ (V)	$I_{C,RMS}$ (A)	P_{in} (W)	P_A (W)	P_B (W)	P_C (W)	P_{out} (W)	T_W (°C)	T_S (°C)	T_H (°C)	T_A (°C)	P_{Cu} (W)	P_{Fe} (W)	$\eta_{control}$ (%)	η_{BLDC} (%)	η_{total} (%)
29.9	0.9	520	12.00	0.75	5.76	1.07	5.75	1.10	5.75	1.04	8.99	1.12	1.14	1.09	1.68	23.4	21.9	20.3	20.0	1.55	0.13	37	50	19
31.1	1.1	915	12.01	0.89	6.13	1.13	6.12	1.15	6.12	1.08	10.70	1.69	1.69	1.60	3.09	24.6	23.0	20.8	20.1	1.71	0.19	47	62	29
31.6	1.3	1392	12.01	1.03	6.48	1.17	6.45	1.18	6.47	1.09	12.38	2.35	2.34	2.18	4.80	25.8	24.0	21.3	20.1	1.80	0.27	56	70	39
30.1	1.5	1848	12.01	1.08	6.72	1.14	6.69	1.14	6.69	1.04	12.91	2.81	2.76	2.54	6.10	26.2	24.4	21.7	20.1	1.67	0.34	63	75	47
30.1	1.6	2271	12.02	1.18	6.98	1.15	6.94	1.15	6.96	1.04	14.17	3.37	3.28	3.02	7.54	26.8	24.9	22.0	20.1	1.70	0.43	68	78	53
29.6	1.7	2715	12.02	1.26	7.22	1.14	7.17	1.13	7.21	1.03	15.13	3.88	3.74	3.45	8.91	27.4	25.5	22.4	20.2	1.67	0.50	73	80	59
30.9	1.8	3101	12.02	1.42	7.51	1.19	7.46	1.18	7.49	1.07	17.03	4.57	4.40	4.07	10.62	28.0	25.9	22.6	20.1	1.82	0.60	77	81	62
30.4	1.9	3507	12.02	1.49	7.71	1.18	7.65	1.17	7.68	1.06	17.93	5.04	4.82	4.46	11.88	28.6	26.4	22.9	20.2	1.79	0.66	80	83	66
30.1	2.0	3902	12.02	1.57	7.91	1.18	7.84	1.16	7.89	1.05	18.88	5.51	5.26	4.88	13.13	29.1	26.9	23.2	20.3	1.77	0.76	83	84	70
30.5	2.0	4302	12.02	1.69	8.12	1.20	8.07	1.18	8.09	1.06	20.28	6.10	5.83	5.41	14.66	29.9	27.5	23.6	20.3	1.82	0.85	85	85	72
30.1	2.1	4737	12.02	1.77	8.30	1.19	8.26	1.16	8.30	1.06	21.26	6.61	6.28	5.84	15.98	30.5	28.1	24.0	20.5	1.80	0.95	88	85	75
31.0	2.2	5089	12.02	1.91	8.52	1.22	8.41	1.19	8.48	1.09	22.97	7.30	6.90	6.46	17.68	31.2	28.6	24.3	20.5	1.91	1.07	90	86	77
31.6	2.2	5567	12.02	2.07	8.74	1.25	8.66	1.22	8.70	1.11	24.84	8.10	7.65	7.15	19.73	31.9	29.2	24.7	20.5	1.99	1.19	92	86	79
30.9	2.3	6011	12.01	2.14	8.91	1.23	8.79	1.20	8.87	1.09	25.66	8.57	8.06	7.56	20.90	32.4	29.7	24.9	20.4	1.93	1.36	94	86	81
37.9	0.9	494	12.04	1.04	6.25	1.34	6.24	1.36	6.24	1.31	12.56	1.54	1.55	1.51	2.00	27.8	25.5	22.9	20.5	2.45	0.14	37	44	16
36.7	1.2	1055	12.04	1.15	6.57	1.33	6.54	1.35	6.54	1.26	13.88	2.30	2.30	2.17	4.18	28.5	26.0	23.0	20.5	2.37	0.22	49	62	30
37.6	1.3	1328	12.04	1.27	6.78	1.37	6.76	1.38	6.79	1.30	15.30	2.79	2.77	2.64	5.41	29.3	26.7	23.4	20.5	2.52	0.27	54	66	35
37.1	1.5	1848	12.03	1.39	7.06	1.37	7.05	1.38	7.05	1.27	16.73	3.54	3.50	3.27	7.46	29.7	27.1	23.7	20.6	2.48	0.36	62	72	45
37.7	1.6	2241	12.03	1.53	7.32	1.39	7.32	1.40	7.33	1.29	18.40	4.21	4.14	3.87	9.22	30.6	27.8	24.0	20.6	2.59	0.42	66	75	50
36.3	1.7	2660	12.03	1.57	7.52	1.36	7.48	1.36	7.50	1.25	18.95	4.70	4.56	4.27	10.59	30.8	28.1	24.3	20.6	2.44	0.50	71	78	56
37.9	1.8	3148	12.03	1.79	7.88	1.42	7.81	1.41	7.82	1.30	21.55	5.70	5.50	5.15	13.08	31.9	28.9	24.7	20.6	2.66	0.61	76	80	61
37.2	1.9	3468	12.03	1.85	7.99	1.41	7.94	1.39	7.96	1.28	22.21	6.10	5.86	5.52	14.21	32.1	29.2	24.9	20.6	2.60	0.68	79	81	64
37.4	2.0	3868	12.03	1.97	8.18	1.41	8.12	1.40	8.17	1.29	23.68	6.73	6.48	6.15	15.96	32.5	29.5	25.2	20.7	2.64	0.77	82	82	67
39.5	2.0	4224	12.03	2.19	8.44	1.49	8.40	1.48	8.41	1.36	26.37	7.74	7.42	7.02	18.39	33.2	30.0	25.4	20.7	2.93	0.87	84	83	70
37.8	2.1	4639	12.02	2.20	8.56	1.44	8.49	1.42	8.53	1.30	26.49	8.05	7.70	7.28	19.36	33.6	30.4	25.7	20.7	2.71	0.96	87	84	73
37.7	2.1	5017	12.03	2.30	8.72	1.44	8.63	1.42	8.68	1.31	27.70	8.63	8.24	7.82	20.91	34.1	30.8	25.9	20.7	2.72	1.07	89	85	75
37.3	2.2	5483	12.03	2.41	8.89	1.43	8.80	1.41	8.86	1.29	28.96	9.30	8.85	8.39	22.65	34.7	31.3	26.1	20.7	2.69	1.19	92	85	78
37.4	2.3	5961	12.02	2.55	9.08	1.44	8.98	1.41	9.05	1.30	30.69	10.09	9.60	9.13	24.75	35.4	31.9	26.5	20.8	2.73	1.34	94	86	81

Table B.7: Results of hybrid pump drive simulation III.

simulated																from measurements				calculated				
T_{AVG} (mNm)	$T_{b,AVG}$ (mNm)	n_{AVG} (rpm)	$U_{DC,AVG}$ (V)	$I_{DC,AVG}$ (A)	$U_{A,RMS}$ (V)	$I_{A,RMS}$ (A)	$U_{B,RMS}$ (V)	$I_{B,RMS}$ (A)	$U_{C,RMS}$ (V)	$I_{C,RMS}$ (A)	P_{in} (W)	P_A (W)	P_B (W)	P_C (W)	P_{out} (W)	T_W (°C)	T_S (°C)	T_H (°C)	T_A (°C)	P_{Cu} (W)	P_{Fe} (W)	$\eta_{control}$ (%)	η_{BLDC} (%)	η_{total} (%)
46.6	0.9	498	12.04	1.42	6.74	1.63	6.73	1.66	6.73	1.59	17.06	2.13	2.13	2.07	2.47	32.3	28.7	24.4	20.9	3.71	0.15	37	39	14
43.7	1.2	980	12.04	1.44	6.89	1.55	6.87	1.58	6.87	1.49	17.34	2.76	2.75	2.63	4.60	32.4	29.0	24.9	21.0	3.33	0.21	47	57	27
44.7	1.4	1465	12.04	1.64	7.23	1.61	7.19	1.62	7.22	1.53	19.77	3.72	3.68	3.51	7.07	33.5	30.0	25.4	21.0	3.54	0.30	55	65	36
44.9	1.5	1907	12.04	1.79	7.46	1.63	7.46	1.64	7.47	1.53	21.54	4.55	4.47	4.24	9.27	34.0	30.4	25.7	21.0	3.61	0.37	62	70	43
43.6	1.6	2235	12.04	1.83	7.62	1.60	7.58	1.60	7.61	1.49	22.01	4.99	4.88	4.62	10.59	35.5	31.7	26.9	21.0	3.46	0.43	66	73	48
44.9	1.7	2717	12.03	2.05	7.92	1.65	7.87	1.65	7.90	1.53	24.64	6.05	5.89	5.57	13.28	35.8	31.8	27.0	20.9	3.68	0.55	71	76	54
44.8	1.9	3217	12.03	2.20	8.17	1.65	8.14	1.64	8.16	1.53	26.45	6.95	6.72	6.40	15.73	36.2	32.1	27.2	21.0	3.69	0.64	76	78	59
45.8	1.9	3525	12.03	2.35	8.41	1.70	8.24	1.67	8.31	1.56	28.27	7.72	7.38	7.08	17.61	36.3	32.2	27.1	20.9	3.85	0.72	78	79	62
43.5	2.0	3924	12.03	2.34	8.48	1.62	8.40	1.60	8.40	1.49	28.17	8.04	7.67	7.34	18.69	36.6	32.5	27.3	20.9	3.53	0.84	82	81	66
45.4	2.0	4305	12.02	2.57	8.68	1.69	8.62	1.67	8.65	1.55	30.93	9.07	8.70	8.32	21.38	37.0	33.0	27.5	21.0	3.83	0.89	84	82	69
44.0	2.1	4707	12.02	2.61	8.82	1.64	8.71	1.63	8.82	1.51	31.42	9.52	9.14	8.71	22.71	37.5	33.4	27.7	21.0	3.64	1.02	87	83	72
44.5	2.1	5068	12.02	2.75	8.96	1.66	8.87	1.64	8.92	1.53	33.11	10.29	9.83	9.42	24.74	38.0	33.8	27.9	21.0	3.73	1.07	89	84	75
45.9	2.2	5560	12.02	3.01	9.18	1.72	9.09	1.70	9.14	1.58	36.19	11.57	11.07	10.64	28.04	38.9	34.4	28.1	21.0	3.99	1.25	92	84	77
44.1	2.2	5876	12.02	2.99	9.24	1.66	9.14	1.64	9.20	1.52	35.93	11.70	11.20	10.73	28.54	39.3	34.8	28.4	21.1	3.73	1.36	94	85	79
51.2	0.9	516	12.04	1.64	6.99	1.79	7.00	1.81	6.99	1.75	19.80	2.53	2.55	2.48	2.82	38.2	33.5	28.4	21.1	4.57	0.16	38	37	14
51.7	1.2	1047	12.04	1.85	7.31	1.82	7.32	1.85	7.32	1.76	22.26	3.62	3.64	3.48	5.80	38.5	33.8	28.4	21.2	4.71	0.24	48	54	26
53.0	1.3	1286	12.04	2.00	7.51	1.88	7.48	1.90	7.52	1.80	24.04	4.24	4.24	4.06	7.31	38.8	33.9	28.5	21.1	4.97	0.26	52	58	30
50.1	1.5	1847	12.04	2.04	7.66	1.80	7.64	1.81	7.67	1.70	24.57	5.08	5.00	4.78	9.98	38.6	34.0	28.6	20.9	4.51	0.38	60	67	41
51.0	1.6	2264	12.03	2.23	7.90	1.84	7.92	1.84	7.90	1.73	26.84	6.05	5.93	5.64	12.47	39.0	34.3	28.6	20.8	4.69	0.45	66	71	46
50.7	1.7	2710	12.03	2.37	8.14	1.84	8.14	1.84	8.16	1.72	28.47	6.92	6.74	6.43	14.87	39.3	34.5	28.7	20.8	4.67	0.55	71	74	52
50.8	1.9	3234	12.03	2.55	8.40	1.85	8.37	1.84	8.40	1.72	30.67	8.04	7.76	7.43	17.83	39.8	34.9	28.8	20.8	4.72	0.68	76	77	58
51.1	1.9	3480	12.03	2.65	8.48	1.86	8.43	1.85	8.51	1.74	31.87	8.56	8.28	7.95	19.31	40.0	35.2	29.0	20.8	4.79	0.70	78	78	61
51.0	2.0	3918	12.03	2.79	8.71	1.87	8.65	1.85	8.70	1.73	33.60	9.46	9.12	8.75	21.74	40.3	35.3	29.0	20.8	4.79	0.80	81	80	65
50.8	2.0	4316	12.03	2.92	8.88	1.87	8.80	1.85	8.84	1.73	35.11	10.25	9.87	9.45	23.91	40.5	35.5	29.1	20.8	4.79	0.88	84	81	68
49.7	2.1	4717	12.02	2.98	8.95	1.83	8.90	1.81	8.93	1.70	35.83	10.81	10.38	9.99	25.57	40.8	35.8	29.3	20.8	4.60	1.00	87	82	71
51.7	2.1	5070	12.02	3.23	9.17	1.90	9.11	1.88	9.14	1.76	38.85	12.00	11.53	11.12	28.58	41.6	36.4	29.5	20.8	4.98	1.09	89	82	74
51.0	2.2	5648	12.02	3.39	9.35	1.88	9.25	1.86	9.31	1.74	40.70	13.05	12.51	12.08	31.48	42.0	36.7	29.6	20.8	4.89	1.28	93	84	77
59.3	1.2	999	12.04	2.22	7.63	2.07	7.63	2.10	7.62	2.01	26.76	4.31	4.32	4.14	6.33	42.5	36.3	29.2	20.7	6.21	0.23	48	50	24
61.3	1.4	1649	12.03	2.58	8.05	2.16	8.06	2.18	8.06	2.08	31.05	6.09	6.01	5.80	10.83	43.8	37.1	29.5	20.6	6.72	0.34	58	61	35
61.5	1.6	2056	12.03	2.75	8.25	2.18	8.23	2.19	8.25	2.08	33.09	7.11	6.99	6.73	13.58	44.3	37.6	29.7	20.6	6.81	0.43	63	65	41
62.1	1.7	2595	12.03	2.99	8.55	2.22	8.49	2.22	8.50	2.09	35.96	8.54	8.32	8.00	17.34	45.0	38.1	30.0	20.6	6.98	0.54	69	70	48
62.2	1.9	3291	12.02	3.27	8.84	2.23	8.80	2.22	8.82	2.11	39.28	10.24	9.94	9.65	22.09	46.0	38.8	30.3	20.6	7.07	0.67	76	74	56
59.9	2.0	4034	12.02	3.40	9.06	2.16	8.97	2.15	9.00	2.03	40.89	11.58	11.19	10.83	26.15	46.2	39.3	30.7	20.6	6.62	0.82	82	78	64
60.9	2.1	4594	12.02	3.68	9.27	2.20	9.20	2.19	9.24	2.06	44.25	13.17	12.70	12.30	30.31	46.9	39.8	30.9	20.6	6.88	0.99	86	79	69
64.2	2.2	5194	12.01	4.14	9.54	2.32	9.45	2.30	9.50	2.17	49.74	15.50	14.92	14.51	36.11	49.2	41.2	31.5	20.7	7.68	1.13	90	80	73

Table B.8: Results of hybrid pump drive simulation IV.

B.2 Efficiency comparison of fan drive

Following tables show measured as well as simulated results for the fan drive. For the simulation results the hybrid BLDC model from section (dummy reference) was used.

measured						calculated						
n -	P_{in} (mW)	P_A (mW)	P_B (mW)	$I_{A,RMS}$ (mA)	$I_{B,RMS}$ (mA)	$P_{A,Cu}$ (mW)	$P_{B,Cu}$ (mW)	P_{Fe} (mW)	P_{out} (mW)	$\eta_{control}$ (%)	η_{BLDC} (%)	η_{total} (%)
1518	435.0	72.0	74.5	35.3	35.3	11.8	11.2	68.1	30.6	34	21	7
1971	504.4	105.3	89.8	48.6	47.7	22.3	20.4	63.7	56.4	39	29	11
1993	501.8	101.0	92.1	47.9	47.3	21.7	20.0	60.8	58.0	38	30	12
2465	603.4	140.8	130.8	61.5	60.5	35.7	32.8	63.3	99.6	45	37	17
2511	600.1	140.7	128.5	61.1	60.0	35.2	32.3	56.0	104.6	45	39	17
3007	739.9	195.0	187.3	76.3	74.8	54.9	50.2	58.4	169.7	52	44	23
3035	746.9	197.1	190.7	77.1	75.7	56.1	51.3	56.7	174.0	52	45	23
3405	927.5	263.5	271.9	94.4	93.3	84.1	77.9	78.7	239.0	58	45	26
3517	929.3	267.1	269.9	94.6	93.2	84.4	77.8	55.6	261.7	58	49	28
3977	1217.1	377.5	394.1	119.1	118.0	133.8	124.7	77.8	370.3	63	48	30
4010	1208.5	377.2	387.0	118.5	117.1	132.6	122.8	64.4	379.0	63	50	31
4472	1589.0	519.4	550.5	145.7	145.6	200.5	189.9	88.6	517.9	67	48	33
4480	1635.4	540.1	567.5	149.5	149.1	210.9	199.3	103.8	520.4	68	47	32
4910	2147.7	736.0	780.9	181.2	182.7	309.8	299.1	149.9	677.9	71	45	32
4956	2152.8	739.4	786.3	181.8	183.4	311.9	301.4	134.9	696.5	71	46	32

Table B.9: Measurement results of fan drive.

measured						calculated						
n -	P_{in} (mW)	P_A (mW)	P_B (mW)	$I_{A,RMS}$ (mA)	$I_{B,RMS}$ (mA)	$P_{A,Cu}$ (mW)	$P_{B,Cu}$ (mW)	P_{Fe} (mW)	P_{out} (mW)	$\eta_{control}$ (%)	η_{BLDC} (%)	η_{total} (%)
1500	56.2	26.7	18.8	26.0	25.8	6.4	6.2	14.1	18.8	81	41	33
2000	113.3	54.2	41.7	42.4	42.0	16.9	16.6	17.9	44.5	85	46	39
2503	189.7	95.3	69.8	55.7	54.7	29.2	28.2	20.4	87.3	87	53	46
3003	297.6	137.9	126.1	70.9	70.0	47.2	46.1	20.0	150.7	89	57	51
3502	461.9	208.3	209.3	88.8	88.8	74.2	74.1	30.2	239.1	90	57	52
4002	692.1	325.0	306.5	112.3	111.1	118.6	116.0	39.9	357.0	91	57	52
4502	950.8	438.1	437.2	133.2	133.1	166.8	166.6	33.7	508.2	92	58	53
5000	1353.4	627.3	628.3	164.0	164.0	252.7	252.8	54.1	696.0	93	55	51

Table B.10: Simulation results of fan drive with simulated iron losses and estimated fan wheel loads.

measured						calculated						
n -	P_{in} (mW)	P_A (mW)	P_B (mW)	$I_{A,RMS}$ (mA)	$I_{B,RMS}$ (mA)	$P_{A,Cu}$ (mW)	$P_{B,Cu}$ (mW)	P_{Fe} (mW)	P_{out} (mW)	$\eta_{control}$ (%)	η_{BLDC} (%)	η_{total} (%)
1500	140.8	71.7	45.9	52.2	51.5	25.6	25.0	37.1	29.8	83	25	21
2001	219.5	94.8	94.5	66.0	66.0	41.0	40.9	48.8	58.5	86	31	27
2503	305.0	134.7	134.0	76.4	76.2	54.9	54.5	55.8	103.5	88	39	34
3002	455.1	190.8	216.3	93.3	94.2	81.8	83.5	73.2	168.7	89	41	37
3502	610.2	262.7	292.0	107.8	109.7	109.2	113.0	74.1	258.4	91	47	42
4001	883.4	391.1	418.2	132.4	134.1	164.8	169.1	98.9	376.4	92	47	43
4500	1153.4	532.4	531.4	153.8	153.5	222.2	221.4	93.0	527.1	92	50	46
5001	1601.2	727.3	761.0	184.3	186.9	319.2	328.4	126.1	714.7	93	48	45

Table B.11: Simulation results of fan drive with measured iron losses and fan wheel loads.